Pseudo-ductility of Unidirectional Thin-Ply Hybrid Composites

By

Putu Suwarta

Department of Aerospace Engineering
UNIVERSITY OF BRISTOL

A dissertation submitted to the University of Bristol in accordance with the requirements of the degree of DOCTOR OF PHILOSOPHY in the Faculty of Engineering.

January 2020

Word count: 60212

ABSTRACT

Fibre composite materials suffer from sudden, brittle failure which limits their usage. It is possible to alleviate this limitation and expand the design space by using unidirectional (UD) thin ply hybrid composites that display non-linear 'pseudo-ductile' stress-strain. In real applications, structural parts made of fibre composites are often subjected to different loading conditions. It is important to be able to design a thin-ply hybrid composite that will fail in a pseudo-ductile manner under different loading conditions such as tension, compression, and bending. The durability of thin-ply hybrid composites under cyclic loading is also an important factor when designing structural parts made of thin-ply hybrids. The aim of this thesis is to explore the pseudo-ductility of unidirectional thin ply hybrid composites under tension, compression, bending and fatigue.

The incorporation of thin, spread tow ply carbon-epoxy prepreg material (ply thicknesses 0.03-0.06 mm) within a UD interlayer glass/carbon hybrid system yielded a non-linear stress-strain response under tensile loading. Hybrid configurations consisting of thin ply carbon layers with standard thickness glass layers were investigated. Video gauge images showed that fragmentation of carbon layers followed by stable delamination is responsible for the pseudo-ductile response. The loading-unloading-reloading response of glass/carbon hybrids shows a gradual loss of stiffness as fragmentation and localised delamination are present and increase with increasing strain. It was deduced that the low energy release rate of the thin ply carbon layers is responsible for the stable delamination.

Favourable pseudo-ductile strain has been achieved for hybrid configurations made of thin high modulus carbon/epoxy layers and standard thickness high strain glass/epoxy layers under longitudinal compression. The pseudo-ductile response is again due to progressive fragmentation and dispersed delamination of the thin ply carbon/epoxy layers. For the hybrid with thicker carbon layers, sudden failure occurs at a lower strain. The different damage behaviours underpin the crucial role of the carbon layer thickness and glass/carbon ratio in the unidirectional glass/carbon hybrid laminates under uniaxial compressive loading. Indirect compression of asymmetric hybrids made with different numbers of layers of high modulus carbon/epoxy sandwiched between high strain glass layers tested in four-point bending also showed a noticeable change of force-strain slope due to fragmentation and dispersed delamination of the carbon/epoxy layers on the compression side.

The flexural response of hybrid laminates made of thin high strength carbon epoxy layers and high strain glass layers has been shown to exhibit a noticeable stiffness change, *via* a combination of gradual failure by fragmentation of the carbon layers on the tensile side and very high fibre strain at failure on the compression side. For the hybrid laminates made of thin high modulus carbon epoxy layers and high strain glass layers, fragmentation has been observed on both the tension and compresson sides of the hybrid beams. Fragmentation and dispersed delamination on the tension side delayed damage accumulation on the compression side until higher final strain to failure. A high fragmentation strain on the tension side was obtained for the hybrid laminates in bending. This value is higher than the fragmentation strain to failure obtained from the static tensile testing.

The tensile fatigue behaviour of hybrid laminates made of high strength carbon epoxy and high strain glass epoxy shows a gradual stiffness reduction due to slow delamination growth when the pristine hybrid laminates were fatigued at 90% load level and no significant damage at 80% load level. When the overloaded hybrid laminates were fatigued at 70% and 80% load level, they showed gradual stiffness reduction and slow damage growth compared to the fatigued overloaded hybrids at 90% load level. At 70%, 80% and 90% load level, the overloaded hybrid laminates did not fail immediately but delaminated slowly. The delamination at different numbers of cycles was visually observable and, therefore, this hybrid system can also be used as an early warning for future maintenance and replacements in structural applications subjected to cyclic loading.

ACKNOWLEDGEMENTS

For their guidance, sharing of knowledge and never-ending support throughout the year, I would like to thank my supervisors Professor Michael R. Wisnom and Dr. Gergely Czél. I would also like to thank Dr. Mohamad Fotouhi, for the interesting discussion and made time to assist me in the lab.

Thanks also to Dr. Meisam Jalalvand who has made time for my questions and giving good advice. Many thanks also to Dr Steve Rae, Dr Oliver Nixon-Pearson, Ian Chorley, Guy Pearn, Peter Whereat, Ian Milnes, Paul Berry for their time and support by providing me with training, advice and equipment to carry out the experimental work. Big thanks also go to Dr. Marco Longana who work with me to developed the code to measure the delamination area which is helpful to complete one of our paper. For checking the English in my thesis and giving new insight in writing, I would like to thank Dr. Thomas Pozegic. For daily support, I would like to thank my colleagues Dr. Xun Wu, Jakub Rycerz, Tamas Rev, Aakash and Jibran. It was and still amazing experience, working with you.

I would also like to acknowledge The Directorate General of Higher Education of the Ministry of Education and Culture of the Republic of Indonesia (DIKTI) for giving me the opportunity to study in Bristol through the DIKTI scholarship. I am also grateful to the Institut Teknologi Sepuluh Nopember for giving me the permission to study in Bristol.

Lastly, A very special gratitude goes out to my parents, my wife and daughter, my sister and her family for all the love, support and patience through the year.

" Therefore, without being attached to the fruits of activities, one should act as a matter of duty; for by working without attachment, one attains the Supreme."
(BhagavadGita Chapter 3, Verse 19)

This work is part of the EPSRC Programme Grant EP/102946X/1 on High Performance Ductile Composite Technology in collaboration with Imperial College, London.

Bristol, 6 January 2020

PUBLICATIONS

Some of the work reported in this PhD dissertation have been presented as a poster, submitted or published as follows.

Journal Paper

Published:

P. Suwarta, M. Fotouhi, G. Czél, M. Longana, M.R. Wisnom. Fatigue behaviour of pseudo-ductile unidirectional thin-ply carbon/epoxy-glass/epoxy hybrid composites. **Composite Structures. 2019 ; 224 : doi.org/10.1016/j.compstruct.2019.110996**

Conference Papers

1. M.R. Wisnom, J. Fuller, **P. Suwarta**, G. Czél. Repeated tensile loading of thin-ply pseudo-ductile laminates. In: **30th Technical Conference, ASC 2015 American Society for Composites.**
2. **P. Suwarta**, M. Fotouhi, G. Czél, M. Longana, M.R. Wisnom. Fatigue behaviour of pseudo-ductile thin-ply hybrid composites. In: **21st International Conference on Composite Materials, Xi'an, August 2017.**
3. G. Czél, **P. Suwarta**, M. Jalalvand, M.R. Wisnom. Investigation of the compression performance and failure mechanism of pseudo-ductile thin-ply hybrid composites. In: **21st International Conference on Composite Materials, Xi'an, August 2017.**
4. **P. Suwarta,** G. Czél, M. Fotouhi, J. Rycerz, M.R. Wisnom. Pseudo-ductility of unidirectional thin-ply hybrid composites in longitudinal compression. In: **33rd Technical Conference, American Society for Composites, September 2018.**

Poster Presentation

P. Suwarta, G. Czél, M. Jalalvand, M.R. Wisnom. Flexural response of pseudo-ductile thin-ply hybrid composites. In: **CompTest, KU Leuven, April 2017.**

AUTHOR'S DECLARATION

I declare that the work in this dissertation was carried out in accordance with the requirements of the University's Regulations and Code of Practice for Research Degree Programmes and that it has not been submitted for any other academic award. Except where indicated by specific reference in the text, the work is the candidate's own work. Work done in collaboration with, or with the assistance of, others is indicated as such. Any views expressed in the dissertation are those of the author.

SIGNED: ..... Bristol, January 06, 2020

TABLE OF CONTENTS

LIST OF FIGURES

LIST OF TABLES

Carbon fibre reinforced polymer composites (CFRP) are an attractive choice of material for the aerospace, transportation, sport equipment, oil and gas industries as they exhibit desirable properties including low density coupled with high stiffness and strength, excellent fatigue and corrosion resistance, resulting in outstanding properties compared to traditional structural materials, such as aluminium or steel.

The aerospace industry has become the prominent consumer of fibre reinforced polymer over the past decade [1] with civil aircraft such as Boeing 787 and Airbus A350 XWB containing a considerable amount of CFRP in their structural part compared to the previous types. For Boeing 787, 50 weight % consists of CFRP materials, mostly used for the fuselage and wing skins [2], [3]. Whereas for the previous Boeing 777, the application of CFRP was restricted within a limited number of components (flaps, stabilisers, fairings, and tail) which cover only 12 weight % of the aircraft parts [2], [3]. **Figure 1.119** shows the increase of CFRP utilization in the Boeing 787 compared to Boeing 777. The Airbus XWB 350 burns 25% less fuel partly because 53% of its airframe weight is composites [4].

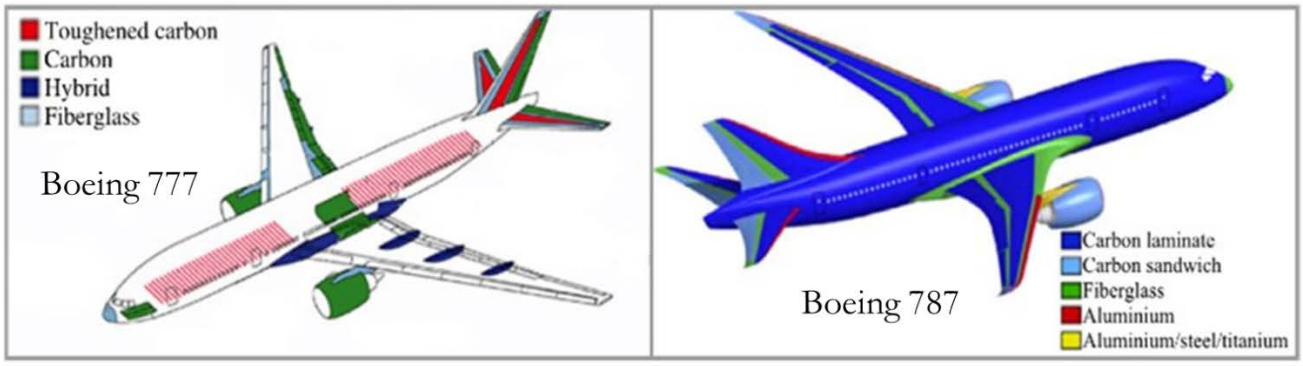

Figure 1.119. Image showing the increasing utilisation of fibre composites in aerospace. Left: Boeing 777, with limited number of components made of composites. Right: Boeing 787, the coloured regions show the location of composite parts. Figure obtained from ref: [2].

Other areas of application such as in the automotive industry have seen the launch of the BMWi3 electric car with extensive use of CFRP for the cabin of the car as a means to save weight and energy [5]. Lamborghini having the experience of using CFRP for its car production for nearly 30 years, has produced its first CFRP monocoque structure, thus improving the power-to-weight ratio of the car [6]. The sports goods industry has also moved steadily towards CFRP materials in the case of golf shafts and tennis racquets to improve the ability of the applicant to swing the shaft or hit faster owing to the low density of CFRP. High durability and greater flexibility to design sports equipment have also helped the increased consumption of CFRP [7] in this field.

The application of CFRP has also extended to the oil and gas industry in the last few decades. With corrosive environments, composites with their low density and high mechanical

properties are gaining attention for application in aggressive environments where metallic pipes could no longer meet the requirements [8]–[10]. Fibre composites have also been used in renewable energy applications such as wind turbines, where the blades are made of either glass fibre, carbon fibre or glass/carbon hybrid composites. These materials offer design flexibility to optimize the aerodynamic performance of the blades, low density, high specific stiffness and strength, also high fatigue resistance [11].

As has been shown, using composites has led to weight and fuel saving as well as improved structural efficiency. However, the brittle nature of a composite structure, as shown in **Figure 1.120** hinders the design freedom and full exploitation of the outstanding mechanical properties.

Figure 1.120. Failed structural component mode of carbon fibre composites showing catastrophic failure. Figure obtained from ref:[12].

Failure of this material type is usually sudden, without sufficient warning and little amount of residual load carrying capacity, which currently limits its application, therefore improvement to enhance the failure mode of fibre composites is needed. Creating pseudo-ductile or ductile fibre composites with progressive failure mechanisms similar to metals' yielding and strain hardening assuring detectable warning and a wide margin between damage initiation and final failure is certainly of high interest. This could stretch the application of fibre composites towards high-volume, safety-critical applications such as in the automotive and construction industries.

Chapter 2 Literature Review

2.1 Composite materials

2.1.1 Definition

A general definition of a "composite" is a "thing made of two or more different parts or elements". A composite material is assembled from two materials or more with significantly different properties, which, when combined, produced a material with a set of performance characteristics different and greater than the individual components. The new materials would be lighter, stronger or less expensive when compared to the traditional monolithic materials which in turn makes them more attractive. Examples of composite materials and their area of application is given in **Table 2.1.** The two constituents in a composite material are known as the matrix and reinforcement respectively. The general definition of those constituents will be given in **Section 2.1.2.**

Table 2.1. Example Composite materials and their application.

Composite type	Matrix	Reinforcement	Areas of Application
Organic matrix composites	Elastomers Rubber Resin	Wood fibre Glass fibre Carbon fibre Microspheres Steel fibre	Packaging Building Woodwork Automobiles Sports
Mineral matrix composites	Cement Carbon Ceramic	Carbon fibre Ceramic fibre	Aviation Biomedicine Sports Space
Metallic matrix composites	Aluminium	Carbon fibre Boron fibre	Space

2.1.2 General characteristics

In a composite material, the reinforcement is distributed within the matrix. In the case where there are several reinforcements of different properties in the matrix, the composite is said to be a hybrid. The reinforcement is usually stiffer and stronger than the matrix, while the matrix typically has a higher elongation to failure compared to the reinforcement. Each constituent in a composite material has its own role with the reinforcement acting as a load carrying component which is bound together by the matrix. The desired properties of composite materials stem from: the properties of the constituents, the geometry of the reinforcement and its distribution, the properties of the matrix-reinforcement interface. The shape, size, concentration and orientation of the reinforcement will determine the characteristics of the composite.

2.1.3 Classification of composite materials

This section will discuss the classification of composites which is particularly based on the geometry of its reinforcement. Two types of reinforcement are generally being used in a composite material: fibres and particles.

2.1.3.1 Fibre composites

The reinforcement being used in a composite material comes in the form of continuous or discontinuous, chopped or short fibres. To tailor the mechanical properties of the composite, it is possible to modify the arrangement of the fibres and their orientation. Fibres are the most widely used form of reinforcement and typically occupy a volume fraction between 0.3 and 0.7. The reinforcing fibres come with various architectures such as:

1. Unidirectional (UD) : all fibres oriented in the same direction.
2. Multidirectional : fibres oriented such that properties are developed in different directions.
3. Cross-ply laminates : alternate UD plies are stacked perpendicular to each other.
4. Woven structures : structure made from two sets of threads interlaced with each other.
5. Chopped strand mat (CSM) : random orientation of fibres in one plane.
6. 3-D random arrangement : random orientation of fibres in all directions.

Continuous fibres are generally used for unidirectional, multidirectional, and cross-ply laminates while discontinuous fibres are used for chopped strand mat (CSM) and 3-D random arrangement respectively. Continuous and discontinuous fibres are distinguished from their different length-to-diameter (l/d) ratio (aspect ratio). Continuous fibres have a preferred orientation, while discontinuous or short fibre may have a random orientation. Examples of composite architectures made of continuous reinforcement such as unidirectional, woven cloth, and helical winding are shown in **Figure 2.1**, while for discontinuous reinforcement, the examples given are chopped fibre and random mat as shown in **Figure 2.2.**

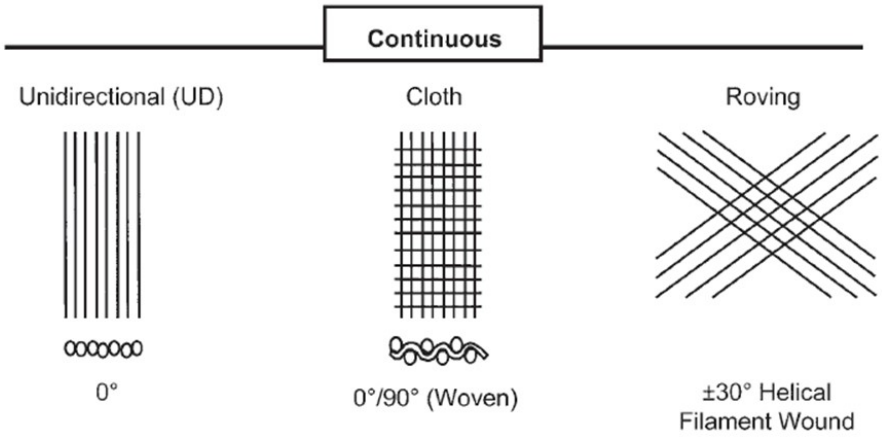

Continuous **fibres** are generally used for unidirectional, multidirectional, and cross-ply laminates while discontinuous fibres are used for chopped strand mat (CSM) and 3-D random arrangement respectively. Continuous and discontinuous fibres are distinguished from their different length-to-diameter (l/d) ratio (aspect ratio). Continuous fibres have a preferred orientation, while discontinuous or short fibre may have a random orientation. Examples of composite architectures made of continuous reinforcement such as unidirectional, woven cloth,

and helical winding are shown in **Figure 2.1**. Fibre architectures made of continuous reinforcement. Figure obtained from ref: [13].

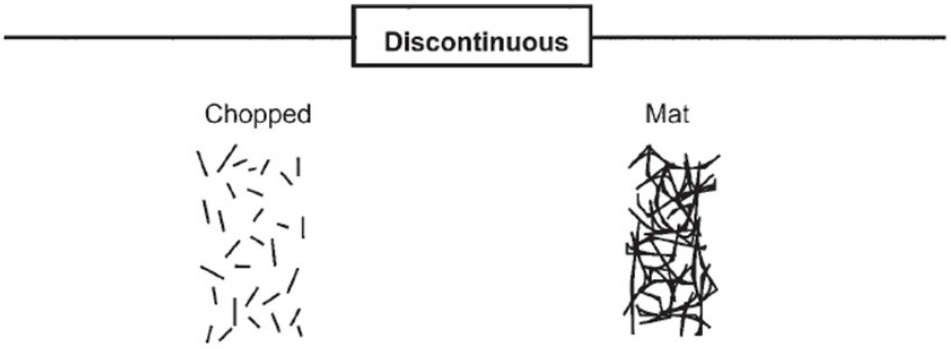

Figure 2.2. Fibre architectures made of discontinuous reinforcement. Figure obtained from ref: [13].

2.1.3.2 Particle composites

For particle composites, the reinforcement is in the form of particles which in contrast to fibres, do not usually have an aspect-ratio and privileged direction. When it comes to strengthening composites, particulate reinforcement is less effective than fibre reinforcement. Certain properties of materials or matrices such as resistance to abrasion, resistance to high temperature, decrease of shrinkage, increase in toughness are generally improved by incorporating particles. Nevertheless, the improvements are less than would be achieved in a fibre reinforced composite. This type of composite is outside the study scope of this thesis and will not be discussed further.

2.2 Damage mechanisms in unidirectional (UD) fibre composites

Damage will occur in structural parts made of fibre composites due to the strength or strain being exceeded. This section is dedicated to explaining the damage mechanisms in unidirectional (UD) fibre composites under tension, compression, bending and fatigue loading.

2.2.1 Tensile damage mechanisms

When the force acting parallel to the axis of the fibres goes beyond the strength or strain of the fibres, it is bound to cause the fibre to fracture into two or more segments. Based on Rosen's work [14], the failure in fibre composites under tensile loading can be explained as due to the statistical distribution of flaws or imperfections. The accumulation of fibre fractures at such defects or flaws within a composite is responsible for failure. The experimental study of the failure mode of a unidirectional glass fibre reinforced composite under tensile loading [14] shows fibre fracture at random locations rather than cumulatively at the site of the initial break which is due to variation

of fibre strength. In his work [14], Rosen explained that the presence of variability in fibre strength will offset the effect of stress concentration in the vicinity of broken fibre which also explains the random fibre fracture locations. The failure model in unidirectional fibre reinforced composites due to multiple fractures within a length close enough to interact, as proposed by Rosen, is shown in **Figure 2.3 (a).**

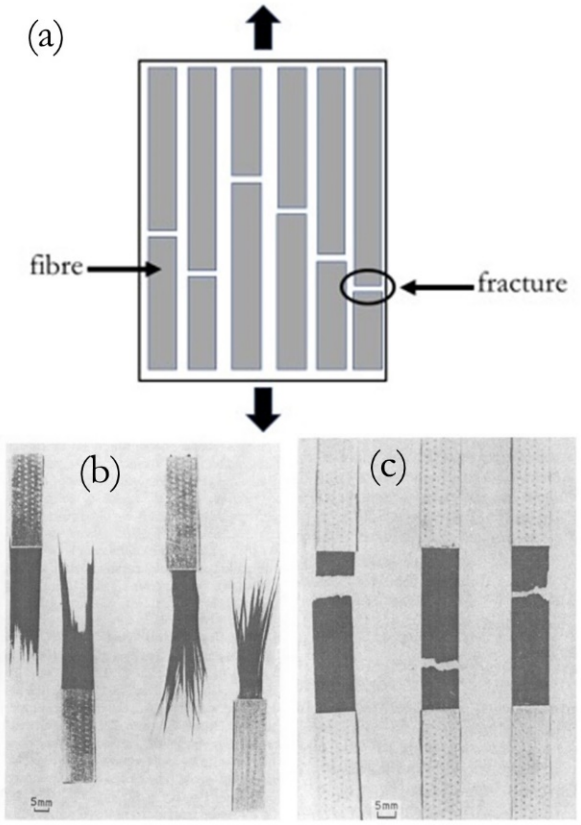

Error! Reference source not found.**.** Tensile failure model of unidirectional fibre composite. **Figure 2.3(a)** adapted from ref: [14] and not to be scaled with **Figure 2.3(b)** and **Figure 2.3(c)** obtained from ref:[15].

There are two different failure modes in tension which have been widely recognized, tensile fracture due to dispersed (scattered) failure of fibres and fracture results from localized failure [15]. In dispersed failure, the fracture surface resembles brushlike, as in **Figure 2.3(b)**, and is associated with fibre composites that have some combination of the following factors: (i) weak interface bonding between matrix and fibre, (ii) a matrix with low yield strength, (iii) fibres with large variability in strength, (iv) composites with smaller fibre volume fraction [15]. In the second failure mode, the initiation and growth of local clusters of fibre breaks becomes unstable creating a catastrophic crack [15]. In the localized failure case, the fracture surface tends to be planar as shown in **Figure 2.3(c).** Closely examining the fracture surface in **Figure 2.3(c)**, the fracture looks like a stair-shape fashion. For this particular failure mode, the fibre-matrix interface bonding tends to be stronger, the matrix is more elastic, the variability in fibre strength is much lower, and the composite contains a larger fibre volume fraction [15].

The tensile behaviour of carbon fibre has also been explored extensively from a statistical [16]–[20] as well as fracture mechanics [21]–[23] point of view. Based on those studies, it is shown that defects, which occur statistically within the fibre, determine the single fibre tensile strength.

From the nanostructure point of view, the tensile strength of PAN-based carbon fibre in the absence of large flaws is controlled by the disordered region rather than the crystallites [24]. This implies that the key to further improvements in the tensile strength of carbon fibre is the fine tuning of the fibre nanostructure.

2.2.2 Compression damage mechanisms

The compressive strength of UD fibre composites is generally 50% lower than their tensile strength which makes it a design limiting feature [25]. The dominant compressive failure mode for UD fibre composites is localized shear instability or fibre kinking; other failure modes such as shear failure may also occur [26]. The kinking mechanism in UD fibre composite is mainly caused by fibre misalignment together with plastic shear deformation in the matrix [27], [28]. The compression responses for glass fibre and carbon fibre composites were found to be different as reported by Lee and Waas [29]. Glass fibre composites exhibit a combination of splitting and kink band failure modes whereas the compressive failure mode for carbon fibre composites is mainly kinking. From their experimental results, it is shown that the carbon fibre composite had a lower compressive strength than the glass fibre composite, while the carbon fibre composite demonstrated higher stiffness [29]. Based on their analytical model to predict splitting, it was shown that the axial stiffness ratio between fibre and matrix, the fibre volume fraction, the fibre diameter, and interfacial toughness are all important parameters which determine the occurrence of splitting failure in compressively loaded fibre reinforced composites [29].

2.2.3 Flexural damage mechanisms

When a UD fibre composite is loaded under bending, different regions through the thickness are subjected to tensile or compressive stresses. The stresses under bending yield different damage mechanisms in the tension and compression regions. Moreno et al. [30], [31] conducted an experimental three-point bending and analytical study to examine the effect of dissimilar behaviour of UD carbon fibre reinforced composites under tension and compression in the fibre direction. Different span to thickness ratios were used to determine whether shear or flexural failure will occur in the specimen. They discovered a shear failure near the neutral axis for low span to thickness ratios and compressive failure for higher span to thickness ratios. The non-symmetrical failure modes found experimentally in their UD fibre composite confirmed the different response of material under tension and compression.

The flexural failure mode under four-point bending for UD glass fibre composite was found to be dependent on the interface strength [32]. When the interface strength decreases, it leads to a reduction of the flexural strength and a change of failure mode to interlaminar shear.. The tensile failure mechanism in laminates was comprised of fibre fracture, transverse matrix cracking and longitudinal matrix cracking. For the glass fibre composite failing in compression, microbuckling of the fibre is responsible for failure on the compression side.

2.2.4 Fatigue damage mechanisms

Fatigue damage mechanisms in UD fibre composites depend on the loading mode, whether it is tensile or compressive mode, and if the loading is parallel or inclined to the fibre direction. This section will only consider tensile loading and discuss the fatigue damage mechanisms for loading parallel to the fibre direction. The strain-life model for carbon, Kevlar and glass fibre composites is thought to comprise of three regimes, as identified by Harris et al. [33] in which each has a separate controlling . Their description is consistentl with the earlier proposed fatigue life model for UD fibre composite presented by Talreja [34]. The fatigue life diagram for UD fibre composites under loading parallel to the fibre direction is shown in **Figure 2.4.** As shown in **Figure 2.4** , the dashed line centred between the horizontal band indicates the static composite fracture strain, ε_c , corresponds to fibre breakage and subsequent interfacial debonding (regime 1).

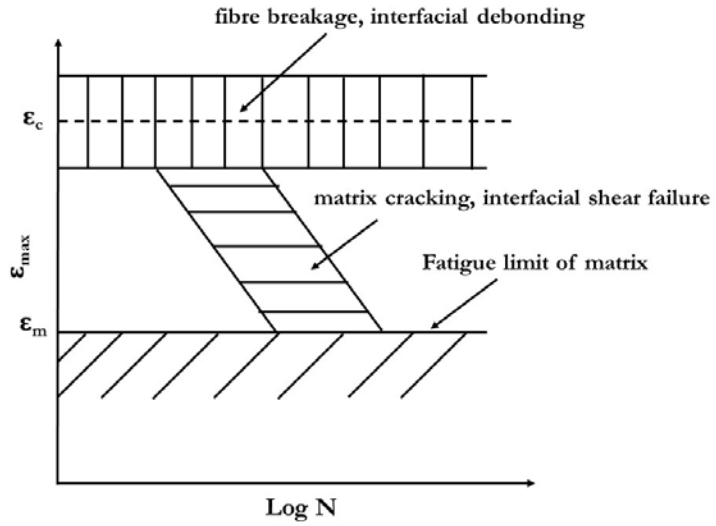

Figure 2.4. Fatigue life diagram for UD fibre composites. Figure adapted from ref:[34].

The vertical line between this horizontal band implies that there is a scatter on the fracture strain. The region below the lower bound of the fibre-breakage scatter band and above the fatigue limit of the matrix, ε_m, is a sloping band (regime 2) corresponds to matrix cracking and interfacial shear failure. These two damage mechanisms may occur simultaneously in one band towards the end of fatigue life. The occurrence of some or all of these stages will clearly depend on the characteristics of the constituents and the lay-up geometry. The fatigue data from Harris et al. [33] replotted in terms of maximum strain versus number of cycles clearly shows the influence of fibre stiffness (**Figure 2.5**). The high applied strains in the glass fibre composite rapidly lead to stage 2 (sloping band) of the Talreja model. The higher stiffness of the aramid fibre delay this stage until an advanced number of cycles, whereas the applied strains in the carbon fibre composite are barely high enough to exceed the matrix fatigue life and so the strain/log life curve remains almost flat.

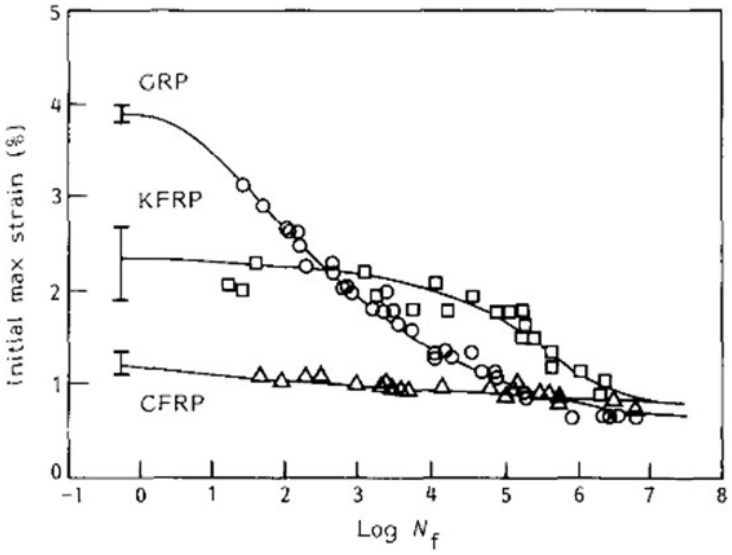

Figure 2.5. Initial strain versus log life curves for fibre composites consisting of carbon, E-glass, kevlar fibre reinforced epoxy resin matrix. The points on the extreme left of this graph (N = ½) are tensile failure strains of the composites. Figure obtained from ref:[33].

The damage mechanisms of UD fibre reinforced composites have been reviewed based on different loading conditions. It is thought that the statistical distribution of flaws within a fibre composite plays a major role in the fibre failure under tensile stresses. While fibre kinking is responsible for the failure of fibre composite under compressive loading. Different span to thickness ratios and interlaminar strength of fibre composite will determine whether flexural (compressive or tensile) or shear failure will occur under flexural loading. The fatigue lifetime of fibre composite under tensile loading is influenced by the applied strain and fibre stiffness. Based on the level of applied strain, different fatigue damage mechanisms are obtained. It can be concluded that the reinforcing fibres as the main load carrying component play a major role in the failure of fibre composites.

2.3 Tensile behaviour of UD hybrid composites

Fibre hybrid composites are a combination of two or more fibres in a matrix. Hybridisation could alleviate the drawbacks of one of the fibre types while keeping the benefits of the other. It could also lead to synergetic effects that neither of the constituents possesses [35]. Due to their attractive properties, they have found a wide range of application and many studies on the mechanical properties have been conducted. The tensile response of UD glass-carbon-glass sandwich laminates was explored by Hayashi et al. [36]. A typical stress-strain curve from this work is displayed in **Figure 2.6.**

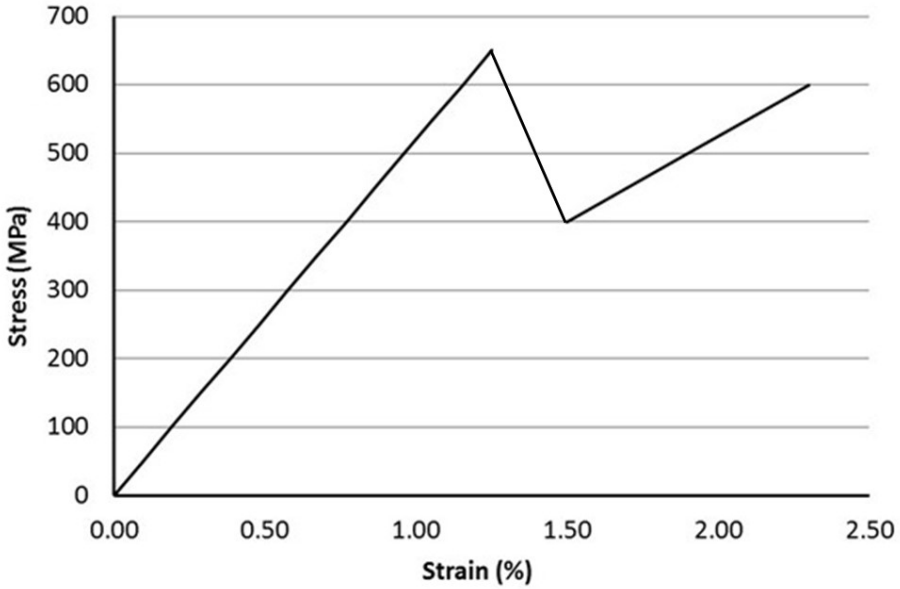

Figure 2.6. Typical experimental stress-strain curve of a unidirectional glass/carbon hybrid composite. Figure adapted from ref: [36].

As can be observed in **Figure 2.6.**, the first carbon ply failure of this hybrid specimen occurs at a peak stress of 650 MPa and 1.19% strain. This was followed by sudden stress drop probably related with unstable delamination between the fractured carbon and the intact glass ply due to excessive released strain energy. The remaining glass ply would continue to carry the load from 1.5% strain until final failure of the hybrid laminate at 2.3% strain. In the original work by Hayashi et al. [36], it was stated that the stress-strain curve was obtained from a load-controlled tension test. It should be noted that if the hybrid specimen were tested under load control, it would have already failed completely at the carbon ply failure strain as load-drops are not tolerated by the test machine. Based on this, it is suggested that the stress-strain curve in **Figure 2.6.** was obtained from a displacement-controlled tension testing. The explanation for the unstable delamination at the first carbon failure is that a thick carbon ply (0.45 – 0.5 mm) was incorporated in this unidirectional hybrid configuration which releases high energy upon fracture.

The behaviour of hybrid composite made of alternating plies of unidirectional glass/carbon-epoxy (interply) under tensile loading was explored by Aveston et al. in [37]. The tensile stress-strain curve of this material is shown in **Figure 2.7** with the non-linearity in this curve is due to multiple fractures (fragmentation) of the carbon ply followed by partial debonding between the glass and carbon ply. The OABC curve shown in **Figure 2.7** is predicted by the de-bonding theory developed by Aveston et.al. [37], [38]. A basic assumption of this theory is that the shear strength has a constant limiting value. For the line A-B, there is a process of multiple fractures of the low strain carbon fibre and delamination between the carbon and glass ply. After the failure of the carbon fibre ply, the stress distribution in the vicinity of this crack varied linearly from zero at the fractured site up to the stress value of the low strain fibres prior to failure at a site away from the fracture. The continuous curve OABC' in **Figure 2.7** itself displays an initial linear slope ($E_fV_f + E_mV_m$) and deviates from linearity when the carbon fibre reinforced ply fractured. In their work,

the subscript 'f' refers to the low strain carbon fibre while 'm' refers to the combination of matrix and high strain glass fibre while E refers to Young Modulus and V refers to volume fraction. The final slope for the experimental curve decreases gradually to the stiffness value of E_mV_m but with an offset, which suggests that there is partial bonding between the carbon and glass ply, which help to transfer some load. The debonded area in their specimen is shown as a visible regular pattern of white regions on the specimen surface running perpendicular to the fibre direction as shown in **Figure 2.8**, which was visible due to the translucent nature of the glass ply, a similar phenomenon found in the work of Czél et al. [39]. Aveston et al. [37] also reported an increase of 50% in carbon strain to failure in the interply hybrid composite compared to the all carbon fibre composite specimen. Caution is needed because the carbon baseline strain is most probably affected by stress-concentration at the end-tabs, causing premature failure of the carbon fibre composite, underestimating the carbon failure strain.

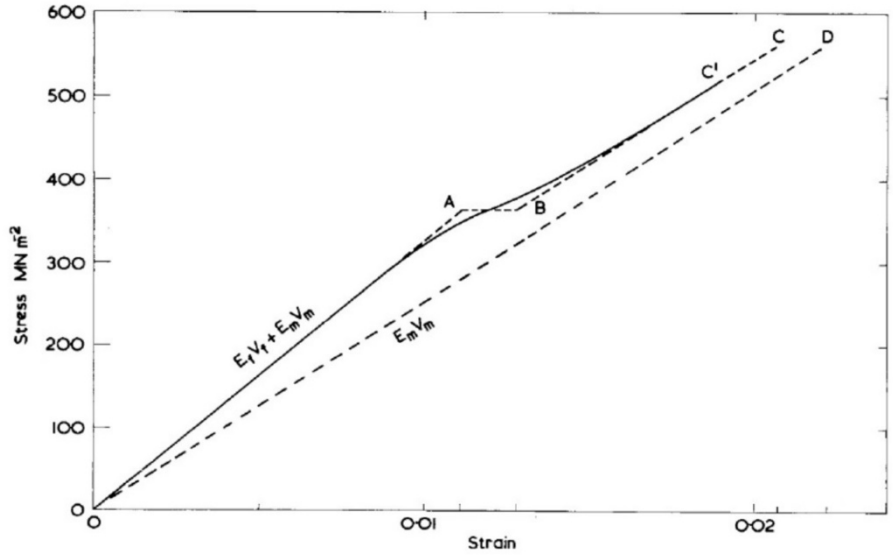

Figure 2.7. Tensile stress-strain curve for hybrid glass/carbon-epoxy-composites. The continuous line represents the experimental work and the short-dashed line (OABC) is the curve predicted by the de-bonding theory. Figure obtained from ref: [37].

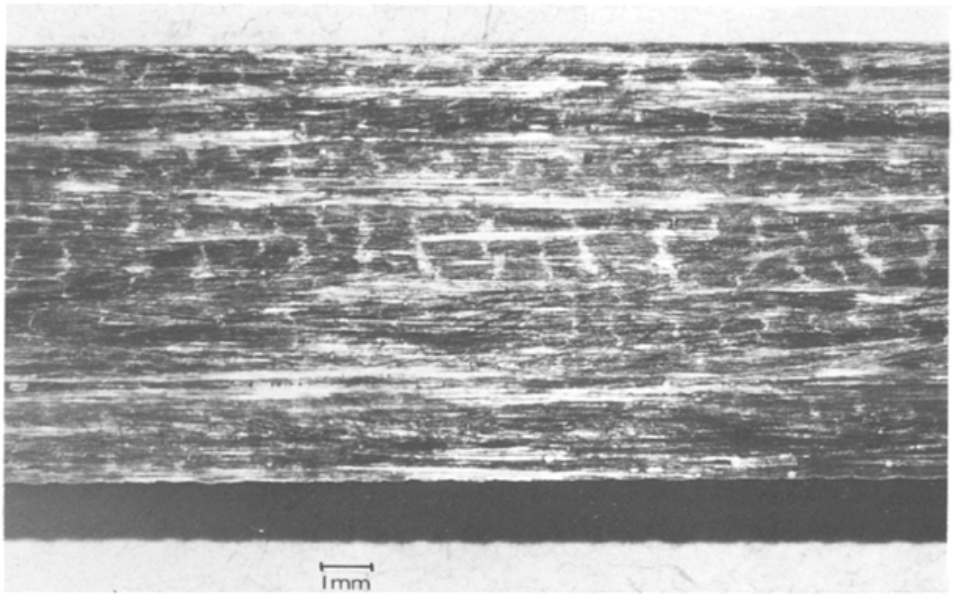

Figure 2.8. Debonded areas (vertical white regions spaced at around 1 mm) seen on the surface of the tested hybrid composite. Figure obtained from ref: [37].

The effect of introducing glass fibre on the failure stress and strain of a hybrid laminate was explored by Aveston et al. [40]. The material configuration in their work was aligned intermingled carbon and glass fibre in an epoxy matrix. Based on their experimental observation, they developed a theory on the failure mode dependency of hybrid composite on carbon-glass volume ratio as can be observed from **Figure 2.9**, a clear transition point from single fracture to multiple fractures (fragmentation) of the carbon fibre is predicted from their theory. The notations in **Figure 2.9** are described as: Vcarbon & Vglass denote the volume fraction of carbon & glass fibre respectively, the stresses σ_c, σ_g and σ'_g are the strengths of the carbon fibre reinforced polymer (CFRP) , glass fibre reinforced polymer (GFRP) and the stress in the glass fibre at the failure strain of the carbon fibre, respectively. Increasing the proportion of carbon fibre will lower the laminate strength and failure will take place as a single fracture, as there is not enough glass fibre to withstand the load transferred by the broken carbon fibre. Increasing the volume fraction (V_f) of glass fibre allows them to carry the load after the carbon fibre fractured, leading to multiple fractures of the carbon fibre. Before the transition to multiple carbon fracture, the laminate fails with a single fracture at the strain to failure of the carbon fibre. After the transition point to multiple fracture of the carbon, the laminate fails at the failure strain of the glass fibres. As also reported from previous work by Aveston et al.[37], the tensile strain to failure of the CFRP ply in this hybrid system occurs at a higher strain than that of the pure CFRP composite laminate [40]. Their work [40] has allowed simple analysis to describe a straightforward relationship presented for the interactions between the high strain and low strain components of hybrid composites.

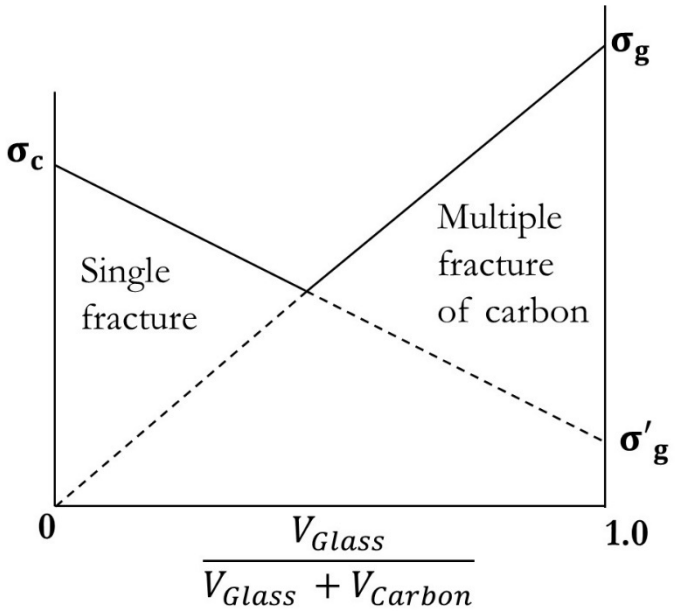

Figure 2.9. The failure mode dependency of intermingled glass-carbon hybrid laminates on carbon-glass volume ratio. Figure obtained from ref: [40].

Bunsell et al. [41] adapted the concept of gradual failure to interply hybrid laminate which contain carbon fibre reinforced polymer (CFRP) and glass fibre reinforced polymer (GFRP) plies in a laminate. The tensile tests were performed on unidirectional laminates with different ratios of

CFRP to GFRP (1:1 and 1:2). The laminate tensile response for the 1:1 ratio did not show any noticeable differences whether the GFRP was on the outside of the CFRP or vice versa. While for the 1:2 ratio, only the CFRP ply sandwiched between the two plies of GFRP was tested to keep the symmetry of the laminate. The different failure strain of the carbon and glass fibres allowed the gradual failure to occur in the hybrid laminates, in the form of multiple fractures (fragmentation) across the entire width of the CFRP ply just like in [38],[40]. The behaviour of unidirectional hybrid laminates with different ratios of CFRP to GFRP under uniaxial tension revealed similar behaviour to the load-strain curves depicted in **Figure 2.10**.

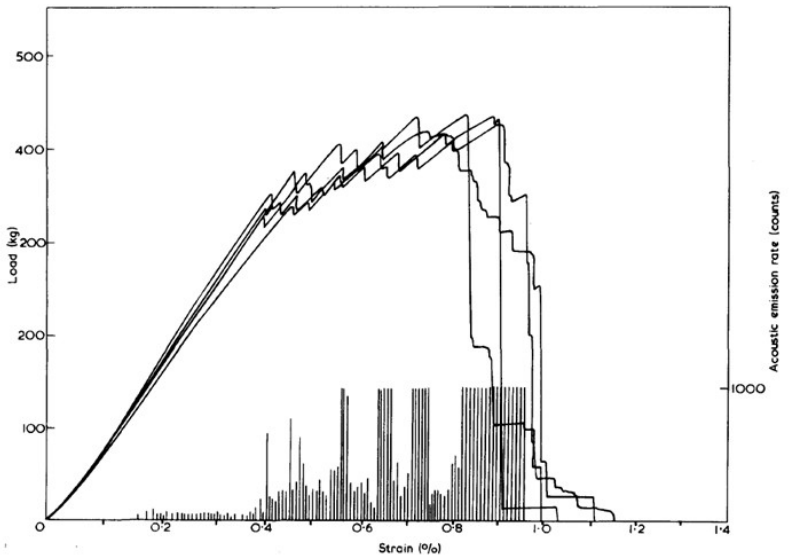

Figure 2.10. Load-strain curves for hybrid specimens consisting of one central CFRP ply sandwiched between two plies of GFRP. Figure obtained from ref: [41].

The load-strain curves shown in **Figure 2.10**. consisting of a linear elastic region before the first failure in the CFRP ply followed by subsequent small load drops due to the multiple fractures of the CFRP ply and final failure due to glass ply fracture. The acoustic emission shown in **Figure 2.10** also recorded increasing amount of multiple fractures.

Manders et al.[42] studied the effect of the glass/carbon volume ratio and the dispersion on the tensile mechanical properties of unidirectional (UD) glass/carbon/glass sandwich laminates. Two different load-strain curves for different carbon to glass ratios are shown in **Figure 2.11**.

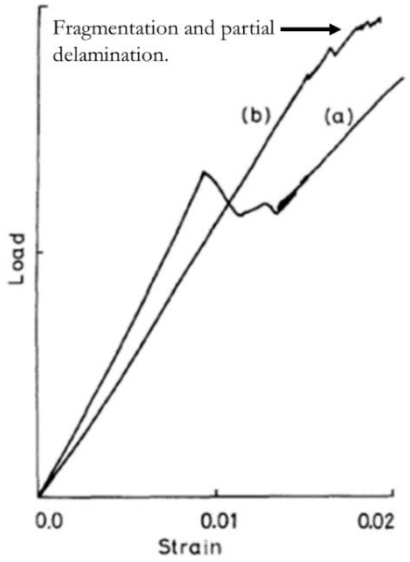

Figure 2.11. Load-strain curves for laminates with thick and thin carbon ply (a) 0.38 mm carbon-ply & 1.02 mm glass-ply and (b) 0.13 mm carbon-ply & 1.14 mm glass-ply. Figure obtained from ref: [42].

The progressive load drops for the thinner carbon ply in **Figure 2.11** (shown by the black arrow) was due to multiple fractures (fragmentation) of the central carbon ply followed by partial delamination between the glass and carbon plies. In the case of the thicker carbon ply (0.38 mm), the sudden load drop was due to carbon fibre ply failure followed by unstable delamination of the failed ply along the gauge length. The stress rises further when only the glass ply is taking the load. Based on the load-strain curve in **Figure 2.11**, it is concluded that for the thinner carbon ply (0.13 mm), higher tensile strains to failure were achieved than in thick-ply, 35% increase in carbon strain to failure was reported in this work [42]. It was also reported that for thinner central carbon plies, or lower carbon to glass ratio, a lower extent of delamination between the glass and carbon plies was observed.

Previous work by Aveston et al. [43] has shown that it is possible to achieve gradual failure by multiple fractures (fragmentation) of the matrix (low strain material) when the strain to failure of the fibre is higher than that for the matrix. To achieve this, the volume fraction of the matrix should be low, and the strength of the fibre should be greater than the strength of the matrix, to avoid fracturing the fibre. This work demonstrated a stress-strain curve with elongation at constant stress which would occur after the initial point of matrix fracture as shown in **Figure 2.12**. The strain increases until the cracks in the matrix saturate and the fibres carry all the load, which is shown as a section of increasing stress up to the failure of the fibres in **Figure 2.12**. For this to occur, the assumptions made in the study are the following: the matrix has uniform stress without a distribution and that it has constant interfacial shear strength. Aveston et al. [43] also assumed that the fibres are able to 'slip' through the fractured matrix material after they have debonded, which is predominantly not the case for the intermingled and interply hybrid composites. The tensile stress–strain response depicted in **Figure 2.12** shows a stress plateau which marks the multiple fracture of the matrix for the partially bonded / frictional case (dashed line) while for the bonded / elastic case (continuous line) is replaced by a slight increase of stress. This stress increase

for the bonded / elastic case is due to the load sharing between the matrix and fibre. At one point, there is a further increase in stress for both curves where the undamaged high strain material (fibre) takes all the load.

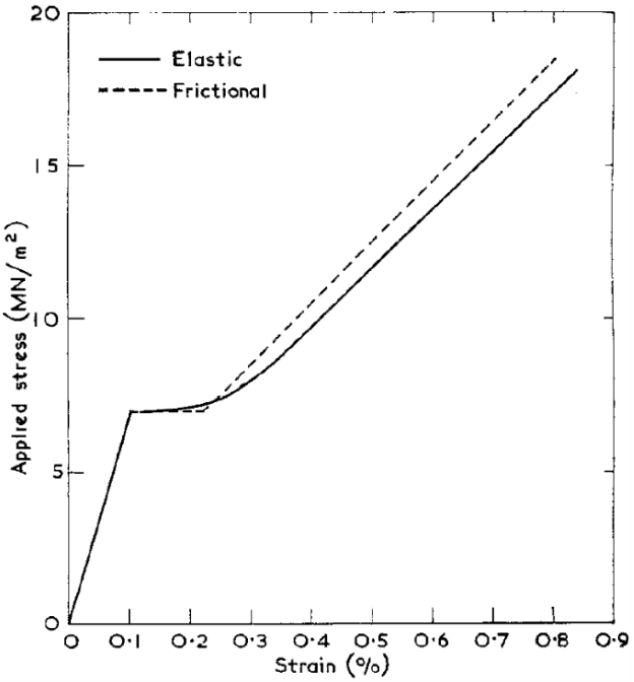

Figure 2.12. Stress-strain curve of the unbonded case (frictional) and bonded case (elastic) as shown by the dashed line and solid line respectively. The stress plateau marks the multiple fracture of the low strain matrix (cement) embedded with high strain fibers. Figure obtained from ref: [43].

An equation based on a stress-criterion developed by Aveston et al. [38] to predict interfacial debonding taking into account the maximum interfacial shear stress was also proposed, which suggests that intermingled and interply laminated composites are prone to partial debonding.

Other work on hybrid composites [44]–[47] has showed the potential to introduce gradual failure over a range of strains by combining different types of fibre, either into an intermingled [48], [49] or by creating interply hybrid structures [41],[36] . Summarising the early published work, there is potential to obtain gradual failure in hybrid composite and higher failure strains than in single fibre type composites by incorporating thin carbon plies or keeping a low carbon to glass ratio in a glass/carbon hybrid composite system.

2.4 Thin-ply composites

The previous work on hybrid composites incorporated relatively thick carbon plies in a glass/carbon epoxy hybrid system [36], [42] The thick carbon ply may cause delamination between the failed ply after the first carbon ply failure due to the high strain energy release rate. The carbon fibre also has low strain to failure which is not of particular interest for industries due to limited exploitation of the carbon fibre mechanical properties. Subsequently, this section will discuss thin-ply composites, which offer a potential new material architecture for composite applications.

Thin-ply technology has drawn industries attention in the past few decades due to the advantages it offers compared to the standard thickness plies, such as more flexibility to design composite laminates. A decrease of ply thickness would result in an increase of delamination initiation stress as shown by Leguillon's model for angle ply [$\pm\theta$]s laminate specimens with different layups = 10^o, 20^o, 30^o [50] due to the lower energy release rate of the thin laminate. It was also shown by Kim [51] that this thickness effect alters the delamination onset stress for different layups of: $[\pm 30_n/90]_s$, $[\pm 30_n/90_n]_s$, $[0_n/\pm 45_n/90_n]_s$, $[0/\pm 45/90_n]_s$, $[0/90_n/\pm 45]_s$, $[0_n/90_n/\pm 45_n]_s$, etc., where n is the number of repeated plies. It should be noted that for the above-mentioned layups, the stacking sequence and volume fraction of each ply orientation remained the same, only the number of repeated plies changed. The overall result shows that with decreasing number *n*, the delamination onset stress increases.

The efforts to reduce ply thickness below the conventional 0.125 mm thickness have proven to be slow and costly. As mentioned by Sihn et al. [52], sometimes the fibres in the ply can be damaged during the process of manufacture [52]. Kawabe [53] introduced a breakthrough technology to make thin-plies by using a pneumatic technique to spread the fibre tows. The tows are drawn over a set of guide rolls with a duct in between that is connected to a vacuum source below the tow. The air is sucked downwards, making the fibre bundle uniformly dispersed (**Figure 2.13**). The pressure differential between the outer and inner fibres of the tow causes the fibres to spread out uniformly as shown in **Figure 2.14**. As a result of the low airflow velocity, the spreading out of the filaments does not cause significant damage to the individual fibres. Kawabe [53] has stated that there is an optimum airflow velocity and tow sag to create uniformly dispersed tow. It should also be noted that the feed velocity of the tow itself has almost no effect on the spreading width of the tow within a reasonable range. This technology has been used to spread-out conventional heavy tows such as 12K filament carbon tows (nominally containing 12000 individual filaments) with an original 11 mm width into a thin tape with a new dimension of 20 mm width [53]. After it has been spread and impregnated with epoxy resin, an aerial weight of 40 g/m^2 CFRP material can be achieved.

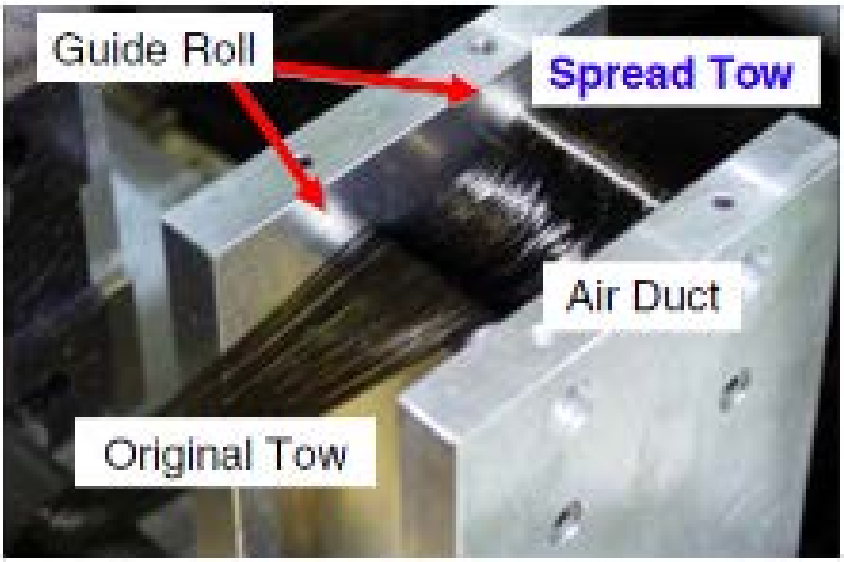

Figure 2.13. Carbon fibre tow guided by the rolls being fed into the air duct which enables them to spread out due to tension-free state. Figure obtained from ref: [52].

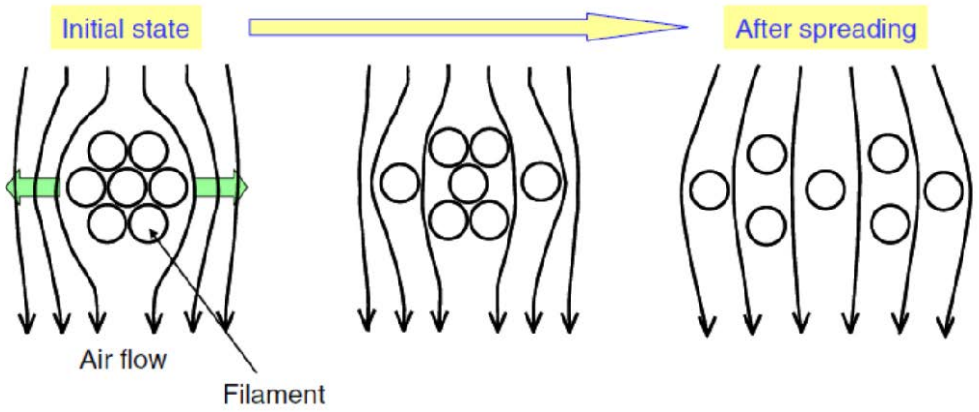

Figure 2.14. Schematic of the pressure gradient from the inner to the outer fibres due to airflow causing fibre spreading. Figure obtained from ref: [52].

This tow spreading technology has been adapted and fully industrialised by several companies such as SK Chemicals, North Thin-ply Technology (NTPT), and Chomarat. SK Chemicals are able to manufacture carbon fibre prepregs with an aerial weight of 20 g/m^2 and a thickness of 0.025 mm. Meanwhile, North Thin-ply Technology can produce thin-ply material covering a wide range of fibre types (carbon, glass, aramid, quartz, polymer fibre) with an aerial weight as low as 18 g/m^2. Bi-axial thin-ply non-crimp fabrics (NCF) using combinations of [0/25] and [0/45] layups in areal weights of 75 g/m^2 or 150 g/m^2 are also being manufactured by Chomarat.

Another experimental study by Kim et al. [54] on the effect of ply thickness on edge delamination in a laminate with a lay-up of $[\pm 45_n/0_n/90_n]_s$, has proven that with decreasing ply thickness, the occurrence of transverse micro cracking and delamination can be suppressed. Experimental and numerical studies conducted by Saito et.al. [55] suggested that by using thin 90° ply in [0°/90°n/0°] laminates, the stress for transverse crack initiation can be increased and thus

crack penetration into the 90° ply can be suppressed. With this potential, several studies of thin-ply materials manufactured by the tow spreading process have been undertaken [52], [56]–[59].

Sihn et al. [52] conducted a series of experimental tests on thin (t_p = 0.04 mm) and thick-ply (t_p = 0.2 mm) laminates. The testing included quasi-static and fatigue tension tests of unnotched and open hole laminates and compression after impact (CAI). Quasi Isotropic (QI) CFRP $[45/0/-45/90]_n$, where n is the number of repeated plies were employed during the experiments. The quasi-static tension tests revealed that the ultimate tensile strength of thin-ply laminates (t_p = 0.04 mm) is approximately 10% higher compared to the thick-ply one (t_p = 0.2 mm) and were linear up until the final failure. As for the fatigue testing, after 50,000 cycles at 60% of the unnotched thin-ply laminate strength, the thin-ply laminate retains its static tensile strength. In contrast, the thick-ply laminate showed strength and stiffness reductions of 17%. X-Ray computed tomography (XCT) images of the thick-ply laminates at 50,000 cycles, showed extensive micro-cracking and delamination from the free edge. While for the thin-ply specimens, there was little or no visible damage after 50,000 cycles. In static open hole tension tests (OHT), the ultimate tensile strength of the thin specimens is approximately 10% lower than that of the thick specimens. XCT images of the thick specimens show fibre splitting and many microcracks near the hole edge as well as the outer free edges. These damage mechanisms relaxed the stress concentration near the hole, which resulted in higher notched strength for the thick specimen. Acoustic emission (AE) event counts of the QI thin and thick specimens monitored during OHT loading, revealed fewer damage events for the thin-ply specimens. This agrees with the lower level of damage observed in the thin-ply laminates on the XCT images. For Impact testing, the results were not conclusive, as the ultrasound c-scans indicated that the thin and thick specimens displayed a similar depth and size of delamination area, nevertheless, the thin specimens sustained a higher stress level for bifurcations from the strain gauge measurement on the front and back faces of the laminate under CAI testing. This higher bifurcation load suggests that the thin-ply laminates are able to withstand higher loads without delamination than the thick-ply laminates.

Yokozeki et al. [58] performed an extensive study on the damage resistance and strength properties of thin-ply and thick-ply quasi-isotropic (QI) carbon fibre reinforced polymer (CFRP) laminates. The QI laminates were made of $[45/0/-45/90]_{ns}$ symmetric lay-up where n is the number of repeated plies. The experimental study covered quasi-static tension, cyclic tension, open hole compression test (OHC), unnotched compression tests (UNC) and compression after impact (CAI). The areal weights of the standard thickness prepreg and the thin-ply prepreg were 145 g/m^2 and 75 g/m^2, respectively. While the thickness of the standard and thin-ply prepregs are 0.14 mm and 0.07 mm, respectively. The thin-ply laminates showed 20% higher ultimate tensile strength than the thick-ply laminates under static tension loading. Acoustic emission (AE) signal monitoring and X-ray images of both laminate types indicated that the thin-ply laminate has higher damage resistance over the course of static loading. The stress-strain curve of the thin-ply laminate is linear up until final failure and it exhibits brittle failure as already shown by Sihn et al. [52]. For the fatigue

tests, thin-ply laminates were found to be less susceptible to the propagation of free-edge delamination over the course of cyclic loading and in turn yielded higher fatigue strength and a longer fatigue life. As for the UNC, OHC and CAI tests, positive trends for the thin-ply laminate were seen. An increase of 16% in compressive strength for the thin-ply laminates under UNC conditions was obtained. The ability of thin-ply laminates to resist delamination growth contributes to the compressive stability and higher strength under OHC and CAI test.

Out-of-plane responses of thin and thick-ply laminates have also been investigated by Yokozeki et al. [59]. The material type and quasi-isotropic (QI) stacking sequence from the previous work [58] were kept and specimens were subjected to quasi-static indentation. It was shown from the experiments, that there are different damage mechanisms between standard ply thickness and thin-ply laminates. The thin-ply laminates were more resistant to damage accumulation compared to the standard ply thickness laminates at the same deflection. Microscopic observations for these two laminate types showed more damage sites developed in the thick laminates. The damage processes for the two laminates were different: accumulation and growth of delamination and matrix cracks were observed in standard ply thickness laminates, while sudden fibre fractures occurred in thin-ply laminates. From their finite element analysis, it is suggested that the different delamination positions affect the damage process in the two laminates. X-ray inspection for both laminate types at the same deflection revealed considerable delamination on the tensile side of standard thickness laminates in contrast to the thin-ply laminates. This implies that the standard thickness laminates are prone to matrix cracking on the tensile side. While for the thin-ply laminates, delamination sites grow in the middle of the laminate away from the tensile side. This shows that thin-ply laminates have more resistance to the growth of matrix cracks on the tension side. By having high resistance against matrix cracking and delaminations near the tensile surface, there is no reduction of stress in the fibre direction and thus fibre failure at the tensile side would suddenly occur in thin-ply laminates as observed during indentation tests. While the fibre fracture on the tensile side is delayed in the standard thickness laminates due to the delamination growth near the tensile side and thus stress in the fibre direction is reduced. The fibre breakage of thin-ply laminates occurs at higher stresses compared to the standard thickness laminates when the same deflection was applied. This implies that the thick laminates suffer extensive delamination growth and loss of stiffness before final failure.

The ply thickness effects in QI laminates of NTPT materials with $[45/90/45/0]_{ns}$ lay-up sequence were investigated by Amacher et al. [57]. The investigated laminates were made with three different areal weights of carbon fibre reinforced polymer material: 30, 100 and 300 g/m^2, referred to as thin, intermediate and thick, respectively. For each of these ply thicknesses, several mechanical tests such as unnotched tension, open-hole tension, fatigue, open-hole compression, bolted joint bearing tests were conducted. For the QI laminates in this work, the number of sub-laminate plies are n=1, n=3 and n=10 for 300, 100 and 30 g/m^2 materials, respectively to keep the same overall thickness. The specimen dimensions including the laminate thickness were kept

constant. Static tensile tests revealed that the thin-ply laminates failed at 1644 MPa (15% higher strength than the thick-ply laminates) as also concluded from the work of Sihn et.al. [52], while the intermediate ply thickness laminates failed between the two values of the other laminates. For the thick-ply laminates, the onset of damage was earlier at 248 MPa, in the form of transverse cracking and delaminations. In contrast, only a limited amount of damage occurred in the thin-ply laminates before brittle final failure with a single crack running perpendicular to the loading direction. The ability of thin-ply laminates to resist damage led to brittle failure at a lower stress compared to the thick-ply one for quasi-static open-hole tension tests, which is comparable with the results from the work of Shin et al. [52]. This was due to damage development that took place in the thick-ply laminates, leading to the redistribution of stresses around the hole. For open-hole fatigue tests, the results that compared well with the work of Shin et al. [52] were identified. During cyclic loading, damage detection of the specimens by using acoustic emission indicated more intense damage accumulation in the thick-ply laminates than in the thin-ply ones. This was also supported by the ultrasound C-scan images that were taken at 50000 cycles when the fatigue testing was stopped. The thick-ply laminates also displayed significantly lower fatigue life, failing at 20000 cycles, at the same stress level (315 MPa) as that for thin-ply laminates which survived for more than one million cycles and did not show any sign of damage. Thin-ply laminates displayed high strength during quasi-static open-hole compression tests, where they failed at 18% higher stress than the thick-ply laminates. The bolted joint bearing tests conducted at both room temperature and in 'hot-wet' conditions at 90°C showed that the thin-ply laminates failed at 23% and 138% higher stresses at each condition, respectively. The thick-ply laminates developed delaminations followed by local crushing of the laminate around the bolt, while the thin-ply laminates only displayed local crushing in the vicinity of the joint.

Thin-ply laminates have also been successfully used to inhibit the instability of fibre composites in compression as reported by Amacher, et al. [56]. They compared the compressive performance between three different ply thicknesses: thick (300 g/m^2), intermediate (100 g/m^2), and thin (30 g/m^2). For the thin laminates there was an increase of 21% and 24% in compressive strength compared to the intermediate and thick laminates, respectively. This is because the resin rich regions usually found in standard thickness laminates are minimised and this could further supress the compressive instability. Based on the state of the art presented above, it has been shown that incorporating thin-plies in laminates (thickness below standard thickness of 0.125 mm) can increase the strength, failure strain and suppress damage. The ability to resist transverse matrix cracking and delamination can increase the peak strength of the thin-ply laminates. Although The final failure of the thin-ply laminates under uniaxial tension is of a brittle nature. Where damage resistance is the key requirement for applications, the behaviour of thin-ply composites is interesting for further investigation.

2.5 Pseudo-ductility of UD thin-ply hybrid composites

As shown in the previous work on hybrid composites [40]–[42], hybridisation can be used to achieve a controlled and gradual failure behaviour of the material when incorporating low thickness carbon plies in a glass/carbon hybrid system. It has been discussed in Section 2.4 on thin-ply composites that this material has the ability to suppress damage such as matrix cracking and delamination due to its low energy release rate. With the advent of tow spreading technology [53] to produce thin carbon prepregs, it is possible to combine this material with high strain glass plies.

The availability of thin-ply prepregs has attracted researchers to develop thin-ply hybrid composites [60]–[64]. These hybrids are made of thin carbon fibre reinforced polymer (CFRP) prepregs (0.03 mm) and standard thickness glass fibre reinforced polymer (GFRP) prepregs (0.155 mm), with the CF ply located in the middle of the laminate, as depicted in **Figure 2.15**.

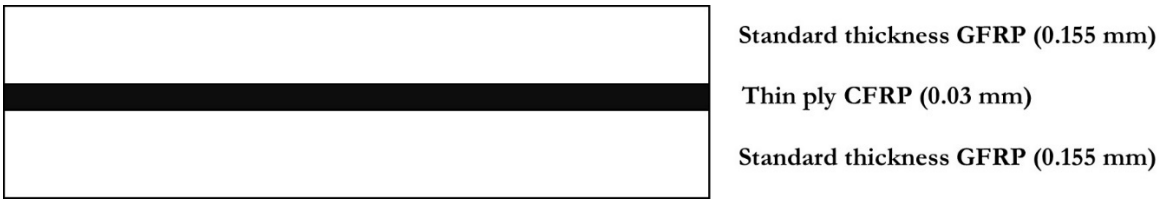

Figure 2.15. Configuration of hybrid laminate showing the location of glass and carbon plies respectively. To achieve pseudo-ductility via gradual failure of the carbon ply, the ratio of glass ply to carbon ply thickness can be adjusted. Not to scale.

Work which was undertaken by Czél et al. recently [21], [22] focuses on combining the benefits of thin-ply laminates with the non-linear, gradual failure that hybrid laminates can exhibit. The work conducted by Czél et al. [39][60] has shown that the thin-ply hybrid configuration (as shown in **Figure 2.15**.) produced gradual failure and pseudo-ductile response as shown in **Figure 2.16.**

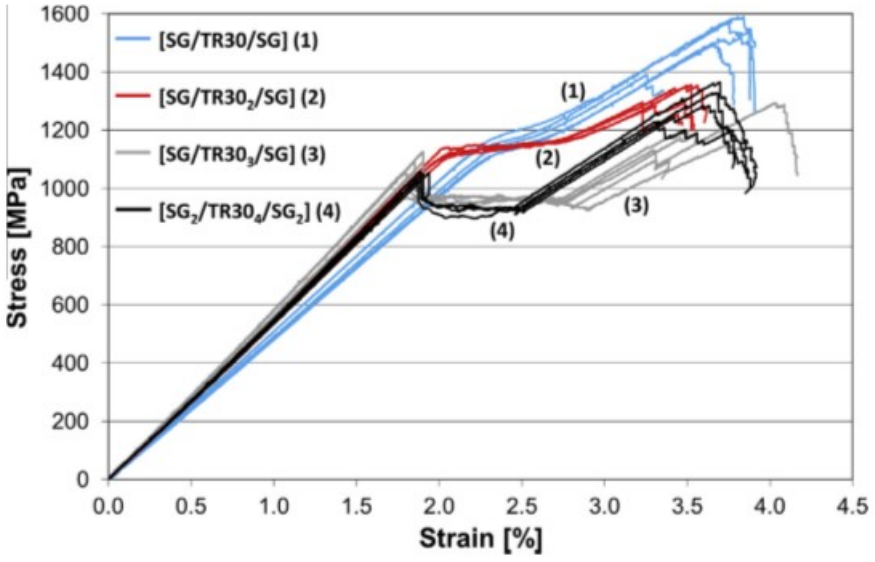

Figure 2.16. Stress-strain curves for selected thin-ply hybrid laminates. The lay-ups are [SG$_2$/C$_n$/SG$_2$] & [SG/C$_n$/SG]. Pseudo-ductile response is shown for n =1 & 2 of the [SG/C$_n$/SG] configuration. Figure obtained from ref: [60].

They demonstrated that if the carbon in a glass/carbon hybrid is thin enough (less than about 0.06 mm which is two carbon plies), catastrophic delamination propagation around the first carbon ply fracture can be suppressed and therefore further fractures in the carbon ply may occur. If the load is increased and the glass ply is not broken, then the fragmented carbon ply may start to pull-out in a stable manner. A change in failure mode occurred as the thickness of the carbon ply was increased. All configurations showed an initial linear stress-strain response up to an initial fracture of the carbon ply. After this point the behaviour was dependent on the number of carbon plies: For a [SG/C_n/SG] hybrid configuration, where SG is the glass ply and C is the carbon ply respectively, a single ply of glass fibre on each side was used so in total two glass plies were utilised. For n = 1 — the stress level continued to rise at a lower slope before final failure of the specimens; for n = 2 — a long, horizontal stress plateau was observed following the initial carbon ply fracture and the failure again occurred after a second rising part in the stress-strain curve; for n = 3 — a load drop corresponding to delamination was seen immediately after initial carbon ply fracture, followed by a plateau at a lower stress than that at first fracture, finally there was an increase in stress prior to failure; for n = 4 — a similar load drop was exhibited, followed by a shorter plateau and a second rising part. As observed by Czél et al. [39] in their experimental work, there was a change in damage mechanisms as the number of carbon plies (n) increased beyond two. During tensile loading of the thin-ply hybrid composites, multiple fractures in the carbon ply occurred for the laminates with n = 1 and n = 2. As **Figure 2.17** presents, the damage patterns are shown as a black and yellow stripe. Well bonded areas appear black and the locally delaminated areas just around the cracks in the carbon layer are visible as the yellow stripes due to the translucent nature of the glass/epoxy outer ply of the hybrid laminate. The yellow stripe corresponds to the colour of the epoxy resin.

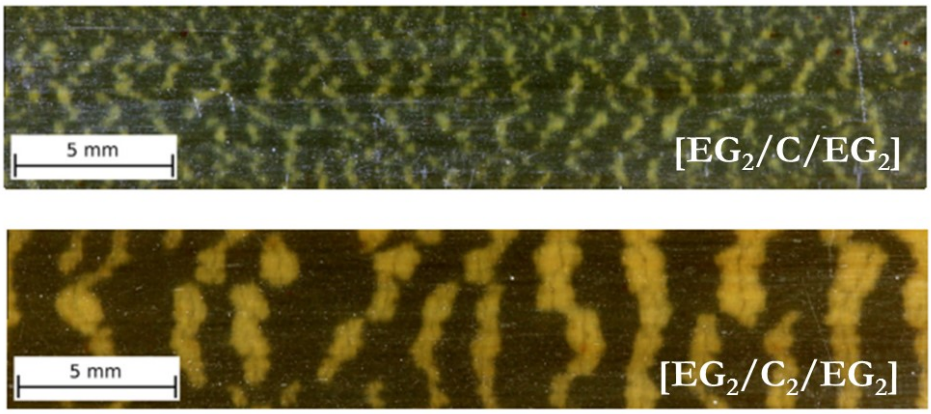

Figure 2.17. Different damage patterns for selected thin-ply hybrid laminates. The lay-ups are [EG_2/C/EG_2] and [EG_2/C_2/EG_2]. The localised delamination is shown as a yellow striped pattern around the visible cracks in the carbon ply. Figure obtained from ref: [39].

The localised delamination shown in **Figure 2.17** took place at either side of the specimens [39], showing that thin carbon ply effectively suppressed the unstable delamination growth after the first carbon fibre fracture. It is also shown that the spacing of fractures changes with carbon

ply thickness. The hybrid with a single carbon ply (n = 1) developed a high density of fragmentations compared to the double carbon ply type specimen. As for the hybrid with three (n=3) and four (n=4) carbon plies, sudden growth of delamination from the initial carbon fracture dominates the failure behaviour. It was observed that a single delamination extended out from the fracture at the carbon-glass interfaces immediately after the first carbon ply fractured. This unstable growth of delamination is responsible for the stress drop as shown in **Figure 2.16** for the hybrid configurations with thicker carbon plies. During the stress plateau, further growth of delamination at the carbon-glass interfaces took place. The stress increase at the end of the plateau marks the load transfer from the damaged carbon ply to the undamaged glass ply. In terms of first carbon strain to failure, the hybrid with single and double carbon plies exhibited different initial carbon strain to failure, where its failure strain increased with decreasing number of carbon plies. The reason behind the strain enhancements in thin-ply hybrid composites is explained by Wisnom et al. [65], as their model illustrated that for thin-ply hybrid laminates, the glass plies were able to delay the failure of the carbon ply by constraining the growth of broken carbon fibre clusters at the boundaries of the thin carbon ply. The final failure of the thin-ply hybrid composites occurred at a strain lower than the glass fibre failure strain mentioned by the manufacturer (5.5%), displaying a similar trend as presented by Kretsis [47] and Swolfs [66]. It should be noted that the pseudo-ductile responses shown in **Figure 2.16** for [SG/C_n/SG] with n =1 and 2 are possible because the selected thin-ply carbon laminates had reduced strain energy release rates at the first carbon ply fracture, as pointed out in the previous work by Czél et al. [39], thereby avoiding catastrophic delamination. These results build on earlier studies [38], [40], [41] which reported that the layup configuration and properties of each material within the hybrid laminate influences the stress-strain response; in other words, the stiffness, failure strain, modulus and thickness of the constituent plies determine the failure type, (brittle or pseudo-ductile).

Jalalvand et.al. [64] investigated the failure mechanisms exhibited by the thin-ply hybrid laminates that were tested in their previous work [39]. Their numerical model is capable of predicting the failure mechanisms, e.g. in glass-carbon-glass hybrids. The finite element analysis (FEA) method in [64] was able to capture the stress-strain behaviour of the four glass/carbon hybrid configurations with varying carbon ratios tested by Czél et al. [39]. For the two thinner laminates, the model successfully captured the initial linear region but underestimated the stress and strain of the first carbon fibre fracture; the predicted amount of pseudo-ductility for those laminates was less than that observed experimentally. For the thicker laminates (n = 3 and 4), where n is the number of carbon ply utilised, better overall predictions were made, as the model was able to predict the strain for the load-drops, their magnitude, the stress plateau and final increases in stress. The predicted damage mechanisms based on the numerical modelling correlated well with those observed experimentally, hence allowing a damage mode map to be constructed showing the dependence of these failure modes on the relative and absolute CFRP thickness.

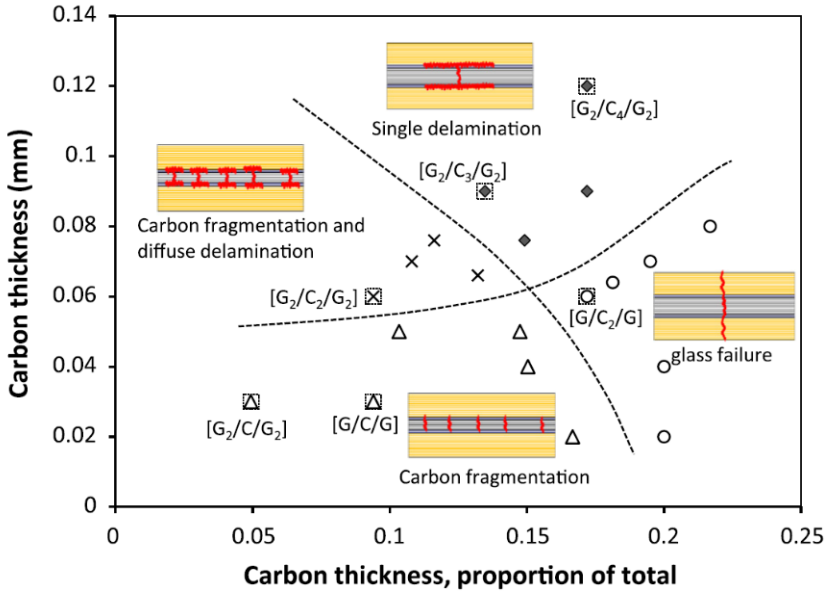

Figure 2.18. Damage mode map showing the damage and failure behaviour of interply hybrid laminates in terms of the absolute and relative thickness of the CFRP ply. The boundaries between different damage processes give a simple method to choose an optimal layup. Figure obtained from ref:[64].

The damage mode map in

Figure 2.18 which shows the boundaries between the areas corresponding to different damage mechanisms of CFRP fragmentation, delamination at the carbon-glass interfaces and catastrophic failure gives a simple and clear method to design thin-ply hybrid composites. Although finite element analysis (FEA) has successfully predicted the damage mechanisms and can inform laminate design through a damage mode map for thin-ply hybrid composites, it is computationally expensive. An analytical method was later developed by Jalalvand et. al. [67] that employed a representative volume element to predict the stress-strain response. To fully capture the thin-ply hybrids behaviour, discrete sections of the response were modelled: initial linear response, first carbon ply failure, subsequent damage and final failure. Different failure criteria were used for the thin-ply hybrid damage mechanisms: a stress-based criterion defined the initial fragmentation of the CFRP ply; an energy-based formulation to describe the onset of delamination and the final failure of the laminate, determined by a probabilistic approach that applied a distribution to the strength of the glass ply in the fibre direction. To build up the stress-strain response, the stress state in the laminate was compared to the stress level needed to trigger a particular type of damage. The stress-strain response from this work agrees well with the experimental results from [39], as shown in **Figure 2.19**.

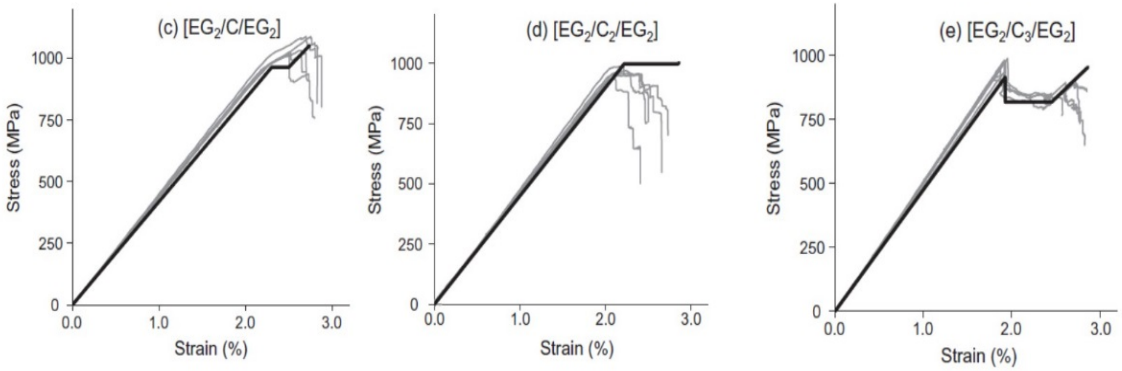

Figure 2.19. Stress-strain curves are shown for a selection of the glass-carbon laminates modelled and tested. The layups shown are [$EG_2/C_n/EG_2$], where n increases, left to right, from 1 to 3. Figure obtained from: [34].

For the hybrid laminates with n=1 and n =2, where n is the number of carbon plies employed, the model was able to predict the stress and strain at initial carbon ply failure. The fragmentation of the carbon ply was predicted as the stress plateau, but the model was not able to capture the fluctuations in stress. For the thick laminates (n = 3), the load drop due to delamination was also predicted, as well as the width of the plateau and the subsequent stress increase. In parallel to this work [67], a new series of experiments with thin carbon ply and standard thickness S-glass ply was performed. By incorporating higher modulus and higher strain S-glass the hybrid laminate could be made more efficient by using fewer S-glass plies to sustain the load transfer from the failed carbon plies. As before, the model developed by Jalalvand et al. [67] correlated well with the experimental results, with all aspects of damage evolution being captured. From the previous work on thin-ply hybrid composites, pseudo-ductile response has been successfully achieved and understood under tension loading. The results discussed in the literature review for pseudo-ductile behaviour so far is related to the design and modelling framework developed for uniaxial tension loading only, while the pseudo-ductile response under compression and bending has not been investigated extensively before.

2.6 Compressive behaviour of UD hybrid composites

The hybrid composites discussed above have shown desirable pseudo-ductile failure in tension by hybridising unidirectional (UD) standard thickness glass and thin carbon prepreg plies and exploiting the stable fragmentation and dispersed delamination of the carbon ply, therefore avoiding catastrophic failure [39],[68]. In practice, there are load scenarios other than tension that need to be considered when designing structural components made of thin-ply hybrid composites. Compression behaviour of fibre reinforced polymer composites is of significant interest in structural design as it usually limits the potential application of the material if the part is not properly designed to withstand compressive loading. It has been shown that the shear instability of the fibre within a relatively unsupportive matrix dictates the compressive failure modes of many fibre reinforced polymer composites. Previous work on the compressive properties of unidirectional (UD) fibre composites have shown that the principle failure mechanism of fibre

micro buckling is governed by this instability which is influenced predominantly by the initial misalignment of the fibres and the stress-strain response of the matrix [26], [28], [77]–[81], [69]–[76]. The instability itself induces high shear strain in the matrix followed by fibre buckling. Instability initiates the failure, creating fibre kinking that leads to catastrophic failure [70],[26],[78]. When initially parallel misaligned fibres are loaded in axial compression, they start to rotate, and this will induce shear stress in and out of plane as shown in **Figure 2.20**. For simplicity, only in-plane shear stress is shown in **Figure 2.20**.

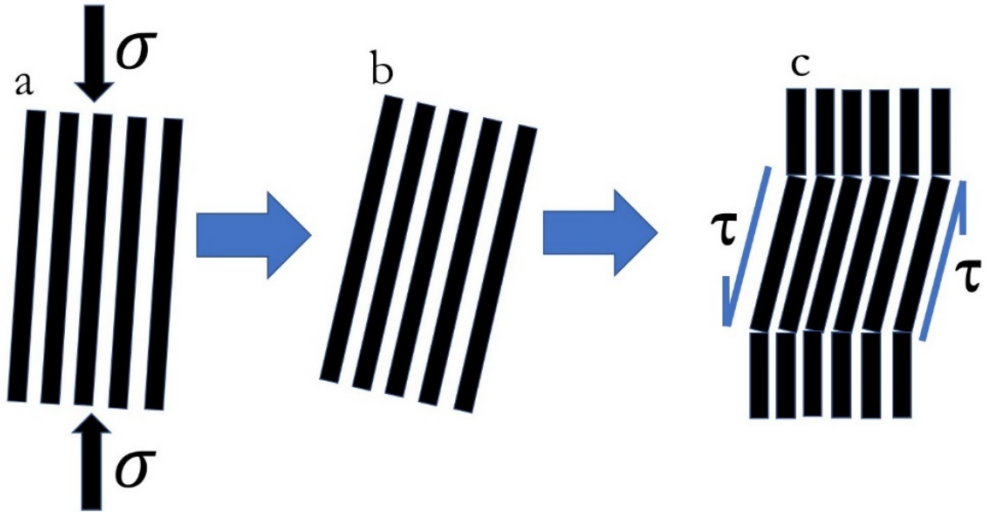

Figure 2.20. Schematic showing the failure mechanisms of a unidirectional fibre composite under longitudinal compression loading. (a) initial misaligned and parallel fibres (b) increased misalignment due to applying load (c) kinking with shear stress between fibre and matrix.

The kinked fibre will deform all together thus reducing the strength of the fibre composite. In other words, it is the overall instability that usually governs the failure of fibre composites under compression. So in general, the compressive performance of fibre composites is mainly governed by initial fibre misalignment, and shear characteristics of the composite – dominated by the matrix and the stress-strain response of the matrix in shear [69] [26],[74],[76],[82]. As already shown by previous studies [74][79], the failure may also initiate at shear stresses lower than the yield strength of the matrix, due to local reduction of modulus caused by the non-linear response of the matrix.

Hybridisation of low strain carbon fibre with high strain glass fibre is one method to improve compressive strength due to the ability to resist kink band propagation as mentioned by Chaudhuri, et.al. [83]. The reason behind this idea is related to the suscepbility of carbon /epoxy composites to initial fibre misalignment due to their shear characteristics (sucah as ultimate shear strain and initial shear modulus) and small fibre diameter [84] causing premature failure under compression. On the other hand, S-glass/epoxy composites are less sensitive to initial fibre misalignment due to their larger fibre diameter and better shear characteristics compared to the carbon/epoxy [82]. To demonstrate this idea, hybrid composites made of unidirectional commingled S-glass fibre at the tow level with carbon fibre were submitted to uniaxial compression loading [83]. A Griffith type fracture criterion was introduced by Chaudhuri et al. [83] to determine the required glass-carbon ratio for the toughness enhancement against kink band formation. From the model, it was concluded that with the minimum glass fibre content of 15%, an increase in

toughness against kink band propagation can be achieved. This translates into a 4.4% increase in compression strength for the hybrids compared to an all carbon composite [83]. There was also a change in failure mode from the all carbon composites to the hybrid one. The commingled carbon/glass/epoxy specimens displayed multiple fracture of fibres, and the baseline carbon composites showed catastrophic brittle fracture.

Sudarisman, et. al. [85] studied the effect of combining silicon carbide fibres with carbon fibres to produce unidirectional interply hybrid composites. They found no significant increase in compressive strength, compression modulus, and work of fracture compared to all carbon fibre composites and due to the higher density of SiC, the specific compressive strength and elastic modulus generally decreased. The failure mode consisted of fibre crushing for pure SiC fibre composites and the presence of longitudinal fibre splitting with kink band for the hybrid specimens. It was noted from their work, that the presence of carbon fibre in the hybrid specimen controlled /limited the compressive properties of the hybrids[85].

The compressive toughness properties of multidirectional hybrid composites composed of a combination of high strength (HS) and intermediate modulus (IM) carbon fibres was explored by Tsampas, et al. [86]. The lay-up of the laminate being used in this study was $[0/90/45/-45]_{2S}$ employed to study the sensitivity to specimen geometry and loading conditions. The result of the compact compression tests of the hybrids revealed superior compressive performance in comparison to the monolithic configurations of HS and IM. An increased peak load of ~18% and 4% relative to the HS and IM plain carbon laminates, respectively, were observed for the hybrids. After the peak load, there was a gradual failure in the compact compression testing for the hybrid material. The improvement in failure load and the gradual failure type of the hybrid material is due to the improvement of the in-plane shear support from the stiffer material and higher delamination fracture toughness [86].

Iqbal et al. [87] explored the effect of glass to carbon fibre ratio and laminate geometry on the compressive properties of hybrid composites. Unidirectional intra-ply and inter-ply hybrid composites were experimentally tested in longitudinal compression loading. When having the same carbon to glass ratio, e.g. 50%, the results for the intra-ply laminates displayed an increase of 31% for the compressive failure strain compared to the plain carbon laminates. Meanwhile for the interply, there was an improvement in failure strain of about 30% compared to the plain carbon one. In general, when the carbon fibre content in the hybrid laminates increases, the compressive failure strain decreases [87]. The compressive strength for the intraply hybrid is 3.5% higher compared to the interply hybrid laminate for 50% carbon-to-glass ratio. The intraply hybrid laminates have better compressive properties compared to the interply one due to the higher degree of carbon ply dispersion within the intraply laminates. The carbon ply is surrounded by higher strain glass plies which constrains the possible damage development. Their findings highlight the importance of a high degree of carbon ply dispersion to gain an improvement of failure strain and strength in compression loading.

Czél et al. [88] have reported a benign change of slope in the load-compressive strain curve of an asymmetric unidirectional hybrid composite made of a thin high modulus M55 carbon/epoxy and thick glass/epoxy plies loaded in four-point bending which was due to the progressive fragmentation of the carbon ply on the compression side of the specimen. The four-point bending method was selected to prevent local failure under the loading nose and to achieve uniform bending moment between the loading noses. This phenomenon of carbon ply fragmentation in compression has not been reported elsewhere and it is also one of the research topics of this thesis.

The previous work to characterize the compressive performance of fibre composites has led to the use of hybridisation between high strain and low strain fibres to prevent kink band propagation. Thin-ply laminates have also been used to inhibit compressive instability. By combining standard thickness glass with thin intermediate modulus carbon ply laminates, it is possible to achieve better performance in compression due to suppression of instability compared to monolithic laminates. However, there is still lacking experimental results on compression characterisation of thin high modulus carbon/epoxy plies with standard thickness s-glass/epoxy to examine if whether the failure behaviour of this hybrid is governed by instability.

2.7 Flexural behaviour of UD hybrid composites

Previous work to achieve gradual failure in fibre composites under tension [21], [22] and compression [87] [88] loading has been successful by hybridising low strain and high strain fibre materials. Based on these successful results, there is a possibility to achieve gradual failure of fibre reinforced polymer composites under flexural loading as different regions of the cross-section simultaneously undergo tensile and compressive loading.

Dong et al. [89] conducted three point bending experiments on unidirectional carbon/glass intraply hybrids with the following stacking sequences: C_6, G_1C_4, G_2C_3, G_5. For each of the hybrid configurations, the glass ply was loaded on the compression side. The chosen configurations were chosen to achieve a thickness around 2 mm. The obtained average flexural strengths for G_2C_3 configuration from the experiments are 40.2% and 9.2% higher than the pure carbon and pure glass reference composites respectively. While for the G_1C_4 configuration, it is 90.6% and 48.2% higher than the pure carbon and glass reference composites. The achieved strength for the hybrids was higher than the values predicted by both finite element analysis and classical laminate theory. From the microscopy of the failed specimens, the hybrid laminates with G_2C_3 configuration failed on the compressive side with the tensile side relatively undamaged. In contrast to the previous hybrid laminates, for the G_1C_4 configuration, failure occurred on the tensile side where carbon ply resides, while the glass ply on the compression side are relatively undamaged. This failure type may have contributed to the higher flexural strength for this particular configuration.

Similarly to Dong et al. [89], Giancaspro et al. [90] employed a three point bending test set-up to assess the flexural properties of unidirectional carbon/glass interply hybrid laminates. Three configurations of hybrid laminates were utilised in this study: E-Glass ply sandwiched between carbon ply, asymmetric carbon/glass hybrid laminates, alternating lay-up of carbon and E-glass ply

to make symmetric hybrid laminates. They noticed that the pure carbon fibre composites failed mainly on the compression side, while the E-glass fibre composites failed on the tension side. As for the hybrid laminates, the flexural strength increased when the carbon fibre plies were added to the tension side, while the addition of the carbon fibre plies to the compression face did not give significant increases in flexural strength. In the latter case, the failure mode changed from failure in the tension side to fibre crushing on the compression side. The same thing could be said for the E-Glass plies sandwiched between carbon ply configurations, where having the carbon on the tension and compression side also did not improve the flexural strength, with failure on the compression side. They discovered that the pre-buckled shape of the carbon tows facilitates local compressive failure, followed by global failure of the specimens.

The flexural properties of hybrid unidirectional polymer composites containing a mixture of silicon carbide (SiC) and carbon (C) fibres were evaluated by Davies et al. [85] using the three point bending method. The examined interply hybrid configuration is an asymmetric SiC/Carbon hybrid laminate where the SiC ply were positioned close to the compressive side. Three different span-to-thickness, (S/d) ratios of 16, 32, 64 were used to study the flexural response of hybrid laminates. In general, the flexural strength, maximum flexural strain, and flexural modulus increased with increasing S/d. This behaviour is attributed to the reduced effect of shear. The failure type for the hybrids tested with three S/d ratios is compressive failure beneath the roller with fibre micro-buckling observed on the compression side. Due to the high stress concentration under the loading nose in three-point bending, compressive failure beneath the roller is considered premature failure. This work demonstrated that replacing 12.5 vol% of carbon fibre on the compression side by silicon carbide fibre increased the flexural strength by 22% compared to a pure carbon fibre laminate. It is also suggested that silicon carbide fibre has a compressive-to-tensile strength ratio similar to glass fibre, higher than that for carbon fibre, therefore they can improve the properties of pure carbon laminates.

According to Giancaspro et al. [90] and Dong et al. [91], an optimal level of glass fibre is required to achieve maximum flexural strength. Dong et al. [91] stated that the highest flexural strength in carbon/glass hybrids was achieved at a relative content of 12.5% of glass fibre, all of which are placed on the compressive side. A symmetric layup is hence not the optimal design for a hybrid composite that will be subjected to flexural loads [89], [91] as agreed by Giancaspro et al. [90]. Further optimisation showed that the flexural strength can be improved if the fibre volume fraction within the glass fibre reinforced plies is higher than in the carbon fibre reinforced plies.

The mechanical properties of unidirectional glass/carbon hybrid laminates under three point bending was examined by Prusty et al. [92]. The examined laminate structures in their study were symmetric and asymmetric glass/carbon interply hybrid lay-ups. For the asymmetric lay-up, they discovered that the presence of carbon/epoxy at the tensile side leads to enhanced strength and modulus but at the same time makes the hybrid prone to catastrophic failure. Whereas, placing the entire carbon/epoxy on the compressive side yielded progressive failure behaviour as seen in

the glass/epoxy composite. While for the symmetric glass/carbon hybrid laminates catastrophic failure and delamination on the tensile side due to the brittle nature of carbon/epoxy was observed.

For all the above-mentioned studies, the failure on the compression side includes sudden carbon fibre failure. The phenomenon of fragmentation of carbon plies on the compression side under bending has not been reported before by other researchers apart from Czél et al [88] for very thin carbon plies, therefore it is interesting to explore the effect of fragmentation on the bending performance of unidirectional thin-ply hybrid composites in this thesis. As the previous work on bending performance of hybrid composites was done by using three-point bending technique, which make the specimen prone to premature failure due to contact forces under the loading nose on the compression side, the work in this thesis will use four-point bending technique to avoid premature failure and to have a uniform bending moment between loading noses.

2.8 Fatigue behaviour of UD hybrid composites

Structural components made of hybrid composites are often subjected to cyclic loading and understanding their long-term behaviour is important as this could help to predict their lifetime and schedule future maintenance. The model presented by Burks et al. [93] demonstrated that CFRP performs better in fatigue loading, in comparison to GFRP, due to the fact that the state of stress within the matrix material is considerably lower for CFRP composites, thus eliminating (or at least delaying) fatigue damage initiation.

The tensile fatigue behaviour of unidirectional carbon and basalt fibre-reinforced composites with their hybrid composites was investigated by Wu et al. [94]. For basalt/carbon hybrid composites, the S-N (strength versus number of cycles) curves were shifted to higher numbers of cycles, in comparison to the all basalt fibre composites. They attributed this behaviour to the different strain to failure between the basalt and carbon fibre where the basalt fibre with higher strain to failure prevents the continuous fracture of the carbon fibre and the rough surface of basalt fibre [95] contributed to mechanical interlocking between the basalt and carbon layers thus promoting sufficient bonding between them, thereby delaying the delamination propagation.

Peijs et al. [96] discovered flat S-N curves for unidirectional hybrid composite made of polyethylene fibre and carbon fibre compared to pure carbon composites. Their finding confirm the work by Wu et al. [94] stating the benefits of using two different modulus fibres on the fatigue properties. The lower modulus PE fibres prevent further rapid crack extension from the first failed carbon fibres. This leads to slower fatigue damage propagation, further demonstrating the excellent mechanical properties of PE/carbon fibre hybrids. Based on their work, the tensile fatigue resistance of hybrid composites can be improved by: (1) increasing the dispersion between the fibres using the intermingling concept and, (2) increasing the fibre– matrix adhesion of the PE fibres by a surface treatment.

Dickson et al. [97],[98] explored the tensile fatigue behaviour of unidirectional (UD) carbon/glass and carbon/kevlar hybrids. A positive hybrid effect was shown for carbon/kevlar hybrids [98] where the fatigue stress level for a given number of cycles to failure was shown to vary

linearly with the increasing relative ratio of carbon and kevlar fibres. As for the carbon/glass hybrids [97], a similar hybrid effect was confirmed as a lower slope for the hybrid's S-N curve compared with that of the pure glass and pure carbon composites for a range of fatigue load level from 40% and 90% of their respective ultimate tensile strength.

Dai et al. [99] presented a 3D model to describe the fatigue behaviour of glass/carbon hybrid composites under tension-tension loading. It was demonstrated in their paper [99] that an improvement in the fatigue lifetime of the hybrid composite compared to the all glass fibre composite was attainable. This was possible because further cracks propagating from the lower strain carbon fibre were delayed by the presence of the higher strain glass fibre, thus reducing the likelihood of further carbon fibre failure and improving the fatigue lifetime of the hybrid composite.

The previous work on characterization of the fatigue behaviour of hybrid composites shows the advantages of mixing two different modulus fibres to enhance the fatigue life of the material by increasing the dispersion between two fibre types with different modulus. The lower modulus fibre prevents further rapid crack extension from the failed high modulus fibres. This leads to slower fatigue damage propagation and enhances the number of cycles to failure. Using thin-ply laminates is another technique to increase the dispersion of the high modulus fibre composite. Although the fatigue response of other hybrid composites was already reported, as mentioned above, the fatigue behaviour of unidirectional (UD) thin-ply hybrid composites has not been explored before according to the author's best knowledge. Fatigue characterization of UD thin-ply hybrid composites will also be explored in this work.

2.9 Overview of pseudo-ductile composites

Several mechanisms have been proposed to add pseudo-ductility or ductility to fibre composites such as (1) fibre reorientation: the design and evaluation of composite architectures that create ductility via geometrical rearrangement of fibre orientation and shearing of the matrix [100], [101] or from excess length due to in or out-of-plane waviness [102], (2) interface modification on the fibre level [103], [104] or ply level [105] or by designing discontinuities on the ply level [73], [106], [107] to delay failure and generate non-linearity through controlled failure, (3) hybridization: the design of laminated composite by using the combination of fibres with different strains to failure [39], [62], [68], [108] to achieve gradual failure, (4) the design and production of novel materials such as carbon nanotube fibres [109] and cellulose nanocrystal (CNC) fibres [110], which can be intrinsically ductile.

The ductility in composite materials resulting from exploiting the fibre reorientation concepts was explored by Fuller et al. [100], [101]. They investigated $[\pm \phi_5]_s$ lay-ups consisting of thin-ply (0.03 mm) carbon-epoxy prepreg material oriented at different angles from 15° to 45°. When under tensile load, a non-linear stress-strain behaviour can be achieved with this configuration, while also suppressing edge delamination that normally causes premature failure for

standard thickness angle-ply laminates [50]. The stress-strain response for these thin-ply angle-ply laminates is shown in **Figure 2.21** demonstrating the ductility in $[\pm 30_5]_s$ laminate.

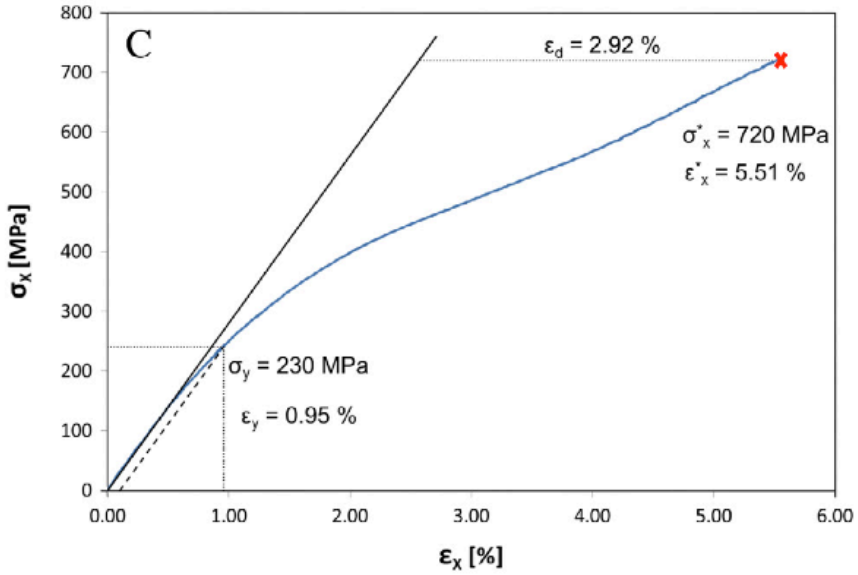

Figure 2.21. Tensile stress-strain curve of typical thin-ply angle-ply laminates showing the pseudo-ductility of $[\pm 30_5]_s$ laminate. Figure obtained from ref: [100].

The non-linearity for stress-strain response in **Figure 2.21** is due to shearing in the matrix. The degree of non-linearity increases after passing the shear yield point of the resin. The matrix contributes to this increase in the rotation as it plastically deforms allowing continued realignment of the fibre. Hence the pseudo-ductile behaviour in the thin-ply angle-ply laminates is due to a combination of plasticity and fibre reorientation [100]. It should also be noted from **Figure 2.21** that with increasing off-axis fibre angle, the yield point (σ_y and ε_y) decreases while the pseudo-ductile strain (ε_d) increases. As a consequence, the final failure strain ($\varepsilon_{x'}$) increases while the final failure stress ($\sigma_{x'}$) decreases with increasing off-axis fibre angle.

Utilising aligned discontinuous fibres to create pseudo-ductile response was explored by Yu et al. [108] after inventing the HiPerDiF technology. This method allows the production of tow or tape type prepregs from highly aligned discontinuous fibres (80% of the fibre can be oriented within ±3°), resulting in high stiffness composites. Two different material configurations were employed with the High-Performance Discontinuous Fibre in full first time (HiPerDiF) method [111], high strength carbon/E-glass and high modulus carbon/E-glass hybrid composites, where both fibre types are discontinuous. The high strength carbon/E-glass hybrid did not produce pseudo-ductility because of the low tensile strength of the E-glass fibres (2400 MPa) compared to the high strength carbon fibres (4344 MPa) and high volume ratio of high strength carbon and E-glass fibres [108]. A pseudo-ductile response was obtained for the intermingled hybrid composites composed of high modulus carbon/E-glass fibre as shown in **Figure 2.22.** In the intermingled hybrid, the high modulus carbon is mixed with E-glass at the fibre level. The high modulus carbon itself has a strain to failure around 0.4% [108]. The observed pseudo-ductile behaviour was the

result of the fragmentation in the low strain carbon fibre.

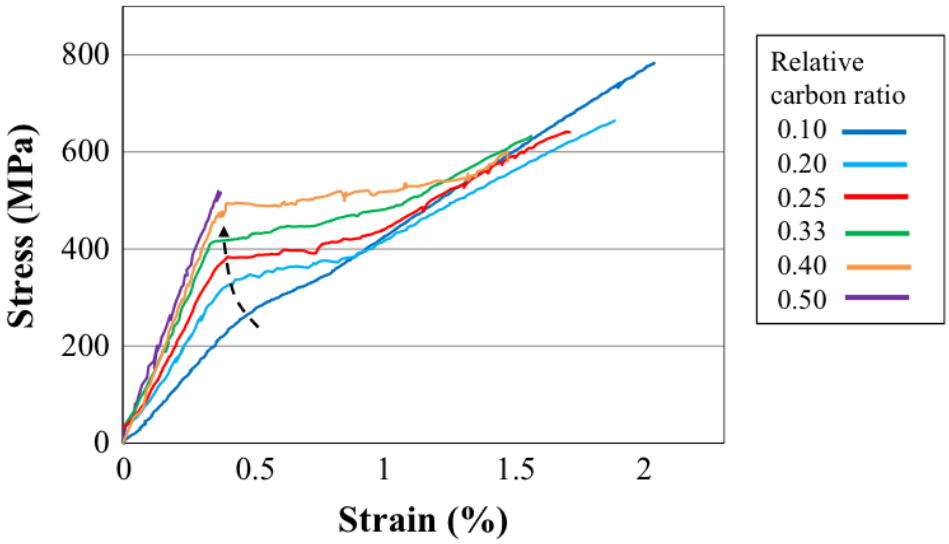

Figure 2.22. Typical tensile stress-strain response of high modulus carbon/E-glass hybrid with different carbon ratios. Pseudo-ductility is clearly shown from 0.2 to 0.4% carbon ratio. Figure obtained from ref: [108].

The knee-point stress-strain in **Figure 2.22** for 0.10-0.40 relative carbon ratio is due to the multiple fractures of the carbon fibres, and this marks the transition between the elastic and plateau part of the curves. With increasing carbon content in the discontinuous hybrids, there is a different shape in the transition. In the specimens with low relative carbon volume ratios, most carbon fibre are surrounded by high elongation glass fibres, and there is little carbon clustering. Therefore, each carbon fibre fragments individually which results in a smooth transition between the elastic and plateau parts in the stress-strain curve in **Figure 2.22**. When the carbon content increases, there is a sharper transition point because of simultaneous fracture of carbon fibre clusters in the hybrid [24].

Czél et al. [39], [68] investigated the mechanical properties and failure modes of unidirectional (UD) interply glass/carbon hybrids incorporating thin carbon ply (0.03 mm) under tensile loading. The glass-carbon hybrid composites show progressive damage mechanisms (i.e. fragmentation of the carbon ply) and stable dispersed delamination after the first carbon ply fracture due to the low energy release rate [39] resulting in a pseudo-ductile stress-strain response. The so-called stable delamination refers to stable pull out of the fragmented carbon ply from the undamaged glass ply, which prevents the catastrophic failure of the hybrid composite after the first carbon ply fracture. To achieve the desirable pseudo-ductile responses in hybrid composites under tensile loading, appropriate material properties, and suitable values of relative thickness (i.e. thickness ratio of low strain material (LSM) to high strain material (HSM)) and absolute thickness of low strain material (LSM) need to be selected, as guided by the design framework developed by Jalalvand et al. [62]–[64].

2.10 Research scope

In real applications, structural parts made of fibre composites are often subjected to variable loading conditions. It is important to be able to design a thin-ply hybrid composites that will fail in a pseudo-ductile manner under different loading conditions such as compression and bending. The durability of thin-ply hybrid composites under cyclic loading is also an important factor when designing structural parts. Only limited research to assess pseudo-ductile behaviour of unidirectional (UD) thin-ply hybrid composite under fatigue, compression and bending has been done to date. The motivation of this study is to understand the mechanical behaviour and damage mechanisms of pseudo-ductile unidirectional thin-ply hybrid composites under tension, compression, bending and fatigue loading by using experimental material characterization, microstructural damage evaluation and analytical methods. In order to achieve the aim of this study, the following objectives have been identified for each loading cases:

1. Explore the response of pseudo-ductile UD thin-ply hybrid composites to repeated quasi-static tensile loading-unloading cycles and to understand the effect of damage accumulation on the load carrying capacity of thin-ply hybrid composites.
2. Explore the pseudo-ductility and gradual failure of UD thin-ply hybrid composites in compressive loading.
3. Investigate the flexural behaviour of UD thin-ply hybrid composites with pseudo-ductile tensile and compressive behaviour.
4. Characterisation of the fatigue behaviour of UD thin-ply hybrid composites, as well as to understand the damage evolution under cyclic loading.

2.11 Thesis outline

To fullfill the objectives above, extensive work has been carried out and presented in the following chapters in this thesis:

Chapter 1 – Introduction

Detailed explanation of the motivation behind the work conducted in this thesis which covers the application of carbon fibre composites, the advantages and disadvantages of fibre composites, engineering effort to alleviate the disadvantages.

Chapter 2- Literature Review

Discussion and evaluation of the available literature work on the definition of composite materials, fibre architecture and damage mechanisms in composites, tensile behaviour of UD hybrid composites, thin-ply composites and pseudo-ductile behaviour of unidirectional thin-ply hybrid composite, several mechanisms proposed to add pseudo-ductility or ductility to fibre composites, the mechanical behaviour (compression, bending and fatigue) of hybrid composites.

Chapter 3 - Quasi-Static Tensile Response of UD Thin-ply Hybrid Composites

Covers experimental static and loading-unloading tensile testing of unidirectional (UD) thin-ply hybrids, covering combinations of high strain and low strain materials to achieve gradual failure. Detailed analysis of the material is performed via stress-strain curve analysis to establish the extent of pseudo-ductility. Analysis on the relation between the damage accumulation and load carrying capacity is also presented.

Chapter 4- Compression Response of UD Thin-ply Hybrid Composites

Examines the potential of thin-ply hybrid composites to exhibit pseudo-ductility under compression. Covering testing of high strain and low strain material combinations to achieve gradual failure. Post-failure analysis is performed via optical microscopy to establish the factors governing the failure. Investigates the parameters that determine the pseudo-ductility under compression.

Chapter 5 - Flexural Response of UD Thin-ply Hybrid Composites

Examines the potential of thin-ply hybrids to exhibit pseudo-ductility under flexural loading. Material combinations which show the most promising results in terms of pseudo-ductility and initial stiffness from **Chapter 3** and **Chapter 4** are selected for further flexural testing. Investigation of the parameters that govern the pseudo-ductility under flexural loading.

Chapter 6 - Fatigue Response of UD Thin-ply Hybrid Composites

Investigation of the cyclic loading behaviour of undamaged (pristine) and damaged (pre-fractured) unidirectional (UD) thin-ply hybrid composites. Based on this study, a safe fatigue load level for UD thin-ply carbon/glass hybrid composites together with damage evolution characterisation and the relation between energy release rate and damage growth is presented.

Chapter 7 - Conclusions and Future Work

This chapter summarises the outcomes and the conclusions drawn from the research. Suggestions and recommendations for possible future research are included as well.

Chapter 3 Response of Unidirectional Thin-Ply Hybrid Composites to Quasi-Static Cyclic Loading

3.1 Introduction

Pseudo-ductile response with gradual failure under tensile loading has been demonstrated by Czél et al. [39], [60] in a unidirectional (UD) thin-ply hybrid composites configuration. Their work on hybrids involved the combination of central thin carbon plies (0.03 mm) sandwiched between standard thickness glass plies (0.155 mm). The responsible damage mechanisms which

lead to pseudo-ductile tensile response were fragmentation of the central carbon ply and stable delamination after the carbon fragmented due to the low energy release rate of the thin-ply hybrid composites [2]. To attract the attention of a wider range of industries on using thin-ply hybrid composites, their mechanical properties which include the behaviour under cyclic loading needs understanding. This chapter is dedicated to studying the response of UD thin-ply hybrid composites to repeated quasi-static tensile loading-unloading cycles and the effect of damage accumulation on the load carrying capacity of thin-ply hybrid composites.

3.2 Experimental methods

3.2.1 Materials

The thin-ply prepreg material being used for this study was carbon fibre reinforced polymer (CFRP) manufactured by SK Chemicals, South Korea. Two different types of thin carbon ply designated 'USN020A' and 'UIN050A' were used in the hybrid system. For the USN020A prepreg type, the code U, S, N, 020 and A indicate unidirectional fibres, standard fibre strength, no scrim, the fibre areal weight in g/m^2 and nominal resin weight content of 41% [112] respectively. While for prepreg type UIN050A, the code U, A, and N have the same indication as for the previous USN020A prepreg type, as for I and 050 indicate intermediate modulus fibre and the fibre areal weight in g/m^2. The carbon fibres for USN020A are a Mitsubishi Rayon TR30, classified as high strength, standard modulus and produced in 6000 filament tows [113] and for UIN050A, the fibres are a Mitsubishi rayon MR40, classified as intermediate modulus and produced in 12000 filament tows [113]. The matrix material is SK Chemicals semi-toughened epoxy, designated K50 [114]. For the high strain material, standard thickness S-glass/epoxy prepreg supplied by Hexcel was used, and the fibres are FliteStrand S ZT S-glass manufactured by Owens Corning [115]. The material data for the fibres and prepregs are presented in **Table 3.1** and **Table 3.2** respectively.

Table 3.1. Fibre properties of the applied UD prepregs (Carbon fibre types: SM-standard modulus and IM- intermediate modulus).

Fibre type	Manufacturer	Tensile modulus [GPa]	Tensile strain to failure [%]	Tensile strength [GPa]	Density [g/cm^3]	CTE α [1/K]
Pyrofil TR30 carbon	Mitsubishi Rayon	234 (SM)	1.9 [88]	4.41	1.79	-4.10^{-7}
Pyrofil MR40 carbon	Mitsubishi Rayon	295 (IM)	1.5	4.41	1.76	$-1.1*10^{-6}$
FliteStrand SZT S-glass	Owens Corning	88	5.5	4.8-5.1	2.45	2.10^{-6}

Table 3.2. Cured ply properties of the applied UD prepregs.

Prepreg type	Property	Fibre mass per unit area[b]	Cured ply thickness	Fibre volume fraction	Initial elastic modulus	Tensile strain to failure
	Unit	[g/m^2]	[mm]	[%]	[GPa]	[%]
TR30 /epoxy	Average	21.2 [39]	0.029 [39]	40.5 [39]	101.7[a] [39]	1.5[a] [39]
	COV [%]	4.0 [39]	-	-	2.8 [39]	7.5 [39]
MR40 /epoxy	Average	50 [60]	0.061[60]	45[b] [60]	134.6 [60]	-
	COV [%]	-	-	-	-	-
S-glass/epoxy	Average	190 [88]	0.155 [88]	51[b] [88]	45.7[88]	3.98 [88]
	COV [%]	-	-	-	3.2 [88]	1.1 [88]

[a] Measured on 16 ply UD laminates with 100/10 mm free length/width.
[b] Based on manufacturer's data.

The actual basic properties of TR30/epoxy prepreg in this study were obtained from the work by Czél et al. [39]. The fibre volume fraction was calculated based on the measured mass fraction of the the thin carbon prepreg. To measure the mass of the carbon fibre, the resin was burnt off in an atmospheric furnace for 60 minutes at 500 ^{o}C from ten 100 mm square thin prepreg samples. The weight of the remaining carbon fibre was then measured on a precision balance AS 220 with 0.1 mg readability. Based on the mass fraction measurement, the calculated carbon fibre volume fraction for the thin prepreg is v_f = 40.5% [39]. The average thicknesses of the cured thin carbon prepreg measured by using an optical microscopy on a polished cross-sectional samples indicate carbon ply thicknesses of 29.3 μm [39].

For MR40/epoxy and S-glass/epoxy, the fibre volume fraction is obtained from the manufacturer's data sheet and the cured ply thickness (CPT) in mm is calculated by using **Equation 3. 1** [116]**.**

$$CPT = \frac{w_f}{\rho_f \times V_f} \times 10 \qquad \textbf{Equation 3. 1}$$

The notation w_f, ρ_f and V_f refers to fibre mass per unit area [g/cm^2] , fibre density [g/cm^3], fibre volume fraction [%] respectively. As for the coeffiecient of thermal expansion (CTE) mentioned in **Table 3.2** , the manufacturer did not give any explanation on how the CTE was measured. A similar value of CTE for the carbon prepregs being used in this work was also reported by Laurin et. al. [117]. There is a reasonable agremeent between the calculated CPT from **Equation 3. 1** [116]**.**with the measured ply thickness for all prepregs with only 1%-3% discrepancy between those two as shown in **Table 3.22.**

Table 3.22. Calculated and measured cured ply thickness of the UD thin-ply hybrid composites (the number in the bracket indicates the coefficient of variation in [%]).

Designation	Lay-up sequence	Calculated thickness	Measured thickness

		[mm]	[mm]
MR40/S-Glass	$[SG_1/MR40_1/SG_1]$	0.371	0.378 (1.40)
TR30/S-Glass	$[SG_1/TR30_1/SG_1]$	0.339	0.342 (2.10)
	$[SG_1/TR30_2/SG_1]$	0.368	0.371(1.90)

The measured thickness in **Table 3.22.** is from an average measurement of six specimens for each hybrid configuration.

3.2.2 Specimen geometry

In this study, the geometry of the UD hybrid specimens tested within the experimental part were UD, parallel edge tensile specimens with the following dimensions 240/160/20/h (mm)-overall length (L)/L_f free length/W-width/h-variable thickness respectively (see **Figure 3.1**).

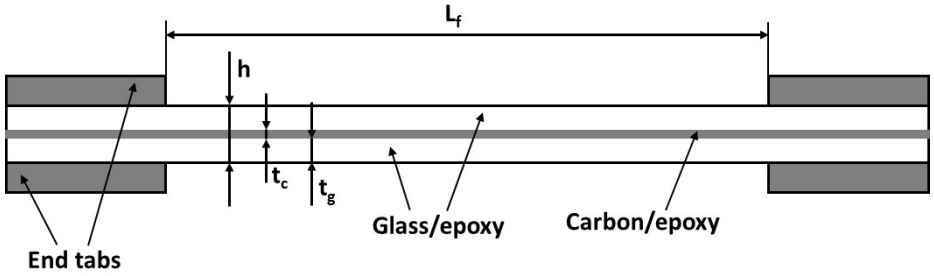

(a)

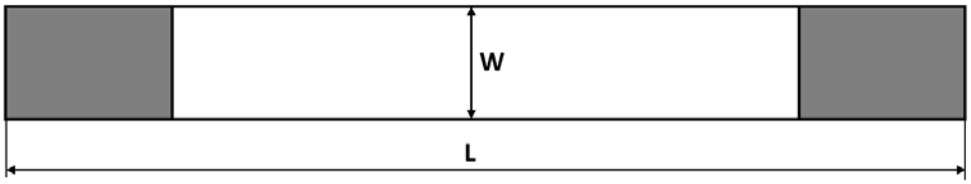

(b)

Figure 3.1. Schematic of thin-ply hybrid composite specimen (a)side view and (b)top view.

The notation t_g and t_c in **Figure 3.1** refers to the nominal thickness of the carbon and glass ply respectively.

3.2.3 Manufacturing method

The required 0° plies were cut from large rolls of Skyflex and Hexcel prepreg with the size of 300 x 300 mm. To preserve the useful lifetime of the material, it was sealed within a plastic bag and stored in a freezer at -20 °C and only removed for lay-up.

The UD hybrid laminates were constructed by placing the 0° plies on top of each other by using a clean, flat surface wooden plate in a temperature- and humidity-controlled clean room. The plies were laid-up on top of a wooden plate to ensure the alignment of the 0° fibres as the plate acts as a guideline. The layup sequence investigated in this work was $[SG/C_n/SG]$, where n = 1,2,

is the number of central carbon plies (C) with SG standing for S-glass. For the hybrid combination of S-glass/MR40 carbon, only a single ply of carbon was used while for S-glass/TR30 carbon, single and double plies of carbon were used. The finished laminates were then placed inside a vacuum bag as shown in a schematic in **Figure 3.2**. In order to have a good surface finish on the hybrid laminates, a silicon plate with a thickness of 2.40 mm was located between the release film and the specimen as shown in **Figure 3.2**.

To consolidate the hybrid laminates, it was necessary to cure them inside an autoclave under the cycle defined by the manufacturer (**Figure 3.3**, adapted from [114]). Both resin systems (K50 and 913) in the hybrid laminates have a curing temperature of 125°C and were found to be compatible, although no details were provided by the suppliers on the chemical formulation of the resins. Curing took place under elevated pressure (6.89 bar), with the laminate itself under vacuum (-0.95 bar). The pressure difference between the autoclave chamber and the vacuum bag helps to consolidate the hybrid laminates.

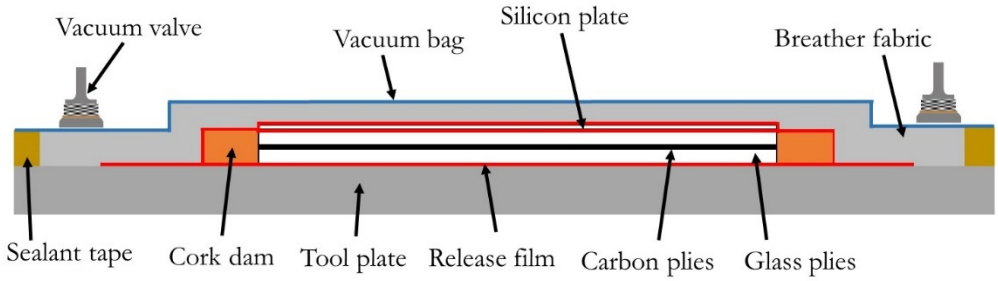

Figure 3.2. Configuration for vacuum bag autoclave cure of a composite laminate.

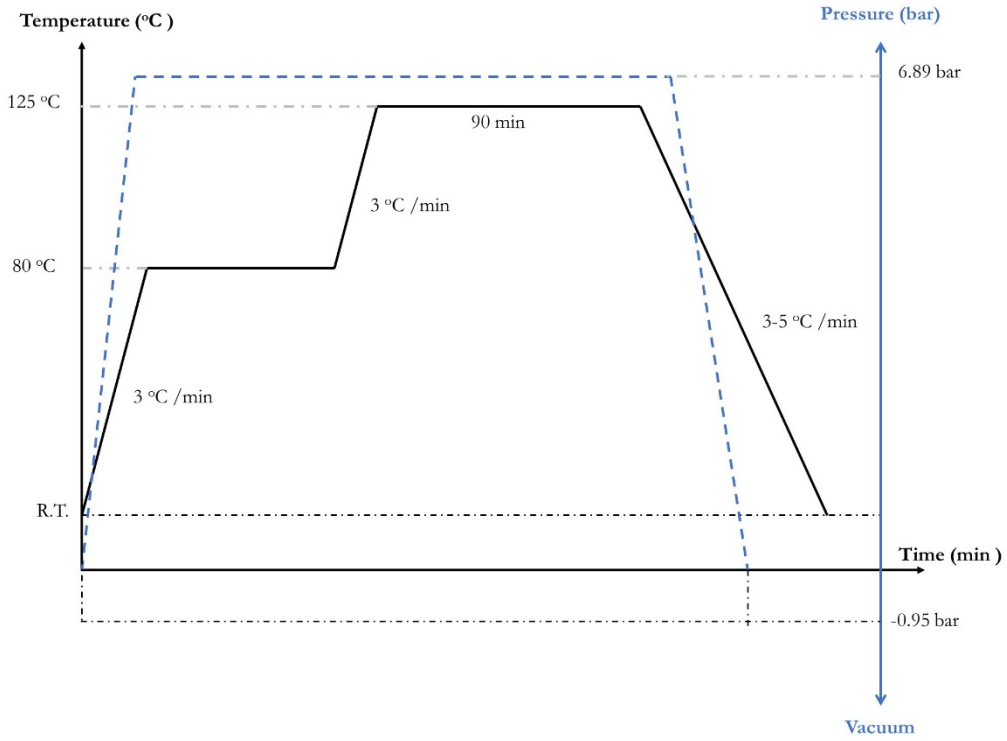

Figure 3.3. The recommended cure cycle for the hybrid laminates. Adapted from [5].

It is worth mentioning that the manufacturing method described in this section and the recommended cure cycle shown in **Figure 3.3** will also be used to cure the hybrid specimens tested under compression, bending and fatigue.

3.2.4 Mechanical test procedure

Two types of mechanical testing were conducted on the UD thin-ply hybrid composites: static tensile and quasi-static cyclic loading. Both of those tests were performed at room temperature on a computer controlled Instron 8801 type 100 kN rated universal hydraulic test machine with wedge type hydraulic grips. A 25 kN rated load cell was used on the machine. For the static tests, the hybrid specimens were loaded in uniaxial tension under displacement control using a crosshead speed of 2 mm/min. For each hybrid configuration, three specimens were tested in static tensile loading. The quasi-static cyclic tests were conducted under displacement control at a cross-head speed of 2 mm/min for both the loading and unloading phases, with immediate reloading. The number of quasi-static loading cycles was chosen based on the static tensile testing results of each hybrid configuration. A sufficient number of cycles was chosen to be able to study the effect of damage development on the load carrying capacity of the UD thin-ply hybrid composites. For the composites with one ply and two plies of TR 30, seven cycles were chosen, each with a certain displacement limit, after which the load returns to zero. The chosen displacements with their corresponding nominal laminate strains in brackets for thin-ply hybrid composites with 1 ply and 2 plies of TR30 were: 2.5 mm (1.56 %), 3 mm (1.87 %), 3.5 mm (2.18%), 4 mm (2.5%), 4.5 mm (2.81 %), 5 mm (3.12%), 5.65 mm (3.53 %). For the other hybrid composite materials with 1 ply of MR 40 carbon fibre, the chosen displacements with their corresponding laminate strains in brackets were: 2.5 mm (1.56 %), 3 mm (1.87 %), 3.5 mm (2.18%), 4 mm (2.5%), 4.5 mm (2.81 %), 5 mm (3.12%), 5.5 mm (3.43 %). For each type of hybrid, three specimens were tested. To measure the strains with a nominal gauge length of 130 mm, an Imetrum video gauge system with 5 Megapixel resolution was used and it allows a precision measurement down to 0.01% strain. The video gauge records with a speed of 17 frames per second. Videos recorded by the video gauge camera were kept for studying the damage development. **Figure 3.4** shows the experimental setup for this study.

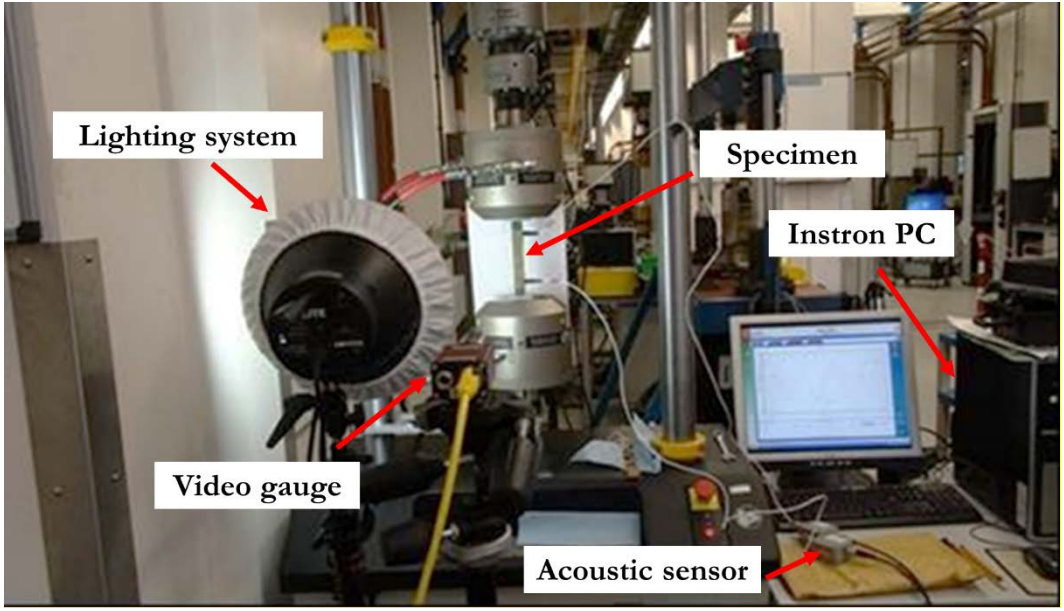

Figure 3.4. Instron test machine set up with the supporting equipment.

3.2.5 Delamination area measurement technique

Typical damage development found during static tensile loading was fragmentation of the carbon/epoxy ply followed by delamination between the fragmented ply and glass/epoxy ply, as reported by Czél et al. [39]. Due to the translucent nature of the glass/epoxy ply on the outside of the hybrid laminate, it was possible to detect the delamination surrounding the fragmented carbon ply [39]. The growth of delamination area will be used as a measure of damage during quasi-static cyclic loading and its correlation with the load carrying capacity of UD thin-ply hybrid composites will be deduced. The delamination area was measured from the images collected by the video gauge using an in-house developed MATLAB code. The images, acquired in grayscale by the video extensometer system (**Figure 3.5**a), are imported into MATLAB and cropped to cover only the specimen gauge length (**Figure 3.5**b). Finally, they are converted into binary black and white images using a predefined threshold (**Figure 3.5**c). The delaminated area was calculated by counting the white pixels and it was then compared against the total surface area to express it in terms of % area. The four white dots shown in **Figure 3.5**a were used to track the uniaxial strain using the video gauge system during the static loading. It should be noted from **Figure 3.5**a that well bonded areas appear black and the locally delaminated areas just around the cracks in the carbon ply are visible as the lighter areas due to the translucent nature of the glass/epoxy outer ply of the hybrid laminate.

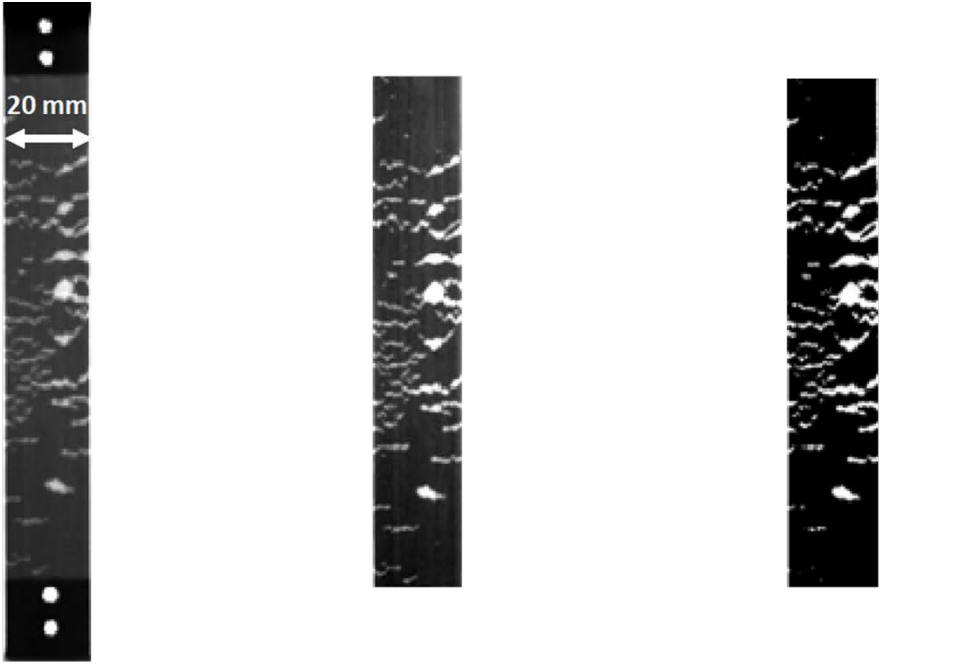

(a) Video gauge image (b) Cropped grayscale image (c) Black and white image

Figure 3.5. Image conversion process to determine the delamination area.

3.3 Results and discussion

3.3.1 Static loading response

Three specimen configurations were tested. These configurations were chosen based on the pseudo-ductile behaviour they have demonstrated in previous research [60]. The stress-strain curves of these hybrids with initial linear elastic behaviour followed by non-linearity and a plateau for the $SG_1/TR30_2/SG_1$ and $SG_1/MR40_1/SG_1$ configurations are shown in **Figure 3.6**. The term "plateau" will be used if there is an increase of strain at a near constant stress in a stress-strain curve response of a hybrid composite. For the $SG_1/TR30_1/SG_1$ hybrids, there is a reduced slope after the non-linearity point. The configurations of the tested specimens are given in **Table 3.4** along with their calculated mode II energy release rate at the expected failure strain of the carbon fibres (ε). The equation to calculate the energy release rate is adopted from the work by Czél et al. [39] and it is written in terms of the overall applied strain ε in **Equation 3.2.**

$$G = \frac{\varepsilon^2 E_c t_c \left(E_g (h - t_c) + E_c t_c\right)}{4 E_g (h - t_c)} \qquad \textbf{(Equation 3.2)}$$

The assumption for the energy release rate in **Equation 3.2.** is that the hybrid laminate loses the contribution from the carbon ply after the low strain ply fractures and delaminates from the laminate. This a reasonable assumption, since after the low strain ply fractures and delaminates, it does not contribute anymore to carrying load. The notation *g* and *c* in **Equation 3.2.** refers to glass/epoxy and carbon/epoxy respectively while *E*, *h*, and *t* are the material modulus, total laminate thickness and thickness of each ply.

Table 3.4. Specimen types tested within the present study (Specimen type designation: SG-S Glass, C- Carbon, with numbers corresponding to the number of constituents prepreg ply, Carbon types: SM-standard modulus, IM-intermediate modulus).

Spec. Type	Carbon fibre type -	Nominal thickness (mm)	Mode II energy release rate at the failure strain of the carbon ply (N/mm)
$SG_1/MR40_1/SG_1$	IM	0.371	0.736 at 1.50%
$SG_1/TR30_1/SG_1$	SM	0.339	0.322 at 1.90%
$SG_1/TR30_2/SG_1$	SM	0.368	0.715 at 1.90%

The calculated energy release rates shown in **Table 3.4** for the three configurations are all lower than the fracture toughness (G_{IIC}) of the glass/carbon composites, 1.1 N/mm [39], which has been measured by Czel et al. [39] on a similar hybrid specimens but with a cut through the entire carbon layer across the width. This indicates that after the first fracture of the carbon ply, unstable delamination and pull-out of the central carbon ply is not expected in these specimen types.

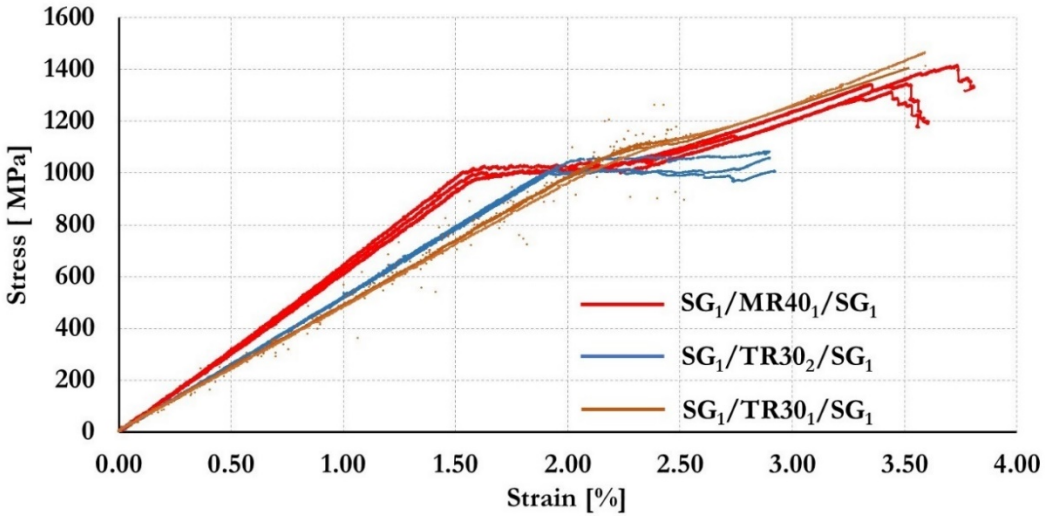

Figure 3.6. Stress-strain curves of various S-glass/high strength carbon hybrid. The outlier dots are the noise coming from the video gauge system.

Figure 3.6 shows the stress-strain response of the hybrid configurations tested in this work, which indicate different responses between the hybrids comprising high strength (standard modulus) TR30 carbon plies with that comprising intermediate modulus MR 40 carbon plies. Comparing the initial modulus of glass/epoxy ply in **Table 3.2** with the that of hybrid configuration in **Table 3.5,** it is noticed that there is a modulus increase of 10.5%, 19.3%, and 38.2% for $SG_1/TR30_1/SG_1$, $SG_1/TR30_2/SG_1$, $SG_1/MR40_1/SG_1$ respectively. The damage mechanism for $SG_1/TR30_1/SG_1$ was observed as a dispersed fragmentation dominated failure, where damage in the form of short cracks develops in parallel across the specimen width. The fragmentation itself, appeared in the carbon ply between the knee transition points (2.19% and 2.50%). Due to the translucent glass ply, the gradual crack development was visible during tensile loading and reached saturation at 2.50%. Between the knee transition points, there is a reduced of slope from the initial linear elastic region and smooth transition due to the damage mechanisms observed. After the second saturation point (2.50%), the stress rises because the tensile machine

still imposes a load on the hybrid specimen and the additional load is mainly carried by the glass plies (this phenomenon is also relevant for the $SG_1/MR40_1/SG_1$ and $SG_1/TR30_2/SG_1$ configurations). The explanation behind the gradual failure in $SG_1/1TR30_1/SG_1$ is the low G_{II}, as shown in **Table 3.4**, for this configuration due to the very low carbon ply thickness.

A favourable pseudo-ductile response was also obtained for the $SG_1/TR30_2/SG_1$configuration, displaying two pronounced knee transition points (1.90% and 2.76%). The first knee transition point (1.90%) referred to as ε_k, is where the fragmentation of the carbon/epoxy ply becomes established [65], and from ε_k, gradual damage development in the form of fragmentation and dispersed delamination appears in the specimen until it saturates at 2.76%. Contrary to the previous hybrid configuration with a single TR30 carbon ply which has short cracks, the fragmentation in $SG_1/TR30_2/SG_1$ consisted of long and relatively straight cracks across the whole specimen width followed by stable pull-out of the fragmented carbon ply. Because of carbon ply fragmentation and dispersed delamination, a wide plateau between the first knee point strain (1.90%) and second knee point strain (2.76%) can be observed in this configuration, thus providing enough strain margin before the final failure event. After careful examination of a typical damaged $SG_1/TR30_2/SG_1$ hybrid specimen when the test was interrupted at 2.76% strain, it can be concluded that the damaged pattern (fragmentation, delamination and intact carbon ply), is identical on the front and back face of the specimen as shown in **Figure 3.7.** The cracks shown in **Figure 3.8** looks like a stair-shaped tortuous path across the whole width of the specimen. The variation of fibre strength results in distributed fibre breaks at random locations rather than cumulatively at the site of the initial break which creates a tortuous crack path [14]. As the fibre breaks, the overload in the adjacent fibre is redistributed, and when it exceeds the strength of a weak fibre segment, the fibre will fracture and serve as an initiation point for the next fibre failure.

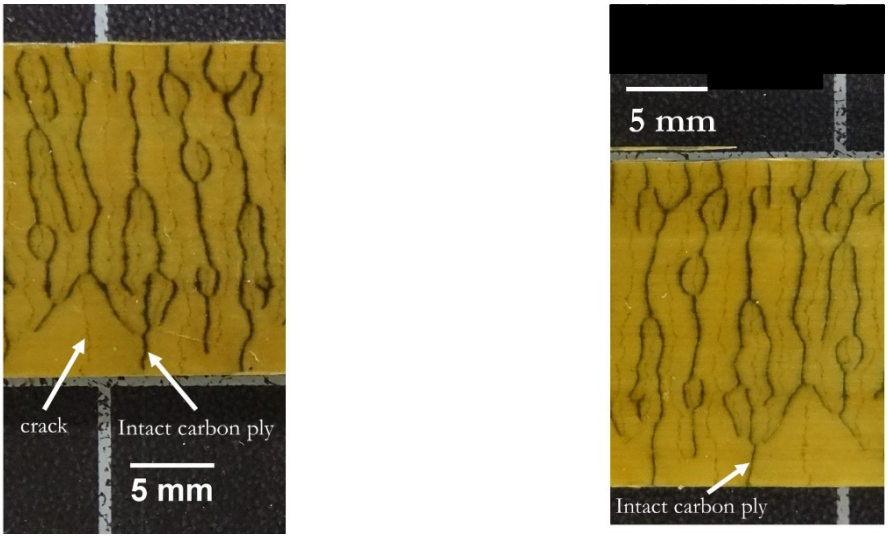

(a) (b)

Figure 3.7. Identical damage pattern on the front face (a) and back face (b) of $SG_1/TR30_2/SG_1$ hybrid specimen at 2.76% strain. The shape of the intact carbon ply is identical on both sides.

It is also expected that an identical damage pattern on both sides is present for $SG_1/TR30_1/SG_1$ and $SG_1/MR40_1/SG_1$ hybrid configurations providing that there is marginal thickness variations across the width.

The hybrid with $SG_1/MR40_1/SG_1$ configuration also displays favourable pseudo-ductile failure behaviour as shown in **Figure 3.6**, with two obvious transition points (1.53% and 2.31%). Multiple fragmentations and dispersed delamination also appear in this hybrid configuration contributing to the failure type and a plateau between the first knee point strain (1.53%) and second knee point strain (2.31%). The type of damage observed in $SG_1/MR40_1/SG_1$ was well distributed multiple crack formation (fragmentation) across the specimen's surface area.

All three hybrid configurations display pseudo-ductile response during static tensile loading with a noticeable difference in their first carbon strain to failure and knee-point strain where the fragmentation of the carbon ply has been established. As shown in **Table 3.5**, the $SG_1/MR40_1/SG_1$ hybrid configuration has the lowest first carbon strain to failure and knee-point strain compared to the $SG_1/TR30_1/SG_1$ and $SG_1/TR30_2/SG_1$ configurations which can be explained due to the lower strain to failure of MR40 carbon fibre shown in **Table 3.4**.

The tensile results summary for the investigated hybrid configurations is shown in **Table 3.5.** Because the tensile test results are affected by the small thermal residual strains arising from the mismatch in the coefficient of thermal expansion between the glass and carbon layers, the strains shown in **Table 3.5** have been corrected for the elastic thermal residual strain in the 0^o fibre direction with the detailed equation shown in Appendix A. The elastic thermal strains were calculated from the equilibrium-force state between the carbon/epoxy and glass/epoxy layers by assuming constant strain through the thickness and a 100 ^oC temperature difference from the cure temperature to room temperature. Classical Laminate Theory was incorporated to calculate the elastic thermal strains as shown in Appendix A. The elastic thermal residual strain in the transverse direction is not taken into account in this work since the fibre in the hyrid laminate is in the 0^o direction and the load is mainly carried by the fibre. The cured ply properties of the applied UD prepregs to determine the elastic thermal residual strain are shown in Error! Reference source not found..

Error! Reference source not found.. Cured ply properties of the applied UD prepregs as an input parameter to determinethe thermal residual strain.

Prepreg type	E_{11} [GPa]	E_{22} [GPa]	CPT [mm]	α_{11} [1/K]	α_{22} [1/K]	G_{12} [GPa]	ν_{12}
TR30/epoxy	101.7	9[116]	0.029	$7.20*10^{-7}$ [a]	$2.6*10^{-5}$[117]	4.4[116]	0.25[116]
MR40/epoxy	134.6	9[116]	0.061	$-3.49*10^{-7}$ [a]	$2.6*10^{-5}$[117]	4.4[116]	0.27[116]
S-glass/epoxy	45.7	10.3[116]	0.155	$3.8*10^{-6}$ [a]	$2.6*10^{-5}$[117]	3.1[116]	0.30[116]

[a] calculated by using the Classical Laminate Theory (CLT) shown in Appendix A.

The calculated residual elastic strains in the carbon for the presented hybrid configuration are -0.0224%, -0.0261%, -0.0266% for $SG_1/TR30_2/SG_1$, $SG_1/TR30_1/SG_1$, $SG_1/MR40_1/SG_1$ respectively and this has been accounted for in the values in **Table 3.5** for the strain at first carbon layer failure and at the knee-point strain.

The knee point stress (σ_k) and strain (ε_k) are found from the intersection of lines fitted to the initial linear (red line) and plateau (green line) parts of the stress-strain curves. For the second knee, the transition strain (ε_y), is determined by the intersection of lines fitted to the plateau (green line) and the second rising part (blue line) of the stress-strain curves, as shown in **Figure 3.8.** It was possible to measure the first carbon fracture strain in the hybrid specimens from the recorded video gauge instrument as the first carbon crack is visible due to the translucent nature of the glass ply. As noted from **Table 3.5**, the strain at first carbon ply failure and knee point strain (ε_k) for the $SG_1/TR30_1/SG_1$ hybrid is higher than for the $SG_1/TR30_2/SG_1$ hybrid. This is due to the 'hybrid effect' which provides a delay of damage initiation due to a restraint on broken carbon cluster development [65]. For the thinner hybrid with a single carbon ply, the fibre failure and fragmentation appear at a slightly higher strain because of the limited number of fibres through the thickness of the ply inhibiting formation of a critical cluster [65].

Table 3.5. Tensile results summary of the specimen types tested (Numbers in brackets indicates the coefficient of variation in [relative %]).

Spec. Type	No. of specimens	Initial elastic modulus [GPa]	Strain at first carbon ply failure [%]	Strain at knee point ε_k [%]	Stress at knee point σ_k [MPa]	Pseudo-ductile ε_{pd} [%]
$SG_1/MR40_1/SG_1$	3	63.11 (2.3)	1.53 (2.4)	1.55 (1.3)	983.9 (2.6)	1.19 (12.40)
$SG_1/TR30_1/SG_1$	3	48.91 (2.1)	2.13 (2.5)	2.19 (1.4)	1106.5 (3.1)	-
$SG_1/TR30_2/SG_1$	3	56.52 (3.8)	1.85 (2.2)	1.90 (1.5)	1074.2 (4.0)	-

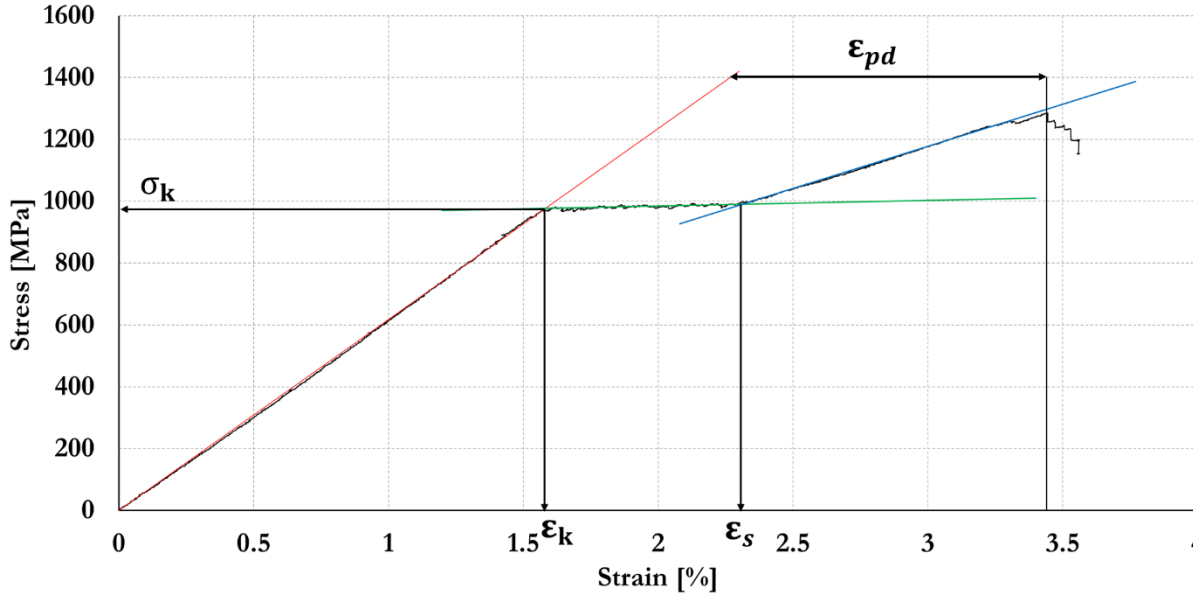

Figure 3.8. Method to determine knee point stress (σ_k) and strain ($_{\varepsilon k}$), second knee transition strain (ε_s) and pseudo-ductile strain (ε_{pd}) for a typical pseudo-ductile response of ($SG_1/MR40_1/SG_1$).

As shown in **Figure 3.8**, the pseudo-ductile strain (ε_{pd}) is defined between the strain of a point on the initial linear elastic line and the strain at the failure stress. The pseudo-ductile strain for $SG_1/TR30_1/SG_1$ and $SG_1/TR30_2/SG_1$ hybrid configurations were not given in **Table 3.5**, because the testing was stopped before the final glass failure took place. Although the method in **Figure 3.8** is shown for the ($SG_1/MR40_1/SG_1$) configuration, it could also be applied to the other hybrid configurations. In **Section 3.3.2** discussing quasi-static cyclic loading response of the three hybrid configurations, the method in **Figure 3.** will also be used as there are knee-points present during the quasi-static cyclic loading.

3.3.2 Quasi-static cyclic loading response

3.3.2.1 [$SG_1/MR40_1/SG_1$] response

The typical loading-unloading behaviour for an [$SG_1/MR40_1/SG_1$] specimen is presented in **Figure 3.9.** The cyclic responses show initial linear behaviour followed by non-linear behaviour and an increase of stress at higher strains after saturation of fragmentation.

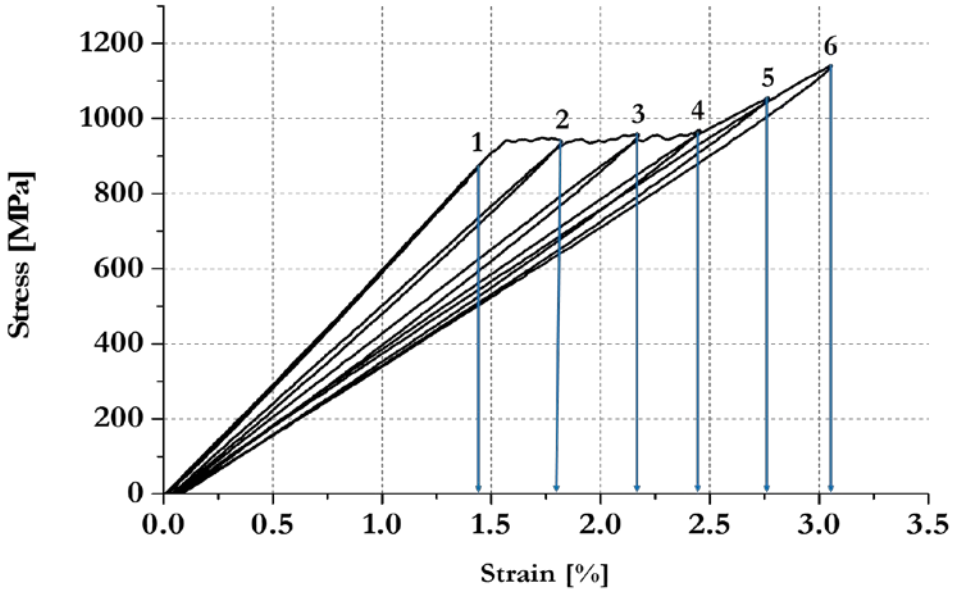

Figure 3.9. Typical cyclic stress-strain curve for [SG_1/$MR40_1$/SG_1].

The notation from 1 until 6 in **Figure 3.9.** refers to the following peak strains: 1.45%, 1.82 %, 2.17%, 2.45%, 2.77 %, 3.05% respectively, from which the specimen was unloaded and subsequently reloaded. It should be noted that when tested under displacement control, each of the peak strains in the actual stress-strain curves shown in **Figure 3.9** did not reach the intended nominal peak strains mentioned, in **Section 3.2.4**. During the first displacement loading, there was an initial linear response, and the subsequent unloading followed almost the same path because the damage threshold was not exceeded. The second loading trajectory overlaid the first but went beyond the initial failure strain of the carbon into the plateau region of the stress-strain response. The damage mechanism of the [SG_1/$MR40_1$/SG_1] configuration within the plateau region shows a progressive fragmentation of the carbon ply followed by dispersed delamination as depicted in **Figure 3.9** for each applied strain. The first knee-point in **Figure 3.9.** which is at 1.57% is where the fragmentation of the carbon ply has been established causing a reduction of stiffness. It is also visible that after 2.45% strain, the fragmentation has attained saturation and the delamination area did not grow significantly further, which agrees with the second knee point (2.45%) in **Figure 3.9.** As shown in **Figure 3.9** for the damage at 2.45% strain, the black-lines correspond to the intact carbon-ply which do not have a sufficient length to carry any more load, as a consequence, the additional load is carried by the glass plies and because there is no more fragmentation or delamination, there is a stress increase as shown in **Figure 3.**.

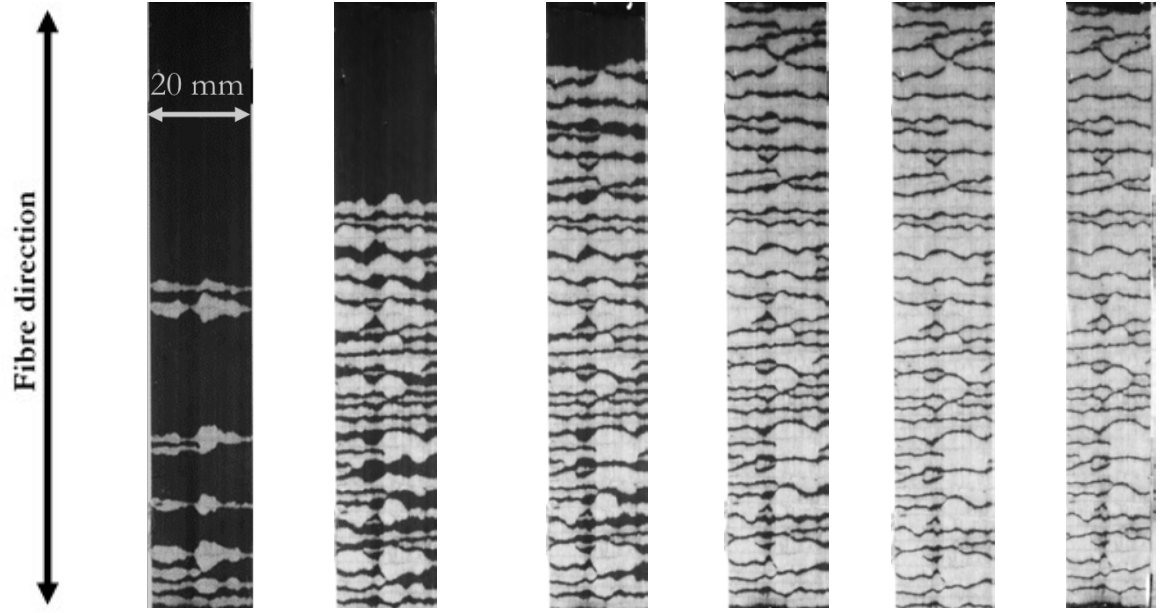

Figure 3.9. Typical damage development at each strain for [$SG_1/MR40_1/SG_1$] hybrid.

Lack of delamination on the intact carbon-ply (residual black-lines) at 3.05% strain shown in **Figure 3.9** is possibly due to insufficient stress. The shear stresses acting on the intact carbon-ply are less than the yield shear stress and thus the material is undamaged, leaving residual black-lines on the hybrid composite. The bright area which corresponds to the delaminated area is where only frictional shear applies and assumed to carry no loads. This mechanism also applies for the formation of residual black-lines in the [$SG_1/TR30_1/SG_1$] and [$SG_1/TR30_2/SG_1$] hybrid configurations.

As shown in **Figure 3.9**., after the specimen is immediately reloaded from zero load, there is a linear elastic behaviour followed by a non-linear behaviour with a knee-point marking the transition. This knee-point is due to fragmentation in the carbon ply. Further fragmentation from the knee-point to the applied peak strain can be attributed to the failure of further weak carbon clusters [10]. When the carbon ply had already fractured across the width as shown in **Figure 3.9.**, the high interlaminar shear stress which developed between the glass and the fractured carbon ply caused delamination between those plies.

As the damage progresses, the hybrid loses its stiffness gradually due to fragmentation and stable delamination. There is also a small amount of hysteresis which is believed to be due to reversed high interlaminar shear stresses in the regions around the carbon ply fractures. Due to the compressive stresses around the fracture tip, friction can also apply some interlaminar shear stresses to the intact carbon ply [118]. The high shear stresses between the carbon and glass plies cause the matrix to deform, leaving a residual strain at zero load for all three hybrid configurations. Another possible explanation for the existence of residual strain is due to the accumulation of debris between the open cracks preventing the surface cracks to return to its original state when unloaded. It is also worth mentioning that all the hybrid configurations mentioned in this work experience vertical ply splitting from the edge as shown in the damage mechanism at 3.05% applied

strain in **Figure 3.9**. It was also observed that residual bonding between the glass and carbon plies still exists at the final peak strain of 3.05% as shown in **Figure 3.9**, in the form of black-lines running perpendicular to the specimen's length which means that the hybrid had not totally delaminated. To quantify the stiffness loss due to damage growth, the secant modulus for all the UD thin-ply hybrid composites was evaluated at each reloading step between 0 MPa and 600 MPa as shown schematically in **Figure 3.10**. This value was chosen as it is in the elastic region before any further damage takes place. The same method was also used to measure the initial modulus of the [$SG_1/TR30_1/SG_1$] and [$SG_1/TR30_2/SG_1$] hybrid composites.

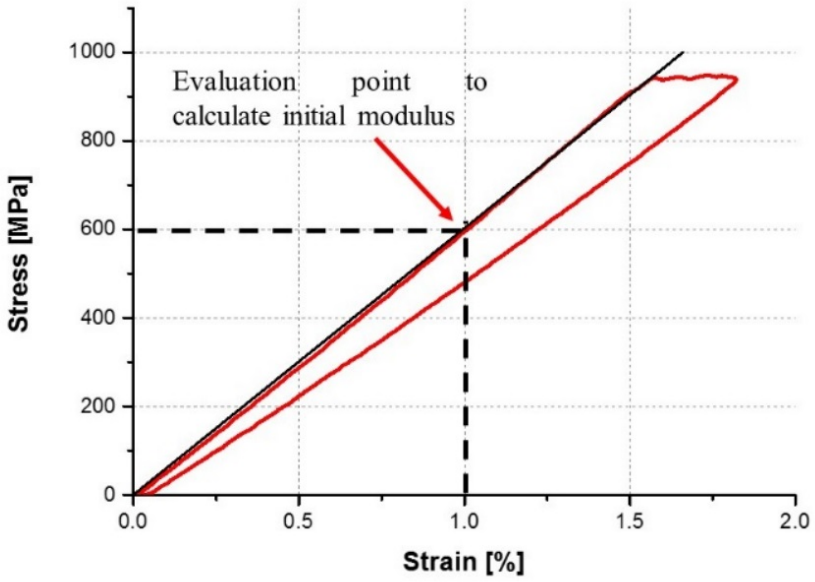

Figure 3.10. Schematic drawing to define the secant stiffness for all thin-ply hybrid composites.

Stiffness loss as a function of applied peak strain is shown in **Error! Reference source not found.**, which shows a gradual loss of stiffness due to fragmentation and stable delamination with increasing applied peak strain from 1.82% to 2.45%, after which the stiffness approaches the expected value with no carbon contribution at higher strain. After the fragmentation reached saturation at 2.45% strain, with further cyclic loading, the measured stiffness remains nearly constant up until 3.05% where the testing was terminated. The stable delamination after fragmentation during quasi-static cyclic loading is due to the low energy release rate of UD thin-ply hybrid composites [39]. The error bar in **Error! Reference source not found.** shows a low coefficient of variation between 1.10%-2.40% which indicates the repeatability of the test series. The initial E_0 and expected final stiffness E_f is calculated by using **Equation 3.3** and **Equation 3.4** respectively adopted from the work by Czél et al. [39].

$$E_o = \frac{\left(E_g(h - t_c) + E_c t_c\right)}{h} \qquad \textbf{Equation 3.)}$$

$$E_f = \frac{\left(E_g(h - t_c)\right)}{h}$$ Equation 3.)

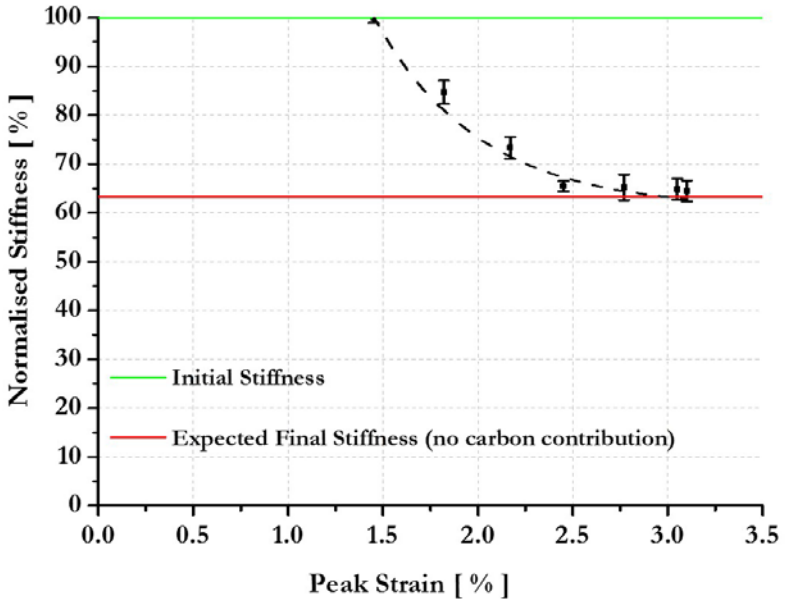

Figure 3.11. Stiffness loss at each applied peak strain for [SG_1/$MR40_1$/SG_1].

There is agreement between the value of the measured initial stiffness with the theoretical initial stiffness calculated using **Equation 3.**. As already mentioned before, the gradual stiffness loss of the hybrid is due to fragmentation of the carbon ply and stable delamination between the glass and carbon ply. Because each fragmentation is associated with delamination area surrounding it, then it would be interesting to be able to draw a relation between delamination growth and stiffness loss for UD thin-ply hybrid composites under quasi-static cyclic loading as delamination in this type of hybrid is visually observable. To correlate the stiffness loss with subsequent delamination growth during quasi-static cyclic loading, the images taken from the recording video gauge at different peak strain levels were analysed using an in-house developed MATLAB code as explained in **Section 3.2.5.**

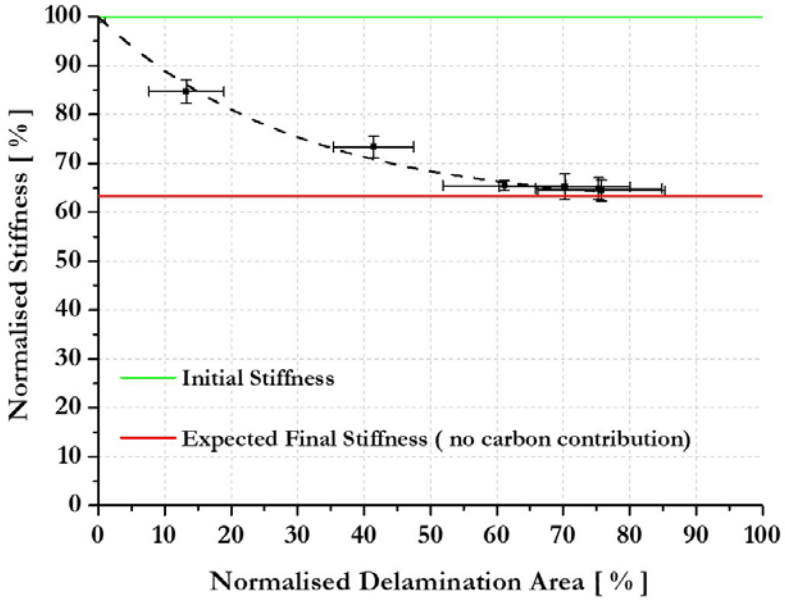

Figure 3.12. Stiffness loss with growing delaminated area for [SG_1/$MR40_1$/SG_1] hybrid configuration showing the error bar in both axes.

Error! Reference source not found. shows a plot of stiffness loss, as a function of normalised delamination area for the average data of 3 specimens. It is shown in **Error! Reference source not found.**, that there is a gradual loss of stiffness from 15% to 61% delamination area. This is because multiple fragmentation of carbon ply followed by delamination growing from those fragmentation sites occurred during quasi-static cyclic loading. The normalised stiffness approached saturation when there was no significant additional fragmentation and delamination growth with further loading. As shown in **Figure 3.9**, for the damage development from 2.45% to 3.05% strain, there is no significant damage growth in the hybrid specimen. At 61% delamination area, the stiffness loss reaches saturation, and this could be attributed to the high shear stress between the intact carbon and glass ply causing deformation at the interface which hinders load transfer and leads to loss of stiffness contribution. Having a closer examination of the normalised delamination area from 61% to 75%, it is seen that the normalised stiffness is around 2% above the expected final stiffness with no carbon contribution. This could mean that the remaining carbon ply shown as black-lines running perpendicular along specimen width in **Figure 3.9** still contributes to minor load carrying capacity. It is also worth mentioning that the error bars shown in **Error! Reference source not found.** for the normalised delamination area, imply significant variation of delamination size between each of the hybrid specimens during the quasi-static cyclic loading.

It would be interesting to measure the width of the residual intact carbon ply fragments which may still contribute slightly to the load carrying capacity. The method to measure the width of the residual black-lines is shown in **Figure 3.13** for a [SG_1/$MR40_1$/SG_1] hybrid specimen after it has been loaded until 3.05% strain. Measurements on six residual black-lines were made to draw

the width distribution. This method is also applicable to measure the width of the residual intact carbon ply on the [$SG_1/TR30_1/SG_1$] and [$SG_1/TR30_2/SG_1$] hybrid configurations.

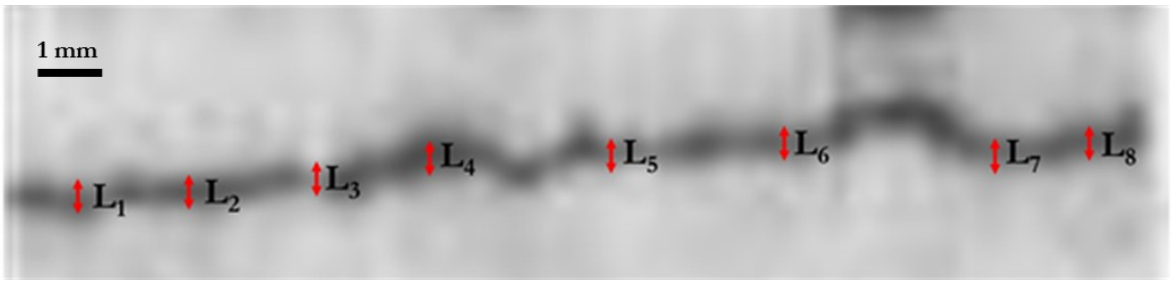

Figure 3.13. Method to measure the width of the residual black-lines on a [$SG_1/MR40_1/SG_1$] hybrid configuration.

Figure 3.14 shows the measured average width distribution of the residual black-lines on a [$SG_1/MR40_1/SG_1$] hybrid configuration at 3.05% strain. The average width of the residual black-lines is between 0.350-0.900 mm where the shear stress would not be able to reach the yield stress, thus leaving the ply interface intact.

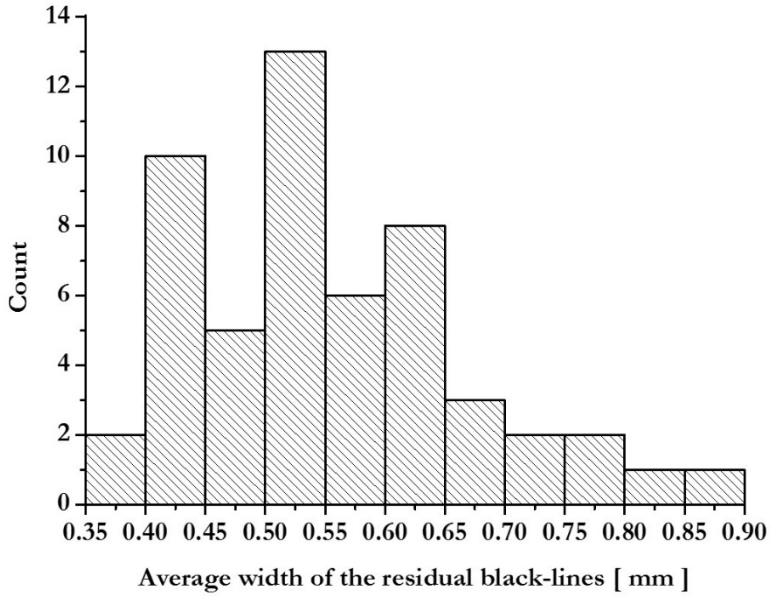

Error! Reference source not found.. Width distribution of the residual black-lines on a [$SG_1/MR40_1/SG_1$] hybrid configuration.

3.3.2.2 [$SG_1/TR30_1/SG_1$] response

A typical experimental result for the [$SG_1/TR30_1/SG_1$] laminate is presented in **Figure 3.15**. In general, there is an initial linear elastic behaviour before the first knee-point followed by non-linear behaviour with a continuous increase of stress at higher strains after the knee-point strain of 2.20% until 3.50%, with the fragmentation saturating before then. It was observed that beyond the knee-point, there was a dense fragmentation and localised delamination in this hybrid configuration which is due to the shorter process zone around the fragmented ply as shown by Jalalvand et al. [64] in their numerical damage analysis of UD thin carbon/glass hybrid composites. As also

explained in [64], in the thinner hybrid laminate, the interface is less damaged so it is possible that the load is being transferred from the intact carbon ply to the glass ply as the fragmentation progresses which means that the [$SG_1/TR30_1/SG_1$] configuration does not delaminate under quasi static cyclic loading and therefore the stress continuously increases beyond the knee-point as shown in **Figure 3.15**. **Error! Reference source not found.** shows the damage pattern at each peak strain for the [$SG_1/TR30_1/SG_1$] configuration, showing a denser fragmentation area compared to the [$SG_1/MR40_1/SG_1$] specimens in **Figure 3.9.** and [$SG_1/TR30_2/SG_1$] in **Figure 3.19**.

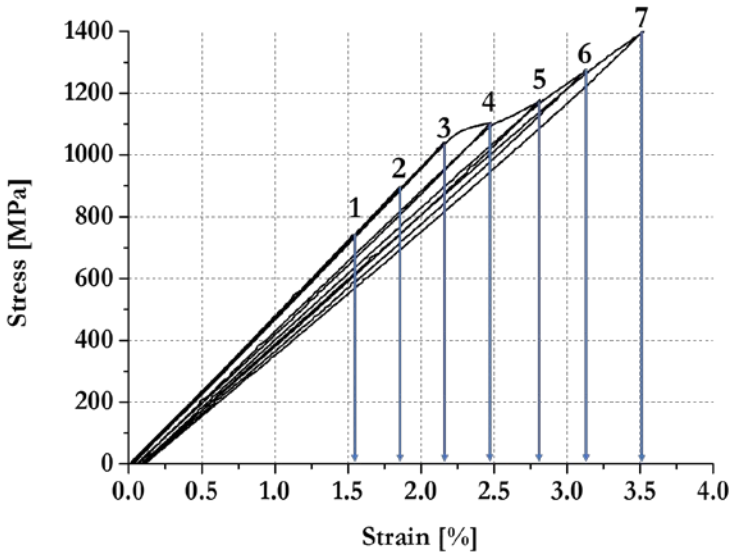

Figure 3.15. Typical cyclic stress-strain curve for [$SG_1/TR30_1/SG_1$] hybrid.

The notation from 1 until 7 in **Figure 3.15** refers to the following peak strains: 1.54 %, 1.86 %, 2.17%, 2.47%, 2.81 %, 3.13%, 3.52% respectively. As shown in **Figure 3.15**, initial linear response is shown for the first, second and third loading cycles, because the damage threshold has not been exceeded. For the fourth loading trajectory, it overlaid the rest but went beyond the initial failure strain of the carbon into the increasing region of the stress-strain response. It was observed from this work, that the carbon ply in this hybrid configuration failed at an initial strain of 2.31% which is higher compared to the 1.90% strain to failure of the fibre mentioned in **Table 3.1**, which means that the outer glass ply provided constraint on further carbon fractures forming a critical broken cluster, thus delaying the initial failure strain of the carbon ply until a higher strain (hybrid effect). It should be noted that the criterion for carbon ply failure is the first visible fracture during loading. Within the non-linear region (from 2.47% to 3.52% strain), progressive fragmentation of the carbon ply with small fragment spacing took place. It was challenging to observe the growth of fragmentation with subsequent loading strain due to its small scale as indicated in **Error! Reference source not found.**.

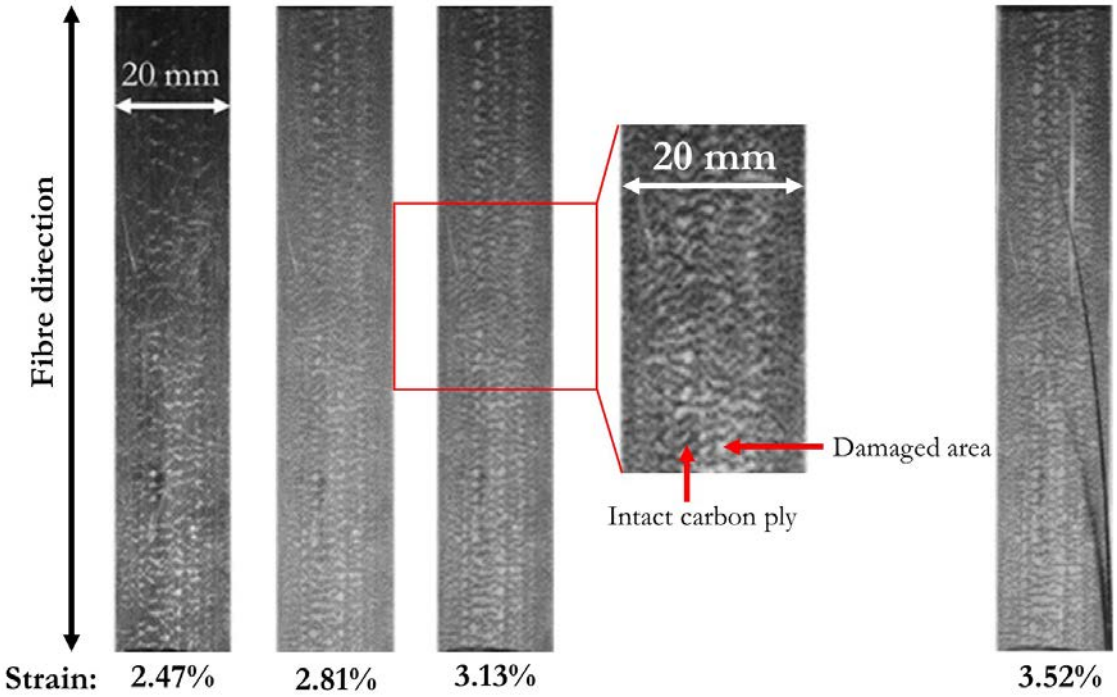

Figure 3.16. Typical damage pattern at each peak strain for [SG_1/$TR30_1$/SG_1] hybrid.

The increasing stress beyond the knee-point means that after fragmentation of the carbon ply, no real delamination develops as occurred in the [SG_1/$MR40_1$/SG_1] configuration. This delamination is the reason behind the plateau in the stress-strain curve of [SG_1/$MR40_1$/SG_1] and [SG_1/$TR30_2$/SG_1] configurations. Dense fragmentation is already shown at 2.47% strain in **Error! Reference source not found.**. and with increasing strain, fragmentation grew continuously. As the damage progressed, a small amount of hysteresis also developed which is attributed to reversed high interlaminar shear stress in the regions around the carbon ply fractures. As explained in **Section 3.2.1**, this shear stress could be affected by friction between the glass and carbon ply because of the presence of compressive stresses around the crack tip. As depicted in **Error! Reference source not found.**, residual bonding between the glass and carbon ply still exists at the final peak strain of 3.52% in the form of black-lines running perpendicular to the specimens' length. After the fragmentation is saturated at 3.52% strain, the [SG_1/$TR30_1$/SG_1] hybrid configuration has lost 50% stiffness contribution from the carbon ply.

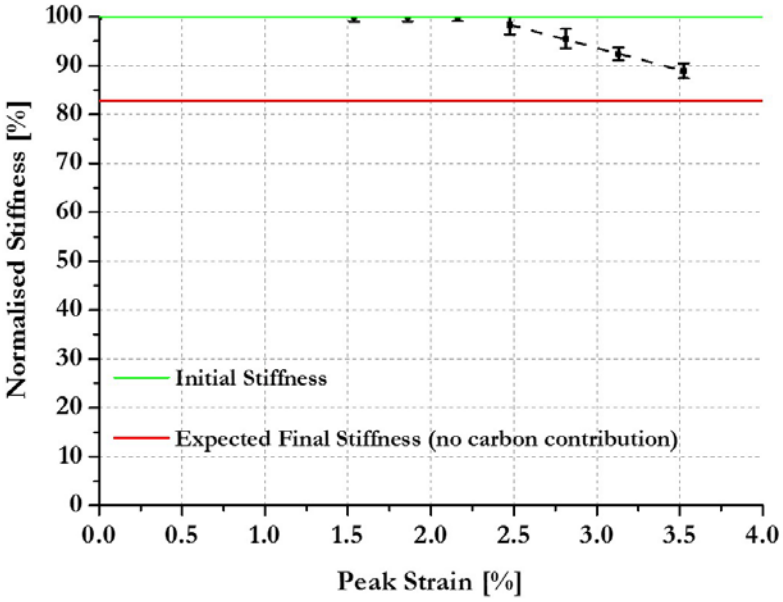

Figure 3.18. Stiffness loss at each peak strain for [SG_1/$TR30_1$/SG_1] hybrid.

Stiffness loss as a function of applied peak strain for [SG_1/$TR30_1$/SG_1] hybrid is shown in **Error! Reference source not found.**, which clearly shows a constant stiffness up to the first three peak strains followed by gradual loss of stiffness from the fourth until the final peak strain due to fragmentation of the UD thin-ply hybrid composites [39]. It is shown in **Error! Reference source not found.** that the final stiffness is substantially higher than the final expected stiffness, which could be attributed to substantial intact area of carbon. The error bar for the normalised stiffness in **Error! Reference source not found.** shows a low coefficient of variation between 0.9%-1.50% which also indicates the consistency of the tests.

The measured width distribution of the residual black-lines in a [SG_1/$TR30_1$/SG_1] hybrid configuration at 3.52% peak strain is shown in **Figure 3.17.** The average width of the residual black-lines is between 0.300-0.850 mm where the shear stress would not be able to reach the yield stress, thus leaving the ply interface intact.

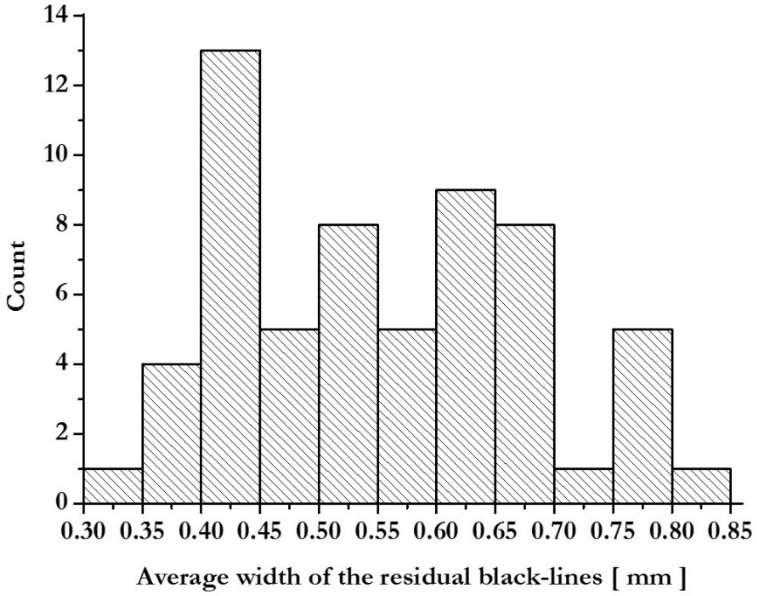

Figure 3.17. Width distribution of the residual black-lines on a [$SG_1/TR30_1/SG_1$] hybrid configuration.

3.3.2.3 [$SG_1/TR30_2/SG_1$] response

A typical experimental result for the [$SG_1/TR30_2/SG_1$] laminate is presented in **Figure 3.18**. The cyclic responses show initial linear elastic behaviour before the first knee-point strain of 2.03% followed by non-linear behaviour after the knee-point strain and slight increase of stress at the final peak strain of 3.13%.

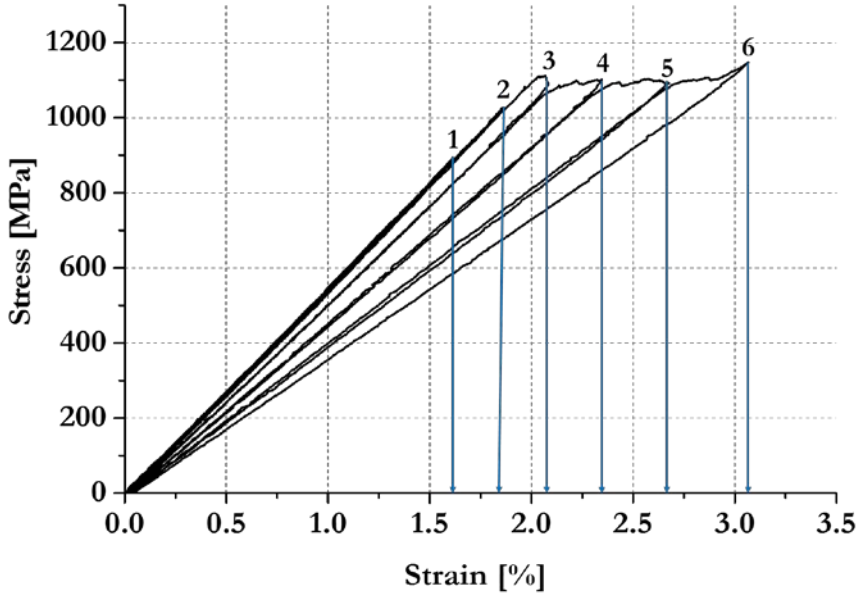

Figure 3.18. Typical cyclic stress-strain curve for [$SG_1/TR30_2/SG_1$].

The notation from 1 until 6 in **Figure 3.18** refers to the following peak strains: 1.61 %, 1.86 %, 2.07%, 2.35%, 2.67 %, 3.13% respectively. **Figure 3.18** shows the initial linear response for the loading and unloading curves for the first and second loading cycles when it was loaded below the damage threshold. The third loading trajectory overlaid the first and second path but

went beyond the knee point strain of the hybrid into the plateau region of the stress-strain response. It was observed from this work, that the first visible carbon fracture occurred at a strain of 2.01% which is higher compared to the failure strain of TR30 fibre mentioned in **Table 3.1**. This hybrid effect is lower than that of the [$SG_1/TR30_1/SG_1$] laminate because of the higher ply thickness which meant that the weak clusters in the [$SG_1/TR30_2/SG_1$] laminate were able to grow into macroscopic fractures at lower strain due to less restriction on forming clusters of broken fibres. Because the weak clusters have more surrounding carbon fibre, once a fibre breaks, it would more easily propagate, thus producing failure at a lower strain. Within the plateau region, progressive fragmentation of the carbon ply followed by dispersed delamination occurred as shown in **Figure 3.19**, a typical damage mechanism for [$SG_1/TR30_2/SG_1$] hybrid configuration. It is shown in **Figure 3.19**, that damage development took the form of carbon ply fragmentation and substantial delamination growth around the fractures at each loading cycle in contrast to the hybrid with single TR30 carbon ply, where the fragmentation pattern was significantly denser, and delamination was limited (see **Error! Reference source not found.**). The damage pattern at 2.07% strain shows a different type of damage growth. The red circle shows a short fibre fracture and smaller average delaminated area compared to the delaminated area shown by the blue circle. The fibre fracture shown by the blue circle was able to extend across the whole width because some individual fibres have failed at those locations and developed into clusters of broken weak fibres via matrix damage or local debonding [119]. The different fracture length across the width shown by the red and blue circles also indicates the strength variability within the carbon fibre. The larger average delaminated area shown by the blue circle indicates a locally thicker carbon ply compared to the area shown by the red circle. The thicker carbon ply will provide enough energy to propagate the delamination further after the carbon fibre fractures.

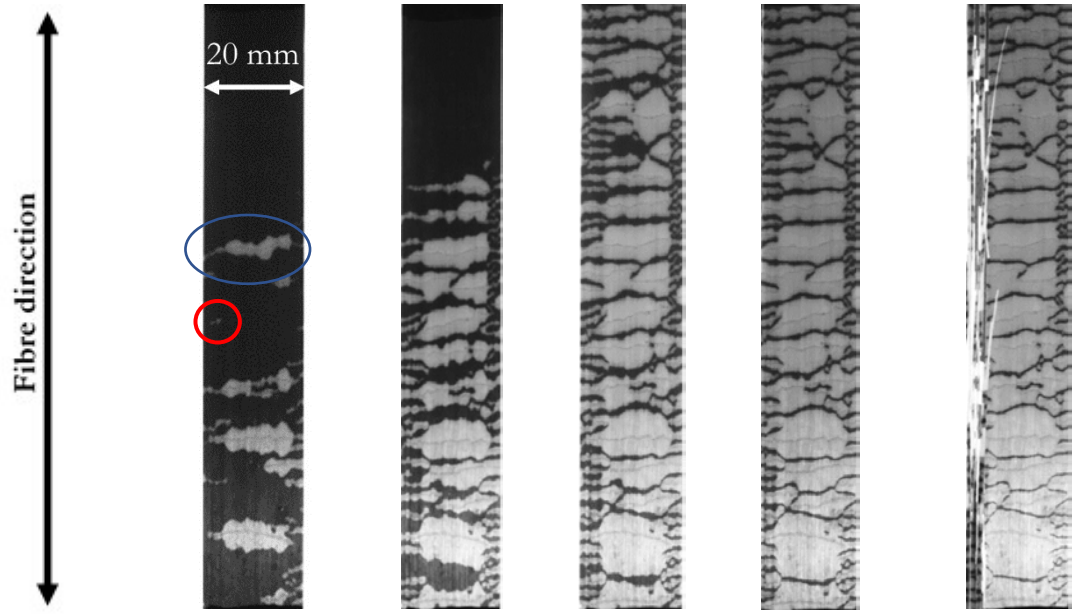

Figure 3.19. Damage pattern at each peak strain for [$SG_1/TR30_2/SG_1$] hybrid.

When the carbon ply is fully fragmented at 3.13% strain as shown in **Figure 3.19**, the additional load is taken by the glass ply and the stress starts to increase at 3.13% as shown in **Figure 3.18**. Because of the compressive stress around the crack tip, friction between plies causes a small amount of hysteresis for the [$SG_1/TR30_2/SG_1$] configuration. Extensive vertical ply splitting from the edge as shown in **Figure 3.19** occurred, causing the final stiffness to go insignificantly below its expected final value without any carbon contribution, as shown in **Error! Reference source not found.**. The black-lines running perpendicular to the specimen shown in **Figure 3.19** are areas of residual bonding between the glass and carbon ply which shows that this hybrid specimen is not fully delaminated and the carbon was still able to carry some load. If there was no vertical ply splitting, the final stiffness of [$SG_1/TR30_2/SG_1$] configuration should not the reach the expected final stiffness line at all because the residual intact carbon-ply was able to carry minor load.

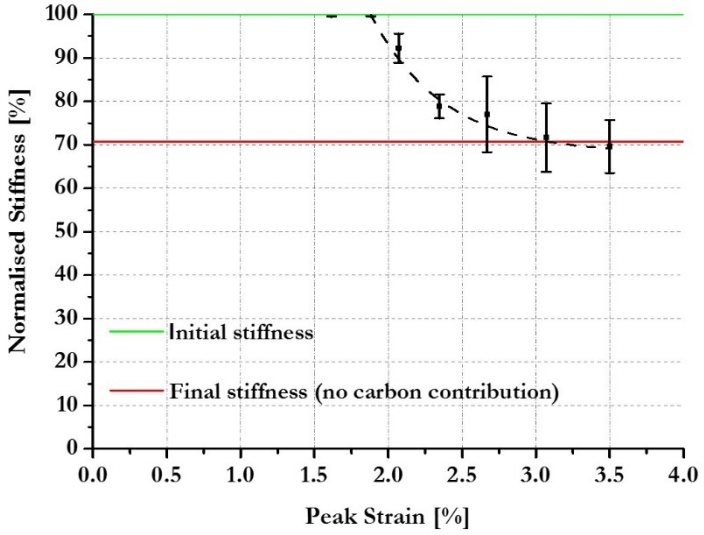

Figure 3.20. Stiffness loss at each applied peak strain for [$SG_1/TR30_2/SG_1$].

Stiffness loss as a function of applied peak strain is shown in **Error! Reference source not found.**, which shows a gradual stiffness loss with increasing fragmentation and stable delamination [39] approaching the expected value with no carbon contribution at higher strain. The error bars in **Error! Reference source not found.** show a coefficient of variation between 0.40%-7.80% which indicates the consistency of specimen responses, but it is still higher compared to the two previous hybrid laminates. This is due the susceptibility of some of the [$SG_1/TR30_2/SG_1$] specimens to vertical ply splitting at higher strains.

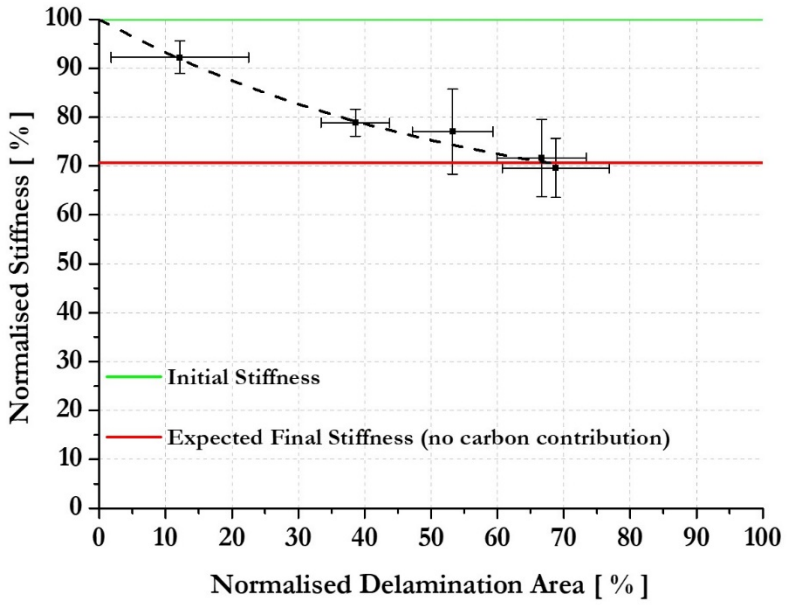

Figure 3.21. Stiffness loss with growing delaminated area for [$SG_1/TR30_2/SG_1$].

Error! Reference source not found. shows a plot of stiffness loss, as a function of normalised delamination area for the averaged measurements of three specimens. It is shown in **Figure 3.**, that there is a gradual loss of stiffness from 12% to 68% delamination area with the final normalised stiffness going insignificantly below the expected final stiffness. The measured width distribution of the residual black-lines in a [$SG_1/TR30_2/SG_1$] hybrid configuration at 3.50% peak strain is shown in **Figure 3.22.** The average width of the residual black-lines of a [$SG_1/TR30_2/SG_1$] hybrid configuration is between 0.200-1.00 mm. With this average width, the shear stress would not exceed the yield stress,thus preventing further delamination into the area of the residual black-lines. By comparing the average width of the residual black-lines of the three hybrid configurations, it seems that the average width is similar. This could be attributed to the similar distance required to go from zero shear stress at the centre of the black area to reach the shear stress at which interfacial damage occurs and changes the appearance. Nonetheless more work is needed to support this argument.

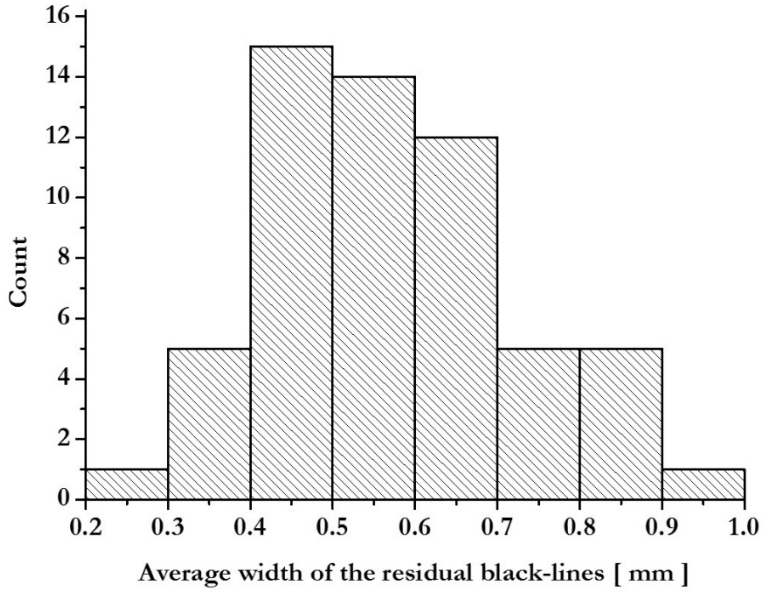

Figure 3.22. Width distribution of the residual black-lines on a [$SG_1/TR30_2/SG_1$] hybrid configuration.

3.4. Conclusions

The following conclusions were drawn from the study of continuous glass/carbon hybrid laminates under quasi-static cyclic loading:

1. The quasi static response of the hybrids is affected by the carbon/glass volume ratio, the carbon ply thickness and the carbon properties (modulus, strain to failure).

2. There is a small amount of hysteresis and residual strain, which can be attributed to two reasons: the significant reversed shear stress at the ply interfaces near the ends of the several delaminated regions of the fragmented hybrid deforming the matrix and the accumulation of debris between the open cracks preventing the surface cracks to return to its original state when unloaded.

3. The response of the UD thin-ply hybrid laminate is considered pseudo-ductile because the damage in the form of ply fragmentation and localized delamination, leads to gradual loss of stiffness [120].

4. The extent of stiffness loss is governed by the density of fragmentation and the corresponding delamination pattern.

5. The existence of the residual black-lines (intact carbon ply) on each hybrid configuration could be attributed to the average width of the intact ply where the shear stress would not be able to reach the value required to damage the interface, thus leaving that particular area intact.

Chapter 4 Compression Response of Unidirectional Thin-Ply Hybrid Composites

4.1 Introduction

It is well known that carbon fibre possesses high specific tensile modulus and strength, which make them an attractive choice for structural application where weight saving is one of the important parameters but one of their limitations is the lower axial compression strength compared with the tensile strength [121]–[124]. In general, the compressive failure of carbon fibre composites is a catastrophic phenomenon and therefore, it is not easy to monitor the nature and sequence of failure mechanisms experimentally. Several works performed to study the compression performance of unidirectional carbon fibre composites [27], [28], [74], [125]–[129] discovered that the initial failure mechanism appears to be shear instability related to yielding of the matrix and the pre-existing fibre misalignment. The failure mechanism of carbon fibre composites suggests that the compressive strength is controlled by the matrix properties and closely related to the in-plane and out-of-plane shear stress-strain behaviour of the lamina and the fibre initial misalignment. It was also reported that there is a decreasing value of compressive strength with increasing thickness of the fibre composite which was attributed to premature failures due to end crushing for the thicker specimens [129].

UD M40JB carbon laminates with three different ply thicknesses were experimentally tested in longitudinal compression by Amacher et al. [57], and it was shown that the compressive strength increased with decreasing ply thickness. The optical microscopy examination of those specimens revealed more uniform microstructure and better fibre alignment with smaller resin rich areas for the thinnest plies, which yielded a better compressive performance.

It has been reported by Czél et al. [88] that there is a distinct change of slope in the load-compressive strain curve of an asymmetric UD hybrid composite made of a thin high modulus M55J carbon/epoxy ply sandwiched between thick glass/epoxy ply and loaded in four-point bending due to the progressive fragmentation of the carbon ply on the compression side. The change of slope was observed at around -0.513% strain which marks the initial fragmentation of the carbon ply, and although it progressively fragmented under compressive loading, the hybrid composite specimens continued carrying load until final failure on the compression side at -2.310% strain. From the observed damaged specimens, they reported fragmentation of carbon plies in this hybrid composite which is not generally observed in compression tests.

Based on the work by Amacher et al. [57] and Czél et al. [88] , there is a possibility to obtain better performance and gradual failure under compressive loading by combining UD thin carbon/epoxy ply with standard thickness glass/epoxy. There is still lacking experimental results on compression characterisation of UD thin high modulus M55J carbon/epoxy plies with standard thickness S-glass/epoxy where the number of carbon plies varies. Therefore, the effect of incorporating different numbers of thin carbon plies in a hybrid configuration under indirect compressive (four-point bending) and direct (longitudinal) compressive loading will be examined in this chapter to explore the pseudo-ductile behaviour of unidirectional thin-ply hybrid composites due to fragmentation of the carbon ply.

4.2 Specimen design for indirect compression (four-point bending) testing

The selected four-point bending test setup was first chosen to study the failure mechanisms of UD thin-ply hybrid composites due to the benefit with this setup of very simple specimen preparation with no need for end-tabbing and precision machining (e.g. grinding) typically utilised for direct compression specimens.

Compressive or tensile strains at a specific "ply", depend on its distance from the neutral axis (centroid) of the beam. For this specimen, there is a strain gradient across the thickness, which is usually assumed to be linear according to the classical beam theory. This is a straightforward method of putting a thin carbon/epoxy ply in compression as a part of a hybrid beam specimen. The chosen design to study the compressive failure mechanisms of UD thin M55J carbon ply was an asymmetric one, where the carbon ply was located close to the compression surface of the specimen. The hybrid specimens were designed to be thick enough to undergo significant surface strains at relatively small deflections in order to minimize the geometric non-linearity of the load-deflection response. This was achieved by adding several plies of cheaper E-glass/epoxy plies to a

three-ply hybrid sub-laminate of S-glass/epoxy plies and various numbers of carbon plies (see **Table 4.1** for the lay-up sequences). The carbon/epoxy volume ratio shown in **The** notation h, w and L in **Table 4.1** is the nominal thickness, width and total length respectively.

Table 4.1 , is calculated based on the ratio between the nominal thickness of the carbon/epoxy plies and the total nominal thickness of the hybrid specimen. The nominal thickness of the constituents to calculate the carbon/epoxy volume ratio is shown in **The** notation h, w and L in **Table 4.1** is the nominal thickness, width and total length respectively.

Table 4.1. The notation h, w and L in **Table 4.1** is the nominal thickness, width and total length respectively.

Table 4.1. Asymmetric hybrid specimen types tested under four-point bending.

Design.	Lay-up sequence	h [mm]	Carbon /epoxy volume ratio [%]	w [mm]	L [mm]	Support span [mm]	Inner span [mm]
Asym. $M55_n$	$[SG_2/EG_{13}/SG_2/M55_1/SG_1]$	2.63	1.14	8	80	60	20
	$[SG_2/EG_{13}/SG_2/M55_2/SG_1]$	2.66	2.25				
	$[SG_2/EG_{13}/SG_2/M55_3/SG_1]$	2.69	3.34				

It is important to note that the proposed setup for the four point-bending tests shown in **Table 4.1** and **Figure 4.3** was to ensure that the carbon ply failure takes place between the inner loading noses where the bending moment is maximum and constant. The cross-sectional schematic of the bending specimens is shown in **Figure 4.1**, where h, y_j and z are the nominal thickness, the distance of the top of the carbon ply from the base, and the neutral axis respectively, which is needed to calculate the compressive strain at the top of the carbon ply using **Equation (4.6** in **Section 4.6.1.** The position of the neutral axis (Z) is calculated through **Equation (4.3** which is based on classical laminate theory. The notations Z_{SG}, Z_{EG}, Z_C are the neutral axis of the S-glass, -E-glass and carbon plies respectively, measured from the bottom surface to the middle of each ply as shown in the schematic in **Figure 4.1,** and a_{11} is the compliance of each ply calculated using the elastic properties shown in **Table 4..** With n is the number of carbon layers. Detailed equation of the neutral axis is shown in **Appendix A** and **Appendix B**.

$$Z = \frac{\overline{Z_{SG2}}\frac{1}{(a_{11})_{SG2}} + \overline{Z_{EG13}}\frac{1}{(a_{11})_{EG13}} + \overline{Z_{SG2}}\frac{1}{(a_{11})_{SG2}} + \overline{Z_{Cn}}\frac{1}{(a_{11})_{Cn}} + \overline{Z_{SG1}}\frac{1}{(a_{11})_{SG1}}}{\frac{1}{(a_{11})_{SG2}} + \frac{1}{(a_{11})_{EG13}} + \frac{1}{(a_{11})_{SG2}} + \frac{1}{(a_{11})_{Cn}} + \frac{1}{(a_{11})_{SG1}}} \quad (4.3)$$

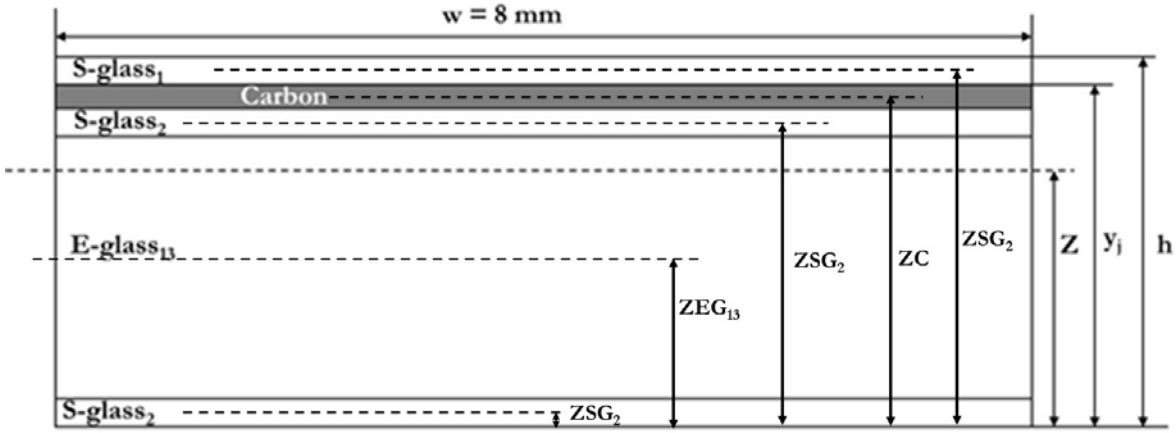

Figure 4.1. Cross-sectional schematic of the asymmetric UD hybrid composite specimens.

4.3 Specimen design for direct (longitudinal) compression testing

To study the longitudinal compression response of UD thin-ply hybrid composites, alternating plies of S-glass/epoxy and M55 carbon/epoxy were chosen (see **Table 4.2** for the lay-up sequences).

Table 4.2. Hybrid specimen types tested under longitudinal compression.

Specimen configuration	Nominal width [mm]	Nominal thickness [mm]	Glass plies	Carbon plies	Carbon/epoxy volume ratio [%]
$[SG_1/(M55_1/SG_1)_{17}]$	10	3.31	18	17	15.4
$[SG_1/(M55_2/SG_1)_{17}]$		3.83		34	26.6
$[SG_1/(M55_3/SG_1)_{17}]$		4.35		51	35.1

As seen from **Table 4.2**, the nominal width and the number of glass plies are the same for all hybrid specimens. The geometry of the hybrid specimens tested under longitudinal compressive loading was chosen to fit the loading rig developed by Häberle et al. [130] and the schematic of the specimen geometry is shown in **Figure 4.2.**

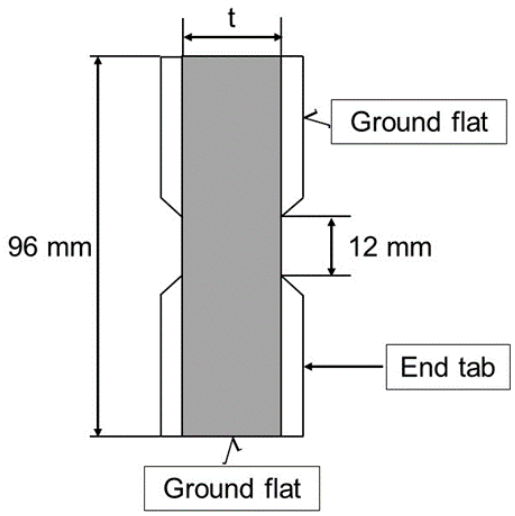

Figure 4.2. Schematic of the UD hybrid composite specimens tested under longitudinal compression.

As shown in **Figure 4.2,** a chamfer was introduced into the end tabs in order to yield less stress concentration at the tab-tip region of the specimen as shown by Xie et al. [131]. The total length and gauge length shown in **Figure 4.2** was chosen based on the slenderness ratio equation developed by Häberle et al. [130] and is shown as **Equation (**4.4 in this chapter.

$$S = \frac{l_g\sqrt{12}}{h} \tag{4.4}$$

Where h is the nominal thickness of the specimen while L_g is the gauge length which is 12 mm. The slenderness ratio for each of the UD hybrid configuration based on its nominal thickness and gauge length are 12.5, 10.8, 9.5 for the specimen with 15.4%, 26.6%, and 35.1% carbon/epoxy volume fraction respectively. As shown by Häberle et al. [130], the composite specimen will attain its ultimate compressive strength when the slenderness ratio is between 10 and 20 with a drop in ultimate compressive strength if the slenderness ratio is above 20. Comparing the slenderness ratio for each of the UD hybrid configuration in this work with the acceptable ratio [130], it implies that macro buckling during testing for the proposed hybrid configurations should be avoided.

4.4 Experimental methods

4.4.1 Materials

The materials considered for the design and used for the experiments were standard thickness S-glass/epoxy and E-glass/epoxy supplied by Hexcel and thin M55J carbon/epoxy supplied by North Thin Ply Technology. The epoxy resins in the prepregs were the aerospace grade 913 (Hexcel) and ThinPreg 120 EPHTg-402 (North TPT). The carbon fibre is a Torayca M55J, classified as high modulus and produced in 6000 filament tows [132]. Basic properties of the applied fibre and prepreg systems can be found in **Table 4.3** and **Table 4.** respectively. The fibre properties in **Table 4.3** are based on the manufacturer's data and were determined from impregnated strands except for the S-glass where single fibre tests were performed.

Table 4.3. Fibre properties of the applied UD prepregs.

Fibre type	Manufacturer	Tensile modulus [GPa]	Tensile strain to failure [%]	Tensile strength [GPa]	Density [g/cm^3]	CTE α [1/K]
Torayaca M55J	Toray	540	0.8	4.02	1.91	$-1.1.10^{-6}$
FliteStrand SZT S-glass	Owens Corning	88	5.5	4.8-5.1	2.45	2.10^{-6}
EC9 756 P109 E-glass	Owens Corning	72	4.5	3.5	2.56	$4.9.10^{-6}$

Table 4.4. Cured ply properties of the applied UD prepregs.

Prepreg type	Property Unit	Fibre aerial weight [g/m^2]	Cured ply thickness [mm]	V_f [%]	E_i [GPa]	ε_t [%]	ε_c [%]	G_{12} [GPa]	ν_{12}
M55J /epoxy	Average	30	0.030	52	280 [a]	0.6[b]	-0.26[b]	3.10[c]	0.31[c]
	COV [%]	-	-	-	-	-	-		
S-glass/epoxy	Average	190	0.155	51	45.7 [73]	3.98	-2.33[b]	3.10[c]	0.30[c]
	COV [%]	-	-	-	3.2	1.1	-		
E-glass/epoxy	Average	192	0.140	54	40.0[a]	3.07[b]	-	3.38[c]	0.30[c]
	COV [%]	-	-	-	-	-	-		

[a] calculated for the given volume fraction.
[b] based on manufacturer's data for 60% carbon fibre volume fraction.
[C] calculated with Rule of Mixtures

For the prepreg systems mentioned in **Table 4.**, the fibre volume fraction is obtained from the manufacturer's data sheet and the cured ply thickness (CPT) is calculated by using **Equation 3.5** in **Chapter 3**. There is a reasonable agreement between the calculated and the measured CPT of the hybrid specimens and this is shown in **Table 4.5.**

Table 4.5. Calculated and measured cured ply thickness of the UD thin-ply hybrid composites (the number in the bracket indicates the coefficient of variation in [%]).

Designation	Lay-up sequence	Calculated thickness [mm]	Measured thickness [mm]
Asym. M55	$[SG_2/EG_{13}/SG_2/M55_1/SG_1]$	2.63	2.65 (3.7%)
	$[SG_2/EG_{13}/SG_2/M55_2/SG_1]$	2.66	2.70 (1.7%)
	$[SG_2/EG_{13}/SG_2/M55_3/SG_1]$	2.69	2.72 (1.5%)
$[SG_1/(M55_n/SG_1)_{17}]$	$[SG_1/(M55_1/SG_1)_{17}]$	3.31	3.33 (1.4%)
	$[SG_1/(M55_2/SG_1)_{17}]$	3.83	3.85 (2.0%)
	$[SG_1/(M55_3/SG_1)_{17}]$	4.35	4.36 (0.5%)

The measured thickness in **Table 4.5** is from an average measurement of six specimens for each hybrid configuration.

4.5 Manufacturing method

The investigated UD hybrid laminates for the indirect compression testing (four-point bending) and longitudinal compression testing were constructed by placing the 0^o plies on top of

each other on a clean and flat surface plate in a temperature and humidity controlled clean room. The finished laminates were then placed inside a vacuum bag as shown in **Chapter 3**. The recommended curing cycle for this hybrid composite is identical with the curing cycle to produce the hybrid composites in **Chapter 3**.

For the tested hybrid specimens under longitudinal compression, it was necessary to attach end tabs by using an adhesive to avoid premature failure in the grip regions. The curing cycle of the adhesive is explained in **Chapter 3**. To ensure good alignment and flat surfaces, the tabs and ends of the specimen were then ground flat by a grinding machine. Fabrication of the all the hybrid specimens was done using a diamond cutting wheel.

4.6 Mechanical test procedure

4.6.1 Indirect compression (four-point bending) tests

Four-point bending tests of the asymmetric hybrid specimens were carried out using a computer controlled Instron 8872 type 25 kN rated universal hydraulic test machine with a 5 kN load cell attached to the machine during the testing. The tests were conducted under displacement control at a cross-head speed of 1 mm/min. The set-up for the four-point bending tests was the following: the support span and inner span were 60 mm and 20 mm respectively. To avoid the possibility of local compressive failure of the surface glass plies under the inner loading noses due to high contact forces, reinforced rubber pads were located between the loading nose and specimen contact surface. To measure the surface strains at the compressive and tensile side, strain gauges of type C2A-06-062LW-120 with 4.45 x 2.03 mm overall length and width respectively were attached to both sides of the specimens in the centre of the gauge length. The four-point bending test set-up is shown in **Figure 4.3**. It is worth mentioning that the gauge length for this strain gauge type is 1.52 mm. The position of the five dots on the edge of the specimens between the inner loading noses was recorded with an Imetrum optical strain measurement system to measure the curvature of the specimen. The notation x in **Figure 4.3** is the distance between centre of support and loading roller which will be used in **Equation (4.8**, and is 20 mm.

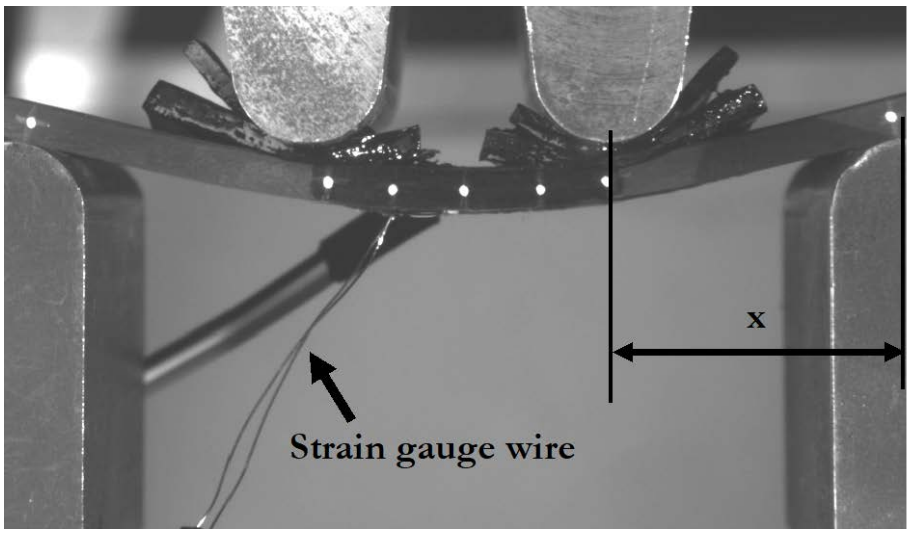

Figure 4.3. Four-point bending test set-up of UD thin carbon/glass hybrid composite samples.

As the strain gauges are measuring the surface strain of the glass on the compression side, it is important to calculate the strain at the top level of the carbon ply on the same side. This can be done through **Equation (4.6**, where ε_c and ε_g are the top-level strain of the carbon ply and the surface strain of the glass ply on the compression side. This equation assumes a linear strain distribution in bending, which is valid as long as the beam does not twist or buckle and the transverse shear stresses are relatively small. The notation y_j, Z, and h has already been explained in **Section 4.2**. At least six specimens were tested of each type.

$$\varepsilon_c = \varepsilon_g . \left[\frac{y_j - Z}{h - Z}\right] \quad (4.6)$$

The input parameters to determine the top-level strain of the carbon ply, ε_c , for each hybrid configuration are shown in **Table 4.6.**

(4.8. Input parameters to determine the strain on the top level of the carbon ply.

Designation	h [mm]	y_j [mm]	Z [mm]
Asym. $M55_1$	2.63	2.47	1.40
Asym. $M55_2$	2.66	2.50	1.48
Asym. $M55_3$	2.69	2.53	1.55

4.6.2 Direct (longitudinal) compression tests

Mechanical testing of the glass/carbon hybrid specimens under longitudinal compression loading was conducted under displacement control using a cross-head speed of 1 mm/min on a computer controlled Instron 600DX type 600 kN rated universal hydraulic test machine. Load and strain readings were logged on a computer. The specimens were end-loaded in the Imperial College test rig shown in **Figure 4.4.** Imperial College compression test rig [130]By using this test rig, the specimen is supported laterally over the whole length of the tabs. Specimens were clamped lightly in position, and then end-loaded between flat hardened plates. The high precision die set used in the rig minimizes frictional effects and ensures combined axial and shear load introduction from the end and the sides respectively. The total weight of the rig shown in **Figure 4.4.** is 37.55 kg and has been taken into account in the load measurement by the Instron machine during testing.

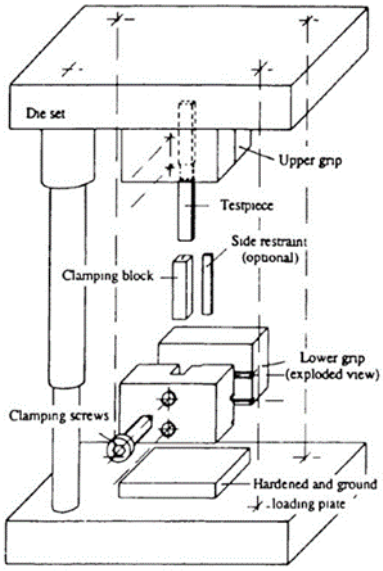

Figure 4.4. Imperial College compression test rig [130].

To measure the longitudinal surface strains, the same type of strain gauges as mentioned in **Section 4.5.1** were used. They were attached to both sides of the specimens in the centre of the gauge length. An Imetrum video gauge system was also used to measure the longitudinal strain of the specimen's gauge length through the thickness by tracking the speckle pattern applied on the side surface using spray paint as shown in **Figure 4.4** and the distance between measurements is 1.60 mm. The thickness of the delaminated part shown in the recorded image was measured using the ImageJ software. Having knowledge of the nominal thickness from each UD hybrid configuration and the pixel size from the video gauge images, a scaling factor (mm/pixel) allows to calculate the thickness of the delaminated part in mm. At least six specimens were tested of each type.

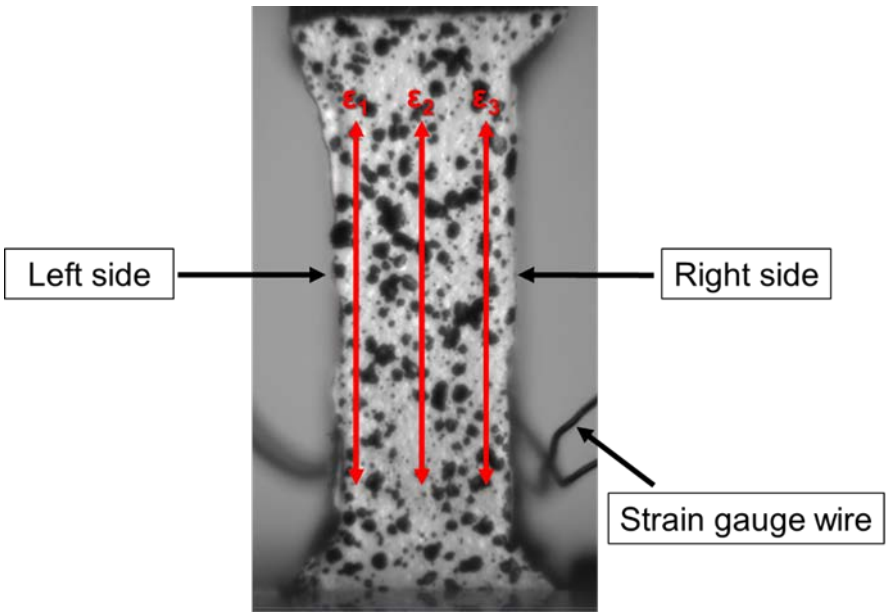

Figure 4.4. Strain measurement at three locations using video gauge system.

4.7 Damage observation under optical microscopy

To observe the damage pattern of the asymmetric carbon/glass hybrid**,** one specimen from each hybrid type was loaded until 700 N in four-point bending and examined under a Zeiss optical microscope. A special device made of stainless steel that resembles the four-point bending loading rig in the 25 kN Instron machine was used to reload the specimens and make the cracks open visibly under the optical microscope. Before being observed, the specimen was ground and polished. **Figure 4.5** shows the experimental set-up of the device with a deformed specimen being examined under an optical microscope.

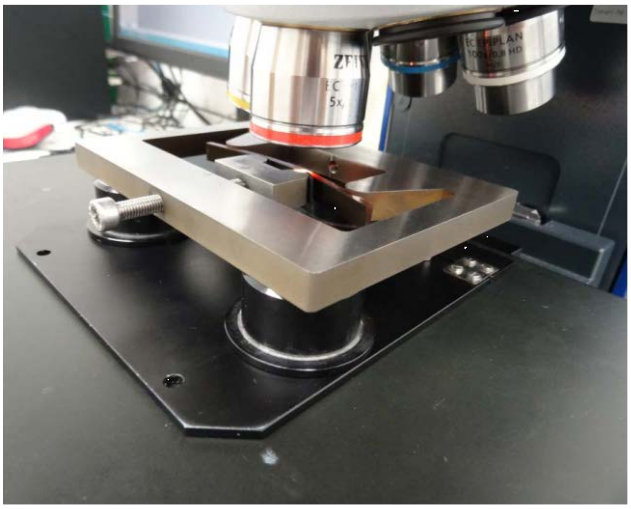

Figure 4.5. Experimental set-up of the four-point bending device with a deformed specimen under the optical microscope.

The specimen position is fixed in place by the two supports and two loading noses. The distance between the loading noses is 20 mm (the notation x in **Figure 4.6**) and between the supports is 60 mm. The part containing the loading noses is connected to a stainless M5 allen screw which actuates them to move towards the specimen and to apply displacement and load as shown in **Figure 4.6.** The specimen is deformed by the loading noses until the opening of the cracks is visible.

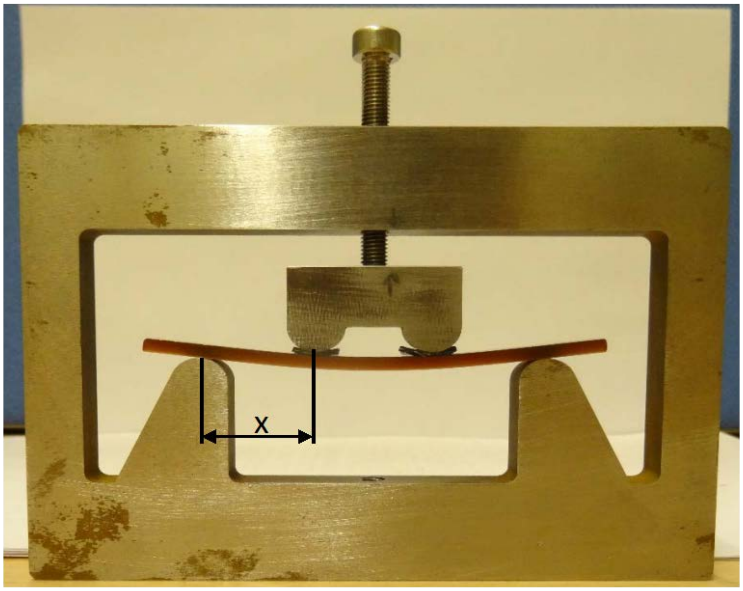

Figure 4.6. A four-point bending device with the specimen on top of two supports being deformed by two loading noses, x is the distance between the centre of loading nose and the centre of support.

4.8 Results and discussion

4.8.1 Indirect compression (four-point bending) response

Typical force-strain response of the asymmetric hybrid specimens under four-point bending is shown in **Figure 4.7**. During four-point bending testing, the hybrid specimen did not twist or buckle which made it feasible to assume a linear strain distribution and to apply (**4.6** to calculate the strain.It is clearly shown, that the initial stiffness increases by having a greater number of carbon ply. An initial linear elastic response is also shown for all three hybrid specimen types until around -0.480% strain where there is a knee-point for the asymmetric $M55_2$ and $M55_3$ configuration which marks the change of the force-strain slope. The first load drop at -1.50% strain for asymmetric $M55_2$ was due to ply splitting along the fibre direction on the compression side of the specimen.

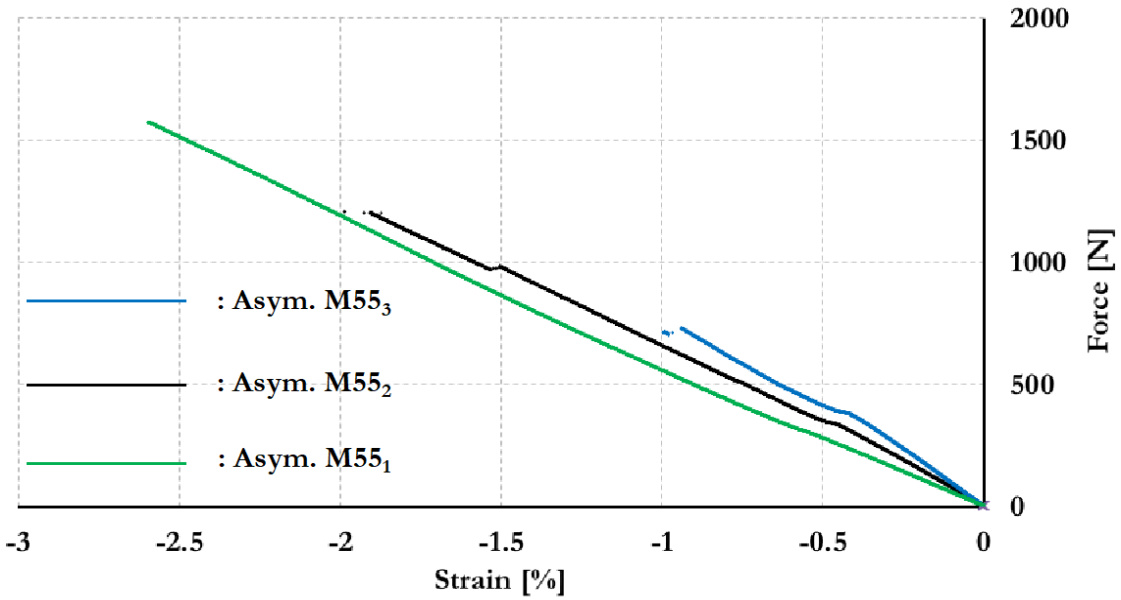

Figure 4.7. Typical four-point bending force-strain response for the three asymmetric hybrid configurations with the strains calculated for the top level of carbon ply.

Typical damage pattern of a failed asymmetric hybrid specimens under four-point bending are shown in Error! Reference source not found., Error! Reference source not found. and Error! Reference source not found. for the asymmetric $M55_1$, $M55_2$ and $M55_3$ hybrid configuration respectively. The damage pattern is shown from the top and side view respectively.

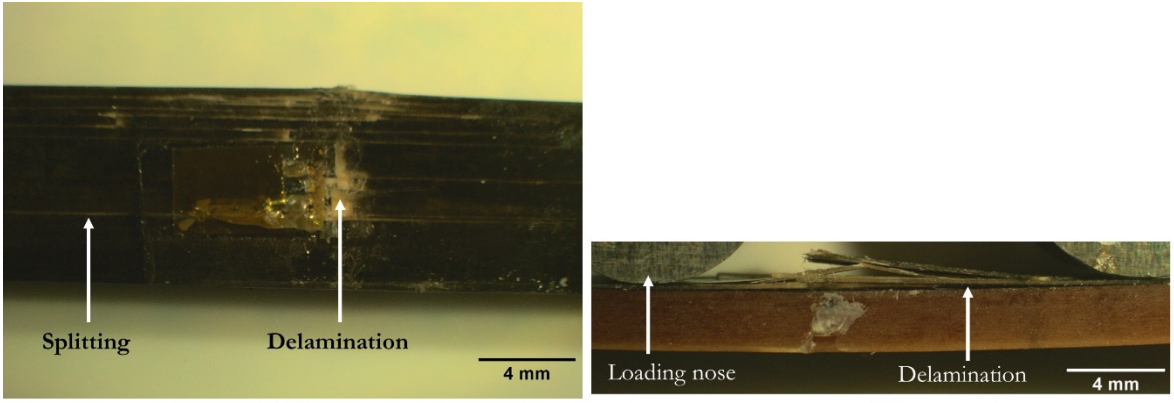

Figure 4.8. Typical damage pattern of an asymmetric $M55_1$ hybrid specimen showing failure at the top view (a) and side view (b).

From the top view (Error! Reference source not found. **(a)**), damage in the compression side consists of ply splitting and delamination for the asymmetric $M55_1$ hybrid. Delamination is seen from the side view (Error! Reference source not found. **(b)**) where an average layer thickness of 0.349 mm has delaminated from the remaining part. Based on this thickness, it can be concluded that the top three layers, which are the $[SG_1/M55_1/SG_1]$ layers have delaminated from the remaining glass layers.

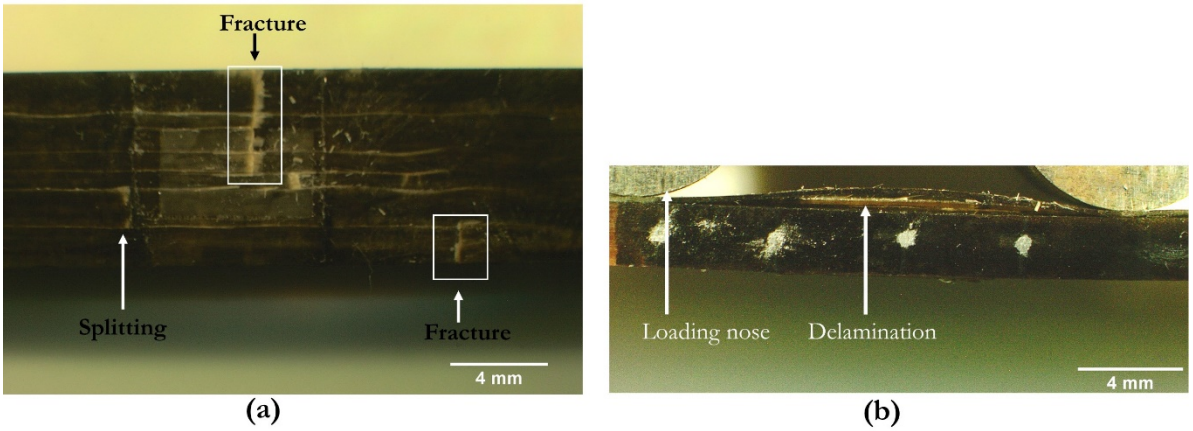

Figure 4.9. Typical damage pattern of an asymmetric $M55_2$ hybrid specimen showing failure at the top view (a) and side view (b).

Ply splitting and fracture midway across the width is the damage pattern seen on the top surface for asymmetric $M55_2$ hybrid (**Figure 4.9 (a)**). From the side view (**Figure 4.9 (b)**), the delaminated part has an average thickness of 0.482 mm. Ply splitting which occurs on the compression side of the asymmetric $M55_1$ and $M55_2$ cases is a typical compressive failure of a glass fibre under bending [133]. This type of damage gradually accumulates near the compressive surface side [133] of the hybrid specimen.

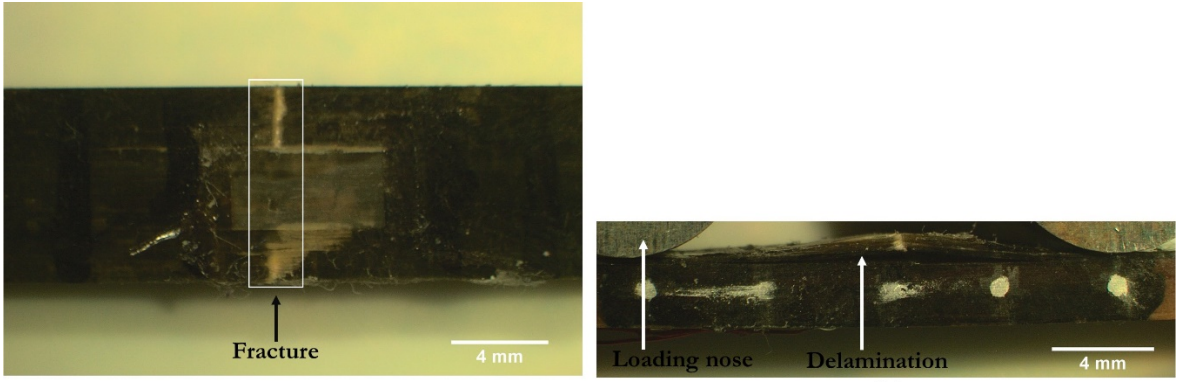

(a) (b)

Figure 4.10. Typical damage pattern of an asymmetric $M55_3$ hybrid specimen showing failure at the top view (a) and side view (b).

Fracture across the width is seen from the top view of the asymmetric $M55_3$ hybrid configuration (**Figure 4.10 (a)**). A delaminated part with an average thickness of 0.661 mm is seen from the side of the specimen (**Figure 4.10 (b)**). For the asymmetric $M55_2$ and $M55_3$ hybrid, the delaminated part includes the hybrid layers on the compression side. The conclusion is made based on the measured average thickness of the delaminated part.

The top view of a typical damaged asymmetric $M55_1$, $M55_2$ and $M55_3$ hybrid configuration tested until 700 N is shown in **Figure 4.11** which shows brighter coloured stripes across the width. It is also shown in **Figure 4.11**, that the extent of the brighter coloured area is different for different hybrid configuration. The asymmetric $M55_1$ hybrid has a denser bright striped area which is likely due to the shorter process zone around the fragmented ply [64]. To study the origin of this damage area, one specimen from each hybrid configuration which was tested until 700 N was observed under optical microscopy. The damage mechanisms observed from the edge of the asymmetric $M55_2$ hybrid configuration is shown in **Figure 4.12**. It is worth mentioning that the damage mechanisms shown in **Figure 4.12** is also active for the other two hybrid configurations based on the observation under optical microscopy.

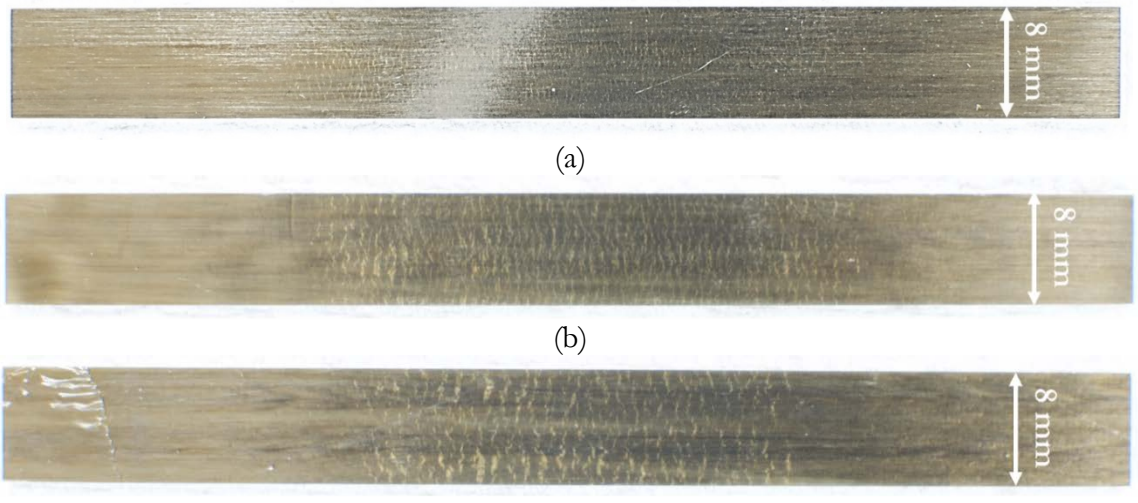

(a)

(b)

(c)

Figure 4.11. Top view image of: (a) asymmetric $M55_1$ (b) asymmetric $M55_2$ (c) asymmetric $M55_3$ hybrid configuration.

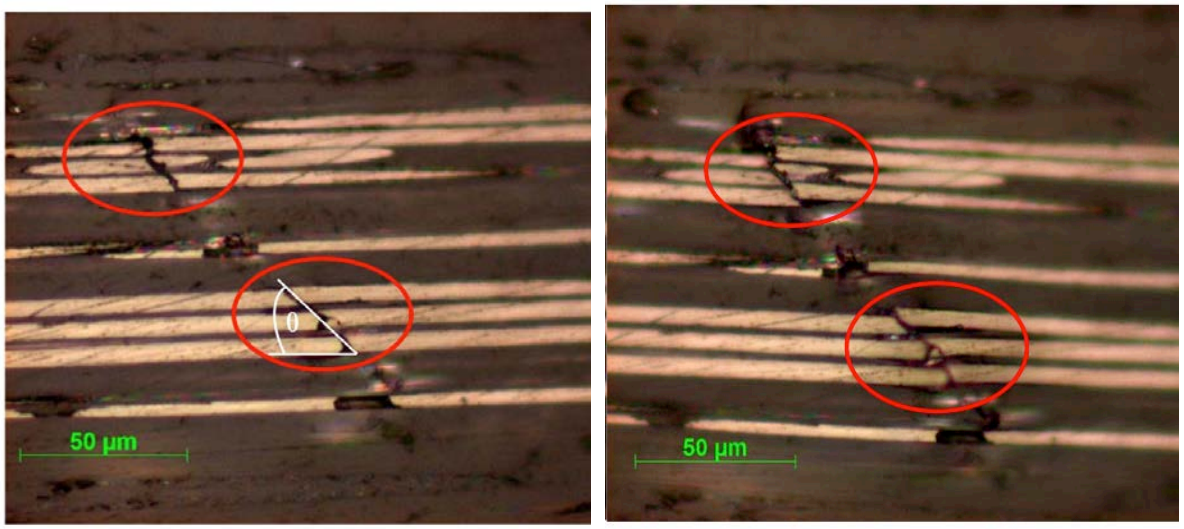

(a) (b)

Figure 4.12. Damage mechanisms of asymmetric $M55_2$ hybrid configuration showing (a) unloaded specimen and fragmentation angle (θ) (b) loaded at -1.4% strain.

Figure 4.12a shows that the carbon ply is fragmented at an angle (θ) when it is unloaded and when it is loaded until -1.4% strain as shown in **Figure 4.12b**, the fragmented carbon ply is displaced in the out of plane and thickness direction causing interfacial damage (in the areas shown by the red circles in **Figure 4.12b**). From the experimental work, it was observed that by removing the load, the fragmented carbon fibres retained to its original position as shown in **Figure 4.12a.** By examining **Figure 4.12 (b)**, the fragmented carbon layer is displaced as far as 0.5 to 1 times the diameter of a single carbon fibre. It is worth mentioning that the single carbon fibre has a diameter of 5.68 µm. Since the carbon layer is fragmented at an angle, it would be interesting to measure this angle. The angle measurement (θ) was made for the fragmentation between the loading noses and the result is shown in **Figure 4.13** as the fragmentation angle distribution**.** The fragmentation angle (θ) is defined from **Figure 4.12a** and measured by using an ImageJ software. Examining the distribution of the fragmentation angle in the carbon ply, it is seen that the angles are distributed mainly between 40^o -55^o. Even though the angle measurement shown in **Figure 4.14** was made for the asymmetric $M55_2$, a similar trend was also found for the other asymmetric configuration and the direct compression specimen.

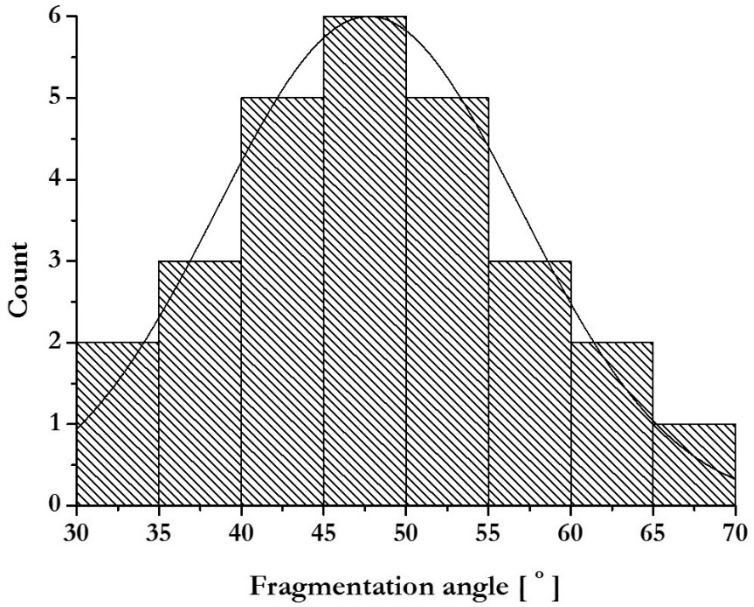

Figure 4.13. Fragmentation angle distribution.

45° angle of fracture in compression for a single carbon fibre tested in recoil compression was reported by Dobb et al. [134]. They argue that the responsible damage mechanism was due to the high degree of order (graphitization) and inherent sheet-like structure, which lead to easier shear between the basal plane than a random structure.

The carbon ply displacement in the thickness direction is possible because of the low transverse modulus (E_{22}) of the hybrid composites and some localised delamination between the glass and carbon ply. This displacement in the thickness direction (wedging action) is the reason for interfacial damage (delamination) between the ply. The schematic evolution of wedging action in the carbon and glass ply is shown in **Figure 4.15.**

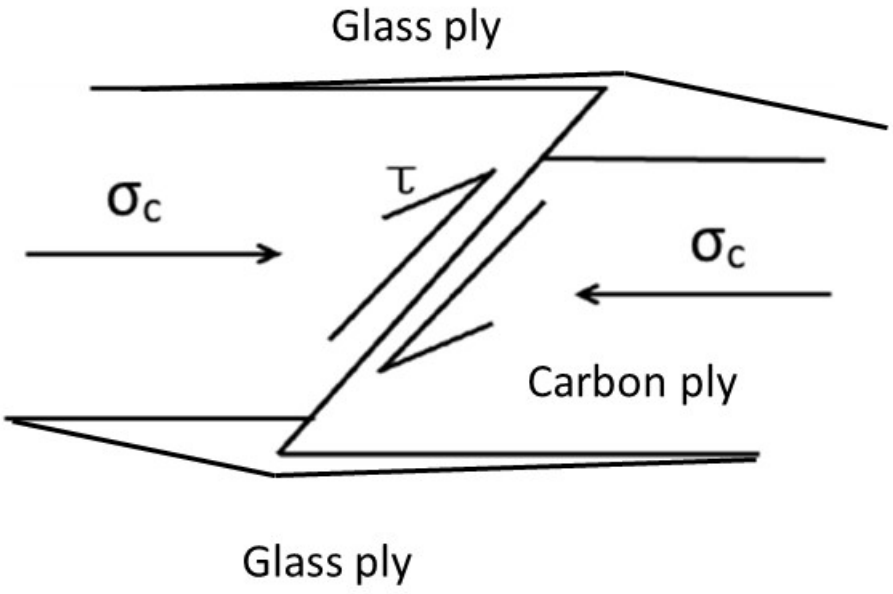

Figure 4.15. Schematic of transverse displacement mechanism in carbon and glass ply.

It is shown in **Figure 4.15**, that with the presence of compressive loading and the ability of the fragmented ply to slide in the thickness direction, there will be a separation between the glass and carbon ply. It should be noted that when transverse displacement takes place, the carbon ply experiences shear stress at the fragmentation interface as shown in **Figure 4.15**. This shear stress would further cause friction between the fragmented surface. Due to delamination between the ply, it was possible to see the brighter coloured stripes shown in **Figure 4.11**. This colour is related to the colour of the glass/epoxy prepreg.

Based on the observed damage mechanisms, the change of slope in the force-strain curve shown in **Figure 4.7** is due to periodic fragmentation of the carbon ply and local delamination between the fragmented carbon and glass ply. After the knee-point strain which marks the start of fragmentation and dispersed delamination, the load continues to rise which indicates that the carbon ply was still carrying some of the load. Due to the irregular shape between the fragmented surfaces as shown in **Figure 4.12**, friction and mechanical interlocking exist which can help to transfer compressive load despite the fracture.

Because there is a change in slope and the load continues to rise after fragmentation of the carbon ply, it would be interesting to examine the expected contribution from the carbon ply before and after the fragmentation. The contribution of the carbon ply is examined by measuring the initial slope and second slope of the force-strain curve as shown in **Figure 4.16**, where the green and red straight lines are the initial and second stiffness respectively. Although **Figure 4.16** is showing the stiffness measurement method for the asymmetric $M55_2$ hybrid configuration, it is also applicable for the other two hybrid configurations.

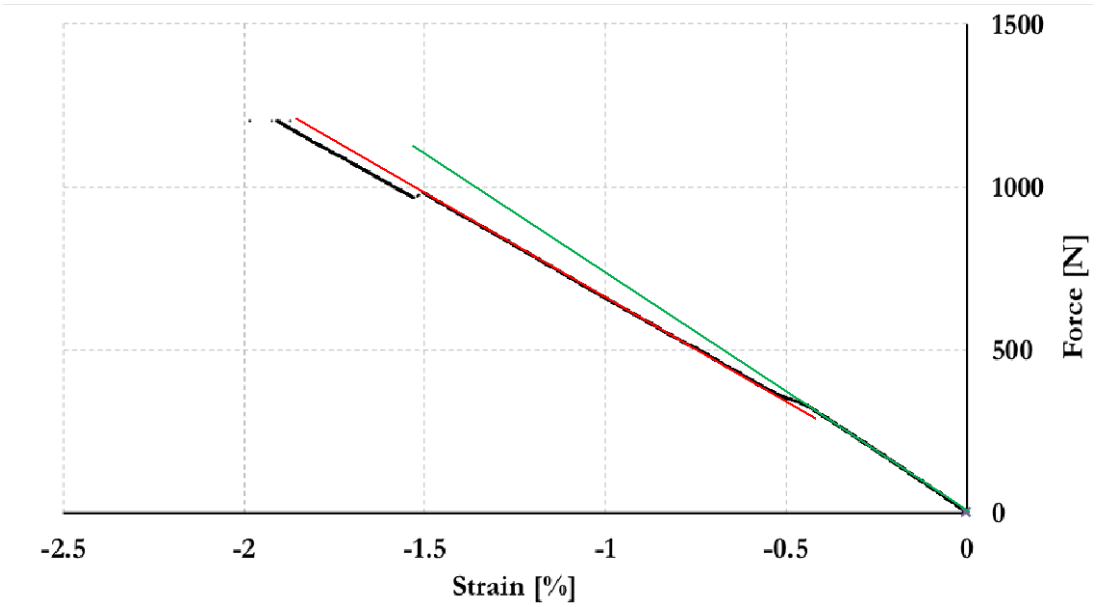

Figure 4.16. The method to determine the change of slope in a typical force-strain curve for an asymmetric $M55_2$ hybrid (the change in the slope is highlighted by the fitted straight red and green lines).

As also shown in **Figure 4.7**, there is a strong dependency of the final failure strain on the number of carbon ply, with the asymmetric $M55_3$ hybrid specimens failing at lower strain compared

to the other two hybrid configurations. This behaviour may be because the strain energy release rate increases with the increased thickness of the carbon plies. The final failure strains shown in **Table 4.7** are calculated for the top level of the carbon ply in the compression side by taking the migration of the neutral axis into consideration. **Table 4.7** gives the test results summary for all the hybrids tested under four-point bending.

Table 4.7. Test results summary for *Asym.* M55 carbon/glass hybrid composites (the number in the bracket indicates the coefficient of variation in [%]).

Designation	Number of specimens	Initial stiffness [N/1%]	Second stiffness [N/1%]	Decrease in slope [%]	Knee-point strain [%]	Final failure strain [%]
Asym. $M55_1$	6	553.9 (3.3)	536.5 (3.7)	3.1 (3.5)	-0.555 (2.2)	-2.724 (10.2)
Asym. $M55_2$	6	713.7 (5.4)	588.0 (5.8)	17.5 (7.6)	-0.522 (6.4)	-1.750 (10.0)
Asym. $M55_3$	6	957.5 (1.9)	750.1 (2.9)	21.6 (6.1)	-0.507 (2.1)	-0.956 (4.3)

The knee-point and final failure strain for each hybrid configuration in **Table 4.7** has already been corrected for the elastic residual strain. The method to calculate residual strain is shown in **Chapter 3.** The residual strains are -0.032%, -0.026%, -0.022% for asymmetric $M55_1$, $M55_2$ and $M55_3$ configuration respectively. The input parameters for each prepreg to calculate the elastic thermal residual strain are shown in **Table 4.8**.

Table 4.. Cured ply properties of the applied UD prepregs as an input parameter to determine the thermal residual strain.

Prepreg type	E_{11} [GPa]	E_{22} [GPa]	CPT [mm]	α_{11} [1/K]	α_{22} [1/K]	G_{12} [GPa]	ν_{12}
M55/epoxy	280	6.3 [116]	0.030	$-7.8*10^{-7}$ [a]	$2.6*10^{-5}$[117]	3.1[116]	0.31[116]
E-glass/epoxy	40	12.5 [116]	0.140	$6.7*10^{-6}$ [a]	$2.6*10^{-5}$[117]	3.3[116]	0.30[116]
S-glass/epoxy	45.7	10.3 [116]	0.155	$3.8*10^{-6}$ [a]	$2.6*10^{-5}$[117]	3.1[116]	0.30[116]

[a] calculated by using the Classical Laminate Theory (CLT) shown in Appendix A.

The measured stiffness loss from the experimental results shown in **Table 4.7** as "decrease in slope" should be compared to the contribution of carbon ply stiffness to the total laminate bending stiffness [D_{11}]. The total laminate bending stiffness is calculated by using **Equation (7.4.** It should be noted that the theoretical carbon laminate bending stiffness is calculated from a given distance from the neutral axis (Z).

$$D_{11} = \frac{1}{3}\sum_{k=1}^{n} Z_k^3 - Z_{k-1}^3 \cdot Q_{11k} \tag{7.4}$$

Where:

D_{11} : total laminate bending stiffness (Nm)

Z_k : coordinate of k^{th} ply from the neutral axis (m)

Z_{k-1} : coordinate of k-$1t^h$ ply from the neutral axis (m)

Q_{11k} : ply stiffness matrix (N/m^2)

It is worth mentioning that the ply stiffness matrix in **Equation (7.4.** is stiffness at the fibre direction (Q_{11}) of a specific reinforced ply located at a certain distance (k) from the neutral axis. Having knowledge of the elastic properties of the carbon plies from **Table 4.**, it is possible to calculate the carbon ply stiffness (Q_{11}). The position of the neutral axis (Z) in **Figure 4.1** is calculated with the classical laminate theory by incorporating the elastic properties of the constituent plies of the hybrid specimens. The properties of the fibre and prepregs can be found in **Table 4.3** and **Table 4.** respectively. By incorporating the material properties from **Table 4.3** and **Table 4.** into **Equation (7.4**, the carbon ply contribution to the total bending stiffness [D_{11}] is presented in

Table 4..

Table 4.9. Carbon ply contribution to bending stiffness according to classical laminate theory.

Designation	Total laminate bending stiffness Nm	Carbon ply bending stiffness Nm	Carbon ply contribution to bending stiffness [%]
Asym. $M55_1$	80.1	9.9	12.3
Asym. $M55_2$	90.5	17.7	19.6
Asym. $M55_3$	100.0	24.0	24.0

The reduction in D_{11} shown in

Table 4.9 can be compared to the decrease in slope from the force-strain curve for all hybrid configuration since bending curvature has a linear relationship with load through **Equation (4.8**:

$$k.D_{11} = F.\frac{x}{2} \quad (4.8)$$

Where:

k : bending curvature

D_{11} : bending stiffness (Nm)

F : bending load (N)

x : perpendicular distance from central loading nose to the central support (m) as shown in **Figure 4.3.**

Comparing the stiffness loss (decrease in slope) in **Table 4.7** with the carbon ply contribution in

Table 4.9 for all three hybrid configurations, it is clearly shown that from the observed experiments, the asymmetric $M55_2$ and asymmetric $M55_3$ hybrid configuration have lost most of their bending stiffness contribution from the carbon ply. However, there is no load drop after the knee-point strain, and so the carbon is apparently still carrying load. For the asymmetric $M55_1$ configuration, an insignificant stiffness loss as shown in **Table 4.7** compared to the other hybrid configurations was found because of the small volume ratio of the carbon/epoxy . Because the carbon ply was still carrying the load, then it should be able to break several times along the specimen's length. To support this hypothesis, it would be interesting to compare the measured fragment length from the experimental results with the theoretical critical carbon fracture length.

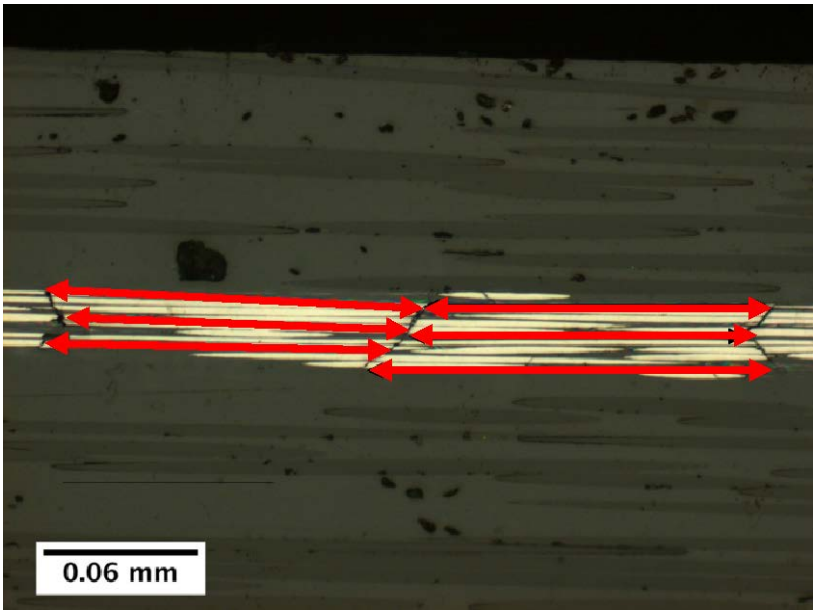

Figure 4.17. Through thickness direction optical microscope image of asymmetric $M55_1$ hybrid configuration showing fragmented carbon ply and the method to measure the distance between fragmentation.

Figure 4.17 shows the fragmented carbon ply and the method to measure the distance between fragmentations. Although the method shown in **Figure 4.17** is for asymmetric $M55_1$ hybrid configuration, it is also applicable for the other two configurations. The fragment length is measured from the optical microscope images of each hybrid configuration by using Image J software. The way this length is measured is shown in **Figure 4.17.** Six measurements between cracks were taken. The average value of these six measurements is taken as the fragment length. The critical carbon ply length is calculated with the following **Equation (4.9** and it does not take account of delamination between the carbon and glass ply.

$$L_c = \frac{E_c . \varepsilon_c . t_c}{\tau_c} \qquad (4.9)$$

Where:

L_c : critical carbon ply length (mm)

E_c : Young's Modulus of carbon composite ply (GPa)

t_c : carbon ply thickness (mm)

τ_c : interlaminar shear yield strength (MPa)

ε_c : compressive failure strain of carbon fibre ply (%)

With Ec = 280 GPa, t_c = 0.030 mm, 0.060 mm, 0.090 mm for asym. $M55_1$, $M55_2$ and $M55_3$ respectively, ε_c = 0.555 %, 0.522 %, 0.507 % for asym. $M55_1$, $M55_2$ and $M55_3$ respectively [88] , τ_c = 77.6 MPa (corrected interlaminar shear strength for 913 E-glass/epoxy taking into account material non-linearity under four-point bending) [135]. The calculated critical carbon ply length for all three-hybrid configurations are shown in **Table 4..**

Table 4.10. Comparison between theoretical critical length and measured fragment length for hybrid specimens under indirect compression (numbers in brackets indicate coefficients of variation in [%]).

Designation	Nominal carbon ply thickness [mm]	Theoretical critical length (L_c) [mm]	Measured fragment length (L_m) [mm]	$(L_c-L_m)/(L_c)$ [%]
Asym. $M55_1$	0.030	0.59	0.18 (5.3)	30
Asym. $M55_2$	0.060	1.11	0.42 (4.1)	37
Asym. $M55_3$	0.090	1.62	0.63 (5.8)	38

As shown in **Table 4.10**, There is a significant discrepancy between the theoretical critical length and measured fragment length for all three configurations. The reason for the inapplicability of **Equation (4.9** to predict the fragment length under compression is described as follows: **Equation (4.9** is originally developed to predict the critical fragment length of fibres under tension loading [136]. This equation assumes that the tensile stress in the fibre builds up from the fibre ends and fragmentation occurs when the stress in the fibre reaches the tensile strength. Further fragmentation continues until the length of the fibre is insufficient to allow the fibre to fail again. The final length defines the critical length (L_c). When the fibres are under a compression load, the fragmentation does not result in a stress discontinuity at the fracture point because the fragments remain in contact and can still transfer a compression load (**Figure 4.15**). This means that unlike in tensile fragmentation, the measured fragment lengths shown in **Table 4.** are unrelated to the critical length as defined by the traditional load transfer model described in **Equation (4.9.**

When a fibre composite is under four-point bending load, the compressive strain to failure increases with increasing strain gradient. Size effect could also play a role into the compressive strain to failure. Longitudinal or direct compression loading of hybrid composites is a test method where the specimen is subjected to a uniform stress on both ends. This test method also eliminates the presence of a strain gradient so it is possible to examine the "true" compressive strain to failure of M55 carbon/epoxy. **Section 4.8.2** will discuss the response of unidirectional thin carbon/glass

hybrid composites under longitudinal compressive loading. It should be noted that the same type of carbon and glass fibre will be used in the direct compressive loading in order to have a comparison with the indirect compression response.

4.8.2 Longitudinal compression response

4.8.2.1 Comparison between each hybrid configuration

Typical stress-strain curve for all the hybrid configurations tested in longitudinal compression is shown in

Figure 4.18. The compression strain is the average strain of the three strain measurements using the video gauge system shown in **Figure 4.4.** By incorporating more carbon plies into the hybrid laminate, the initial stiffness increases, as expected, which can be seen from the different initial elastic slope of each stress-strain curve in

Figure 4.18, where the $[SG_1/(C_3/SG_1)_{17}]$ configuration has the highest initial stiffness. The images of the failed hybrid specimens under longitudinal compression loading are shown in

Figure **4.19**,

Figure **4.20** and

Figure **4.21** for the $[SG_1/(C_1/SG_1)_{17}]$, $[SG_1/(C_2/SG_1)_{17}]$ and $[SG_1/(C_3/SG_1)_{17}]$ hybrid configuration respectively.

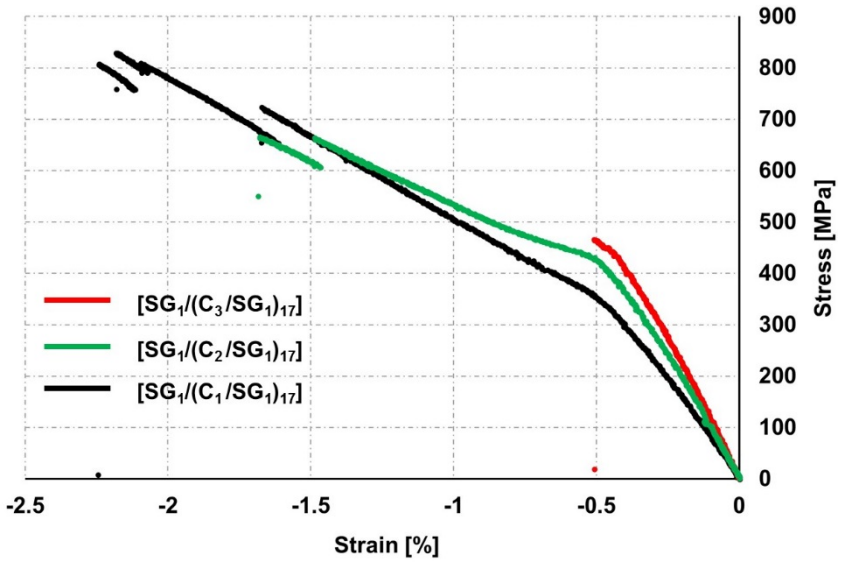

Figure 4.18. Typical stress-strain curve for UD thin carbon/glass hybrid configurations with different numbers of carbon ply.

Figure 4.19 shows the damage region in the gauge section for the failed hybrid $[SG_1/(C_1/SG_1)]_{17}$ configuration. Delamination and fibre fracture in the gauge length are shown in **Figure 4.19.** As also shown in the same figure, delamination between the end tabs and hybrid

specimen occurred at the gripping region for the $[SG_1/(C_1/SG_1)]_{17}$ hybrid. An explosive type of failure is typically observed for this hybrid configuration at the final stage of loading.

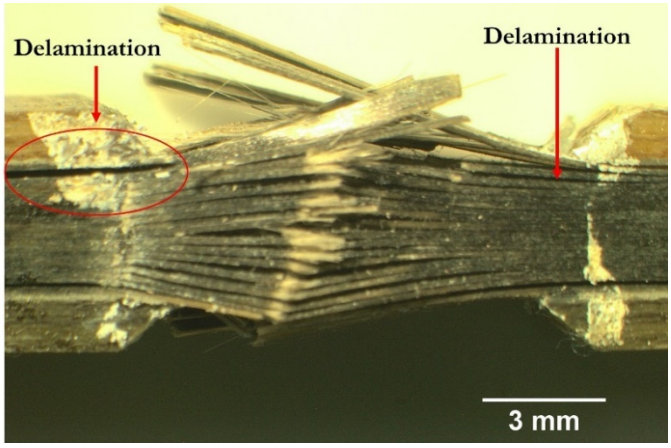

Figure 4.19. Typical image of a failed hybrid $[SG_1/(C_1/SG_1)]_{17}$ specimen showing final failure under longitudinal compression loading.

Delamination and shear fibre fracture in the gauge length are shown in **Figure 4.20** for the failed $[SG_1/(C_2/SG_1)]_{17}$ hybrid. Delamination near the surface of the specimen is also shown in **Figure 4.20.** Only one from six specimens from this configuration has delamination between the end tabs and the specimen.

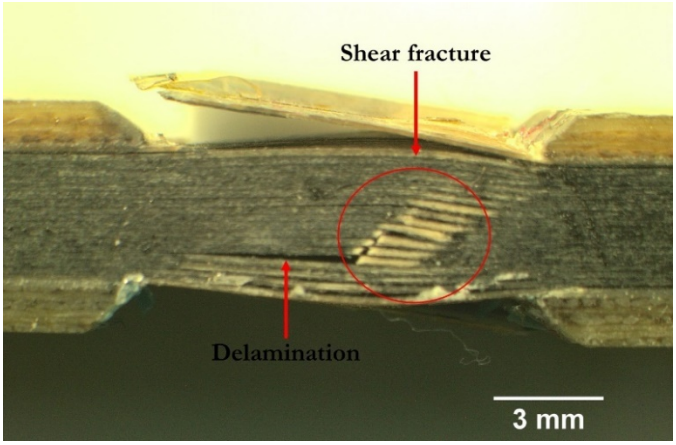

Figure 4.20. Typical image of a failed hybrid $[SG_1/(C_2/SG_1)]_{17}$ specimen showing final failure under longitudinal compression loading.

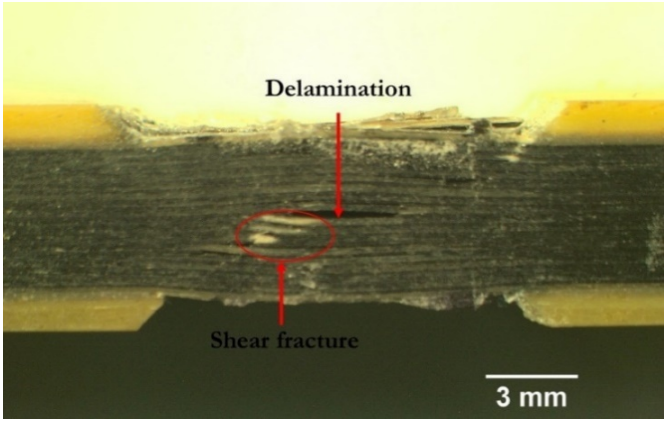

Figure 4.21. Typical image of a failed hybrid $[SG_1/(C_3/SG_1)]_{17}$ specimen showing final failure under longitudinal compression loading.

The failed $[SG_1/(C_3/SG_1)]_{17}$ hybrid configuration in **Figure 4.21** shows shear fibre fracture and delamination without any delamination in the end-tab regions. It is worth mentioning that different end-tabs type was used between $[SG_1/(C_3/SG_1)]_{17}$ with the remaining hybrid configurations. This is because the end-tab used for the $[SG_1/(C_1/SG_1)]_{17}$ and $[SG_1/(C_2/SG_1)]_{17}$ was no more available. It was then decided to use an equal modulus end tabs for the $[SG_1/(C_3/SG_1)]_{17}$ configuration although the thickness is 1.50 mm which is 0.1 mm below the end-tabs used for two hybrid configurations. The following section will describe the behaviour of each hybrid composite configuration under longitudinal compression in detail.

4.8.2.2 $[SG_1/(C_1/SG_1)_{17}]$ compression response

During compression loading of the $[SG_1/(C_1/SG_1)_{17}]$ configuration, a change of slope in the stress-strain curve appears at an average strain of -0.555% which is due to fragmentation of the carbon plies under compression [88]. This strain value has been corrected for the elastic residual strain calculated by using the method described in **Chapter 3**. The residual strain for $[SG_1/(C_1/SG_1)_{17}]$ configuration is -0.021%. The damage mechanisms behind the reduction in stiffness contribution from the carbon/epoxy ply in an asymmetric M55/S-glass hybrid specimen under four-point bending explained in **Section 4.8.1**, revealed multiple translaminar shear fractures running at an angle of around 40°-55° through the thickness of the carbon ply and local opening delamination at the intersections between the inclined cracks and the glass/carbon ply interfaces. This damage mechanisms has also been discovered by Czél et al. [88] for asymmetric $M55_2$ under four-point bending. The low transverse stiffness and low through thickness interlaminar strength promoted this delamination [137]. It is also believed that these same damage mechanisms were active in direct compression for these S-glass/M55 hybrids. It is clearly seen in

Figure 4.18 that after -0.555% strain, the stress continues to rise further. The strain where the carbon plies fragmented is taken as the -0.555% "knee-point strain" on the stress-strain curve and is determined from the intersection point of initial non-linear curve (black curve) and reduced slope regions (red line) as shown in **Figure 4.22** for the $[SG_1/(C_1/SG_1)_{17}]$ and $[SG_1/(C_2/SG_1)_{17}]$ hybrid configurations.

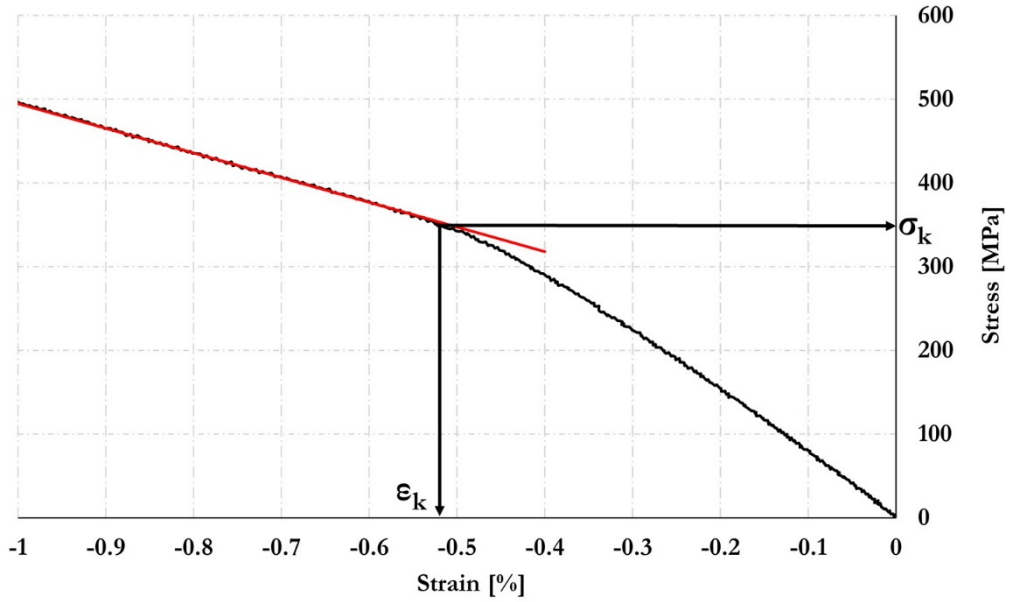

Figure 4.22. Knee-point stress (σ_k) and strain (ε_k) determined from the intersection point of initial non-linear curve (black curve) and reduced slope region (red line).

As shown in **Figure 4.18** for the $[SG_1/(C_1/SG_1)_{17}]$ configuration, after the knee-point strain the stress rises further until it reaches strain values of -1.660%, after which there is a load drop associated with delamination at the glass and carbon interface on one side of each hybrid configuration. The average thickness of the delaminated part on the right side of $[SG_1/(C_1/SG_1)_{17}]$ laminate shown in **Figure 4.23** at the first load drop (-1.660% strain) is 0.33 mm. The failure modes of $[SG_1/(C_1/SG_1)_{17}]$ configuration at each strain level and eventually at the final failure strain are depicted within the stress-strain curves shown in **Figure 4.23.**

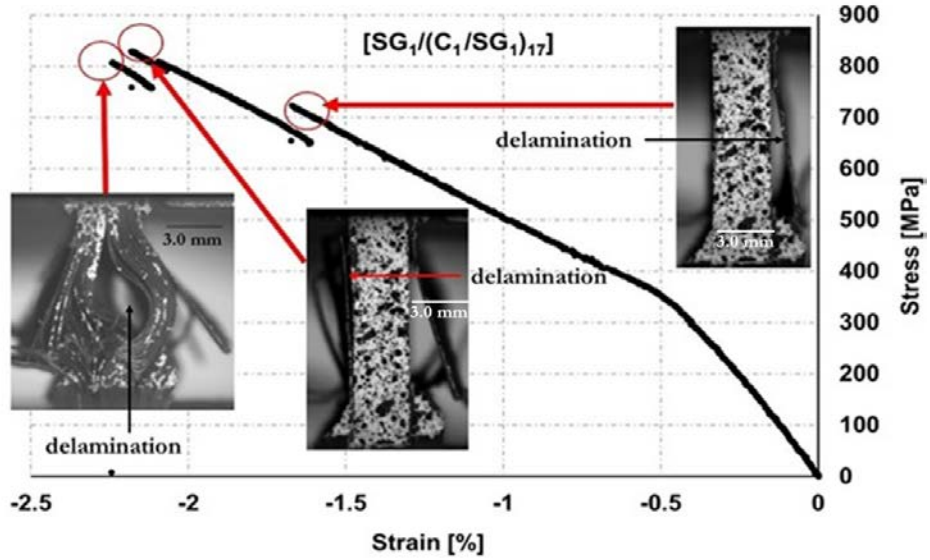

Figure 4.23. Failure sequence of $[SG_1/(C_1/SG_1)_{17}]$ configuration at each strain level.

After partial delamination between the glass and carbon plies at the right side of the $[SG_1/(C_1/SG_1)_{17}]$ laminate resulting in the first load drop in the stress-strain curve at -1.660% strain shown in **Figure 4.23**, the load is carried by the remaining intact plies. The stress then increases until

another partial delamination at an average depth of 0.28 mm appears on the left side of the laminate near the surface, resulting in a second load drop at -2.180% strain as shown in **Figure 4.23**. The final failure at -2.23% strain for this $[SG_1/(C_1/SG_1)_{17}]$ laminate is characterised as compressive failure together with delamination of the laminate resulting in a catastrophic/exploding failure type as shown in **Figure 4.23.**

4.8.2.3 $[SG_1/(C_2/SG_1)_{17}]$ compression response

A change of slope in the stress-strain curve at an average strain of -0.554% strain also appears for the $[SG_1/(C_2/SG_1)_{17}]$ hybrid configuration due to fragmentation of the carbon plies under compression. This value has been corrected for the elastic residual strain. The residual strain for $[SG_1/(C_2/SG_1)_{17}]$ configuration is -0.014%. As shown in **Figure 4.18** for the $[SG_1/(C_2/SG_1)_{17}]$ configuration, after the knee-point strain the stress rises further until it reaches strain values of -1.480%, after which there is a load drop associated with delamination at the glass and carbon interface on one side of each hybrid configuration. The failure mode for the $[SG_1/(C_2/SG_1)_{17}]$ laminate consists of partial delamination between the glass and carbon plies with an average depth of 0.36 mm at the right side near the surface of the laminate which took place at -1.480% strain causing the first load drop followed by an increase of stress until final failure at -1.670% strain when a catastrophic/explosive failure type took place. The failure modes of $[SG_1/(C_2/SG_1)_{17}]$ configuration at each strain level and eventually at the final failure strain are depicted within the stress-strain curves shown in **Figure 4.24.**

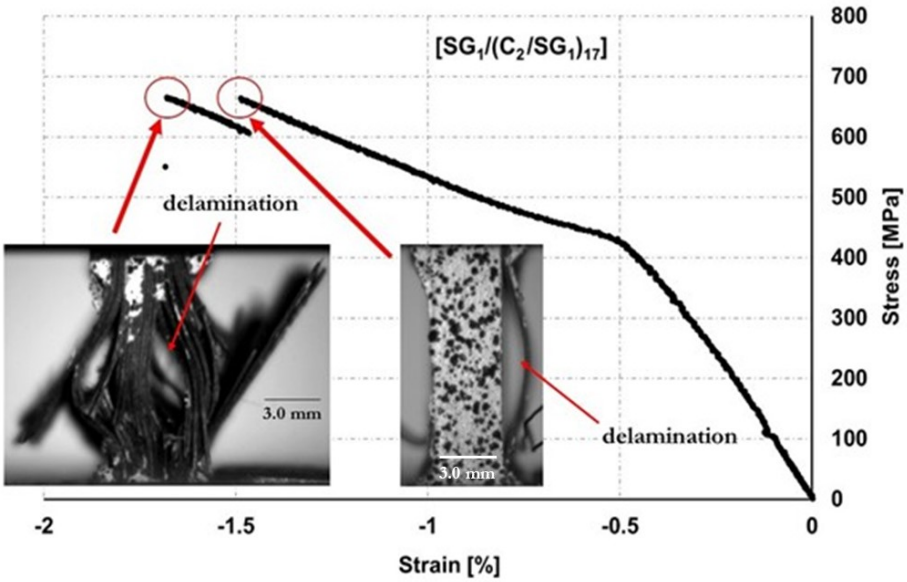

Figure 4.24. Failure sequence of $[SG_1/(C_2/SG_1)_{17}]$ configuration at each strain level.

4.8.2.4 $[SG_1/(C_3/SG_1)_{17}]$ compression response

The thickest laminate ply with $[SG_1/(C_3/SG_1)_{17}]$ configuration, experienced sudden failure at an average strain of -0.50% with the typical damage modes of fragmentation followed by delamination. This value has been corrected for the elastic residual strain. The residual strain for the $[SG_1/(C_3/SG_1)_{17}]$ configuration is -0.010%. The evidence of fragmentation in $[SG_1/(C_3/SG_1)_{17}]$

configuration is shown in **Figure 4.29** which also shows delamination between carbon and glass plies. It is worth mentioning that the optical image in **Figure 4.29** was taken from the $[SG_1/(C_3/SG_1)_{17}]$ specimen shown in **Figure 4.26**(c). For the $[SG_1/(C_3/SG_1)_{17}]$ hybrid, only the final failure mode at -0.50% strain is shown in **Figure 4.25** with its typical stress-strain curve, because no load drop was observed before the final failure.

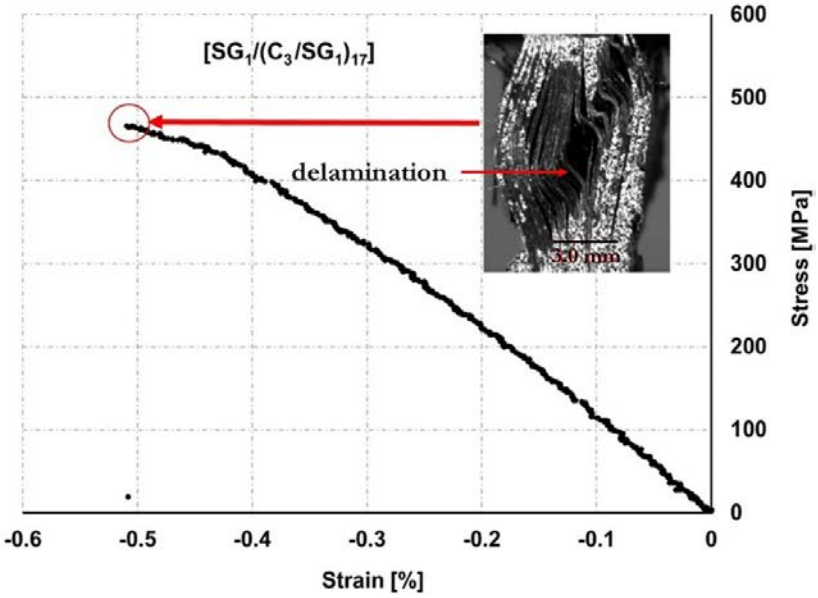

Figure 4.25. Final failure mode of $[SG_1/(C_3/SG_1)_{17}]$ configuration.

It should be noted that the same stress-strain curves shown in **Figure 4.23 -Figure 4.25** are the same as those shown in **Figure 4.18**. Overall, the behaviour of $[SG_1/(C_1/SG_1)_{17}]$ and $[SG_1/(C_2/SG_1)_{17}]$ laminates are considered as pseudo-ductile. The responsible damage mechanisms behind the pseudo-ductile behaviour are fragmentation of carbon ply and localised delamination between glass and carbon ply. Fragmentation of carbon ply and stable delamination are also responsible for the pseudo-ductile behaviour of unidirectional thin carbon ply/glass hybrid composites [60] under tensile loading.

4.8.2.5 Damage mode under direct compression

One specimen from $[SG_1/(C_1/SG_1)_{17}]$ and $[SG_1/(C_2/SG_1)_{17}]$ hybrid configuration discussed above was loaded under direct compressive loading until -0.80% strain when the test was terminated. The edge of each specimen was then grounded and polished before examined under Zeiss optical microscopy. For the $[SG_1/(C_3/SG_1)_{17}]$ configuration, an interrupted test was conducted at -0.41% strain, well below the final failure strain of -0.50% to see if any damage had occurred, but unexpected premature failure took place. **Figure 4.26** shows the top view image of a typical damaged found in $[SG_1/(C_1/SG_1)_{17}]$, $[SG_1/(C_2/SG_1)_{17}]$ and $[SG_1/(C_3/SG_1)_{17}]$ hybrid configuration. From the interrupted tests of the type laminates at -0.80% strain, it is shown that the typical damage mode for the hybrid configuration under compression includes carbon-ply fragmentation and localized delamination. It was possible to observe the delamination between the glass/epoxy and carbon/epoxy ply due to the translucent nature of the glass/epoxy ply. The delamination area is seen as a yellow pattern

surrounding the dispersed fractures in the carbon ply and running across the width of the specimen, as shown in **Figure 4.26**. A larger delamination area near the surface of the laminate, is shown as a yellow pattern, in **Figure 4.26(c)** for the $[SG_1/(C_3/SG_1)_{17}]$ laminate. Ply splitting was also observed as shown in **Figure 4.26(c)** (marked by red rectangles).

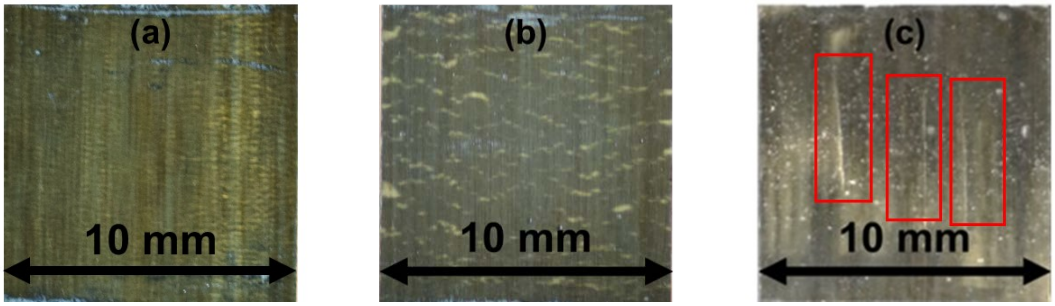

Figure 4.26. Typical damage mode for the different hybrid laminates under direct compression (a) $[SG_1/(C_1/SG_1)_{17}]$ at -0.8%, (b) $[SG_1/(C_2/SG_1)_{17}]$ at -0.80%, and (c) $[SG_1/(C_3/SG_1)_{17}]$ at -0.41%.

The optical image taken from the edge of all three hybrid configurations in **Figure 4.26** is shown in **Figure 4.27-Figure 4.29** for $[SG_1/(C_1/SG_1)_{17}]$, $[SG_1/(C_2/SG_1)_{17}]$ and $[SG_1/(C_3/SG_1)_{17}]$ respectively. As shown in **Figure 4.27** and **Figure 4.28**, carbon ply is seen fragmented periodically along the fibre length. For clarity a typical fragmented carbon ply is marked with red rectangle in **Figure 4.27** for $[SG_1/(C_1/SG_1)_{17}]$ configuration.

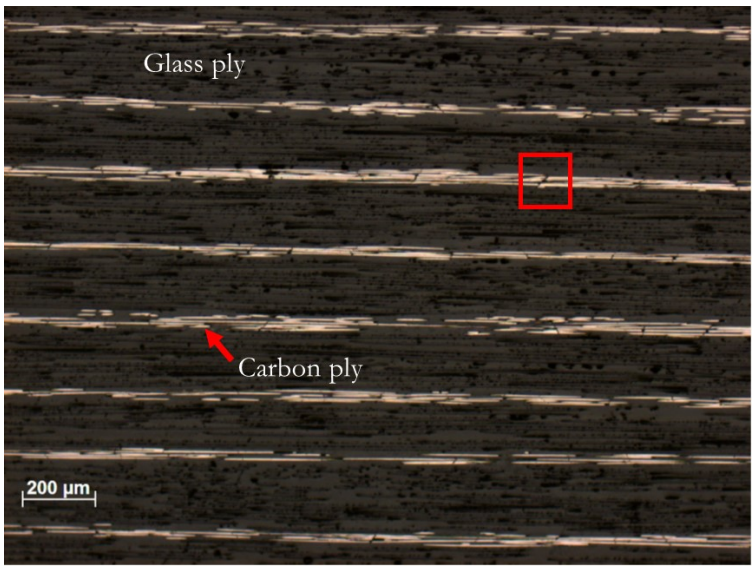

Figure 4.27. Damage mode of $[SG_1/(C_1/SG_1)_{17}]$ configuration at -0.80% strain.

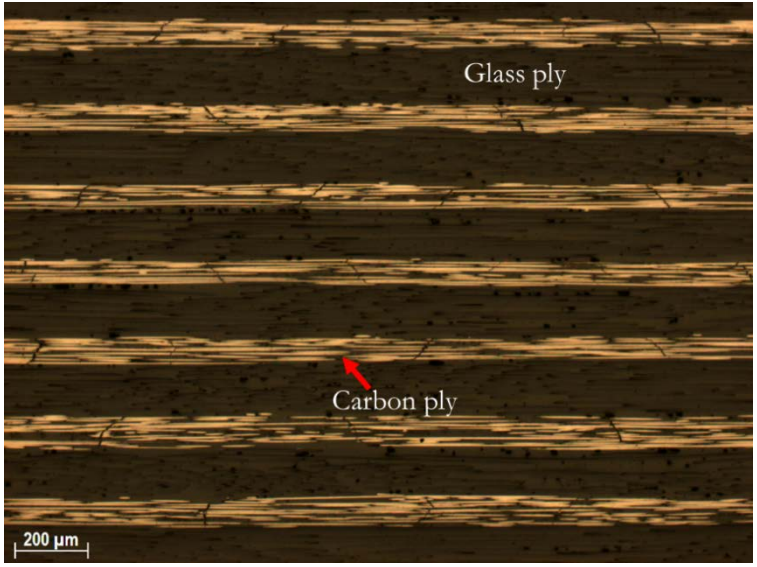

Figure 4.28. Damage mode of $[SG_1/(C_2/SG_1)_{17}]$ configuration at -0.80% strain.

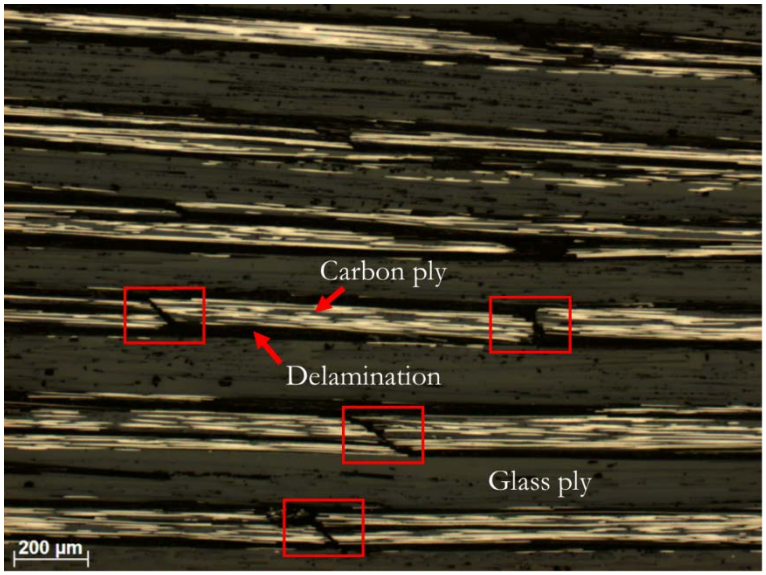

Figure 4.29. Damage mode of $[SG_1/(C_3/SG_1)_{17}]$ configuration at -0.41% strain.

For $[SG_1/(C_3/SG_1)_{17}]$ configuration shown in **Figure 4.29**, fractures running at an angle of around 45° through the thickness of the carbon ply are indicated with the red rectangles. The distance between fragmentation shown in **Figure 4.27** - **Figure 4.28** is measured using the same method explained in **Figure 4.17**. The comparison between the measured fragment length with the calculated critical carbon ply length for $[SG_1/(C_1/SG_1)_{17}]$, $[SG_1/(C_2/SG_1)_{17}]$, $[SG_1/(C_3/SG_1)_{17}]$, configurations are shown in **Table 4..**

Table 4.11. Comparison between theoretical critical length and measured fragment length for hybrid specimens under direct compression (numbers in brackets indicate coefficients of variation in [%]).

Designation	Total nominal carbon ply thickness [mm]	Theoretical critical length (L_c) [mm]	Measured fragment length (L_m) [mm]	$(L_c-L_m)/(L_c)$ [%]
$[SG_1/(C_1/SG_1)_{17}]$	0.52	0.85	0.21 (5.9)	75
$[SG_1/(C_2/SG_1)_{17}]$	1.03	1.71	0.53 (9.1)	69
$[SG_1/(C_3/SG_1)_{17}]$	1.55	2.56	0.98 (8.2)	62

As seen in **Table 4.,** there is a discrepancy between the measured fragment length and the calculated theoretical critical length which indicates the inapplicability of the traditional transfer load model to predict the fragment length in compression.

4.8.2.6 Mechanical properties of UD thin-ply hybrid composites under direct compression

The test results summary of all three hybrid configurations under direct compression is shown in **Table 4..** It should be noted that the strains mentioned in **Table 4.12** have been corrected for elastic residual strain. The notation Ei, E_f, ε_1, ε_f in **Table 4.** is the initial stiffness, final stiffness, first load drop and final failure strain respectively. The first load drop and final failure are explained in **Figure 4.23 - Figure 4.25** respectively. The method to measure the initial stiffness (Ei) and final stiffness (E_f) are shown in

Figure 4.30

Figure 4.32 for $[SG_1/(C_1/SG_1)_{17}]$, $[SG_1/(C_2/SG_1)_{17}]$ and $[SG_1/(C_3/SG_1)_{17}]$ respectively in which a tangent stiffness is being used to determine those values.

Table 4.4. Mechanical properties of hybrid composites under direct compressive loading (numbers in brackets indicate coefficients of variation in [%]).

Designation	Property	No. of specimens	E_i	E_f	ε_k	σ_k	ε_1	ε_f
			[GPa]	[GPa]	[%]	[MPa]	[%]	[%]
$[SG_1/(C_1/SG_1)_{17}]$	Average	6	76.53	30.22	-0.555	344	-1.690	-2.150
	COV (%)		(3.3)	(3.4)	(3.4)	(3.6)	(10.9)	(8.1)
$[SG_1/(C_2/SG_1)_{17}]$	Average	6	98.54	23.63	-0.554	429	-1.210	-1.440
	COV (%)		(6.8)	(7.6)	(3.3)	(1.0)	(14.2)	(8.7)
$[SG_1/(C_3/SG_1)_{17}]$	Average	6	118.90	53.48	-	-	-0.500	-0.500
	COV (%)		(5.9)	(10.0)	-	-	(6.9)	(6.9)

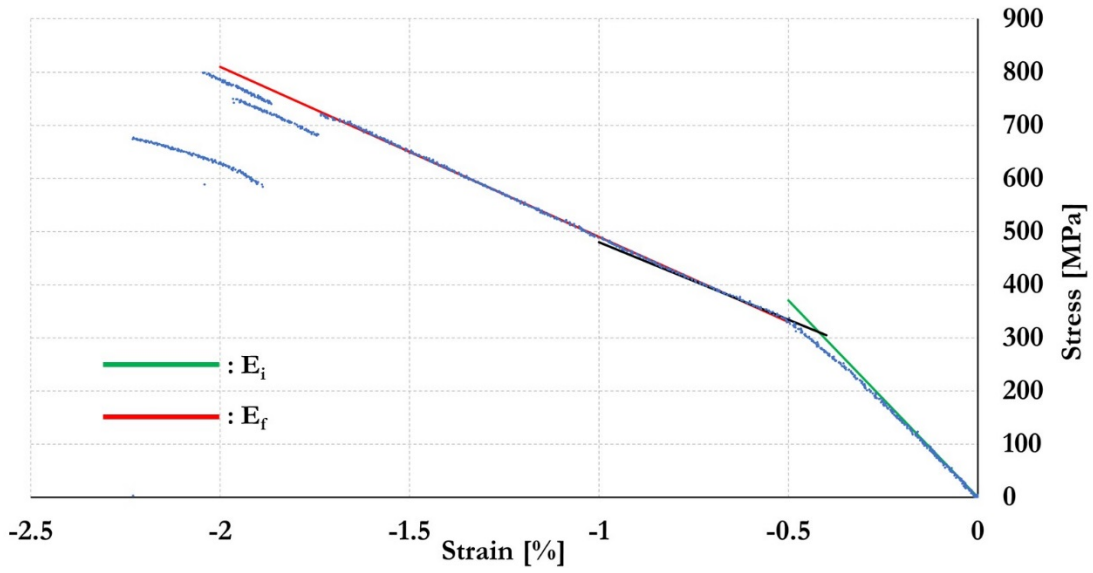

Figure 4.30. The method to determine initial and final stiffness for $[SG_1/(C_1/SG_1)_{17}]$ configuration.

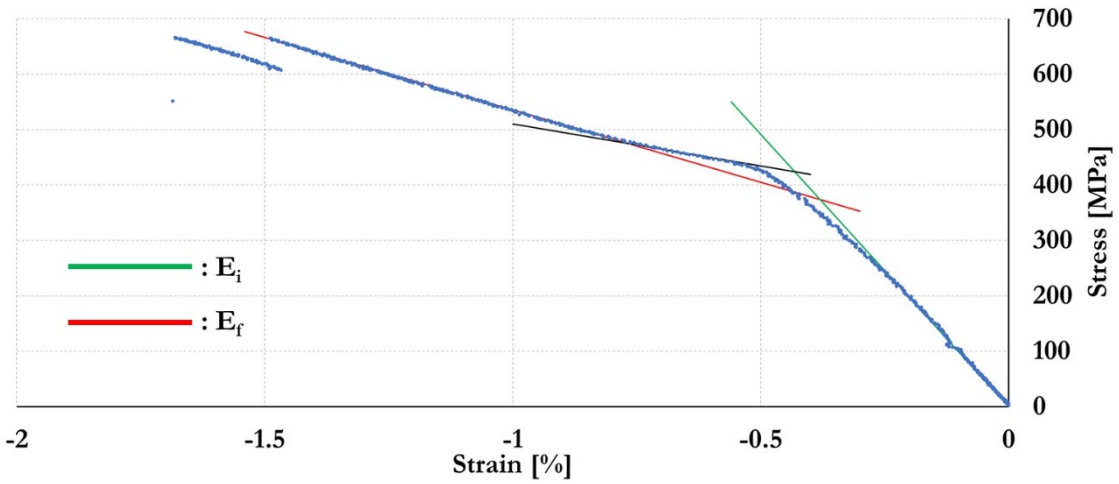

Figure 4.31. The method to determine initial and final stiffness for $[SG_1/(C_2/SG_1)_{17}]$ configuration.

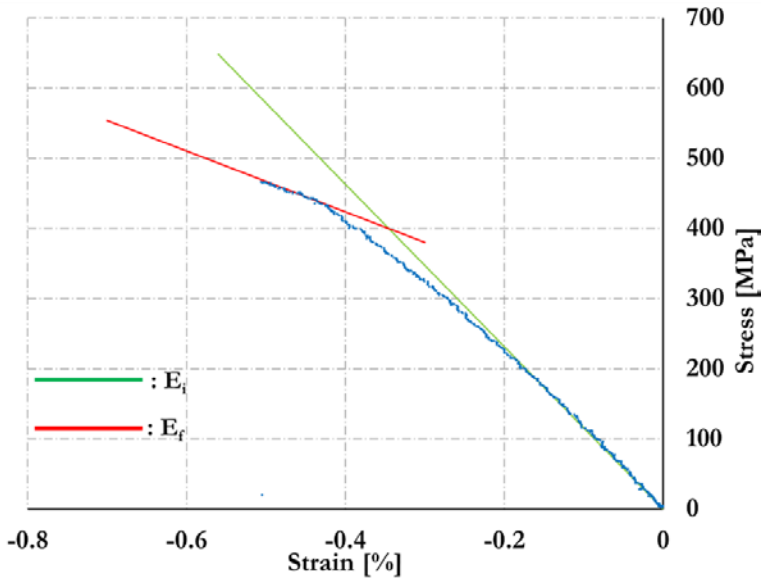

Figure 4.32. The method to determine initial and final modulus for $[SG_1/(C_3/SG_1)_{17}]$ configuration.

As shown in

Figure 4.30 and

Figure 4.31, the initial and final stiffness are determined by the green and red line respectively. The red lines were chosen as a measurement for the final stiffness because at those slopes, the fragmentation has reached saturation and the load is mainly carried by the glass plies. Part of the curve in

Figure 4.30 and

Figure 4.31 where the black line runs over is where fragmentation of carbon ply and localised delamination occurred. During compression loading of all three hybrid configurations, there is a non-linear behaviour before the knee-point strain. This is due to the non-linear behaviour of the carbon fibre itself which has been explained by several researchers [25], [138]. From **Table 4.5**, it

is seen that with increasing number of carbon plies incorporated in the hybrid laminates, the first load drop strain decreases. **Figure 4.33** gives an illustration of the reduction of first load drop strain and final failure strain with increasing carbon ply thickness for all three hybrid configurations.

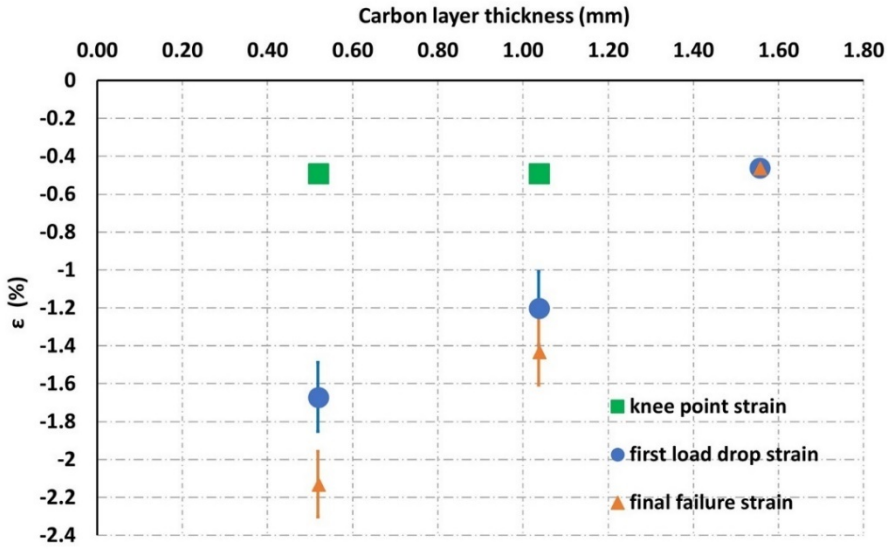

Figure 4.33. First load drop strain and final failure strain as a function of carbon ply thickness.

Different values of first load drop and final failure strains shown in **Figure 4.33** is due to the different energy release rates for delamination after fibre fracture in the different hybrid configurations. Because energy is proportional to the thickness of the carbon layer as explained by Czél et al. [39], delamination occurs at a lower strain for the hybrid with double compared with single carbon plies. It is also interesting to note that the -0.50% final failure strain for $[SG_1/(C_3/SG_1)_{17}]$ configuration is higher than the manufacturer's data sheet for M55J/epoxy shown in **Table 4.** which is -0.26%. This could be attributed to the better testing method used in this work and the advantage of using hybrid design in which the glass plies provided protection for the carbon plies from the high clamping force.

The comparison between knee-point strain and final failure strain from the direct and indirect compression testing is shown in **Table 4.6** for the hybrid configuration with different number of carbon plies. The notation DCT and IDCT in **Table 4.6** refers to Direct Compression Testing and Indirect Compression Testing respectively.

Table 4.6. Strain comparison between direct compression and indirect compression testing results (numbers in brackets indicate coefficients of variation in [%]).

Number of carbon plies	Knee-point strain [%]		Final failure strain [%]	
	DCT	IDCT	DCT	IDCT
1	-0.555 (3.4)	-0.555 (2.2)	-2.150 (8.1)	-2.720 (10.2)
2	-0.554 (3.3)	-0.552 (6.4)	-1.440 (8.7)	-1.750 (10.0)
3	-	-0.507 (2.1)	-0.500 (6.9)	-0.956 (4.3)

Examining the knee-point strain results from **Table 4.6**, the difference values obtained for all three hybrid configurations are not significantly large. This could suggest, that those knee-point strains mentioned in **Table 4.6** are the compressive failure strain for M55J carbon fibre. The final

failure strains shown in **Table 4.6** for the hybrids obtained from indirect compression testing are higher compared to the strains from direct compression testing. This could suggest that the strain gradient and the high strain embedding glass layers provided support for the carbon/epoxy layers in the compression thus delaying the final failure until higher strain.

4.9 Conclusions

This chapter has presented the mechanical properties of unidirectional thin-ply hybrid composites subjected to indirect (four-point bending) and direct compression testing. The effect of different hybrid configurations was examined. The following was concluded:

1. The compression response of unidirectional thin ply hybrids has been established. Gradual failure with a significant decrease in stiffness at around -0.50% strain and final failure at -2.15% and -1.44% strain has been obtained for the $[SG_1/(C_1/SG_1)_{17}]$ and $[SG_1/(C_2/SG_1)_{17}]$ hybrid configurations respectively.

2. For the $[SG_1/(C_3/SG_1)_{17}]$ configuration, sudden failure occurs at an average strain of -0.500%. Even this lower strain is higher than the compression failure strain calculated from the manufacturer's data sheet of -0.26%. This is attributed to a better testing method being used and the protection from the high clamping force provided by the glass layers.

3. From the indirect compressive loading, it was found that comparison between the change of force-strain slope and contribution of carbon bending stiffness from Classical Laminated Plate Theory (CLPT) indicated that the hybrid laminates with two and three carbon plies has lost most of the bending stiffness contribution from the carbon. However, there is no load drop and apparently, the carbon is still carrying load after fragmentation. Due to the irregular shape between the fragmented surfaces, friction and mechanical interlocking may exist which can help to transfer compressive load despite the fractures.

4. The measured fragment length from hybrid specimens tested under indirect and direct compression is less than the critical length calculated from the usual constant shear stress assumption with linear increase in stress from zero at both ends of the fragment.

5. The traditional load transfer model is inable to predict the fragment length of carbon layer in compression because the fibre fragment is in contact and still able to transfer load.

6. The carbon ply fractured at an angle is displaced in the transverse direction and this transverse displacement is responsible for interfacial damage (delamination) which causes the stiffness degradation.

7. A similar value of knee-point strains was obtained from indirect and direct compression testing which suggest that this value is the compressive strain to failure of the M55J carbon fibre.

8. The final failure strain of the hybrids decreases with increasing carbon ply thickness which qualitatively complies with the energy release rate concept.

Chapter 5 Flexural Response of Unidirectional Thin-Ply Hybrid Composites

5.1 Introduction

Unidirectional (UD) hybrid composites made of thin carbon/epoxy plies and standard thickness S-glass/913 epoxy plies have shown favourable pseudo-ductile response under static tensile loading as already shown in **Chapter 3** in this thesis. This response was achieved by the progressive fragmentation of the carbon layer and stable delamination of the fragments from the embedding glass layers [1]. Previous work on the characterisation of the compression behaviour of unidirectional hybrid composites made of thin high strength carbon/epoxy plies sandwiched between several glass/epoxy plies has shown a very high strain to failure in compression, even higher than the tensile strain to failure of the carbon fibre quoted by the manufacturer as shown in **Chapter 4** in this thesis. For hybrid composites consisting of thin high modulus carbon/epoxy plies, fragmentation of the carbon layer and stable delamination under compression was reported by Czél et al [88]. Based on the previous characterisation work of UD hybrid composites under tension [60] and compression [88], it seems possible to exploit the pseudo-ductile behaviour of this material in flexural loading as well where there is a combination of tensile and compressive loading on different sides of the hybrid. Demonstration of pseudo-ductility under flexural loading is essential to demonstrate their suitability for a wide range of applications. It would also be interesting to compare the flexural response of the UD thin ply hybrid composites with its tension and compression behaviour. It should be noted that indirect compression methods will be used in this chapter to obtain the compression properties of TC35 carbon/epoxy. In this chapter, two types of thin carbon plies with different modulus were used, M55J carbon/epoxy and TC35 carbon/epoxy which are known as high modulus and standard modulus carbon fibre respectively.

5.2 Experimental methods

5.2.1 Materials

The hybrid composite constituent materials considered for the design and used in the experimental part of the study were standard thickness S-glass/epoxy supplied by Hexcel, thin M55J carbon/epoxy supplied by North Thin Ply Technology, thin TC35 carbon/epoxy plies

commercially available from SK Chemicals under the trade name of SkyFlex USN020A. The epoxy resins in the prepregs were the aerospace grade 913 (Hexcel), ThinPreg 120 EPHTg-402 (North TPT) and K50 (SK Chemicals). The carbon fibers were Tairyfil TC35 and Torayca M55J, where TC35 is classified as a standard modulus carbon fibre [139] while M55J is a high modulus carbon fibre and produced in 6000 filament tows [132]. Basic properties of the applied fibre and prepreg systems can be found in Error! Reference source not found. and **Table 5.11.** The fibre properties in Error! Reference source not found. are based on the manufacturer's data and were determined from impregnated strands except for the S-glass where single fibre tests were performed.

Table 5.7. Fibre properties of the applied UD prepregs.

Fibre type	Manufacturer	Tensile modulus [GPa]	Tensile strain to failure [%]	Tensile strength [GPa]	Density [g/cm^3]	CTE α [1/K]
Tairyfil TC35	Formosa	240	1.60	4.00	1.80	-4.10^{-7}
Torayaca M55JB	Toray	540	0.80	4.02	1.91	$-1.1.10^{-6}$
FliteStrand SZT S-glass	Owens Corning	88	5.50	4.8-5.1	2.45	2.10^{-6}
EC9 756 P109 E-glass	Owens Corning	72	4.5	3.5	2.56	$4.9.10^{-6}$

Table 5.8. Cured ply properties of the applied UD prepregs.

Prepreg Type	Property Unit	Fibre mass per unit area [g/m^2]	Cured ply thickness [mm]	Fibre volume fraction [%]	Initial elastic modulus [GPa]	Tensile strain to failure [%]	Compressive strain to failure [%]
TC35/epoxy [140]	Average	22[a]	0.027[b]	46.9[b]	114.3[b]	1.95[c]	-
	COV [%]	-	-	-	-	7.08	-
M55 /epoxy [88]	Average	30	0.030	52	280 [d]	0.6[e]	0.26[e]
	COV [%]	-	-	-	-	-	-
S-glass/epoxy [88]	Average	190	0.155	51	45.7 [73]	3.98	2.33[e]
	COV [%]	-	-	-	3.2	1.1	-
E-glass/epoxy [88]	Average	192	0.140	54	40.0[b]	3.07[e]	-
	COV [%]	-	-	-	-	-	-

[a] Based-on manufacturer's data.
[b] Calculated based on manufacturer's data.
[c] First carbon layer fracture measured on [S-Glass/Carbon$_2$/S-Glass] UD interlayer hybrid in static tension.
[d] Calculated for the given fibre volume fraction.
[e] Based on manufacturer's data for 60% carbon fibre volume fraction.

The baseline failure strain for TC35/epoxy is an average of 5 specimen measurements in a [S-Glass/Carbon$_2$/S-Glass] type sandwich hybrid specimen and it is defined as the first carbon ply crack visible in the specimen during static tensile loading. It should be noted that the strain to failure for TC35/epoxy was measured from a thin hybrid configuration, so it is expected that there is an enhancement in the measured strain due to the 'hybrid effect' [141].

For the prepreg systems mentioned in **Table 5.11**, the fibre volume fraction is obtained from the manufacturer's data sheet and the cured ply thickness (CPT) is calculated by using **Equation 3.1** in **Chapter 3.** There is a reasonable agreement between the calculated and the measured CPT of the hybrid specimens and this is shown in **Table 5.12** and **Table 5.9** for the four-point bending and tensile UD thin-ply hybrid specimens, respectively. The measured thickness in **Table 5.12** is from an average measurement of five specimens for each hybrid configuration. For the measured thickness in **Table 5.10**, an average measurement of seven specimens for $[SG_1/TC35_1/SG_1]$, $[SG_1/M55_1/SG_1]$, $[SG_1/M55_2/SG_1]$ configurations was taken while for $[SG_1/TC35_2/SG_1]$, only an average measurement of five specimens was taken.

Table 5.11. Calculated and measured cured ply thickness of the four-point bending UD thin-ply hybrid composites (the number in the bracket indicates the coefficient of variation in [%]).

Designation	Lay-up sequence	Calculated thickness [mm]	Measured thickness [mm]
TC35/S-glass	$[SG_1/TC35_1/SG_1]_{4s}$	2.710	2.740 (1.13)
	$[SG_1/TC35_2/SG_1]_{4s}$	2.940	2.970 (1.18)
M55/S-glass	$[SG_1/M55_1/SG_1]_{4s}$	2.720	2.750 (0.74)
	$[SG_1/M55_2/SG_1]_{4s}$	2.960	2.980 (1.65)

Error! Reference source not found.**.** Calculated and measured cured ply thickness of the tensile UD thin-ply hybrid composites (the number in the bracket indicates the coefficient of variation in [%]).

Designation	Lay-up sequence	Calculated thickness [mm]	Measured thickness [mm]
TC35/S-glass	$[SG_1/TC35_1/SG_1]$	0.333	0.343 (3.48)
	$[SG_1/TC35_2/SG_1]$	0.356	0.368 (2.73)
M55/S-glass	$[SG_1/M55_1/SG_1]$	0.340	0.340 (2.86)
	$[SG_1/M55_2/SG_1]$	0.370	0.371 (2.86)

5.2.2 Specimen geometry

Symmetric hybrid specimens (see Error! Reference source not found.) made of thin carbon/epoxy plies sandwiched between several glass/epoxy plies were tested in four-point bending. This testing method was chosen to ensure a uniform bending moment between the loading noses and to avoid premature failure under the loading noses encountered more often in three point-bending tests. The total length of the symmetric hybrid specimens tested in four-point bending was 110 mm. This length was chosen to avoid premature shear failure and to ensure a compressive failure.

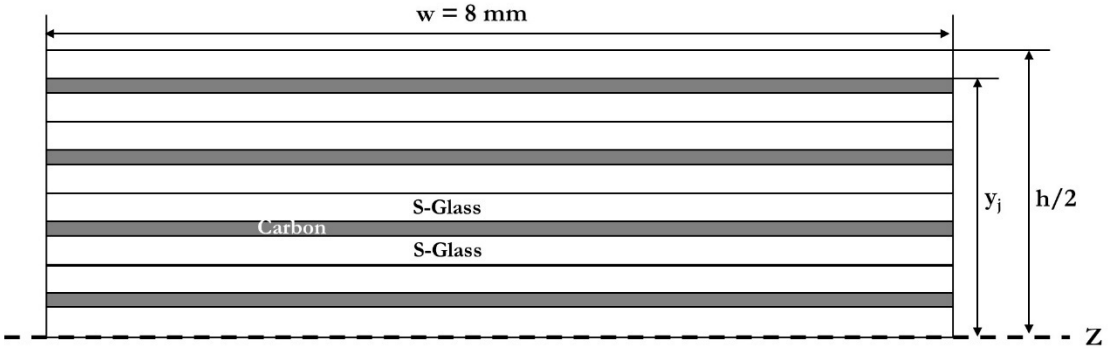

Figure 5.34. Cross-sectional schematic of the symmetric UD hybrid composite specimens tested in bending.

Error! Reference source not found. shows half of the cross-sectional schematic of the symmetric hybrid composites where the notation yj, h and Z are the distance from the surface of carbon ply to the neutral axis, nominal thickness of the specimen and neutral axis respectively. Only half of the cross-sectional thickness is shown in **Error! Reference source not found.** as the hybrid specimen is symmetric. The lay-up sequences for the tested hybrid configuration under flexural loading are shown in **Table 5.5.** The carbon/epoxy volume ratio shown in Error! Reference source not found. is calculated based on the ratio between the nominal thickness of the carbon/epoxy plies and the total nominal thickness of the hybrid specimen. The nominal thickness of the constituents to calculate the carbon/epoxy volume ratio is shown in **Table 5.11**. The notation h, w and L in **Error! Reference source not found.** refer to the nominal thickness, width and total length respectively.

Error! Reference source not found.. Symmetric hybrid specimen types tested under four-point bending.

Design.	Lay-up sequence	h [mm]	Carbon /epoxy volume ratio [%]	w [mm]	L [mm]	Support span [mm]	Inner span [mm]
TC35/S-glass	$[SG_1/TC35_1/SG_1]_{4s}$	2.71	8.55	8	110	90	30
	$[SG_1/TC35_2/SG_1]_{4s}$	2.94	15.76				
M55/S-glass	$[SG_1/M55_1/SG_1]_{4s}$	2.72	8.95				
	$[SG_1/M55_2/SG_1]_{4s}$	2.96	16.44				

5.2.3 Mechanical test procedure

The tensile tests for the hybrid specimens in this chapter were carried out using a computer controlled Instron 8872 Type 25 kN rated universal hydraulic test machine with wedge type hydraulic grips. A 25 kN rated load cell was used on the machine. The tests were conducted under displacement control at a cross-head speed of 2 mm/min. The tensile strain in the composite specimens was measured using an Imetrum video gauge within a nominal gauge length of 130 mm. The procedure for conducting indirect compressive testing can be found in **Chapter 4**, as the procedure is the same as in this chapter.

For the four-point bending tests, the hybrid composite specimens were tested in the same Instron machine used for tensile testing. A 5 kN rated load cell was used on the machine for this testing. The set-up for the four-point bending tests was the following: support span = 90 mm, inner span = 30 mm. To avoid the possibility of local compressive failure of the surface glass plies under the inner loading noses due to high contact forces, reinforced rubber pads were located between the loading nose and specimen contact surface. To measure the surface strains on the compressive and tensile side, strain gauges of type C2A-06-062LW-120 with 4.45 x 2.03 mm overall length and width respectively were attached to both sides of the specimens in the centre of the gauge length. It is worth mentioning that the gauge length for this strain gauge type is 1.52 mm. The four-point bending test set-up is shown in **Figure 5.66**. The white dots shown in **Figure 5.66** are used to measure the curvature of the hybrid specimens.

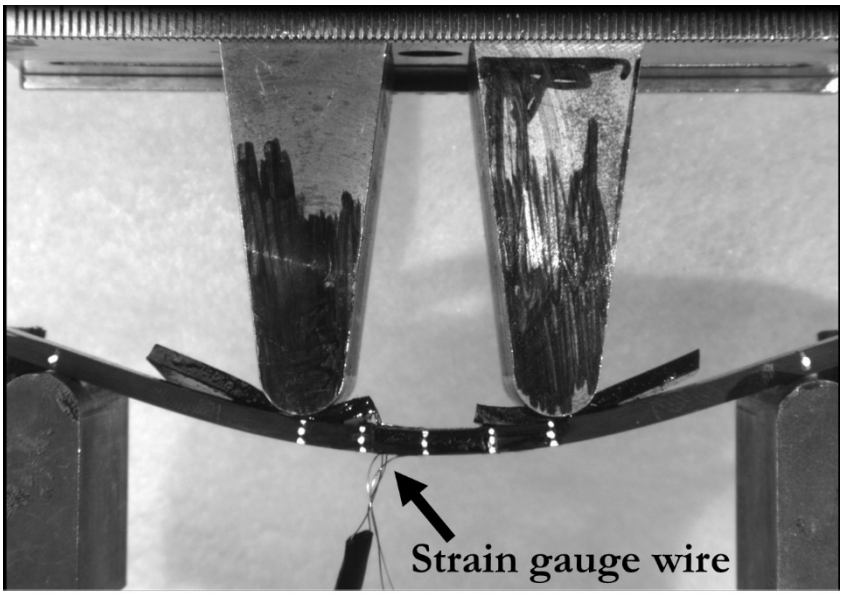

Figure 5.35. Four-point bending test set-up of symmetric UD thin carbon/glass hybrid composites.

5.3 Results and discussion

5.3.1 Tensile response of [SG/TC35$_n$/SG] & [SG/M55$_n$/SG] configurations

The comparison between [SG/TC35$_1$/SG] and [SG/TC35$_2$/SG] stress-strain response under tensile loading is shown in Error! Reference source not found.. For both configurations, there is an initial linear elastic response followed by non-linear behaviour due to fragmentation of the carbon plies and dispersed delamination. After fragmentation reaches saturation and the glass plies partly carry the load, the stress continues to rise as the strain increases until the hybrids failed, which is marked by a load drop, as seen in Error! Reference source not found.. For the [SG/TC35$_2$/SG] specimens, three out of five specimens were not loaded until failure and two of them failed at a lower strain compared to the [SG/TC35$_1$/SG] configuration. The lower strain to failure of the [SG/TC35$_2$/SG] configuration could be attributed to the higher load transfer/stress concentration from the double carbon plies in the [SG/TC35$_2$/SG] compared to [SG/TC35$_1$/SG] configuration.

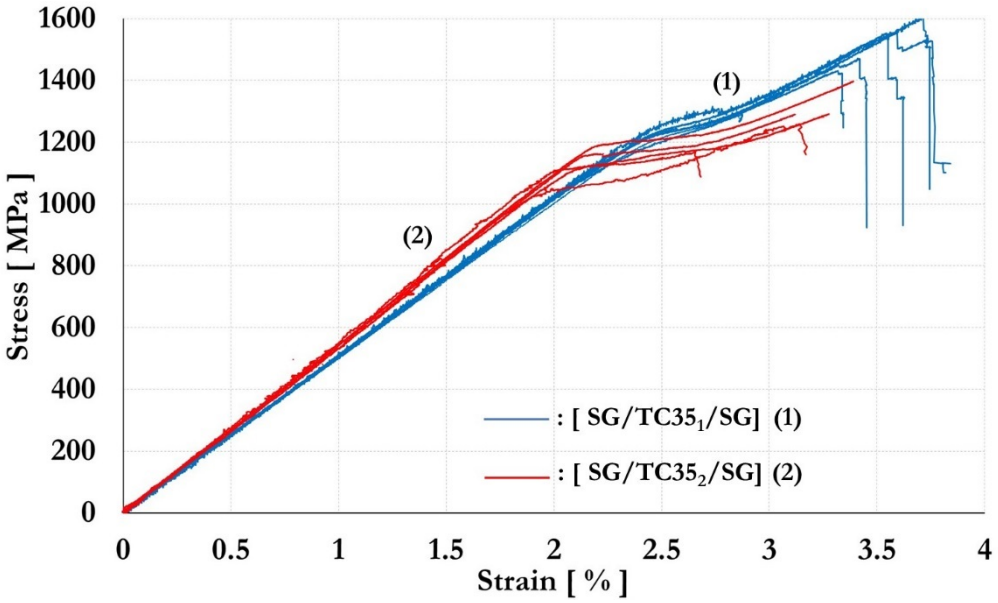

Figure 5.36. Stress-strain curves for [SG/TC35$_1$/SG] and [SG/TC35$_2$/SG] configurations.

The knee-point shown in Error! Reference source not found. marks the transition from the linear elastic behaviour to the non-linear behaviour due to the establishment of fragmentation in the carbon. Beyond the knee-point, there is a non-linear region for the [SG/TC35$_2$/SG] configuration due to gradual fragmentation and dispersed delamination. For the [SG/TC35$_1$/SG] configuration, there is no obvious plateau region as shown in Error! Reference source not found. and the stress continues to rise even after the knee-point. It is worth mentioning that the method to determine the knee-point is already explained in **Chapter 3**. To explain the tensile response of [SG/TC35$_1$/SG] and [SG/TC35$_2$/SG], the recorded images during tensile loading were studied. Typical damage development for [SG/TC35$_1$/SG] and [SG/TC35$_2$/SG] configurations due to static tensile loading are shown in **Figure 5.68** and **Figure 5.69** respectively.

The tensile damage development for the [SG/TC35$_1$/SG] configuration in **Figure 5.68** shows a very dense fragmentation pattern from 2.34% to 3.23% strain with no obvious delamination. This damage pattern is due to the shorter process zone around the fragmented ply as shown by Jalalvand et al. [64] in their numerical damage analysis of UD thin carbon/glass hybrid composites. As also explained in [64], in the thinner hybrid laminate, the interface is less damaged so it is possible that the load is being transferred from the intact carbon ply to the glass ply as the fragmentation progresses (which mean there is no true delamination in this hybrid configuration) and therefore the stress continuously increases beyond the knee-point as shown in Error! Reference source not found..

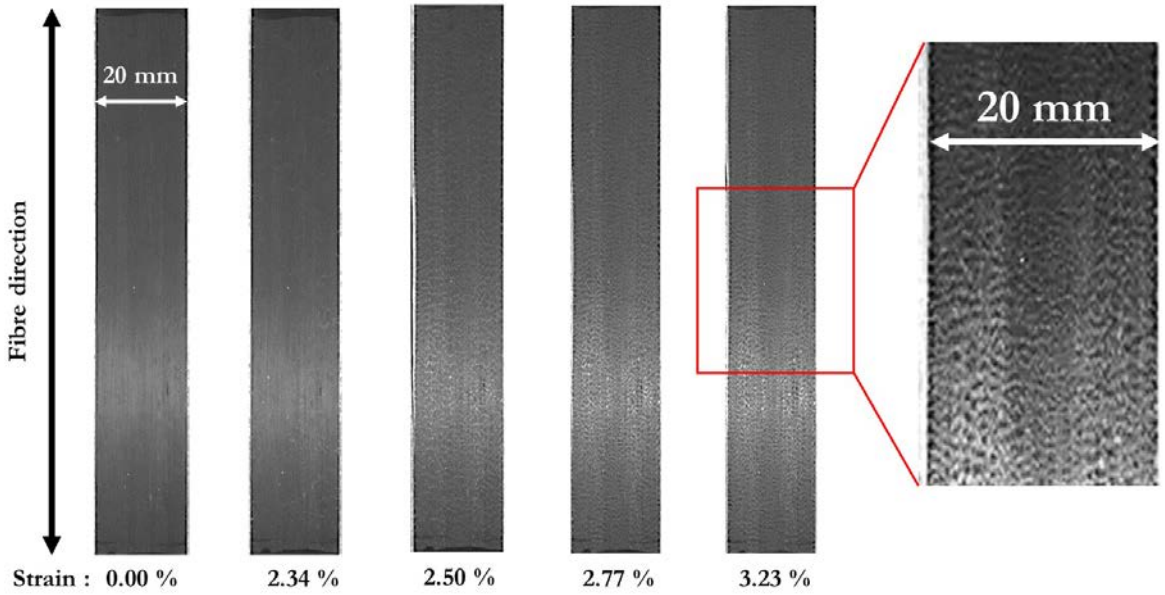

Figure 5.37. Typical damage development of [SG/TC35$_1$/SG] during tensile loading.

The damage pattern for the [SG/TC35$_2$/SG] configuration in **Figure 5.69** shows fragmentation and obvious delamination with increasing tensile strain. Due to the translucent nature of the glass/epoxy plies, it was possible to detect the delaminated area visually in this hybrid specimen type. The delamination area is shown as the lighter area which corresponds to the colour of the epoxy resin. While the darker area shown in **Figure 5.69** is the intact area between the carbon and glass plies. The irregular delamination patch sizes shown in **Figure 5.69** are due to variation of the carbon plies thickness, where the thicker parts tend to produce larger delamination patches. Fragmentation and dispersed delamination in this hybrid configuration are responsible for the non-linear region in the stress-strain curve shown in Error! Reference source not found..

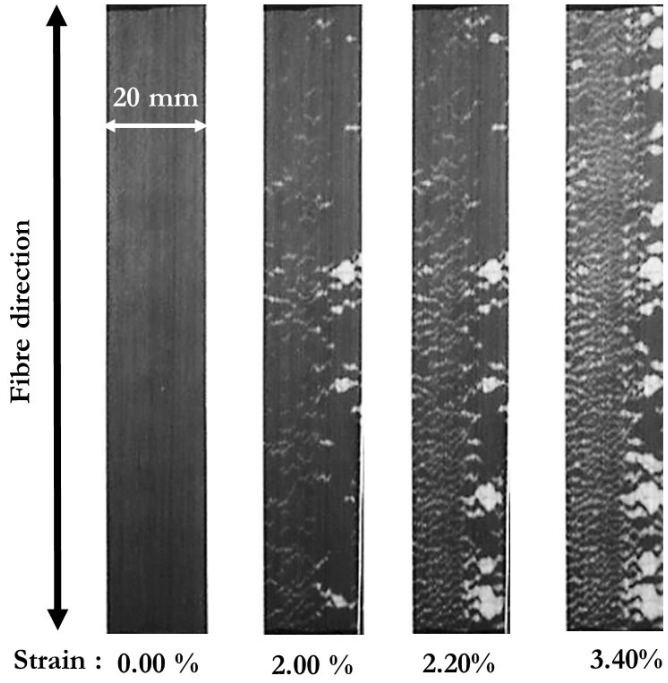

Figure 5.38. Typical damage development of [SG/TC35$_2$/SG] during tensile loading.

Error! Reference source not found. shows the stress-strain response of [SG/M55$_1$/SG] and [SG/M55$_2$/SG] configurations respectively. There is an initial linear elastic response followed by non-linear behaviour and increase of stress at higher strain as also shown by the two previous hybrid configurations. As shown in Error! Reference source not found., the non-linear region/plateau in the stress-strain response for both configurations is more obvious compared to the plateau on the [SG/TC35$_1$/SG] configuration which could also suggest more pronounced delamination for [SG/M55$_1$/SG] and [SG/M55$_2$/SG]. This argument is supported by the damage development during tensile loading shown in **Figure 5.71** and **Figure 5.72** for both hybrid configurations.

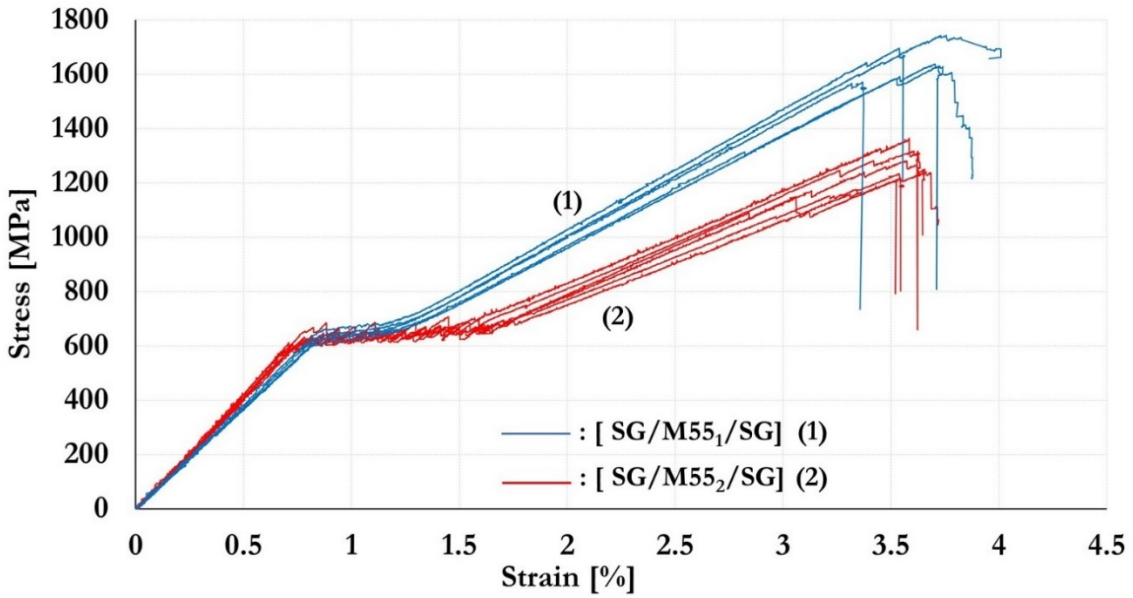

Figure 5.39. Stress-strain curves for [SG/M55$_1$/SG] and [SG/M55$_2$/SG] configurations.

The tensile damage development for the [SG/M55$_1$/SG] configuration in **Figure 5.71** shows fragmentation and dispersed delamination. The fragmentation in this hybrid was established at 0.84% strain, leading to a knee-point in the stress-strain curve as shown in Error! Reference source not found.. From 0.84% to 1.26% strain there was further gradual damage growth as shown in **Figure 5.71** which is responsible for the non-linear region/plateau in the [SG/M55$_1$/SG] stress-strain curve.

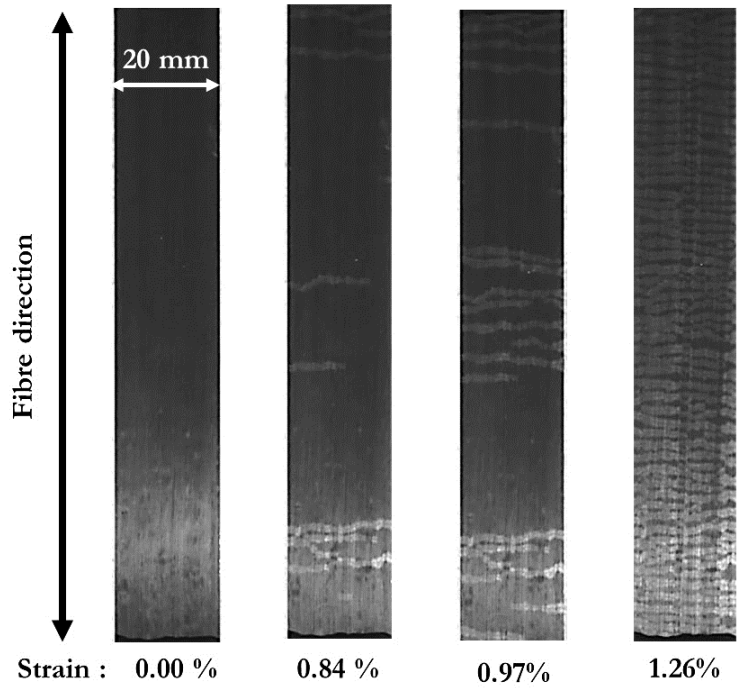

Figure 5.40. Typical damage development of [SG/M55$_1$/SG] during tensile loading.

Figure 5.72 shows fragmentation and dispersed delamination growth of the [SG/M55$_2$/SG] configuration with increasing tensile strain. As shown in **Figure 5.72**, at 0.80% there is an establishment of fragmentation which corresponds to the knee-point in the stress-strain curve. Comparing the delaminated area in **Figure 5.72** and **Figure 5.71**, it can be seen that [SG/M55$_2$/SG] has extensive delaminated area compared to [SG/M55$_1$/SG]. This could be attributed to the higher energy release rate of the hybrid with double M55 plies compared to the hybrid with single M55 ply.

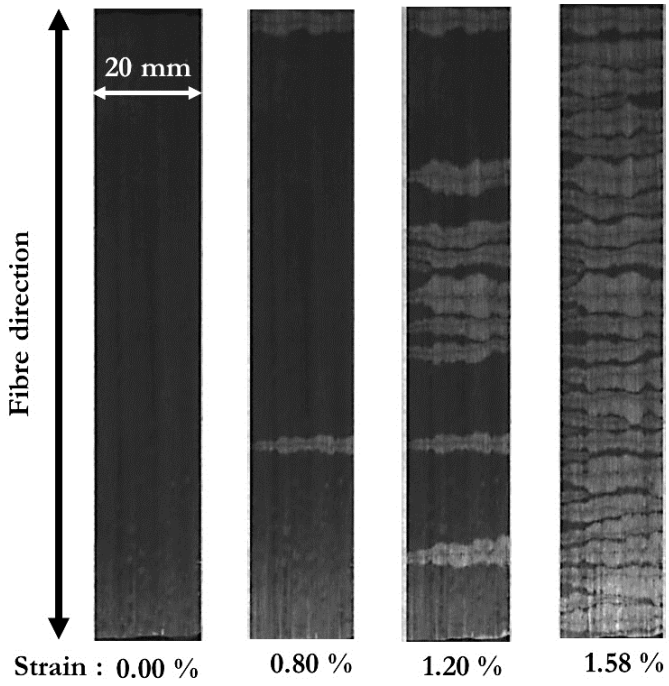

Figure 5.41. Typical damage development of [SG/M55$_2$/SG] during tensile loading.

The input parameters for each prepreg to calculate the elastic thermal residual strain are shown in **Table 5.13**. The transverse (E_{22}) and shear modulus (G_{12}) for TC35/epoxy and M55/epoxy are assumed similar for a high strength and high modulus carbon epoxy composites respectively taken from the Hexcel product datasheet [116]. While the transverse CTE (α_{22}) for all the prepregs is assumed similar to T300/5208 carbon/epoxy prepregs since the properties in transverse direction is governed mainly by the resin [117].

The tensile test results summary for all four hybrid configurations being discussed is shown in **Table 5.** which will be compared later with the four-point bending test results. The compared parameters will be the knee-point and final failure strain. The knee-point strain and final failure strain in **Table 5.** have been corrected for the compressive thermal residual strain for each configuration. The method to calculate the thermal residual strain is shown in **Chapter 3**.

Table 5.12. Cured ply properties of the applied UD prepregs as an input parameter to determine the thermal residual strain.

Prepreg type	E_{11} [GPa]	E_{22} [GPa]	CPT [mm]	α_{11} [1/K]	α_{22} [1/K]	G_{12} [GPa]	ν_{12}
M55/epoxy	280	6.3 [116]	0.030	$-7.80*10^{-7}$ [a]	$2.6*10^{-5}$[117]	3.1[116]	0.31[116]
TC35/epoxy	114.3	11 [116]	0.027	$4.39*10^{-7}$ [a]	$2.6*10^{-5}$[117]	4.4[116]	0.30[116]
E-glass/epoxy	40	12.5[116]	0.140	$6.70*10^{-6}$ [a]	$2.6*10^{-5}$[117]	3.3[116]	0.30[116]
S-glass/epoxy	45.7	10.3[116]	0.155	$3.80*10^{-6}$ [a]	$2.6*10^{-5}$[117]	3.1[116]	0.30[116]

[a] calculated by using the Classical Laminate Theory (CLT) shown in Appendix A.

The calculated residual strain in the carbon fibre is -0.028%, -0.025%, -0.029%, -0.021% for the [SG/$TC35_1$/SG], [SG/$TC35_2$/SG], [SG/$M55_1$/SG], [SG/$M55_2$/SG] configurations respectively.

Table 5.. Tensile results summary of the specimen types tested (Numbers in brackets indicates the coefficient of variation in [relative %]).

Spec. Type	Number of specimens	Initial elastic modulus [GPa]	Strain at knee-point ε_k [%]	Final failure strain ε_f [%]	Nominal thickness [mm]	Mode II energy release rate at the failure strain of the carbon ply [N/mm]
[SG/$TC35_1$/SG]	7	48.87(3.7)	2.31(2.9)	3.38(8.7)	0.333	0.27 at 1.95%
[SG/$TC35_2$/SG]	5	53.32(2.1)	1.95(7.1)	2.89[a] (11)	0.356	0.54 at 1.95%
[SG/$M55_1$/SG]	7	75.26(2.6)	0.84(1.3)	3.68(4.1)	0.340	0.29 at 0.80%
[SG/$M55_2$/SG]	7	83.31(2.4)	0.80(2.1)	3.54(1.8)	0.370	0.51 at 0.80%

[a] average failure strain of two specimens.

As shown in **Table 5.**, the calculated energy release rate for the hybrids with double carbon plies are much higher compared to the single ply hybrids which explains the more extensive delaminated area for the former. It is worth mentioning that the method to calculate the energy release rate is explained in **Chapter 3**.

The compression response of TC35/S-glass hybrid has not been explored before according to the author's best knowledge and to study its behaviour, an asymmetric TC35/S-glass configuration under four-point bending with the carbon ply on the compression side was studied. **Section 5.3.2** will discuss the compression response of the asymmetric TC35/S-glass hybrid.

5.3.2 Compression response of asymmetric TC35/S-glass hybrid configuration

The force-strain response of the asymmetric $TC35_2$/S-glass hybrid under four-point bending is shown in **Figure 5.73.** The design lay-up for the asymmetric $TC35_2$/S-glass was $[SG_1/EG_{14}/SG_2/TC35_2/SG_1]$ and the nominal thickness (h) for this configuration is 2.63 mm. It should also be noted that the carbon/epoxy plies were under compressive loading. The compressive strain shown in **Figure 5.73** is calculated for the top level of the carbon plies under compression while the tensile strain is measured on the bottom tensile surface of the glass plies. The method to calculate the strain at the top carbon ply is described in **Chapter 4**. The input parameter to determine the strain for this hybrid configuration is y_j = 2.47 mm and z = 1.50 mm with yj and z described in **Chapter 4**. It is worth mentioning that the force-strain curve in **Figure 5.73** is only for one hybrid specimen which failed on the compression side while the other five hybrid specimens failed on the tension side where the glass plies are located. For the asymmetric $TC35_1$/S-glass configuration, all six specimens failed on the tension side without any failure on the compression side, so are not included in this section.

In the force-strain curve for the asymmetric $TC35_2$/S-glass hybrid, a non-linear hardening behaviour can be observed on the tensile side and softening on the compression side. This behaviour is likely due to departure from linear elastic behaviour of the carbon fibres, with the tensile modulus increasing with increasing strain [25], [142]–[145]. The softening on the compression side could be due to the tangent modulus of the carbon fibre decreasing with increasing compression strain [25] which can be explained due to accelerated rotation of the cyrstallites structure within the carbon fibre [138]. Another explanation for the non-linearity on the compression side and also on the tension side just before final failure is the increasing geometrical non-linearity of the hybrid specimen at large deflections [88].

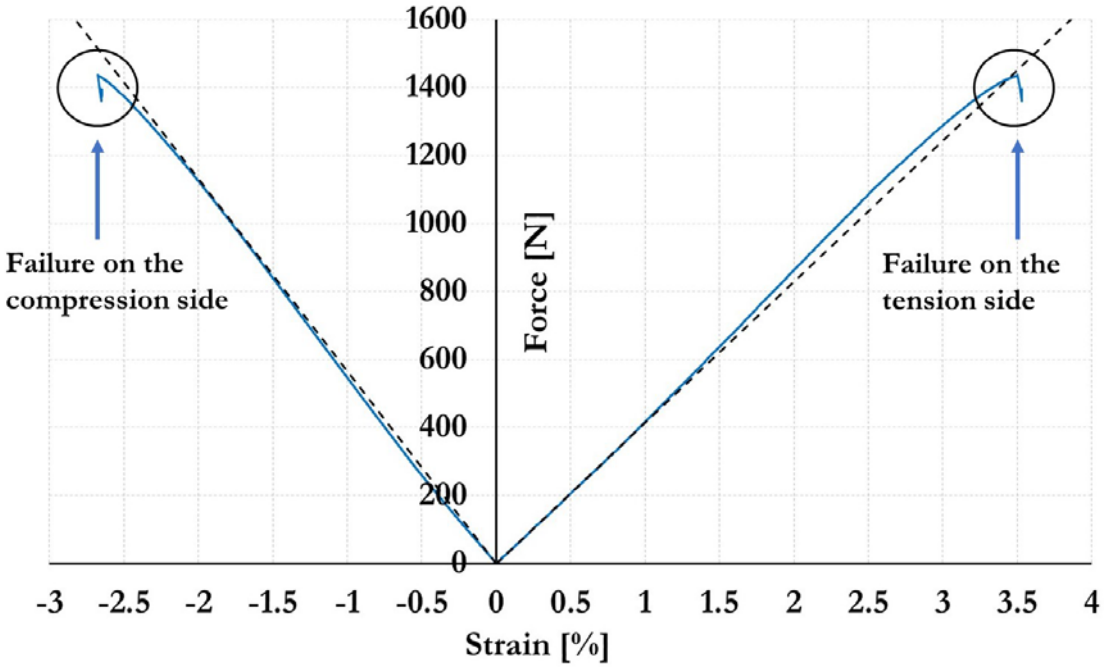

Figure 5.42. Force-strain curve for asymmetric $TC35_2$ / S-glass hybrid composites under four-point bending.

A non linear hardening behaviour can be observed on the tensile side and softening on the compression side As seen in **Figure 5.73**. There is a load drop at -2.64% due to fibre failure followed by delamination on the compression side and then followed by failure of the glass plies on the tension side at 3.50% as observed from the recorded video gauge. The calculated residual strain in the carbon ply for the asymmetric $TC35_2$ / S-glass configuration is -0.025% and when this is considered to recalculate the compressive strain to failure, the strain is -2.665%. The compression strain to failure of this hybrid configuration is higher than the knee-point tensile strain shown in **Table 5.** for [SG/$TC35_2$/SG] configuration. The knee-point strain was taken as the comparison parameter at this point, because the carbon plies had already failed (fragmented).

As observed from the experimental work and microscopy examination, the lack of stiffness loss and sudden final failure at high strains indicates that the high strength TC35 carbon/epoxy did not fragment under compression. However, further work is required to understand the mechanism behind the catastrophic failure of TC35/S-glass hybrid composites in compression. A possible explanation for the high compressive strain to failure compared with typical values for carbon/epoxy is due to (i) elimination of stress concentration by the use of the 4 point-bending set-up, (ii) the strain gradient and the high strain embedding glass layers which can suppress shear instability, delaying the failure process of the thin carbon plies [88].

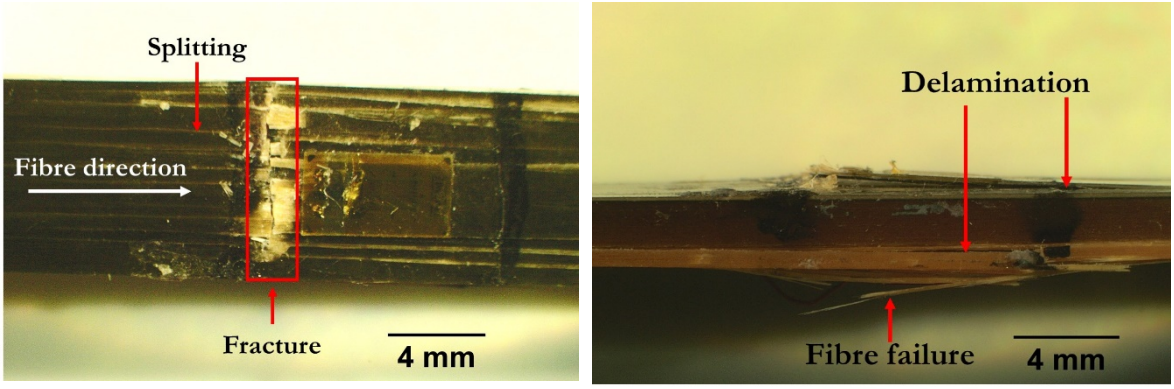

(a) (b)

Figure 5.43. Image of an asymmetric $TC35_2$/S-glass hybrid specimen failed in compression: (a) top view (b) edge view.

The compressive failure pattern shown in **Figure 5.74 (a)** for this hybrid configuration indicates a fracture perpendicular to the fibre direction (shown by the red box) which is a typical compressive failure in fibre composites. Examining the damage pattern from the side view, indicates fibre failure and delamination on both the compression and tension side as shown in **Figure 5.74 (b)**. Examining the average thickness of the delaminated part on the compression side which is around 0.21 mm, it is concluded that the top glass and the carbon layers has delaminated from the rest of the hybrid.The failed hybrid specimen shown in **Figure 5.74** is linked to the force-strain response in **Figure 5.73.**

5.3.3 Flexural response of symmetric TC35/S-glass hybrid configuration

The force-strain response under four-point bending for the $[SG/TC35_1/SG]_{4s}$ and $[SG/TC35_2/SG]_{4s}$ configurations is shown in **Figure 5.75**. It should be noted that the strain in **Figure 5.75** is calculated for the top level of the carbon layer on the compression side and the bottom level of the carbon layer on the tension side. For the TC35/S-glass and M55/S-glass hybrid configuration, the assumed strain distribution through the thickness is linear because there was no twisting, buckling or shear deformation of the specimen during the testing.

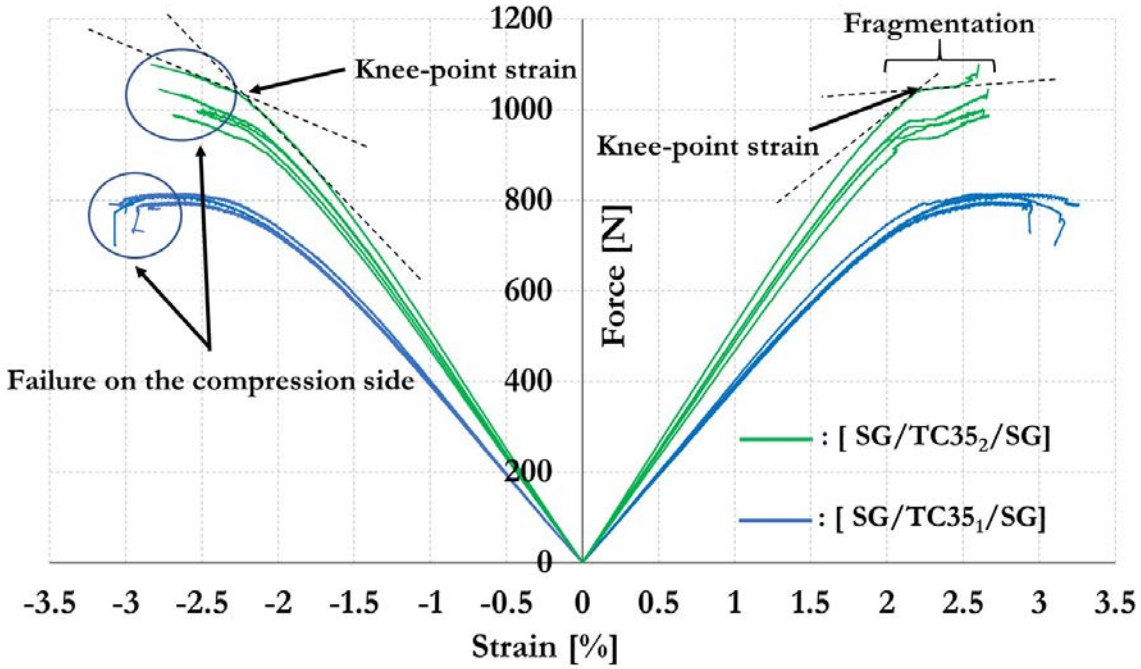

Figure 5.44. Force-strain curve for $[SG/TC35_1/SG]_{4s}$ and $[SG/TC35_2/SG]_{4s}$ configurations.

For both hybrid configurations shown in **Figure 5.75**, there is an initial linear elastic response which is followed by a non-linear response. There is an obvious change of slope for the $[SG/TC35_2/SG]_{4s}$ force-strain curve with a knee-point which marks the establishment of fragmentation in the carbon layers. The fragmentation from the tension side is responsible for the change of slope on the force-strain curve of this hybrid. Fragmentation was then followed by stably dispersed delamination between the glass and carbon plies resulting in a non-linear region as shown in **Figure 5.75** for the $[SG/TC35_2/SG]_{4s}$ configuration. The final failure for this hybrid configuration occurred on the compression side due to carbon fibre failure followed by delamination at an average compressive strain of -2.692%. For the $[SG/TC35_1/SG]_{4s}$ configuration, there is no obvious knee-point seen in **Figure 5.75**, only initial linear response followed by a gradual change of slope to a plateau at constant load and final failure at the compression side due to the same damage mechanism as that of the $[SG/TC35_2/SG]_{4s}$ configuration. The final failure for this configuration occured at an average compressive strain of -2.988%. Although there is no obvious knee-point shown in the force-strain curve for $[SG/TC35_1/SG]_{4s}$ configuration, fragmentation on the tensile side was observed for this hybrid after the test was terminated due to failure on the compression side. The images of the failed hybrid specimens under four-point bending taken from the compression and tension side are shown in **Figure 5.76** and **Figure 5.77** for the $[SG/TC35_1/SG]_{4s}$ and $[SG/TC35_2/SG]_{4s}$ respectively.

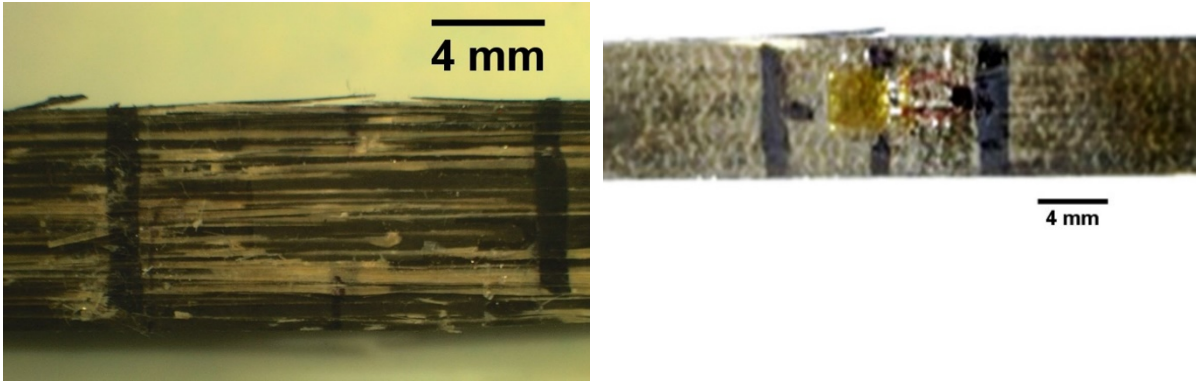

(a) (b)

Figure 5.45. Image of a typical failed $[SG/TC35_1/SG]_{4s}$ specimen showing (a) failure on the compression side and (b) failure on the tension side.

As shown in **Figure 5.76a**, the failure pattern on the compression side for $[SG/TC35_1/SG]_{4s}$ contained splitting along the fibre direction and delamination while dense fragmentation and dispersed delamination are observed on the tension side as shown in **Figure 5.76b.** The damage consists of ply splitting along the fibre direction distributed across the width and localized surface delamination typically found on fibre composites with a tough matrix under flexural loading [133], [29]. Ply splitting is likely to be involved in both the glass and carbon fibre failure under compressive loading. As observed from the experimental work, ply splitting coincides with the development of the plateau on the force-strain curve in **Figure 5.75** for the $[SG/TC35_1/SG]_{4s}$ configuration. This could also suggest that the gradual development of ply splitting is partially responsible for the occurence of the plateau. Another responsible damage mechanism leading to the development of the plateau is fragmentation of the carbon from the tension side. When multiple fractures of the ply occur as it fragments, the hybrid will lose the stiffness contribution from the carbon ply and thus the slope will change.

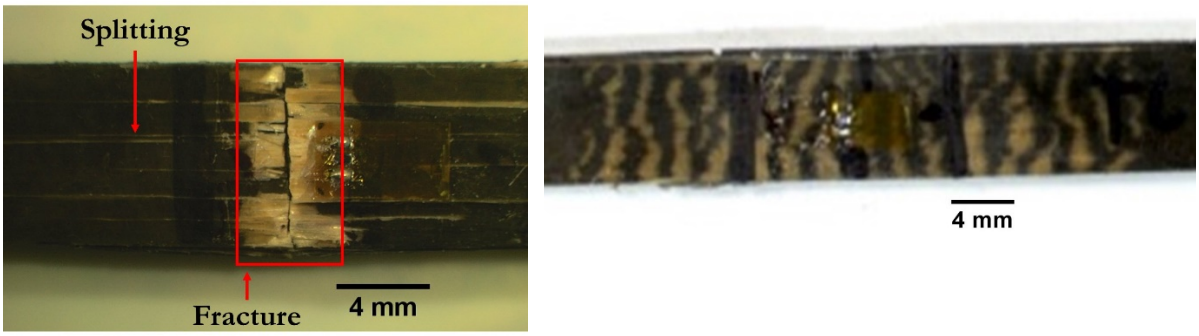

(a) (b)

Figure 5.46. Image of a typical failed $[SG/TC35_2/SG]_{4s}$ specimen showing (a) failure on the compression side and (b) failure on the tension side.

Figure 5.77(a) shows the compression failure pattern of the $[SG/TC35_2/SG]_{4s}$ configuration which includes fracture across the whole width (marked by the red rectangle) and ply splitting along the fibre direction. More extensive delamination areas, as shown in **Figure 5.77(b)**, were found on the tension side for this hybrid compared to the $[SG/TC35_1/SG]_{4s}$ configuration. The extensive delamination is due to the higher energy release of the $[SG/TC35_2/SG]_{4s}$ configuration.

Since non-linearity was observed for the $[SG/TC35_1/SG]_{4s}$ and $[SG/TC35_2/SG]_{4s}$ configurations under four-point bending, the force-displacement curve for both hybrids is shown in **Figure 5.78** for examination. For the $[SG/TC35_2/SG]_{4s}$ hybrid, there is a non-linear response before the knee-point and this behaviour is due to geometrical non-linearity of the hybrid specimens at large deflections. While for the $[SG/TC35_1/SG]_{4s}$ hybrid, there is a continuous change of slope without a pronounced knee-point until it reaches around 800 N after which a plateau developed. At a constant load of around 800 N, the displacement increases from around -18 mm to -25 mm as shown in **Figure 5.78** which indicates geometrical non-linearity at large deflections and fragmentation of the carbon ply from the tension side .

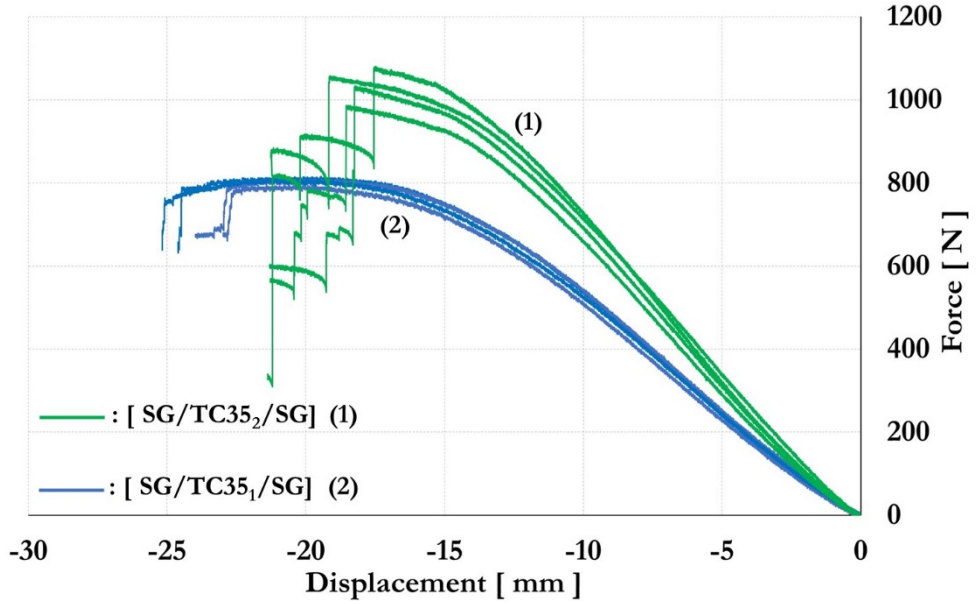

Figure 5.47. Force-displacement curve for $[SG/TC35_1/SG]_{4s}$ and $[SG/TC35_2/SG]_{4s}$ configurations.

Because different regions of the hybrid specimens through the thickness are being subjected to tension and compression, it would be interesting to study the damage sequence under four-point bending. This could be done by assessing the evolution of the neutral axis based on the strain gauge measurements during four-point bending. **Figure 5.79** shows the evolution of the neutral axis with increasing tensile strain for the $[SG/TC35_1/SG]_{4s}$ configuration. The neutral axis shift shown in **Figure 5.79** calculated from the surface strains is measured from the bottom tensile surface. This method to calculate the neutral axis shift is also applied to the other hybrid configuration.

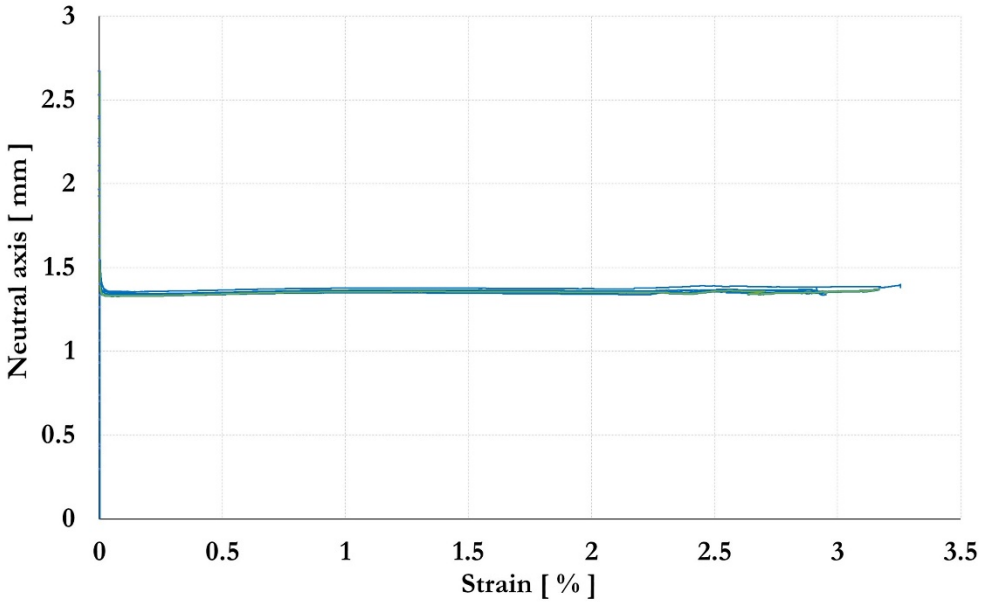

Figure 5.48. Neutral axis evolution with increasing tensile strain for $[SG/TC35_1/SG]_{4s}$ configuration.

As seen in **Figure 5.79**, there is no obvious shift of the neutral axis during the loading which made it difficult to determine the damage sequence. This could be attributed to the fact that the damage in the carbon layers, fragmentation and delamination, is not sufficient to cause a shift of the neutral axis. Typical damage pattern for the $[SG/TC35_1/SG]_{4s}$ hybrid from the edge of the specimen is seen in **Figure 5.213.**

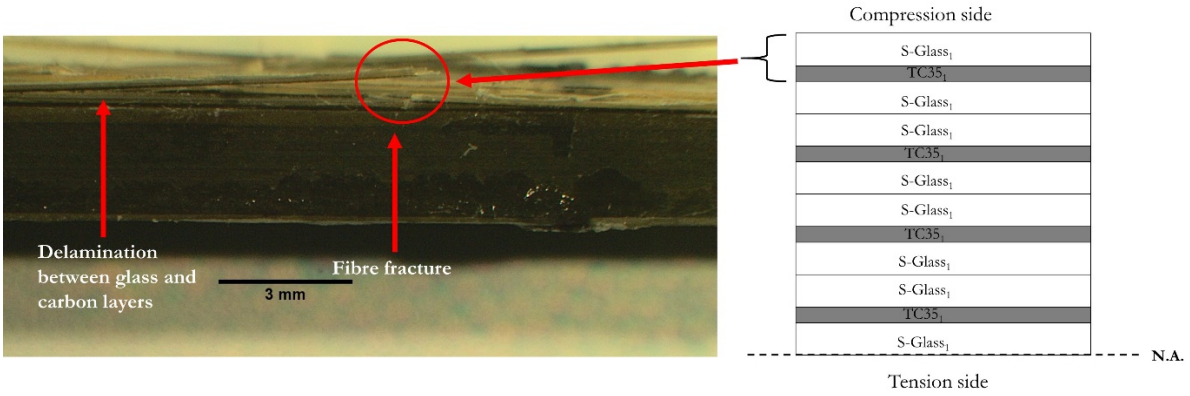

Figure 5.213. Typical damage for $[SG/TC35_1/SG]_{4s}$ hybrid shown from the edge of the specimen (both glass and carbon fibre fractured).

As seen from **Figure 5.16** there is glass and carbon fibre failure and delamination on the compression side. The fibre fracture itself is also responsible for the ply splitting experienced by this hybrid. The average thickness of the delaminated part is 0.185 mm which can be related to the total thickness of the top glass and the top carbon layers on the compression side.

To further study the damage sequence of the $[SG/TC35_1/SG]_{4s}$ configuration, an interrupted test of one specimen from this hybrid type was conducted at -20 mm displacement. The edge of this specimen was then observed under optical microscopy to see if there was any fragmentation on the tension side. Before being observed by optical microscopy, the edge was ground and polished.

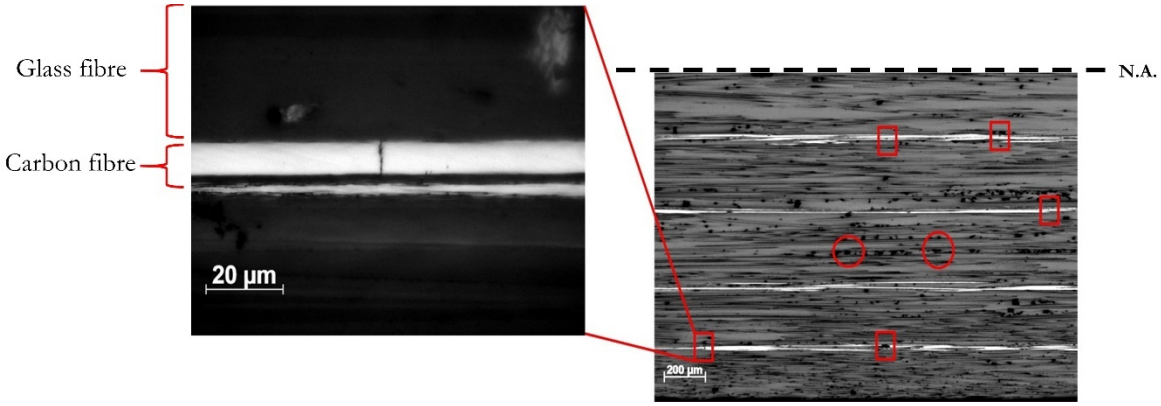

Figure 5.17. Optical image of $[SG/TC35_1/SG]_{4s}$ specimen taken from the tension side after being loaded until -20 mm.

Figure 5. shows the tension side of the hybrid specimen indicating carbon fibre failure/fragmentation (marked by the red rectangles) and an enlarged image of the carbon fibre failure which shows that the fracture runs perpendicular to the fibre direction. The dark areas around the glass plies (marked by the red circles) shown in **Figure 5.17** are left over contamination from the polishing machine. It is suggested from **Figure 5.17** that damage in the carbon layers initiated from the tension side but due to the relatively low carbon/epoxy volume ratio, the damage was not sufficient to cause a shift in the neutral axis.

From microscopy examination of this hybrid, no clear indication of carbon fibre kinking was found on the compression side for the $[SG/TC35_1/SG]_{4s}$ hybrid configuration.

Figure 5.80 shows the evolution of the neutral axis with increasing tensile strain for the $[SG/TC35_2/SG]_{4s}$ configuration. The neutral axis in **Figure 5.80** is measured from the bottom, tensile surface. It is shown in **Figure 5.80** that there is a slight upward shift of the neutral axis towards the compression side due to fragmentation of the carbon plies on the tension side. Examining the neutral axis shift in **Figure 5.80**, the tensile strain in which the shift occurred is at an average strain of 2.290%. This strain also corresponds to the average knee-point strain shown in **Figure 5.75.**

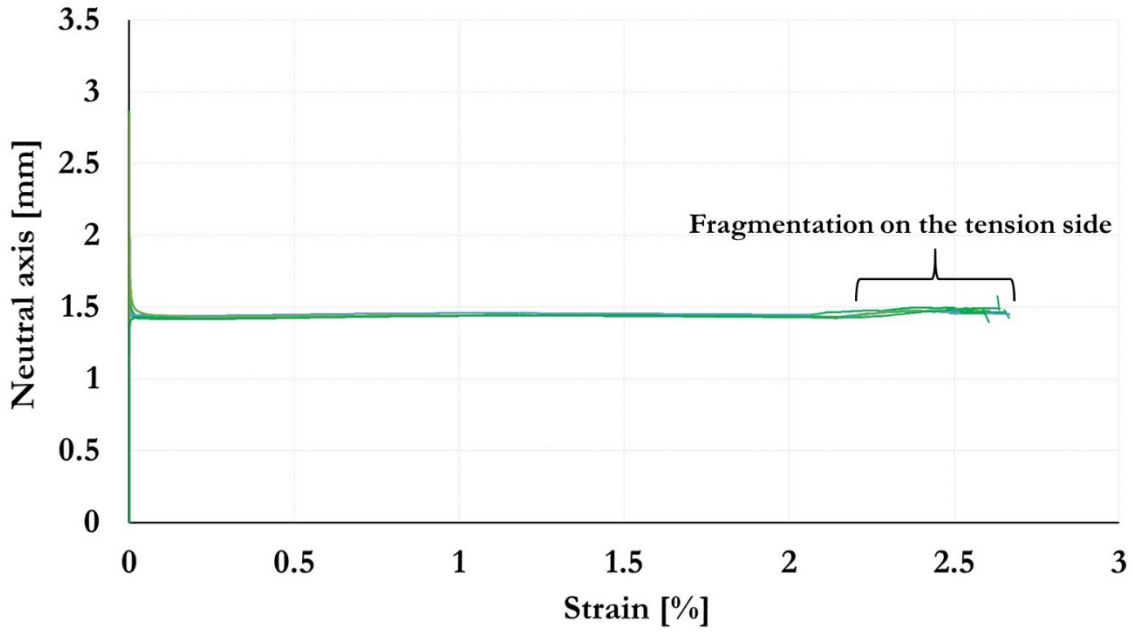

Figure 5.50. Neutral axis evolution with increasing tensile strain for $[SG/TC35_2/SG]_{4s}$ configuration.

As shown in **Figure 5.51,** There is a neutral axis shift towards the compression side due to fragmentation on the tension side. The shift of the neutral axis towards the compression side will likely reduce the strain increase on the compression side. This behaviour leads to a delay of the final failure on the compression side for the $[SG/TC35_2/SG]_{4s}$ hybrid. To study the damage pattern of this hybrid, a microscopy image taken from the edge of a failed $[SG/TC35_2/SG]_{4s}$ specimen is shown in **Figure 5.19.**

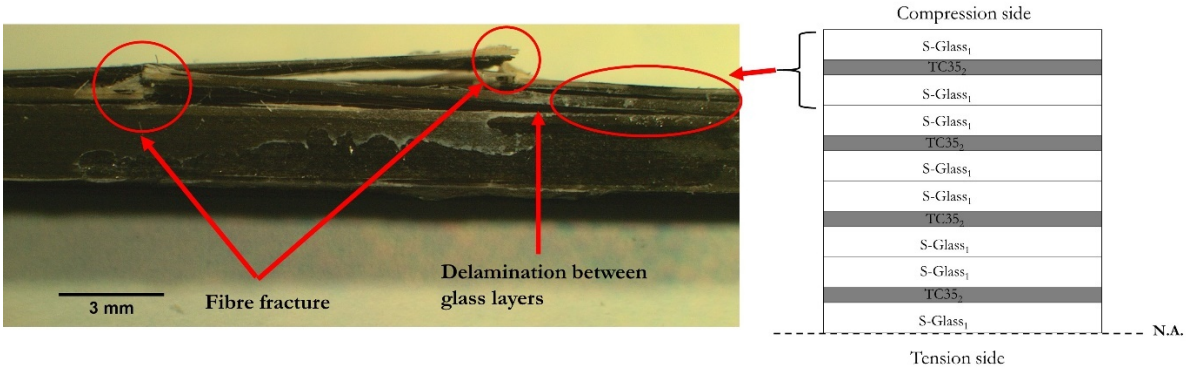

Figure 5.19. Typical damage for $[SG/TC35_2/SG]_{4s}$ hybrid shown from the edge of the specimen.

A typical damage shown in **Figure 5.19** is fibre fracture and delamination on the compression side. The ply splitting experienced by this hybrid also incorporates fibre fracture. The average thickness of the delaminated part is 0.368 mm which can be related to one hybrid sub-laminate on the compression side. The thickness of the delaminated part of this hybrid is thicker than the $[SG/TC35_1/SG]_{4s}$ because there are two carbon plies and the glass failed on both sides of the carbon plies. The failed glass plies could also indicate carbon failure on both sides due to compressive stress but more work is needed to verify this statement.

An interrupted test of one specimen from the $[SG/TC35_2/SG]_{4s}$ hybrid configuration was conducted under four-point bending at -18 mm (which has passed the knee-point) when the test was stopped. The edge of the specimen was examined by optical microscopy and the image is presented in **Figure 5.,** showing the failed/fragmented carbon fibres (marked by the red rectangles) on the tension side. Most of the fragmented carbon fibres shown in **Figure 5.** have a fracture running perpendicular to the fibre direction as found in the $[SG/TC35_1/SG]_{4s}$ hybrid.

From the microscopy examination on the compression side for this hybrid, no clear indication of carbon fibre kinking was found. Further work is needed to fully understand the carbon fibre failure on the compression side for both $[SG/TC35_1/SG]_{4s}$ and $[SG/TC35_2/SG]_{4s}$ hybrides.

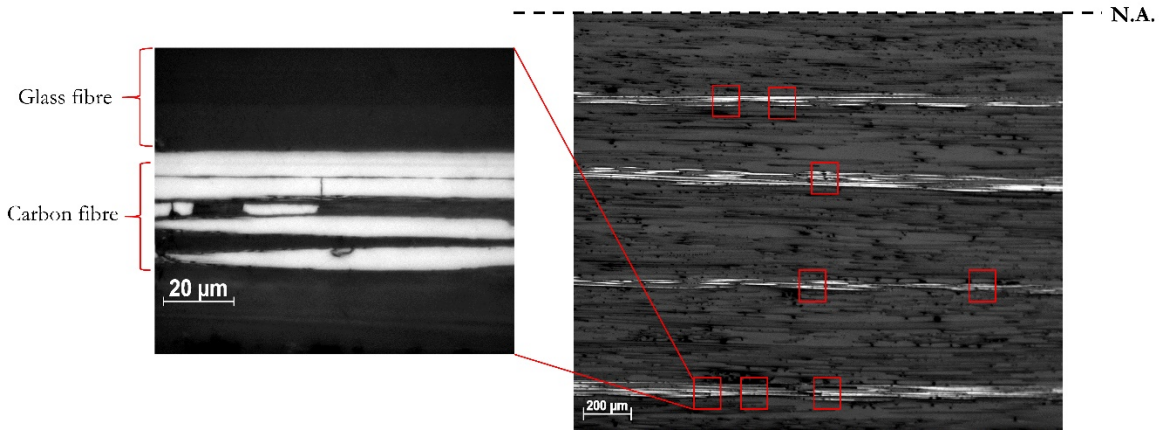

Figure 5.20. Optical image of $[SG/TC35_2/SG]_{4s}$ specimen taken from the tension side after being loaded until -18 mm.

It is worth mentioning that no fragmentation of the carbon plies on the compression side has been observed for the $[SG/TC35_1/SG]_{4s}$ or $[SG/TC35_2/SG]_{4s}$ configurations under four-point bending which could mean that the change of slope and shifting of the neutral axis is likely due to carbon ply fragmentation from the tension side. The comparison between the knee-point and failure strain of the symmetric TC35/S-glass hybrid composites obtained from tension, bending and indirect compression is shown in **Table 5.**. It should be noted that the knee-point strain was not observed from the indirect compression test of this hybrid configuration as shown in **Figure 5.73.** The knee-point and failure strain in tension is obtained from **Table 5.**. The calculated elastic thermal residual strains for the $[SG/TC35_1/SG]_{4s}$ and $[SG/TC35_2/SG]_{4s}$ configurations is -0.032% and -0.026% respectively which has been considered for the knee-point and failure strains shown in **Table 5.**.

Table 5.138. Comparison between bending, tensile, and indirect compression response of $[SG/TC35_1/SG4]_{4s}$ and $[SG/TC35_2/SG]_{4s}$ configurations (the number in the bracket indicates the coefficient of variation in %).

Designation	No. of specimens	Knee-point strain [%]			Failure strain [%]			
			Bending			Bending		IDC[a]
		Tension	Tension	Comp.	Tension	Tension	Comp.	
$[SG/TC35_1/SG]_{4s}$	5	2.340 (2.9)	-	-	3.411 (8.7)	3.060 (5.0)	-2.988 (3.2)	-
$[SG/TC35_2/SG]_{4s}$	5	1.950 (7.1)	2.290 (9.2)	-2.20 (8.8)	2.890 (11)	2.642 (8.7)	-2.692 (5.3)	-2.665[b]

[a] IDC = Indirect compression.
[b] failure strain result from one asymmetric hybrid specimen.

It should be noted that the knee-point and failure strains for the $[SG/TC35_1/SG]_{4s}$ and $[SG/TC35_2/SG]_{4s}$ configurations shown in **Table 5.8** are calculated for the top level of the carbon ply under compression and bottom level of the carbon ply under tension. As seen from **Table 5.**,

the knee-point strain in the tension and compression side for the $[SG/TC35_2/SG]_{4s}$ configuration is higher compared to the knee-point strain obtained from the static tensile testing. It is known that the higher strength in bending than in tension can be explained in terms of Weibull statistical strength theory [146]–[149]. It is assumed that the strength depends on critical defects which are statistically distributed. For the bending case, a much smaller volume of material is being subjected to the maximum stress than in a tension test. Due to this smaller volume, the chances of a critical defect are lower and thereby the strength is higher. The relationship between bending and tensile strength taking account of the different stressed volumes according to Weibull strength theory can be explored through **Equation** Error! Reference source not found. [147] :

$$\frac{S_b}{S_t} = \left(\frac{V_t}{V_b}\right)^{\frac{1}{m}} \tag{5.2}$$

Where S_b and S_t are the mean strengths of the two specimens which can be expressed in either stress or strain to failure, V_t and V_b are the volumes and m is the Weibull modulus, which is a measure of the variability in the material. The Weibull modulus (m) considered in this work is the modulus obtained for TR30/S-glass hybrid which is 25.3 [150]. Although the Weibull modulus used in **Equation** Error! Reference source not found.**.** is from another hybrid system, for a qualitative explanation of the size effect in the TC35/S-glass and M55/S-glass hybrid, it is sufficient to use this number. To examine the size effect in the hybrid specimens under bending, the knee-point strain results from the tension and bending tests shown in **Table 5.** are compared with the strain ratio calculated from **Equation** Error! Reference source not found.**.** It should be noted that the work in this chapter is not intended to quantify the exact strain ratio in bending for the hybrid systems. The volumes for the tensile and bending specimens for the $[SG/TC35_2/SG]_{4s}$ are calculated as follow. It should be noted that only the thickness of the carbon plies is taken into account because the Weibull modulus is applicable for brittle failure and each fragmentation established at the knee-point is a brittle failure.

For the tensile specimen, only the thickness of the two central carbon plies (t) is taken into account:

t (mm)	w (mm)	Lg (mm)	$V_t = t \times w \times L_g$ (mm^3)
0.06	20	130	156

For the bending specimen, only the thickness of the two carbon plies (t) on the tension side is taken into account, assuming constant stress in the ply:

t (mm)	w (mm)	Lg (mm)	$V_b = t \times w \times L_g$ (mm^3)
0.06	8	30	14.4

Having knowledge of the [SG/TC35$_2$/SG] specimen's geometry for tension and bending, the knee-point strain ratio obtained from the experimental is compared with the theoretical ratio calculated by using **Equation** Error! Reference source not found. and shown in **Table 5.**. The experimental knee-point ratio is the ratio between the knee-point strain on the tension side of the bending specimen and knee-point strain obtained from tensile testing.

Table 5.9 Comparison between knee-point strain ratio for [SG/TC35$_2$/SG] configuration.

Designation	V_t (mm)	V_b (mm)	m	Knee-point ratio (experimental)	Knee-point ratio (theoretical)
[SG/TC35$_2$/SG]$_{4s}$	156	14.4	25.3	1.17	1.10

The knee-point ratio in **Table 5.** implies that the higher knee-point strain in bending could be partly attributed to the size effect present in the hybrid specimen. It is also well known that a "hybrid effect" is present for the hybrid specimen under tensile loading where growth of a broken carbon cluster is restrained but the importance of this "hybrid effect" in bending is not understood yet. Further work is required to study the contribution of the "hybrid effect" in bending for the UD thin-ply hybrid composites.

5.3.4 Flexural response of symmetric M55/S-glass hybrid configuration

For the [SG/M55$_1$/SG]$_{4s}$ and [SG/M55$_2$/SG]$_{4s}$ configurations, the force-strain response under four-point bending is shown in **Figure 5.81**. It should be noted that the strain in **Figure 5.81** is calculated for the top level of the carbon layer on the compression side and the bottom level of the carbon layer on the tension side.

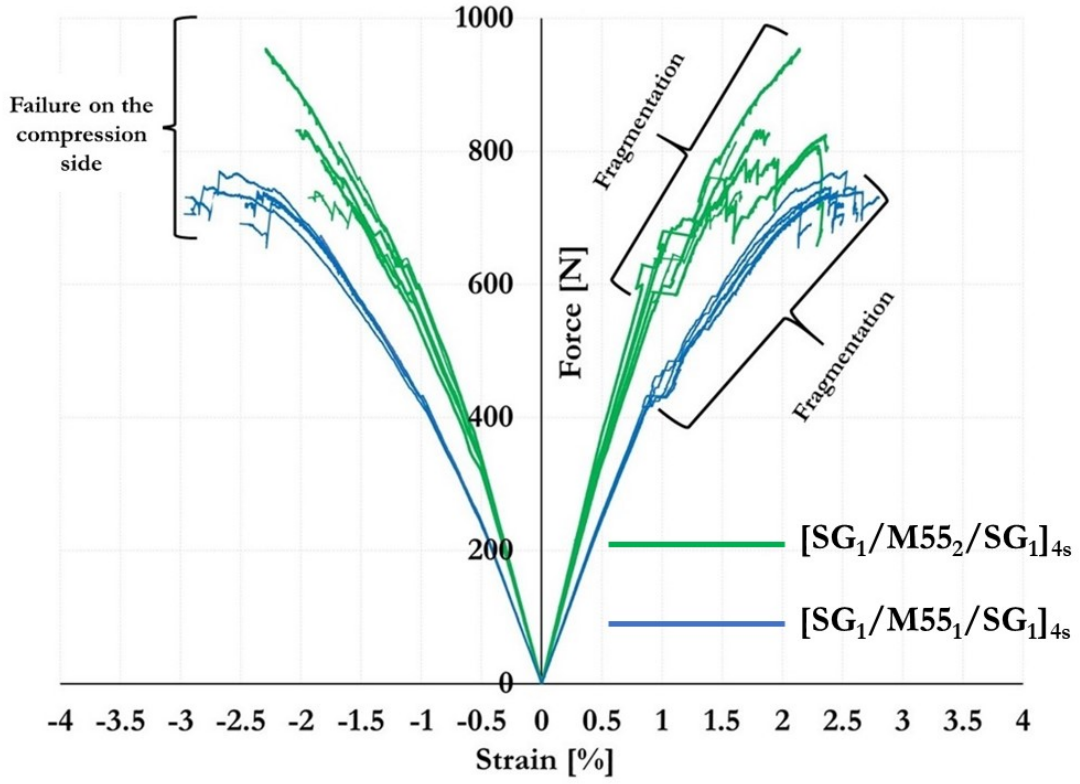

Figure 5.52. Force-strain curves for [SG/M55$_1$/SG]$_{4s}$ and [SG/M55$_2$/SG]$_{4s}$ configurations.

For both hybrid configurations shown in **Figure 5.81**, there is an initial linear elastic response which is followed by a non-linear response. There is an initial change of slope at an average strain of -0.540% and -0.529% for $[SG/M55_1/SG]_{4s}$ and $[SG/M55_2/SG]_{4s}$ respectively, which is attributed to fragmentation of the carbon plies on the compression side. Fragmentation of carbon plies in compression has also been reported by Czel et al. [88] and in **Chapter 4** in this thesis in an asymmetric $M55_2$/S-glass hybrid configuration tested under four-point bending with the carbon plies on the compression side. From his work, it was observed that the fragmentation of carbon plies in compression occurred at -0.513% strain. Fragmentation of carbon plies under direct compression of $[SG_1/(C_n/SG_1)_{17}]$, where n is the number of carbon plies, has also been presented in **Chapter 4**. It was discovered that under direct compression, fragmentation of carbon plies for n = 1 and n = 2 carbon plies occurred at -0.555% and -0.554% strain respectively. All those mentioned fragmentation strain values have been corrected for residual thermal elastic strain. Comparing the similar values of fragmentation strain from Czel et al. [88] and Suwarta et al. [151] and from Chapter 4 in this work, it can be concluded that those values represent the compressive strain at failure for M55 carbon fibre/epoxy.

From **Figure 5.81**, it is seen that for the $[SG/M55_1/SG]_{4s}$ configuration, a second knee-point on the tensile side occurred at an average strain of 0.940%. While for the $[SG/M55_2/SG]_{4s}$ configuration, a second knee-point on the tension side occurred at an average strain of 0.922%. Both of those second knee-points are attributed to the fragmentation of the carbon plies on the tension side. The method to determine the first and second knee-point strain is shown in **Figure 5.22.**

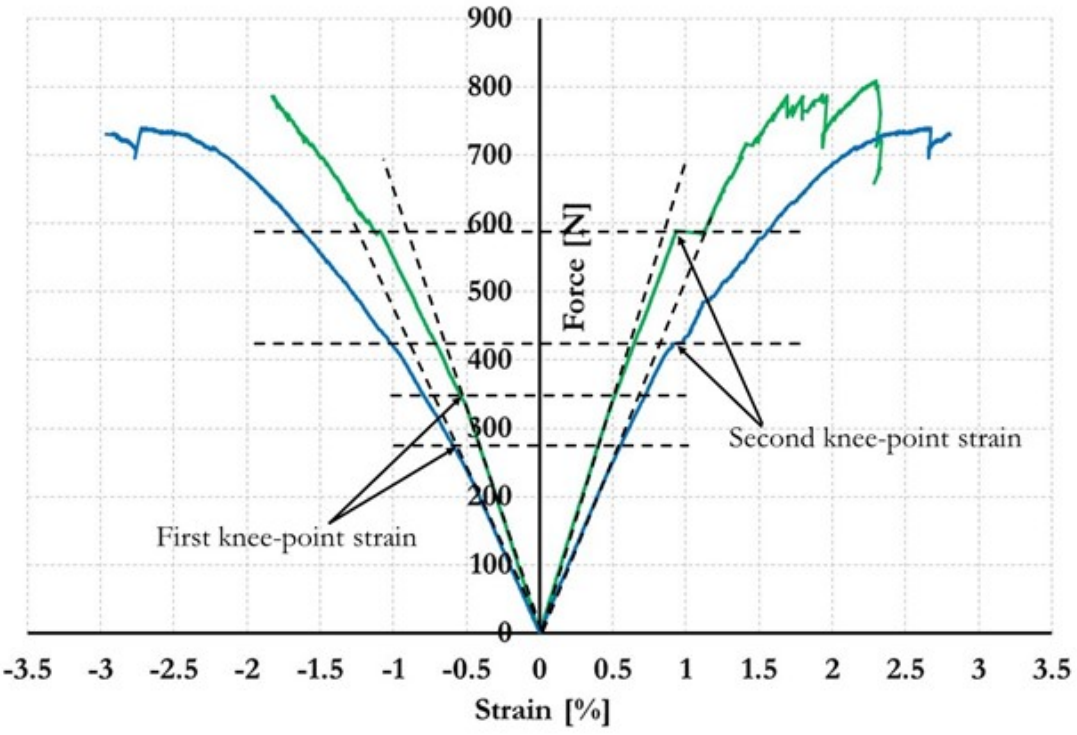

Figure 5.22. Method to determine the first and second knee-point strain for $[SG/M55_1/M55]_{4s}$ and $[SG/M55_2/SG]_{4s}$.

As seen from **Figure 5.81**, there are repeated load drops after the second knee-point for both hybrid configurations. For the $[SG/M55_2/SG]_{4s}$ configuration, the load drops are more pronounced compared to the $[SG/M55_1/SG]_{4s}$ configuration, and this behaviour is similar to the $[SG/M55_2/SG]$ hybrid tested in static tensile loading shown in **Figure 5.70**. Those load drops are associated with repeated fragmentation and dispersed delamination in the hybrid composite. The images of the failed hybrid specimens under four-point bending are shown in **Figure 5.82** and **Figure 5.83** for $[SG/M55_1/SG]_{4s}$ and $[SG/M55_2/SG]_{4s}$ respectively.

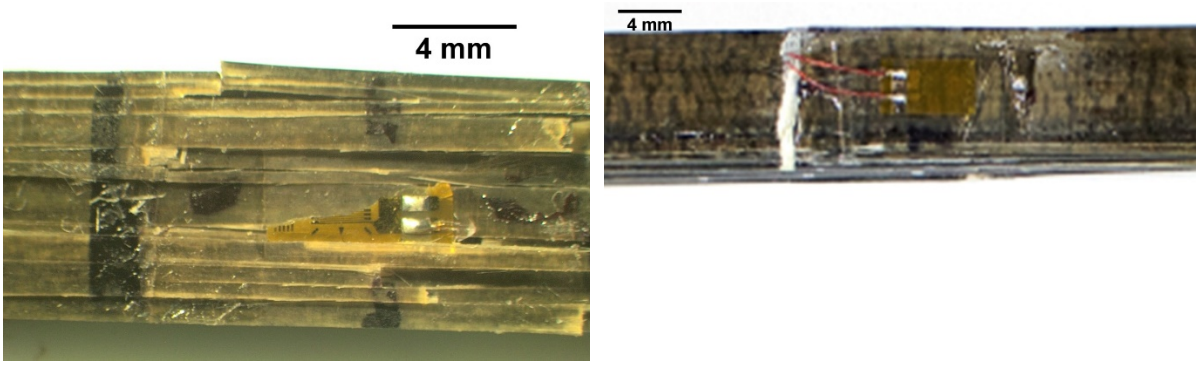

(a) **(b)**

Figure 5.53. Image of the failed $[SG/M55_1/SG]_{4s}$ specimen showing (a) failure on the compression side and (b) failure on the tension side.

The failed $[SG/M55_1/SG]_{4s}$ hybrid specimen in **Figure 5.82(a)** shows the compression failure pattern which contained ply splitting along the fibre direction. The ply splitting also incorporates fractured fibres. As also seen in **Figure 5.82(a)** , there are fractured fibres distributed randomly across the width, while the fragmentation and dispersed delamination on the tensile side are shown in **Figure 5.82(b)** for the same hybrid specimen. The fragmentation on the tensile side was responsible for the repeated load drops for the $[SG/M55_1/SG]_{4s}$ configuration as shown in the force-strain curve in **Figure 5.81.**

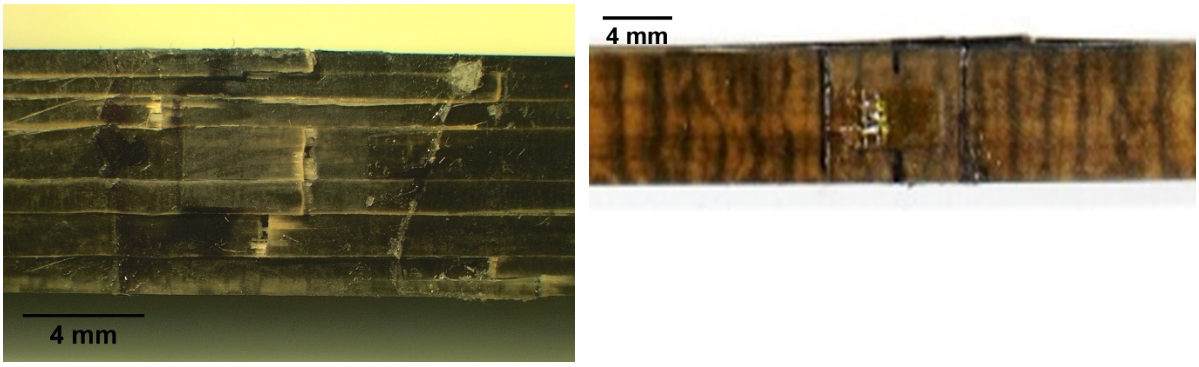

(a) **(b)**

Figure 5.54. Image of the failed $[SG/M55_2/SG]_{4s}$ specimens showing (a) failure on the compression side and (b) failure on the tension side.

In contrast with the $[SG/M55_1/SG]_{4s}$ configuration, the tensile failure pattern for the $[SG/M55_2/SG]_{4s}$ configuration shows extensive delamination in **Figure 5.83(b).** This is due the higher mode II energy release rate for the hybrid with thicker M55 carbon layers. There is also ply

splitting due to broken fibres distributed randomly across the width as also found in the $[SG/M55_1/SG]_{4s}$ hybrid.

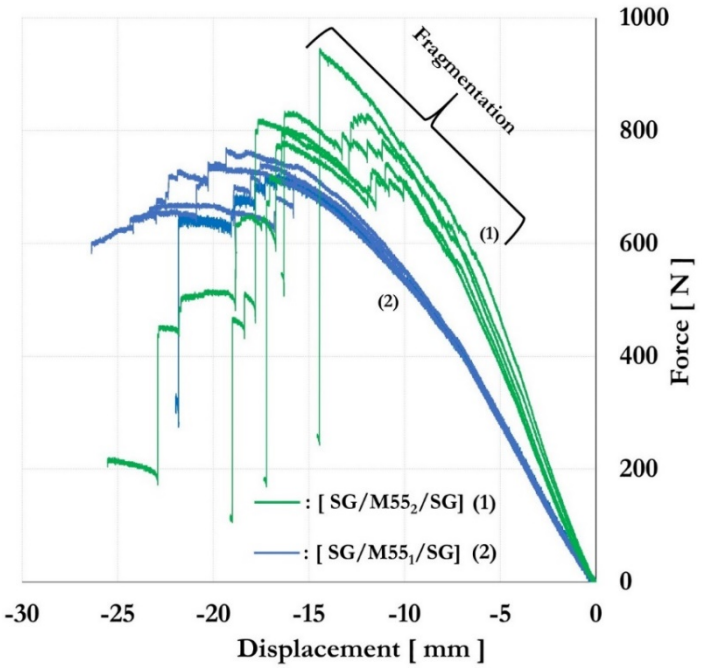

Figure 5.55. Force-displacement curve for $[SG/M55_1/SG]_{4s}$ and $[SG/M55_2/SG]_{4s}$ configurations.

The force-displacement curves shown in **Figure 5.84** for both hybrid configurations indicated that before the specimens reached large deflections, there was a change in the slope due to fragmentation on the compression and tension sides. The evolution of the neutral axis during four-point bending for the $[SG/M55_1/SG]_{4s}$ and $[SG/M55_2/SG]_{4s}$ configurations is shown in **Figure 5.85** and **Figure 5.86** respectively to help explain the damage sequence.

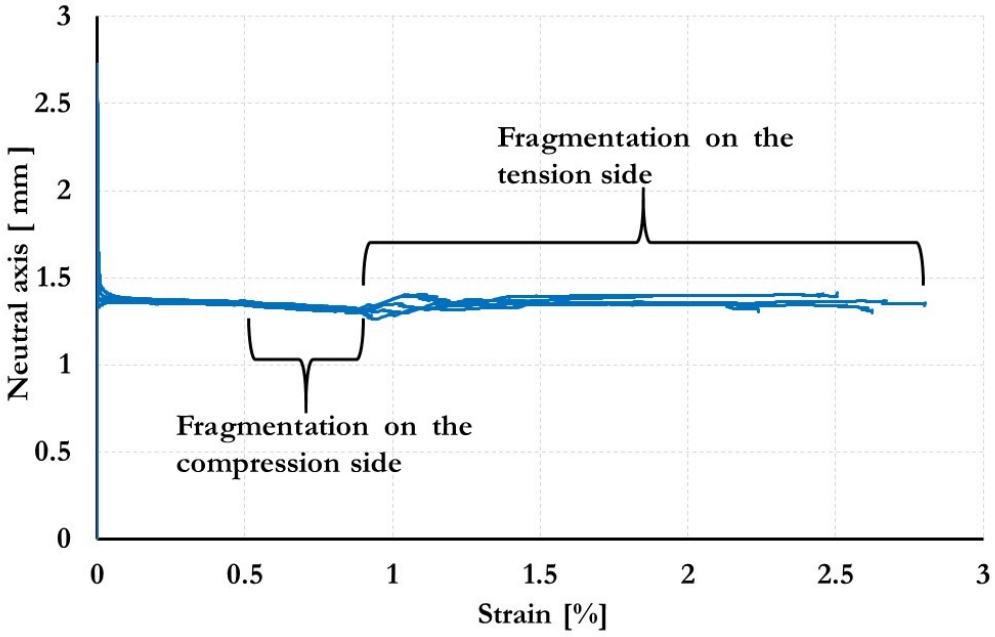

Figure 5.56. Neutral axis evolution with increasing tensile strain for $[SG/M55_1/SG]_{4s}$ configuration.

As seen in **Figure 5.85**, there is a neutral axis shift towards the tension side when the carbon plies fragmented on the compression side. The shift occurred at around -0.540% which corresponds to the average first knee-point strain for the $[SG/M55_1/SG]_{4s}$ configuration. The

neutral axis continues to shift towards the tension side with further fragmentation on the compression side. After reaching an average strain value of 0.940% on the tension side, fragmentation on the tension side occurred causing a shift of the neutral axis back towards the compression side as shown in **Figure 5.85.** With further loading, there is no further shift of the neutral axis until final failure on the compression side was reached. The overall gradual failure for this hybrid is partly due to fragmentation of the carbon ply on the compression side. Shifting of the neutral axis due to fragmentation on the tension side is likely to slow down the strain decrease on the compression side. This will result in a delay of the final failure on the compression side.

To study the damage pattern of this hybrid, a microscopy image taken from the edge of a failed $[SG/M55_1/SG]_{4s}$ specimen is shown in **Figure 5.27.** There is carbon and glass fibre fracture with delamination on the compression side. The fibre fracture itself is also responsible for the ply splitting experienced by this hybrid. The average thickness of the delaminated part is 0.186 mm which can be related to the total thickness of the top glass and top carbon layer on the compression side.

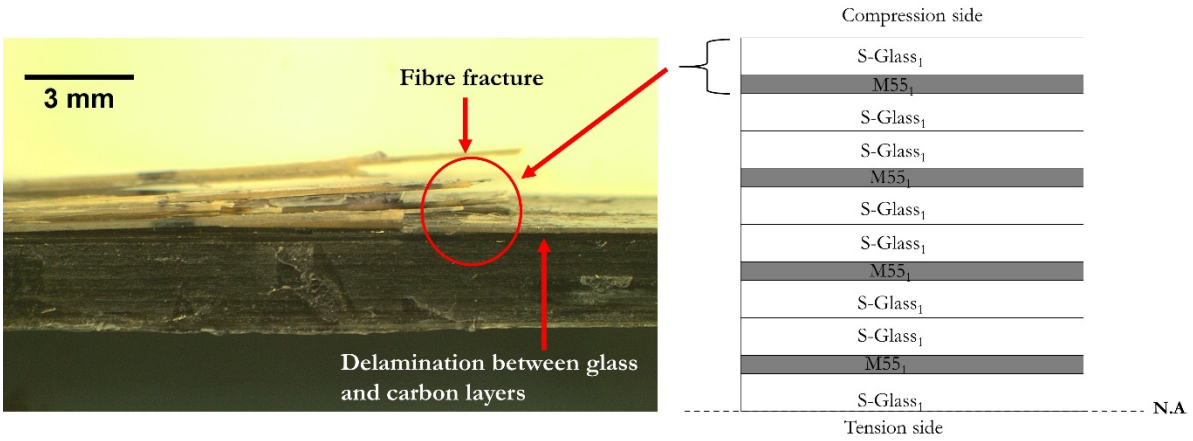

Figure 5.27. Typical damage for $[SG/M55_1/SG]_{4s}$ hybrid shown from the edge of the specimen.

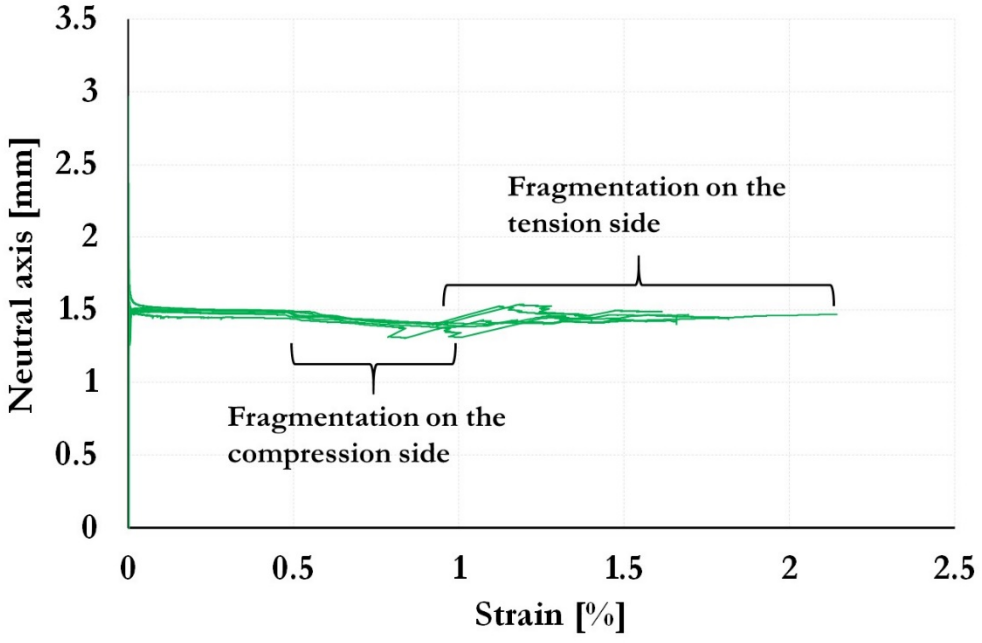

Figure 5.57. Neutral axis evolution with increasing tensile strain for $[SG/M55_2/SG]_{4s}$ configuration.

The neutral axis evolution of the $[SG/M55_2/SG]_{4s}$ configuration is shown in **Figure 5.86**. The initial neutral axis shift for $[SG/M55_2/SG]_{4s}$ also occurred when the carbon plies fragmented on the compression side at an average strain of -0.529% which again corresponds to the first knee-point strain shown in **Figure 5.81**. With further fragmentation from the compression side, the neutral axis continues to shift towards the tension side. When the average tensile strain of this hybrid configuration reaches 0.922%, fragmentation of the carbon plies on the tension side occurred, causing the neutral axis to shift back towards the compression side. This behaviour will result in delay of the final failure on the compression side for the $[SG/M55_2/SG]_{4s}$ hybrid. As seen in **Figure 5.81**, it seems that there is a greater shift of the neutral axis during fragmentation of the carbon plies on the tension side than in the $[SG/M55_1/SG]_{4s}$ hybrid. This is likely because there is more damage, fragmentation and delamination, on the $[SG/M55_2/SG]_{4s}$ hybrid due to the greater number of carbon plies which act as damage sites. This behaviour continues until failure on the compression side occurred. Typical damage for the $[SG/M55_2/SG]_{4s}$ hybrid from the edge of the specimen is shown in **Figure 5.58.** There are delaminations on the compression and tension side for this hybrid configuration. The average delamination thickness on the compression side is 0.372 mm which is related to the first hybrid sub-laminate on the compression side, $[SG/M55_2/SG]$. While, on the tension side, the average delamination thickness is 0.215 mm. Delamination on the tension side for this hybrid is due to the high energy release rate when incorporating thicker central carbon layers. The delaminated thickness is higher on the compression side compared to the tension side because the compressive failure fractured the glass ply on both side of the carbon as well**.**

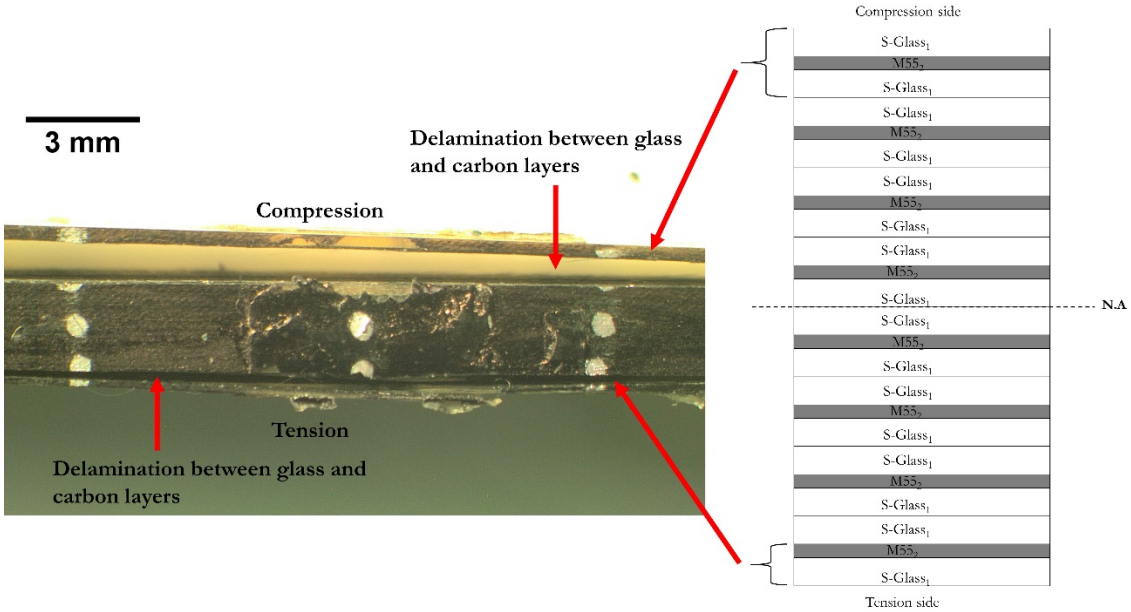

Figure 5.59. Typical damage for $[SG/M55_2/SG]_{4s}$ hybrid shown from the edge of the specimen.

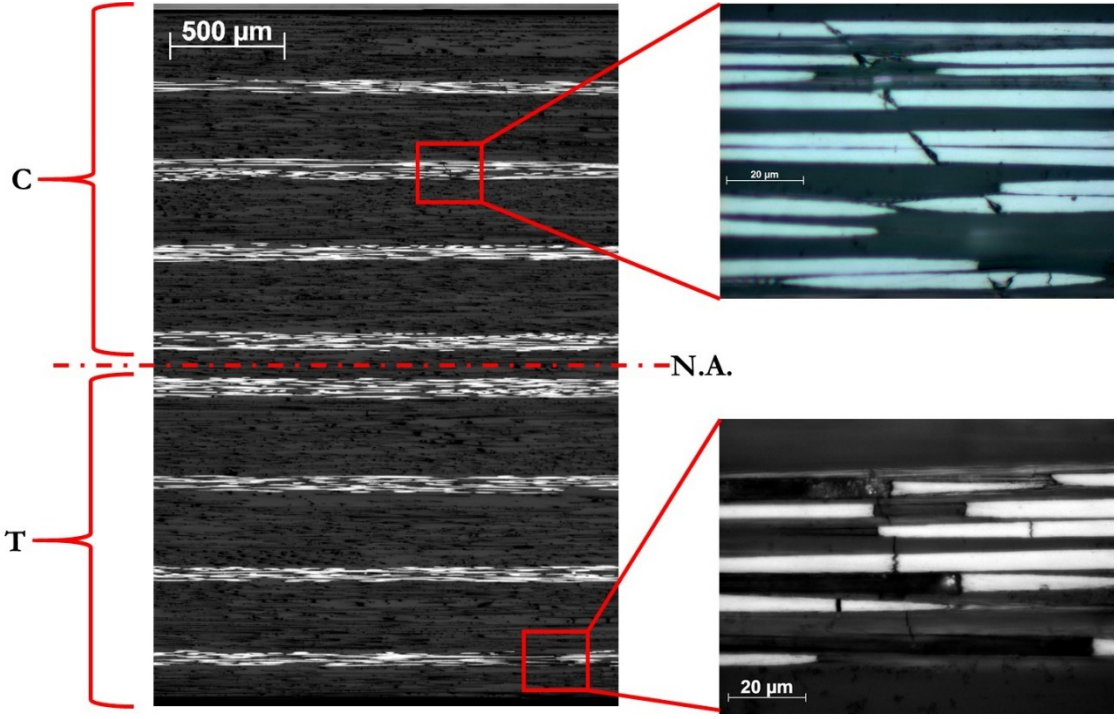

Figure 5.30. Optical image of $[SG/M55_2/SG]_{4s}$ specimen after being loaded until -14 mm.

Error! Reference source not found. shows an optical image taken from the edge of a $[SG/M55_2/SG]_{4s}$ specimen after it was loaded under four-point bending until -14 mm. By looking at the force-displacement curve in **Figure 5.84** for $[SG/M55_2/SG]_{4s}$, this displacement was chosen because fragmentation on the tensile and compression side has already occurred. From this point of view, it would be interesting to study the different damage morphology of the M55 carbon fibre due to tensile and compressive loading respectively. It should be noted that the N.A. notation in Error! Reference source not found.**30** is the neutral axis which passes through the glass/epoxy plies, while C and T notation refers to compression and tension regions respectively. The different fracture patterns of the carbon fibre on the compression and tension regions are shown in the enlarged images in Error! Reference source not found.**30.** On the compression side, the carbon fibre fractured at an angle while the carbon fibres on the tensile side are fractured perpendicular to the fibre direction. Examining the fracture on the tension side, it is seen that the fractures on the carbon fibre are randomly distributed which shows the strength distribution of carbon fibres . With further loading, the carbon layers which failed at an angle on the compression side could cause delamination between the glass and carbon plies. This mechanism is also explained in **Chapter 4** which discusses the direct compression response of unidirectional thin-ply hybrid composites made of M55/epoxy and S-glass/epoxy plies.

The comparison between the knee-point and failure strains of the symmetric M55/S-glass hybrid composites obtained from tension, bending and direct compression is shown in **Table 5..** The knee-point and failure strains in tension are obtained from **Table 5..** The calculated thermal residual strains for the $[SG/M55_1/SG]_{4s}$ and $[SG/M55_2/SG]_{4s}$ configurations are -0.022% and -0.013% respectively which have been considered for the knee-point and failure strain shown in **Table 5..** It should be noted that the direct compressions strain values are obtained from **Chapter 4.** It is worth mentioning that five specimens for each $[SG/M55_1/SG4]_{4s}$ and $[SG/M55_2/SG]_{4s}$

configurations were tested in four-point bending. The notation DC in **Table 5.** refers to the direct compression testing of $[SG_1/(C_n/SG_1)_{17}]$ where n is the number of carbon plies which is either 1 or 2.

Table 5.1410. Comparison between bending, tensile, and direct compression response of $[SG/M55_1/SG_4]_{4s}$ and $[SG/M55_2/SG]_{4s}$ configurations (the numbers in the brackets indicate the coefficients of variation in [%]).

Designation	First knee-point [%]			Second knee-point [%]			Failure strain [%]		
		Bending			Bending		Bending		
	DC	Tension	Comp.	Tension	Tension	Comp.	Tension	Comp.	DC
$[SG/M55_1/SG]_{4s}$	-0.555	0.520	-0.540	0.840	0.940	-0.982	2.620	-2.780	-2.15
	(3.5)	(3.3)	(1.4)	(1.3)	(1.9)	(2.3)	(8.5)	(9.7)	(8.1)
$[SG/M55_2/SG]_{4s}$	-0.554	0.512	-0.529	0.800	0.922	-0.960	2.030	-1.850	-1.44
	(3.4)	(1.9)	(3.8)	(2.1)	(6.5)	(6.7)	(7.6)	(14)	(8.7)

As seen in **Table 5.10**, the values for the first knee point between the results obtained from direct compression and bending testing for both configurations are similar, from which again it can be concluded that this value is the failure strain of M55 carbon fibre under compression. The second knee point in **Table 5.** refers to the fragmentation of carbon plies on the tension side of the bending specimen. Comparing these values with the ones obtained from static tension testing, the strain at which fragmentation occurred on the tension side during four-point bending is higher compared to the fragmentation strain in tension. To examine the size effect in the hybrid configuration shown in **Table 5.**, the theoretical second knee-point ratios on the tension side are calculated by using **Equation** Error! Reference source not found.**.** The volumes for the tensile and bending specimens for the $[SG/M55_1/SG]_{4s}$ and $[SG/M55_1/SG]_{4s}$ are calculated as follow:

For $[SG/M55_1/SG]_{4s}$ tensile specimen:

T (mm)	w (mm)	Lg (mm)	$V_t = t \times w \times L_g$ (mm^3)
0.03	20	130	78

For $[SG/M55_1/SG]_{4s}$ bending specimen:

T (mm)	w (mm)	Lg (mm)	$V_b = t \times w \times L_g$ (mm^3)
0.03	8	30	7.2

For $[SG/M55_2/SG]_{4s}$ tensile specimen:

T (mm)	w (mm)	Lg (mm)	$V_t = t \times w \times L_g$ (mm^3)
0.06	20	130	156

For $[SG/M55_2/SG]_{4s}$ bending specimen:

T (mm)	w (mm)	Lg (mm)	$V_b = t \times w \times L_g$ (mm^3)
0.06	8	30	14.4

The comparison between the experimental second knee-point ratio on the tension side with the theoretical calculated from **Equation** Error! Reference source not found. is shown in **Table 5.**.

Table 5.1511. Comparison between knee-point strain ratio for $[SG/M55_1/SG]$ and $[SG/M55_2/SG]$.

Designation	Knee-point ratio (experimental)	Knee-point ratio (theoretical)
$[SG/M55_2/SG]_{4s}$	1.11	1.10
$[SG/M55_1/SG]_{4s}$	1.15	1.10

The knee-point ratio shown in **Table 5.** indicates that the second knee-point strain in bending is higher compared to the tension knee-point strain as also found in **Section 5.3.3** for the $[SG/TC35_2/SG]$ configuration and could be due to the size effect present in the hybrid specimen. The final failure strain on the compression side for the bending specimen is higher compared to the failure strain obtained from direct compression. This could be attributed to the shifting of the neutral axis towards the compression side due to fragmentation of the carbon ply on the tension side.

5.4 Conclusions

This chapter has presented the mechanical properties of unidirectional thin-ply hybrid composites subjected to four-point bending and tension. The effect of different hybrid configurations was examined. The following was concluded:

1. Gradual failure has been obtained for $[SG/M55_1/SG]_{4s}$, $[SG/M55_2/SG]_{4s}$, $[SG/TC35_1/SG]_{4s}$, $[SG/TC35_2/SG]_{4s}$ under four-point bending.

2. The sequence of damage mechanisms for the $[SG/TC35_1/SG]_{4s}$ and $[SG/TC35_2/SG]_{4s}$ hybrid configurations was carbon ply fragmentation and stable delamination on the tension side and the final failure was sudden compressive failure due to fibre failure followed by delamination.

3. For the $[SG/M55_1/SG]_{4s}$ and $[SG/M55_2/SG]_{4s}$ hybrid configurations, the damage started from the compression side in the form of carbon ply fragmentation and stable delamination followed by fragmentation and stable delamination on the tension side. The final failure observed for this hybrid configurations occurred on the compression side due to delamination between the glass and carbon layers propagating from the fragmentations.

4. The evolution of the neutral axis could be used to assess the damage sequence of hybrid composites during four-point bending.

5. The shift of the neutral axis towards the compression side will likely reduce the strain increase on the compression side. This behaviour leads to a delay of the final failure on the compression side for the hybrid configurations.

6. A high fragmentation strain on the tension side of the bending specimens was obtained for $[SG/TC35_2/SG]_{4s}$ and $[SG/M55_1/SG]_{4s}$, $[SG/M55_2/SG]_{4s}$. This value is higher than the fragmentation strain to failure obtained from the static tensile testing. This behaviour could be attributed to a size effect present in the bending specimens. Further work is required to study the contribution of the "hybrid effect" in bending for the UD thin-ply hybrid composites.

Chapter 6 Fatigue Response of Unidirectional Thin-Ply Hybrid Composites

6.1 Introduction

Pseudo-ductility was observed in static tensile response of unidirectional (UD) thin-ply interlayer hybrids made from thin-ply carbon/epoxy plies sandwiched between standard thickness glass/epoxy plies, due to the fragmentation of the carbon plies and dispersed delamination between the carbon/glass interfaces as shown in **Chapter 3** and **Chapter 5** of this thesis.

Structural components made of hybrid fibre composites are often subjected to cyclic loading and understanding their long-term behaviour is important as this could help to predict their lifetime and schedule future maintenance. Several authors, [94], [97], [152], have reported experimental results for the fatigue behaviour of UD hybrid composites made of a combination of high strain and low strain fibres. They were fatigued between 40% and 90% of their respective ultimate tensile strength. The UD hybrid composites in their experiments, [94], [97], [152], showed an improvement regarding the number of life cycles compared to the parent constituent material. They attributed this behaviour to the higher strain fibres which prevented further rapid crack extension from the first failed lower strain fibres. This led to slower fatigue damage propagation and enhanced the number of cycles to failure.

A separate work to study the tensile fatigue behaviour of thin-ply quasi-isotropic (QI) carbon laminates by Sihn et al. [153] reported superior mechanical properties (higher residual tensile strength) compared to the quasi-isotropic thick ply laminates up to 50000 cycles at 60% of the ultimate tensile strength of the QI thin specimens. The reason behind this is the absence of microcracks and delamination for the thin-ply specimens due to the low energy release rate.

A power-law relation between delamination growth and energy release rate was discovered by O'Brien [154] for a QI carbon composite when it was tension fatigued. At the three-fatigue loading levels, 86%, 93% and 100% of the maximum failure strain, the delamination grew from the edge of the specimen towards the centre. A linear relation between the stiffness loss and delamination growth was also observed and based on this, measurement of stiffness was also proposed to determine the extent of damage during fatigue loading.

This chapter differs from other work on the fatigue of hybrid composites e.g. [94], [97], [152], as fragmentation of the stiffer constituents never occurred on their specimens during fatigue loading. This chapter is also the first detailed characterisation of the fatigue behaviour of UD thin-ply carbon/glass hybrid composites. Two scenarios are investigated: (1) before any damage is introduced (pristine hybrids) and (2) after the introduction of damage (overloaded hybrids). Based on this study, a safe fatigue load level for UD thin-ply carbon/glass hybrid composites together with damage evolution characterisation and the relation between energy release rate and damage growth is presented.

6.2 Experimental methods

6.2.1 Materials

The hybrid composite constituent materials considered for the design and used in the experimental part of the study were a) standard thickness unidirectional (UD) prepreg made of S-glass reinforced epoxy supplied by Hexcel and b) thin ply UD prepreg made from carbon reinforced epoxy commercially available from SK Chemicals under the trade name of SkyFlex USN020A. The epoxy resin systems in the prepregs were the aerospace grade 913 (Hexcel) and K50 (SK Chemicals). Material data of the applied fibres and prepreg systems used in this chapter is described in **Chapter 5**, **Subsection 5.2.1.** The measured thickness for the hybrid configuration

in this chapter is similar to the measured thickness of [SG/TC35$_2$/SG] hybrid mentioned in **Table 5.4** in **Chapter 5.**

6.3 Test procedure

Static tension and tension-tension fatigue tests were performed on the UD interlayer thin-ply hybrid laminates at room temperature on a computer controlled Instron 8872 type 25 kN rated universal hydraulic test machine with wedge type hydraulic grips. For the static tests, the hybrid specimens were loaded in uniaxial tension under displacement control using a crosshead speed of 2 mm/min. Five specimens were tested in static tension to determine the fragmentation initiation stress level referred to as the knee-point stress (σ_k). The knee-point stress (σ_k) together with the strain (ε_k) are found from the intersection of lines fitted to the initial linear (red line) and plateau (green line) parts of the stress-strain curve as shown in **Figure 6.60**. The saturated stress (σ_s) and strain (ε_s) shown in **Figure 6.60**. are determined by the intersection of lines fitted to the plateau (green line) and the second rising parts (blue line) of the stress-strain curve. The notation knee-point (k) and saturated (s) are the damage states of the hybrid during tensile loading which is explained in Section 6.7.1. The inserted image of a damaged hybrid specimen shown in **Figure 6.60**. displays localized delaminations surrounding the carbon ply cracks. Well bonded areas appear black and the locally delaminated areas just around the cracks in the carbon layer are visible as the lighter areas due to the translucent nature of the glass/epoxy outer layers of the hybrid laminate. The formation of the well bonded areas is already explained in **Chapter 3**. It should be noted that the inserted image in **Figure 6.60** was recorded using a video gauge system.

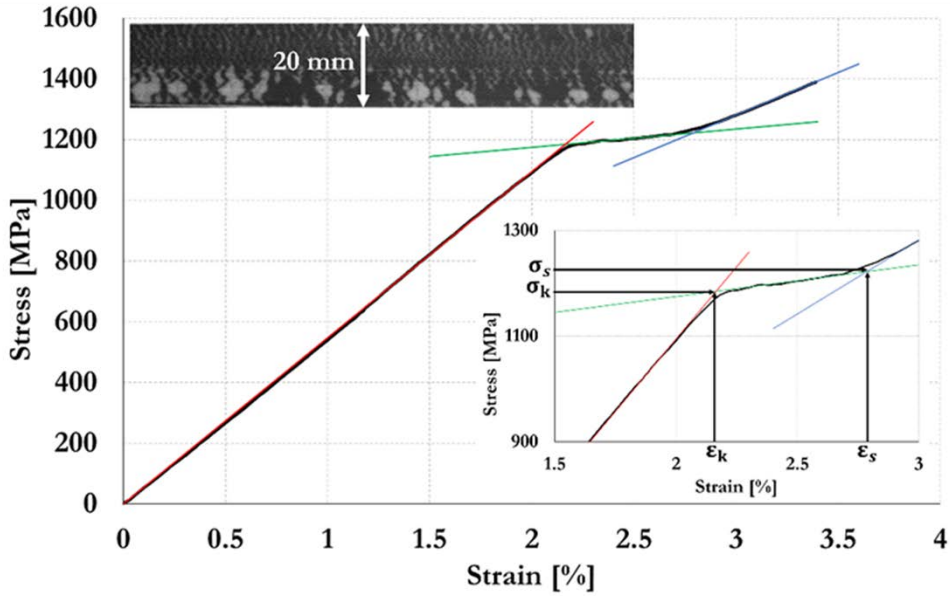

Figure 6.60. Typical stress-strain response of [SG/C$_2$/SG] configuration displaying σ_k and ε_k as the knee-point stress and strain. The inserted image shows the damage state of the specimen at 3.4% strain.

The fatigue testing was performed for two different scenarios, pristine and overloaded hybrid laminates. The pristine specimens were fatigued at two different stress levels below σ_k (90%

and 80%). For the pristine case, four specimens for each load level were tested. It should be noted that the knee-point stress (σ_k) used as a reference in the case of fatigue testing of pristine specimens is taken from an average value of five hybrid composites tested in static tensile loading. To pre-fracture the other specimens, uniaxial static tensile loading was performed on the specimens under displacement control using a crosshead speed of 0.5 mm/min. The tests were stopped when the delaminated area had covered around 10%-20% of the total surface area. They were then fatigued at three load levels (90%, 80%, 70% of σ_k of the particular specimen). In the case of the overloaded hybrid, four specimens each were tested at 90% and 80% load levels respectively while for the 70% load level; three specimens were tested. All fatigue tests were conducted under load control by applying a sinusoidal load around the mean load at a frequency of 2 Hz and a stress ratio ($R=\sigma_{min}/\sigma_{max}$) of 0.1. Strains were measured using an Imetrum video gauge system with a nominal gauge length of 130 mm. Overall videos were recorded at increasing numbers of cycles by a video gauge camera with 5 Megapixel resolution and it allows a precision of measurement down to 0.01% strain. The video gauge records with a speed of 17 frames per second. The delaminated area was evaluated from the recorded images by using a MATLAB code.

6.4 Delamination area measurement technique

The growth of delamination area during fatigue loading is an important damage parameter. Since the delaminated area for UD thin-ply hybrid composites is visible as explained in **Section 6.3**, it is possible to capture the delamination growth area and measure it. The delamination area was measured from the images collected by the video gauge using an in-house compiled MATLAB code. The images, acquired in grayscale by the Imetrum system (**Figure 6.61**a), were imported in Matlab and cropped to cover only the specimen gauge length (**Figure 6.61**b). Finally, they were converted into binary black and white images using a predefined threshold (**Figure 6.61**c). The delaminated area was calculated by counting the white pixels; a scaling factor (dimension mm^2/pixel) allows to calculate the delaminated area in mm^2. To calculate the average delamination length in mm during fatigue loading, the delaminated area is divided to the nominal width of the hybrid specimen. The four white dots shown in **Figure 6.61**a were used to track the uniaxial strain using the video gauge system during the static loading.

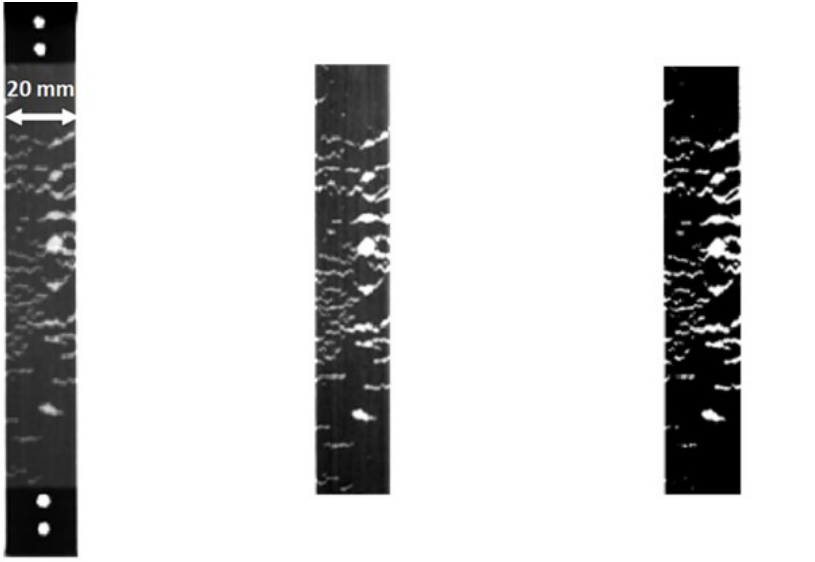

(a) Video gauge image (b) Cropped grayscale image (c) Black and white image

Figure 6.61. Image conversion process to determine the delamination area.

6.5 Stiffness reduction due to delamination

During uniaxial fatigue loading, the longitudinal stiffness (E_N) of composite laminates degrades as damage develops [155], [156]. Because stiffness loss is easily measurable and it is a direct indication of damage, it has been proposed as a fatigue failure criterion [157]. In this work, the equation developed by O'Brien [154] to predict the stiffness loss due to delamination in composite laminates is used as shown in **Equation (6.3**. This equation is developed based on a simple rule of mixtures.

$$\frac{E_o - E_N}{E_o - E_f} = \frac{A_N}{A_o} \tag{6.3}$$

Where E_o is the initial stiffness of the hybrid laminate before delamination of the central carbon layer, E_f is the final stiffness of the hybrid laminate after the central carbon layer is fully delaminated, E_N and A_N is the stiffness and delaminated area at a certain number of cycles, A_o is the total interfacial area. E_o and E_f can be expressed as in **Equation (6.4** and **Equation (6.5** respectively [61]:

$$E_o = \frac{\left(E_g(h - t_c) + E_c t_c\right)}{h} \tag{6.4}$$

$$E_f = \frac{\left(E_g(h - t_c)\right)}{h} \tag{6.5}$$

From **Equation (6.3**, the stiffness at a certain number of cycles is given as in **Equation (6.6**:

$$E_N = E_o + (E_f - E_o)\frac{A_N}{A_o} \quad (6.6)$$

Equation (6.6 provides a means to correlate the observed delamination area in the UD hybrid laminate to the measured stiffness reduction.

6.6 Calculation of the energy release rate

The strain energy release rate is an important parameter to characterize delamination growth from fragmentations in the carbon plies during fatigue at a constant load level. To calculate the strain energy release rate in terms of the carbon layer stress (σ_c), **Equation (6.7** is adopted from Czel et al. [61]:

$$G = \frac{\sigma_c^2 t_c\left(E_g(h - t_c) + E_c t_c\right)}{4E_g E_c(h - t_c)} \quad (6.7)$$

Where E and t is the stiffness and nominal cured layer thickness while the subscript g and c refer to the glass and carbon layers respectively. The stress in the carbon layer (σ_c) can be expressed in terms of the overall applied stress (σ), with the assumption of equal strain through the thickness of the laminate [61]:

$$\sigma_c = \frac{\sigma h E_c}{E_g\,(h - t_c) + E_c t_c} \quad (8.6)$$

The notation σ in **Equation (8.6** is defined as the applied fatigue stress level which was 90%, 80% and 70% of σ_k. Delamination growth under fatigue loading can be described with respect to a cyclic energy release rate (ΔG) [158]:

$$\Delta G = G_{max} - G_{min} \quad (6.9)$$

Where G_{max} and G_{min} refer to the strain energy release rate at the maximum stress (σ_{max}) and minimum stress (σ_{min}).

6.7 Results and discussion

6.7.1 The static tensile behaviour of the UD thin-ply hybrid composites

Figure 6.60 shows a typical stress-strain curve of the UD interlayer thin-ply hybrid composites under static tension. During tensile loading, a recorded video taken from the specimen by the strain measurement system was visually studied to determine the first carbon layer fracture. The first appearance of carbon layer fracture of this hybrid composite is at 1.95% strain which is an average value of five specimen measurements. Starting from 2.00% strain, which is the knee-point strain (ε_k), a process of multiple carbon layer fragmentation was established resulting in a

plateau on the stress-strain curve in **Figure 6.60**. The initial carbon layer fracture and the start of fragmentation occurred at higher strain than the manufacturer's data sheet failure strain of 1.60% as shown in **Chapter 5**. This could be attributed to the constraint provided by the adjacent glass layers to delay the formation of broken carbon fibre clusters and to delay the establishing of stable fragmentation process. The behaviour itself is known as the 'hybrid effect' and detailed explanation of this behaviour is provided by Wisnom et al. [141] which used a statistical strength model and ply level finite element model to explain and quantify the ' hybrid effect'. Upon further loading, the localized delaminations grew gradually until they almost completely joined together, with the fragmentation reaching saturation at 2.78% strain (ε_s), and 1221 MPa stress (σ_s). After this point, the additional load is carried mainly by the glass layers and the stress rises further until 3.4% strain. The inset in **Figure 6.60** shows a specimen after the test has been interrupted at 3.4% strain and the irregular delamination patch sizes shown are due to carbon layer thickness variation where the thicker parts tend to produce larger delamination patches. **Table 6.16** summarises the average of the five hybrid specimens tested in static tension loading showing the important parameters such as first carbon fracture strain, knee-point stress and strain used later to determine the fatigue load level in the pristine hybrid case. These values have been corrected for the calculated residual elastic strain in the carbon layer. The coefficient of thermal expansion (CTE) of the UD composite, α_{comp}, was calculated from **Equation (6.10** adopted from [88]:

$$\alpha_{comp} = \vartheta_f \,.\, \alpha_f \,.\, \frac{E_f}{E_{comp}} + \left(1 - \vartheta_f\right) .\, \alpha_m \,.\, \frac{E_m}{E_{comp}} \qquad (\mathbf{6.10})$$

where ϑ_f , α_f and E_f are the volume fraction, the CTE and the elastic modulus of the fibres respectively while α_m and E_m are the CTE and modulus of the matrix material. **Chapter 5** provides the CTE values for the different fibres which were taken from the product datasheets. For both epoxy matrices in the hybrid composites, typical values of α_m = 6.10^{-5} [1/K] and E_m = 3 GPa were assumed from the general literature. The principal method and detailed equation to calculate the elastic residual strain is shown in **Chapter 3** and **Appendix A** respectively.

The compressive thermal residual strains were calculated from the equilibrium-force state between the carbon/epoxy and glass/epoxy layers by assuming constant strain through the thickness and a 100 °C temperature difference from the cure temperature to room temperature [88]. The calculated residual elastic strain in the carbon for the presented hybrid configuration is -0.025% and this has been accounted for in the values in **Table 6.16** for the strain at first carbon layer failure and at the knee-point strain.

Table 6.16. Results summary of the quasi static tests (Numbers in brackets indicate the coefficient of variation in [relative %]), the strains are corrected for residual strains.

Specimen Type	Initial elastic modulus	Strain at first carbon layer failure	Strain at knee-point ε_k	Stress at knee-point σ_k

	[GPa]	[%]	[%]	[MPa]
[SG /C_2/SG]	53.32 (2.13)	1.95 (7.08)	2.00 (4.82)	1098 (6.77)

The knee-point stress and initial stiffness were evaluated using the nominal thicknesses of the hybrid specimens assuming constant fibre areal densities and fibre volume fractions, neglecting the effect of thickness variation due to variations in resin distribution [159].

6.7.2 Fatigue behaviour of the pristine UD thin-ply hybrid composites

6.7.2.1 Fatigue response

To determine the fatigue loading level where there is no damage in the hybrid laminates, a series of fatigue tests was conducted at two different load levels: 80% of σ_k which is at 878.4 MPa or in terms of strain level is at 1.60%, and at 90% of σ_k which in terms of stress and strain is at 988.2 MPa and 1.81% respectively. From the experimental results for the four specimens loaded at 80% of σ_k, there was no fragmentation observed and a negligible stiffness reduction up until 100000 cycles. From the static tension test results in **section 6.7.1,** the first carbon fracture was observed at 1.95% strain so when the hybrid composites were fatigued at 1.60% strain level, no fragmentation was observed because the strain was well below that for the first carbon fracture. Because no damage was observed at 80% of σ_k for the UD pristine hybrid composites, it was not necessary to conduct fatigue testing at 70% of σ_k for the same specimen type.

For the fatigue characterisation of the UD pristine hybrid composites at 90% of σ_k, the specimens were tested until they delaminated. **Figure 6.62** shows the typical normalised stiffness reduction (E_N/E_o) and normalised delamination growth (A_N/A_o) as a function of number of cycles at 90% of σ_k, where E_N is the laminate stiffness at a certain number of cycles and E_o is the initial laminate stiffness at zero cycles. To exclude the effect of thickness variations, E_N and E_o were evaluated using the nominal thicknesses of the hybrid specimens.

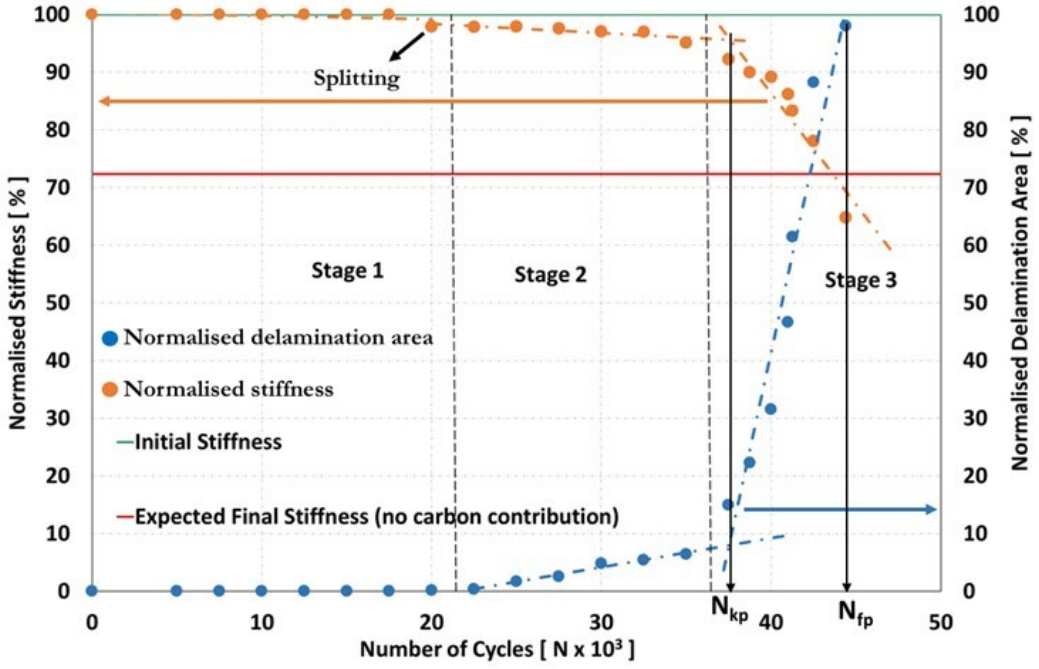

Figure 6.62. Typical stiffness reduction and delamination area development for UD pristine hybrid at 90% σ_k showing the three stages with the transition (N_{kp}) and final number of cycles (N_{fp}).

The typical stiffness reduction and delamination development for UD pristine hybrid fatigued at 90% of σ_k shown in **Figure 6.62** indicates three stages. These stages are defined based on the changes in delamination growth and stiffness reduction and this approach was also applied to the overloaded hybrid composites. It should be noted that the fatigue behaviour shown in **Figure 6.62** is for specimen 2 mentioned in **Figure 6.63**. Initially there was negligible delamination growth in the first stage when the hybrid was fatigued from 0 to 20000 cycles and therefore the stiffness remained constant, but ply splitting took place at the edge of this particular specimen at 20000 cycles, causing a 2% drop of stiffness. Although ply splitting had taken place, the delaminated area was compared against the original area of that laminate. In the second stage, from 22500-35000 cycles, the carbon layers fragmented partially across the width, resulting in a slow localised delamination growth and stiffness loss rate. After reaching a transition point, N_{kp}, as shown in **Figure 6.62**, the carbon fragmentations grew across the whole width, resulting in an accelerated delamination growth and stiffness loss rate between 37500 and 44500 cycles at stage 3. The transition point, N_{kp}, is found from the intersection of lines fitted to stage 2 and stage 3 of the graph as shown in **Figure 6.62** . The fatigue testing was then terminated at final loading cycles, $N_{fp,}$ when delamination had covered almost the whole area of the specimen. As indicated in **Equation (6.6**, a linear relation is expected between stiffness loss and the growth of delaminated area, which has been confirmed from this fatigue test and is shown in **Figure 6.63**. It should be noted that the initial stiffness was measured experimentally, and the expected final stiffness was calculated from the rule of mixtures in **Equation (6.5** considering that the hybrid composites lost the contribution from the central carbon layers. By comparing the first carbon fracture strain from **Table 6.16** with the applied strain level at 90% of σ_k, it is seen that the applied strain level of 1.81% is within the statistical range for carbon fracture to take place, and therefore it is not surprising that fragmentation events occurred during fatigue loading, which were followed by delamination. Due to the low energy release rate of the UD thin-ply hybrid composites determined as explained in **Section 6.6**, the delamination grew slowly with advancing number of cycles at stage 2.

Figure 6.63 shows the plot between stiffness loss and delamination growth at 90% of σ_k along with the predicted stiffness loss calculated by using **Equation (6.6** developed by O'Brien [154] based on a simple rule of mixtures. As shown in **Figure 6.63**, there is an approximately linear relation between the stiffness loss and delamination growth obtained from the experimental results. The deviation in the results shown in **Figure 6.63** from the rule of mixtures is due to the different extent of ply splitting between individual hybrid specimens.

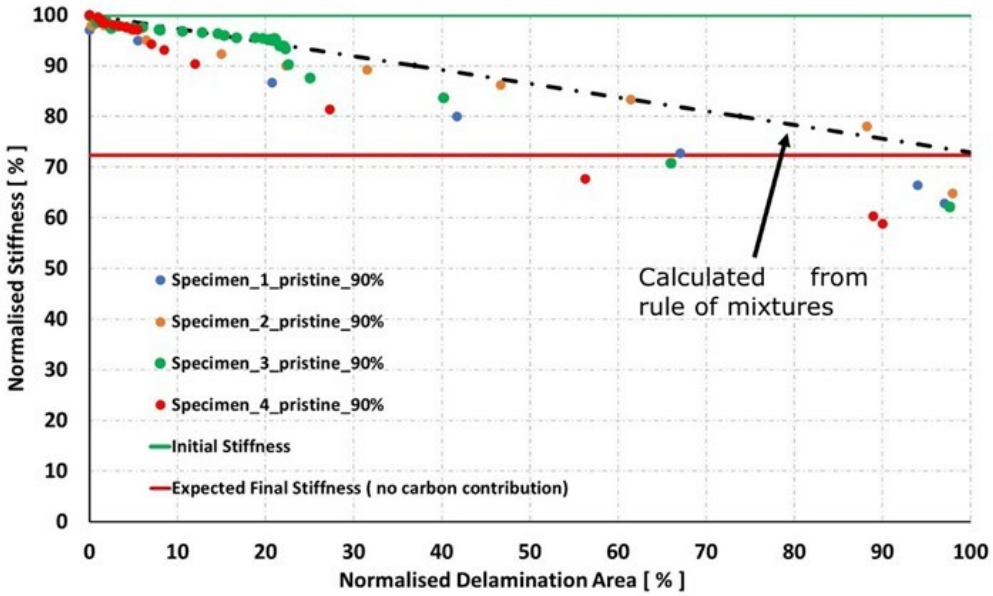

Figure 6.63. Stiffness and delamination area relationship for UD pristine hybrid at 90% of σ_k.

The predicted relation between stiffness loss and delamination growth calculated from the rule of mixtures shows that at 100% total delamination, the hybrid should have lost 27.70% of its stiffness which yields a final stiffness of 72.30%. The final stiffness of the tested hybrid specimens went below the expected final stiffness without any carbon contribution, due to ply splitting from the edge of the specimens observed during testing. Because the applied strain level at 90% of σ_k is only 1.81%, well below the strain to failure of glass/epoxy which is 3.98%, the glass fibre is unlikely to be fractured during fatigue loading or after reaching full delamination. **Table 6.17** provides the stiffness loss rate summary at 90% of σ_k for the UD thin-ply hybrid composites at stages 1, 2 and 3 respectively and the average number of cycles N_{kp} and N_{fp}. The stiffness loss rates shown in **Table 6.17** are measured by plotting a linear fitted line to the respective data at stage 2 and stage 3 respectively as shown in **Figure 6.62**. Variability is typically high in fatigue of fibre reinforced composites, but enough specimens have been tested to provide a reasonable overall characterization of the behavior. Comparing the Coefficient of Variation (CV) from **Table 6.17 - Table 6.21** , the CV on the final numbers of cycles of 29%-61% is actually quite low compared to other published work , e.g. 57%-166% reported in Wu et al. [94]. While the CV on delamination growth rates of 22%-58% is also low compared to 100%-198% reported in Wisnom et al. [158].

Table 6.17. Stiffness loss rate with transition (N_{kp}) and final number of cycles (N_{fp}) summary for all 4 pristine hybrid composite specimens tested at 90% of σ_k (Numbers in brackets indicates the coefficient of variation in [relative %]).

Specimen number	Stage 1 %/ 1000 cycles	Stage 2 %/ 1000 cycles	Stage 3 %/ 1000 cycles	N_{kp} Cycles	N_{fp} Cycles
1	-0.00	-0.45	-3.66	35000	45740
2	-0.06	-0.34	-4.39	38190	44400
3	-0.05	-0.26	-3.34	99630	110000
4	-0.04	-0.42	-5.47	33100	36500
average	-0.04 (26)	-0.36 (23)	-4.21 (22)	51480 (62)	59163 (57)

It is worth mentioning that the individual data for each specimen in **Table 6.17** and **Table 6.42** which shows the stiffness reduction and delamination area development for pristine hybrid specimens fatigued at 90% of σ_k is given in the appendix.

6.7.2.2 Failure modes

During cyclic loading at 90% of σ_k, the delamination growth is visible due to the translucent nature of the glass plies. This is an advantage as it is possible to monitor the delamination growth visually. Typical delamination growth as a function of load cycles is shown in **Figure 6.64**, where in general, there is negligible delamination growth at stage 1, a slow growth of delamination at stage 2, followed by faster growth at stage 3. Between stage 2 and stage 3 delamination growth, there is a transition point which has already been defined in **section 6.7.2.1.** The summary of delamination growth rates at 90% of σ_k at the three different stages is shown in **Table 6.3**. It is worth mentioning that the method to measure the delamination growth rates is also the same as the method to measure the stiffness loss rates mentioned in **Section 6.7.2.1.**

Table 6.3. Delamination growth rate summary for all 4 pristine hybrid composite specimens tested at 90% of σ_k (Numbers in brackets indicates the coefficient of variation in [relative %]).

Specimen number	Stage 1 %/ 1000 cycles	Stage 2 % / 1000 cycles	Stage 3 %/ 1000 cycles
1	0.00	0.85	13.00
2	0.01	0.64	13.20
3	0.03	0.44	8.40
4	0.02	0.76	17.54
Average	0.02 (22)	0.67 (26)	13.04 (28)

It is shown in **Table 6.3** that there is considerable scatter in the delamination growth rate at all three stages, this behaviour could be attributed to statistical strength distribution of the carbon fibres [141] and the variability in the carbon layer thickness [160] in each hybrid specimen. **Figure 6.64** shows typical damage development in a UD pristine hybrid specimen fatigued at 90% of σ_k, where it is shown that the carbon fractures and delamination at 32500 cycles do not develop across the full width of the specimen. It is also interesting to note that the carbon fractures also develop at different locations within the specimen's gauge length as seen for the damage development at 32500 cycles in **Figure 6.64**, because some individual fibres have failed early at those locations and developed into clusters of broken weak fibres via matrix damage or local debonding [119]. Each stage of damage development shown in **Figure 6.64** is linked to the specific stiffness loss stage shown in **Figure 6.62**.

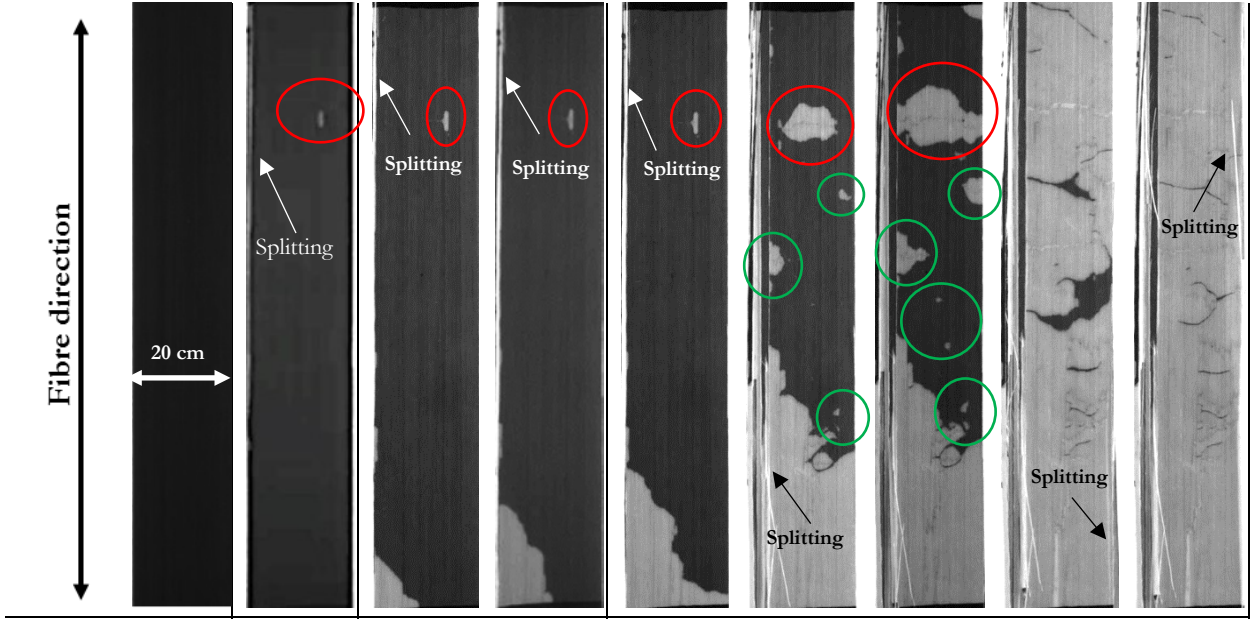

Cycles	0	20000	32500	35000	37500	42500	42545	42680	44425
Stage	-	1	2		3				

Figure 6.64. Typical fatigue damage development for pristine UD thin-ply hybrid composite at 90% σ_k.

Looking at the damage behaviour at 20000 cycles in **Figure 6.64**, there is an initial very small patch of delamination (as shown by the red circle) and minor ply splitting at the edge of the specimen (shown by the arrow). Although there is a small delaminated area at 20000 cycles, it was not sufficient to cause a stiffness reduction, instead the ply splitting was responsible for the minor stiffness loss. At 32500 cycles, the small delaminated area increases in size and there is a partial delamination at the bottom left corner (which is near the end tabs). The delamination at the left corner of this specimen grew with a slow rate when cycled from 25000 to 35000 cycles and this refers to stage 2. From 32500 to 35000 cycles, the delamination originating at the left corner accelerated faster compared to the small patch. After reaching 37500 cycles, the partial delamination from the left corner becomes established across the full width of the specimen, indicating that the carbon fracture has also extended. Ply splitting also took place during cyclic loading from 32500-42500 cycles, where the width of the split grew from approximately 0.4 mm to 3.9 mm. From 37500 to 42500 cycles, the small patch area (as shown by the red circle) grew further, indicating that the corresponding carbon layer fracture has extended, while the delaminated area from the bottom part of the specimen has covered 25 % of the area of the specimen. Small patches of delamination (shown by the green circles) also appeared at 42500 cycles which originated from fragmented carbon layers. With increasing number of cycles from 42545 to 44425 cycles, the delaminated area which originated from the small patches grew in size along the specimen and eventually covered most of the specimen's surface at the final stage (44425 cycles). It was also observed that the width of ply splitting extended from approximately 4 mm to 6.6 mm during fatigue loading between 42500 to 44425 cycles. Based on the observed damage from the four hybrid specimens under fatigue loading at 90% of σ_k, the stiffness loss shown in **Figure 6.62** during fatigue loading is mainly caused by fragmentation of the carbon layers followed by the growth of delamination. At the final stage of fatigue loading, there is still some residual bonding

between the carbon and glass layers, visible as narrow black lines running across the width of the specimen. It should be noted that this residual bonding is too small to be able to transfer significant load.

6.7.3 Fatigue behaviour of the overloaded UD thin-ply hybrid composites

6.7.3.1 Fatigue response

Figure 65.6 shows typical stiffness loss and delamination growth for an overloaded specimen pre-fractured until 2.3% strain and fatigued at 70% of σ_k. This load level is chosen to be described first as it is representative of the fatigue behaviour of the other two load levels and allows a higher number of cycles and therefore can give better insight into damage development.

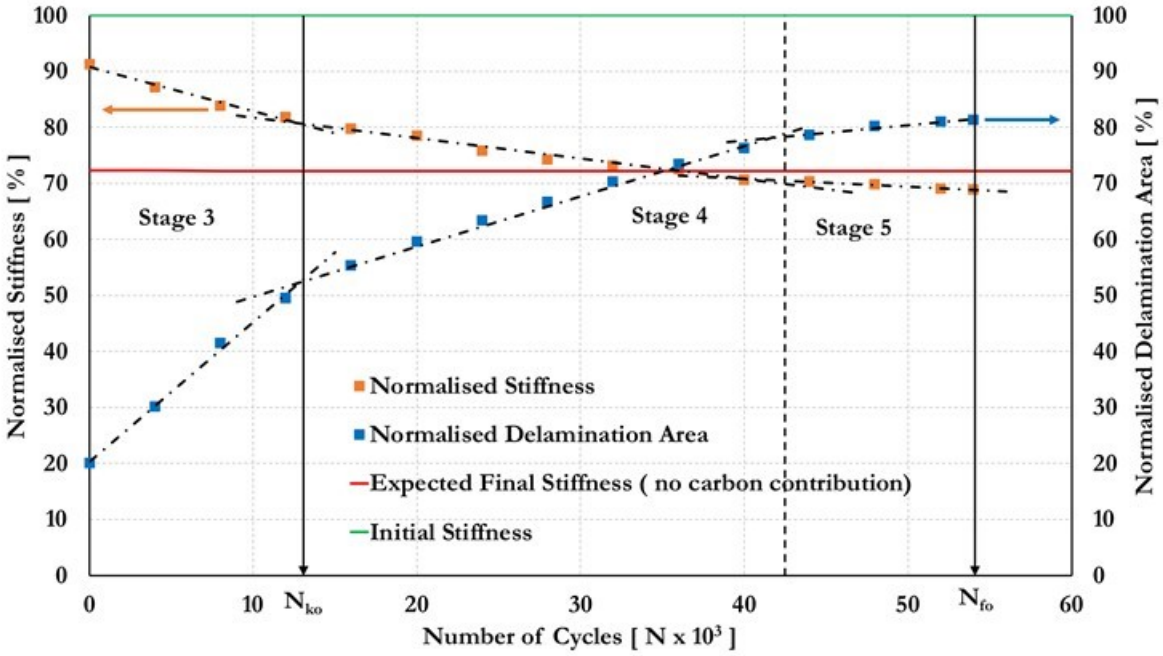

Figure 65.6. Typical stiffness loss and delamination area development for UD overloaded hybrid at 70% of σ_k.

The initial normalised stiffnesses on **Figure 65.6** for all the overloaded hybrid composites do not start from 100% as there was already damage introduced in the form of fragmentation and dispersed delamination during the static overload, as shown in **Figure 6.66** for the damage state at 0 cycles. It should be noted that the fatigue damage development shown in **Figure 6.66** is related to each specific stiffness loss stage shown in **Figure 65.6**.

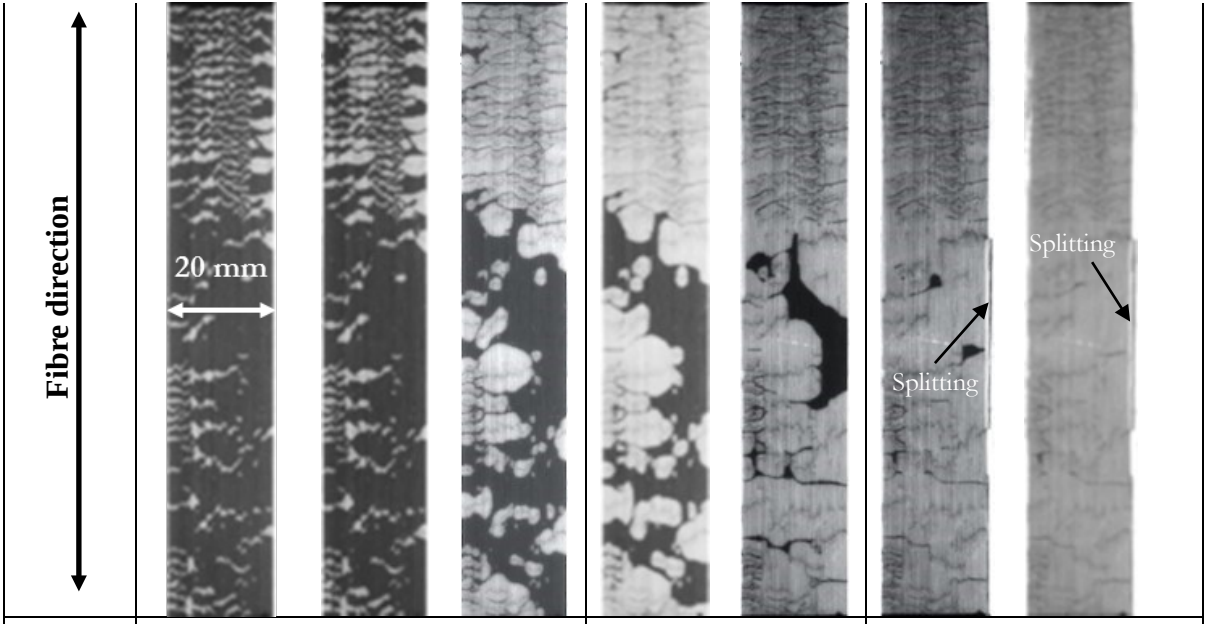

Cycles	0	2000	14000	20000	34000	48000	54000
Stage	3			4		5	

Figure 6.66. Typical fatigue damage development for overloaded UD thin-ply hybrid composites at 70% of σ_k.

There was a challenge to introduce a consistent extent of damage into the hybrid composites through a controlled static tension loading, and the initial amount of damage in terms of delaminated area between specimens differed. One of the reasons contributing to this behaviour is the local variation in the carbon layer thicknesses, where the hybrid specimens with thinner central carbon layers tend to have a finer distribution of fragmentation and smaller delamination area while for thicker central layers, a coarser distribution of damage was observed. During static tension loading, the initial amount of damage introduced in the hybrid composites was visually monitored. When the delaminated area had covered around 10%-20% of the total surface, the loading was stopped, and this was found to be related to approximately 95%-90% of the initial hybrid composite stiffness. Because there was already initial damage in the hybrid specimens across the full width, when they were fatigued, the normalised stiffness reduction enters directly into the stage of rapid stiffness loss equivalent to stage 3 of the UD pristine hybrid shown in **Figure 6.62**. After the delaminated area had covered 55%-89% of the total surface, a transition point, $N_{ko,}$ is reached where the stiffness loss rate decelerates in stage 4 because a reduced area is available for delamination. The transition point, $N_{ko,}$ for the overloaded hybrid is determined from the intersection point of the linear lines fitted to the accelerated stiffness loss at stage 3 and decelerated stiffness loss at stage 4 respectively as shown in **Figure 65.6** After this particular specimen delaminated, the fatigue test was kept going until 54000 cycles to see if the glass layers would fail but they did not, so the test was stopped. This shows that the glass layers could still carry the load even after the carbon layers had already fractured and delaminated. This is shown as stage 5 in **Figure 65.6**, where a lower slope is reached for the stiffness loss and delamination growth rate because only a limited area is available for further delamination to occur and the load is mainly carried by the glass layers. The fatigue testing for the remaining overloaded UD hybrid composites

at the three load levels was terminated at the final loading cycles, N_{fo}, when the specimens were fully delaminated.

The comparison of typical stiffness losses for the three different fatigue load levels for the UD hybrid specimens is shown in Figure 6.67. Stiffness loss comparison for UD overloaded hybrids **at** 90%, 80% and 70% of σ_k. which indicates the dependency of stiffness loss on load level with significantly faster loss of stiffness at 90% of σ_k compared to the other two load levels. It is also shown in **Figure 6.67** that even when the hybrid composites lose the carbon layers contribution when fatigued at 80% and 90% of σ_k, it did not fail immediately because the glass layers were still carrying the load.

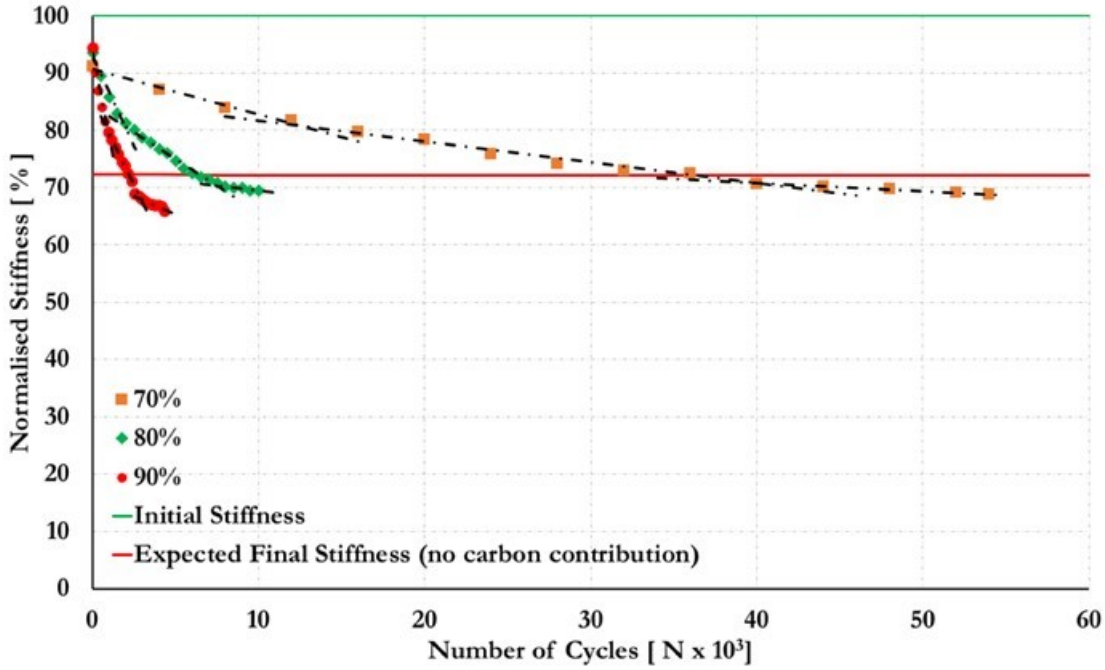

Figure 6.67. Stiffness loss comparison for UD overloaded hybrids at 90%, 80% and 70% of σ_k.

The three stages of stiffness loss for 80% and 90% of σ_k are compacted in **Figure 6.67** due to the scale chosen but are similar to those at 70% of σ_k. For the UD overloaded hybrid specimens fatigued in stage 3, the average stiffness loss rates were -0.66%/1000 cycles, -4.15%/1000 cycles, -11.45%/1000 cycles for 70%, 80% and 90% of σ_k respectively. The stiffness loss rate in stage 3 for the UD overloaded hybrid specimens fatigued at 90% of σ_k is approximately 40% higher than the loss rate for the UD pristine hybrid specimens fatigued at the same load level because there are already more carbon layer fractures in a well distributed pattern which act as sites for delamination propagation. The delamination growth rate is therefore also higher for the UD overloaded hybrids compared to the pristine ones. For all the UD overloaded hybrid specimens tested at the three load levels, the stiffness loss is mainly due to propagation of delamination. As shown in **Figure 6.67** the final stiffness of the hybrids went below the expected final stiffness without the carbon contribution due to ply splitting from the edge of the specimen as shown in **Figure 6.66** and possibility of glass fibre reinforced epoxy degradation in fatigue. The summary of stiffness loss rates at stages 3, 4 and 5 respectively for overloaded UD thin-ply hybrid composites with transition points (N_{ko}) and final loading cycles (N_{fo}) described in terms of the number of cycles is shown in

Table 6.43.

Table 6.43. Stiffness loss rate with transition (N_{ko}) and final number of cycles (N_{fo}) summary for overloaded hybrid composites (Numbers in brackets indicates the coefficient of variation in [relative %]).

Load level [%]	Specimen number	Stage 3 %/ 1000 cycles	Stage 4 % / 1000 cycles	Stage 5 % / 1000 cycles	N_{ko} Cycles	N_{fo} Cycles
70	13	-0.30	-0.20	-	8240	72000[a]
	15	-0.78	-0.36	-0.14	12480	54000
	17	-0.92	-0.20	-0.06	13470	82000
	average	-0.66 (48)	-0.25 (37)	-0.10 (58)	11393 (24)	68000 (29)
80	5	-3.66	-0.80	-0.16	5500	20000
	6	-6.23	-1.87	-0.34	1940	10000
	7	-2.70	-1.44	-0.36	4200	12000
	8	-4.00	-1.53	-0.38	4800	30000
	average	-4.15 (36)	-1.41 (31)	-0.31 (32)	4110 (37)	18000 (50)
90	1	-15.30	-6.01	-1.30	1020	4400
	2	-8.60	-7.13	-1.00	980	3000
	3	-10.10	-4.02	-0.67	1050	4600
	4	-11.20	-4.48	-0.86	1700	10800
	average	-11.45 (27)	-5.41 (26)	-0.95 (26)	1187 (29)	5700 (61)

[a] fatigue testing was terminated before the specimen was fully delaminated

For specimen 13 shown in

Table 6.43., the fatigue testing was terminated before full delamination was attained due to a sudden fault in the testing machine. The noticeable scatter in the stiffness loss rate shown in

Table 6.43., is due to variability of the initial damage between specimens and different extents of ply splitting. The faster stiffness loss rate of the overloaded UD hybrid composites at higher load levels is mainly due to the higher cyclic energy release rate.

6.7.3.2 Failure modes

The damage modes of the overloaded UD thin-ply hybrid composites at 70%, 80% and 90% of σ_k consist mainly of delamination growing from the multiple fragmentation sites. The delamination growth as a % of the total area is taken as the damage parameter because when a hybrid composite is fully delaminated, it has lost the load carrying capability of the stiffer carbon

layers. Comparison of delamination growth as a function of load cycles for the three loading levels is shown in **Figure 6.68**, where an accelerated growth rate for a number of cycles is followed by reduced growth rate. As already shown in **Figure 65.6** for specimens fatigued at 70% of σ_k, there are three stages of delamination growth rate for overloaded UD hybrid composites which also apply for the damage growth rate at 80% and 90% of σ_k. The delamination growth rates at the three stages were measured by applying a linear fit to the respective data as shown in **Figure 6.68** for the three-fatigue loading levels.

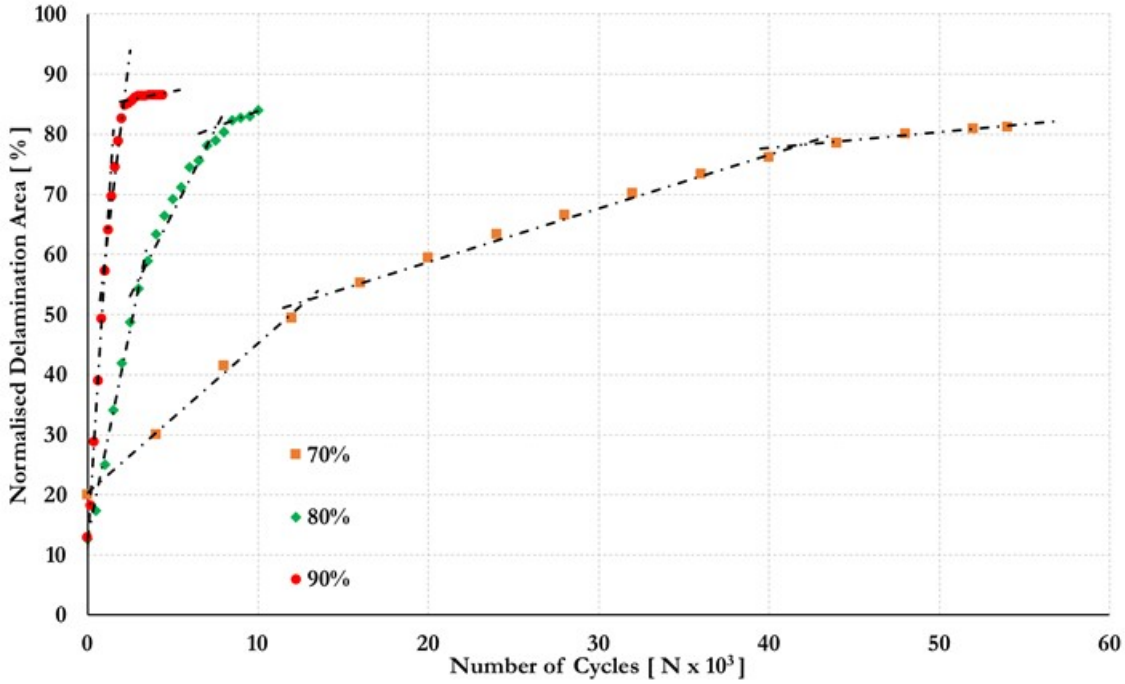

Figure 6.68. Typical delamination development curve for overloaded UD thin-ply hybrid at 70%, 80%, 90% of σ_k.

Typical damage development in an overloaded UD thin-ply hybrid composites is shown in **Figure 6.66**. This is representative of the fatigue damage accumulation of all specimens at 70%, 80% and 90% of σ_k. As shown in **Figure 6.66**., at 0 cycles, after static tension loading had been applied, initial damage in the form of fragmentation and delamination was present in the specimen. It was noticeable that the fractured areas had an irregular and staggered shape and the corresponding delamination areas covered around 20% of the specimen's surface. Most of them did not develop into a single linear crack front across the complete specimen width. The lighter delaminated areas around the carbon layer fractures also indicated various crack densities, with the fine areas corresponding to the thinner parts of the central carbon layers while the more coarsely cracked areas show the thicker parts, highlighting the thickness variability of the thin carbon prepreg. With increasing number of cycles at constant amplitude fatigue loading, the delaminated areas surrounding the fragmentations grew stably and joined with the neighbouring delamination areas as seen in **Figure 6.66** at stage 3. It is interesting to note that even though some of the carbon layer crack lengths are initially less than the full specimen width, the surrounding delamination areas were still able to grow because with advancing number of cycles, the carbon crack lengths were able to extend further. The normalised delamination growth rates shown in **Figure 6.68** for

the three load levels display an initial accelerated growth rate followed by a reduced growth rate due to less area available for delamination to progress. It was also observed that ply splitting occurred for the majority of the UD overloaded hybrid specimens tested in fatigue causing a minor reduction in stiffness.**Table 6.44** shows the summary of delamination growth rates for the overloaded UD thin-ply hybrid composites at the three different fatigue loading levels.

Table 6.44. Delamination growth rates summary for overloaded hybrid composites (Numbers in brackets indicate the coefficient of variation in [relative %]).

Load level [%]	Specimen number	Stage 3 %/ 1000 cycles	Stage 4 % / 1000 cycles	Stage 5 % / 1000 cycles
70	13	1.00	0.81	-
	15	3.26	0.90	0.07
	17	2.49	0.89	0.10
	average	2.25 (51)	0.86 (6)	0.08 (25)
80	5	11.68	4.44	0.10
	6	14.07	5.53	0.11
	7	12.10	7.30	0.13
	8	16.80	6.67	0.13
	average	13.66 (17)	5.9 (21)	0.11 (12)
90	1	46.47	23.05	0.54
	2	39.38	19.67	0.59
	3	34.80	21.00	0.49
	4	33.00	11.15	0.30
	average	38.41(15)	18.71 (28)	0.48(26)

The individual data for each specimen in

Table 6.43 and **Table 6.44** which shows the stiffness reduction and delamination area development for the overloaded hybrid specimens are given in the appendix.

6.7.3.3 Delamination growth rates as a function of cyclic energy release rates

It is possible to correlate the delamination growth rate with the cyclic energy release rate at a constant load level to quantify the life of the overloaded UD hybrid composites under fatigue loading by adopting a Paris law type equation, assuming growth in a self-similar manner as shown in **Equation (6.11**:

$$\frac{da}{dN} = C(\Delta G)^m \qquad (\mathbf{6.11})$$

Where a is the delamination length, N is the number of cycles, ΔG is the cyclic energy release rate, and C and m are parameters that characterise the propagation rate. This assumes that the delamination length grows linearly with advancing number of cycles at constant-amplitude loading. The parameters C and m need to be determined to have a complete relation of **Equation (6.11** by plotting the delamination growth rates in mm/cycle as a function of cyclic energy release rates.

This plot on a logarithmic scale is shown in **Figure 6.69** for the three fatigue load levels. The delamination growth rate, da/dN, is determined from the linear portion of the plot of normalised delamination area versus number of cycles under each constant load amplitude. The linear portion is fitted with a line as shown in **Figure 6.68** and the initial linear portion (stage 3) is used as the delamination growth rate, da/dN, plotted in **Figure 6.69**. It should be noted that the delamination growth rates shown in **Table 6.44** which are in %/ 1000 cycles need to be converted to mm/cycle. **Table 6.21** shows the summary of delamination growth rates in mm/cycle with the cyclic energy release rates at the three-load levels which are used to produce the plot in **Figure 6.69**.

Table 6.21. Delamination growth rate and cyclic energy release rate summary for overloaded hybrid composites (Numbers in brackets indicate the coefficient of variation in [relative %]).

Load level [%]	Specimen number	Delamination growth rate mm/cycle	ΔG N / mm
70	13	0.0012	0.30
	15	0.0010	0.41
	17	0.0009	0.41
	average	0.0010 (14)	0.37 (17)
80	5	0.015	0.46
	6	0.026	0.55
	7	0.014	0.49
	8	0.020	0.54
	average	0.019 (29)	0.51 (8)
90	1	0.055	0.64
	2	0.043	0.67
	3	0.041	0.52
	4	0.039	0.53
	average	0.045 (16)	0.59 (13)

As seen in **Table 6.21**, there are slight differences between the cyclic energy release rates at the same loading level. The reason behind this is because the load levels were taken as fixed percentages of the different values of knee-point stress, σ_k, for each hybrid specimen.

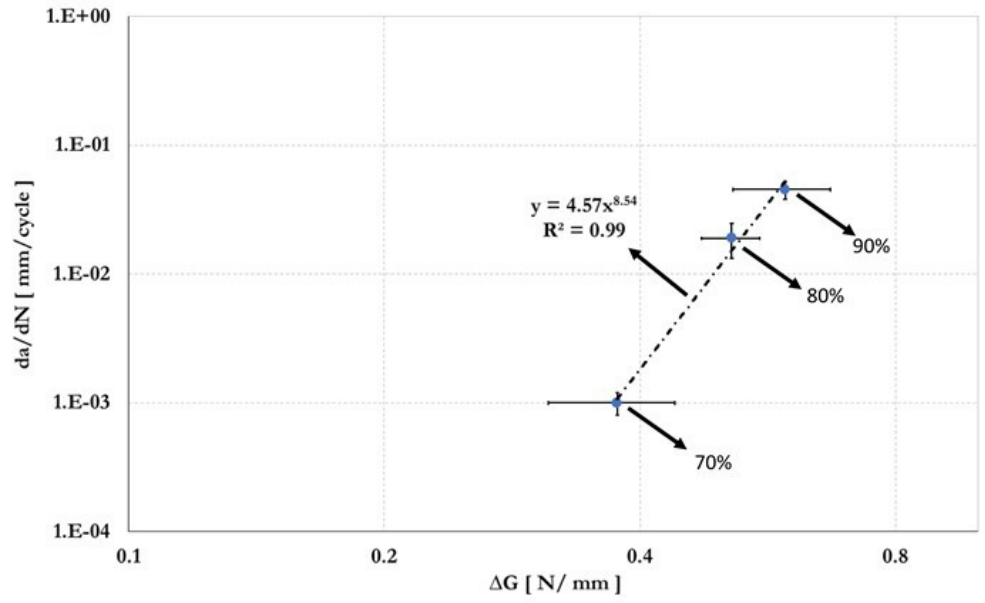

Figure 6.69. Delamination growth per cycle as a function of cyclic energy release rates for overloaded UD thin-ply hybrid composites at 70%,80%,90% of σ_k.

As seen in **Figure 6.69** the C and m parameters are 4.57 and 8.54 respectively and although there are only three points, the fit to a straight line is good, which implies that the delamination growth rates as a function of cyclic energy release rates comply with the Paris law in **Equation (6.11**. This could be used as a basis for life estimation during fatigue loading of UD thin-ply hybrid composites. There is a wide range of Paris law parameters for fibre reinforced composites, but none published for this material. The exponent, m, of 8.54 lies within the range from 3.1 to 9.6 reported for other carbon fibre/epoxy materials [154][158][161][162].

6.8 Conclusions

This chapter has presented the mechanical properties of unidirectional thin-ply hybrid composites subjected to static and cyclic tensile loads. The effect of different loading conditions was examined. The following was concluded:

1. When pristine hybrid specimens were fatigued at 80% of σ_k no stiffness reduction up until 100000 cycles was observed because the specimens were loaded well below the first carbon layer fracture strain.

2. It was observed that there are three stages of damage growth when UD pristine hybrid specimens are fatigued at 90% of σ_k. The first stage has negligible stiffness loss, the second stage involves slow growth of delamination from fragmentations, and the third stage when the delamination becomes established across the full width, with higher delamination rate.

3. For the overloaded hybrid composites, there are three stages of damage growth. The initial stage, which is equivalent to the third stage for the UD pristine hybrid specimens, involves rapid stiffness loss and accelerated delamination growth from the existing initial fractures, the next stage with slower stiffness loss due to delamination approaching saturation, and the last stage with negligible stiffness loss rate when the specimen is fully delaminated, but the glass layers are still able to carry the load. When the overloaded hybrid laminates were fatigued at 70% and 80% of σ_k, they showed more gradual stiffness reduction and slower damage growth compared to the fatigued overloaded hybrids at 90% load level.

4. The stiffness loss rate of the overloaded UD thin-ply hybrid composites fatigued at 90% of σ_k is higher compared to the pristine UD thin-ply hybrid composites because there are already more carbon layer fractures in a well distributed pattern which act as sites for delamination propagation.

5. Delamination growth as a function of strain energy release rate for overloaded UD thin-ply hybrid composites complies with the Paris law and this could be used as the basis for life estimation.

Chapter 7 Conclusions and future work

7.1 Conclusions

The work in this thesis presented a comprehensive investigation on the response of unidirectional (UD) thin-ply interlayer hybrids made from thin-ply carbon/epoxy plies and standard thickness glass/epoxy plies subjected to different loading cases including quasi-static tensile cyclic loading, compression, bending, and fatigue loading. The response of the hybrid

composites in each loading case was shown to be heavily dependent on the selection of material and the design of the relevant stacking sequences. The ability of the thin-ply laminate to suppress damage allows considerable non-linearity to develop, which is governed by fibre fragmentation and dispersed delamination, bringing a unique failure response compared to the traditional composite laminates under given specific load cases. The key findings from this experimental work described in **Chapter 3-6** are discussed below:

Chapter 3: Quasi-static cyclic loading of UD thin-ply hybrid composites was conducted to assess the extent of stiffness loss with increasing applied strain. For this study, three types of hybrid configuration were examined: $SG_1/MR40_1/SG_1$, $SG_1/TR30_1/SG_1$, $SG_1/TR30_2/SG_1$, where MR40 is an intermediate modulus carbon fibre while TR30 is a standard modulus carbon fibre. The strain at first carbon ply failure and the knee point strain (ε_k) for the $SG_1/TR30_1/SG_1$ hybrid is higher than for the $SG_1/TR30_2/SG_1$ hybrid. This is due to the 'hybrid effect' which provides a delay in damage initiation due to a constraint on broken carbon cluster development. For the thinner hybrid with a single carbon ply, the fibre failure and fragmentation appear at a slightly higher strain because of the limited number of fibres through the thickness of the ply inhibiting formation of a critical cluster. For $SG_1/MR40_1/SG_1$ and $SG_1/TR30_2/SG_1$ configurations, the stiffness reduction over the course of loading was governed by fragmentation of the carbon plies and delamination between the carbon and glass plies. A smaller stiffness reduction for the $SG_1/TR30_1/SG_1$ configuration compared to the other hybrid configurations was observed with the fragmentation of the carbon ply as the main damage mechanism responsible for the reduction. With each loading cycle, there was a small amount of hysteresis and residual strain, which could be attributed to the significant reversed shear stress at the ply interfaces near the ends of the delaminated regions of the fragmented hybrid. The high shear stresses between the carbon and glass plies cause the matrix to deform, leaving a residual strain at zero load for all three hybrid configurations. Another possible explanation for the existence of residual strain is due to the accumulation of debris between the open cracks preventing the surface cracks to return to its original state when unloaded. At the final loading cycle for each hybrid configuration, there is a residual black-lines (intact carbon ply). The existence of the residual black-lines on each hybrid configuration could be attributed to the average width of the intact ply where the shear stress would not be able to reach the value required to damage the interface, thus leaving that particular area intact. Based on this study, it was found that the quasi-static response of the hybrids is affected by the carbon/glass volume ratio, the carbon ply thickness and the carbon properties (modulus, strain to failure). The response of the UD thin-ply hybrid laminates are considered pseudo-ductile because the damage in the form of ply fragmentation and stable delamination, leads to gradual loss of stiffness. The stable delamination of this hybrid material is due to the low energy release rate of the thin carbon ply.

Chapter 4: The compression response of UD thin-ply hybrid composites was examined under two different loading configurations: indirect compression (four-point bending) and direct

compression (longitudinal) tests. The hybrid material was made of standard thickness S-glass/epoxy ply and thin M55J carbon/epoxy ply. This carbon fibre is a high modulus type. The direct compression response of unidirectional thin-ply hybrids has been established. Gradual failure was obtained, with a decrease in stiffness at an average strain of -0.555% and -0.554% while the final failure strain was at an average strain of -2.150% and -1.440% for the $[SG_1/(C_1/SG_1)_{17}]$ and $[SG_1/(C_2/SG_1)_{17}]$ hybrid configuration respectively. For the $[SG_1/(C_3/SG_1)_{17}]$ configuration, sudden failure occurred at an average strain of -0.500% strain. Even this lower strain is higher than the compression failure strain calculated from the manufacturer's data sheet of -0.260%. For asymmetric $M55_1$, $M55_2$ and $M55_3$ hybrid configuration, a decrease of stiffness was observed at around -0.555%, -0.522%, -0.507% strain respectively while the final failure strains are at around -2.724%, -1.750% and -0.956% strain respectively. The decrease of stiffness for the hybrid configuration was marked by a knee-point in the stress-strain response and a similar value was obtained from the indirect and direct compression tests. The final failure strain of the hybrids decreases with increasing carbon ply thickness which qualitatively complies with the energy release rate concept because energy release rate is proportional to the thickness of the carbon plies. From the indirect compression loading results, it was found that the asymmetric hybrid laminates with two and three M55J carbon plies lost most of the bending stiffness contribution from the carbon ply after the knee point due to more extensive damage (fragmentation and dispersed delamination), while negligible stiffness loss was found for the asymmetric hybrid laminate with a single carbon ply compared to the other two asymmetric hybrid configurations. The stiffness loss for all three hybrid configurations was assessed by comparing the change of force-strain slope and contribution of carbon bending stiffness from Classical Laminated Plate Theory (CLPT). From the optical microscopy observation of the damaged asymmetric hybrid specimens, fragmentation of the carbon plies and localised delamination between the carbon and glass plies was discovered. The measured fragment length is less than the critical length calculated from a traditional load transfer model with the usual constant shear stress assumption with linear increase in stress from zero at both ends of the fragment normally applied for tension. The traditional load transfer model is unable to predict the fragment length of carbon layer in compression because the fragments are in contact and still able to transfer load. Due to the irregular shape between the fragmented surfaces, friction and mechanical interlocking exist which can transfer compressive load despite the fractures, and break the carbon into even smaller pieces than the critical length. The fragmented carbon layers fractured at an angle that is displaced in the transverse direction. This transverse displacement is responsible for interfacial damage (delamination) which causes the stiffness degradation. The different final failure strains underpin the crucial role of the carbon/epoxy ratio and carbon layer thickness in unidirectional glass/carbon hybrid laminates under compressive loading both in indirect and direct loading configurations.

Chapter 5: From the four-point bending testing of symmetric hybrid laminates, it was observed that gradual failure was obtained for the $[SG/M55_1/SG]_{4s}$, $[SG/M55_2/SG]_{4s}$, $[SG/TC35_1/SG]_{4s}$,

$[SG/TC35_2/SG]_{4s}$ hybrid configurations under four-point bending. The sequence of damage mechanisms for the $[SG/TC35_1/SG]_{4s}$ and $[SG/TC35_2/SG]_{4s}$ hybrid configurations was carbon ply fragmentation and stable delamination on the tension side and the final failure was sudden compressive failure due to fibre failure followed by delamination. The knee-point strain for the $[SG/TC35_2/SG]_{4s}$ hybrid is due to fragmentation on the tension side and was found to be 10% higher than the knee-point strain obtained from the static tensile testing of the $[SG/TC35_2/SG]$ configuration. While for the $[SG/M55_1/SG]_{4s}$ and $[SG/M55_2/SG]_{4s}$ hybrid configurations, the damage started from the compression side in the form of carbon ply fragmentation and stable delamination followed by fragmentation and stable delamination on the tension side. The first knee-point strain for $[SG/M55_1/SG]_{4s}$ and $[SG/M55_2/SG]_{4s}$ hybrid configurations is related to carbon ply fragmentation on the compression side and it occurred at a similar knee-point strain (around -0.500%) obtained from direct compression testing for $[SG_1/(C_1/SG_1)_{17}]$ and $[SG_1/(C_2/SG_1)_{17}]$ hybrid configurations. The second knee-point strain for the $[SG/M55_1/SG]_{4s}$ and $[SG/M55_2/SG]_{4s}$ hybrids was found to be around 11% higher than the knee-point strain obtained from the static tensile test for $[SG/M55_1/SG]$ and $[SG/M55_2/SG]$ configuration. The final failure strain on the compression side for $[SG/M55_1/SG]_{4s}$ and $[SG/M55_2/SG]_{4s}$ hybrids is higher compared to the failure strain obtained from direct compression. This could be attributed to the shifting of the neutral axis towards the compression side due to fragmentation of the carbon ply on the tension side. This behaviour leads to a delay of the final failure on the compression side. A high fragmentation strain on the tension side of the bending specimens was obtained for $[SG/TC35_2/SG]_{4s}$, $[SG/M55_1/SG]_{4s}$ and $[SG/M55_2/SG]_{4s}$. This value is higher than the fragmentation strain to failure obtained from the static tensile testing. This behaviour could be attributed to a size effect present in the bending specimens. The final failure observed for all hybrid configurations occurred on the compression side. The evolution of the neutral axis could be used to assess the damage sequence of hybrid composites during four-point bending.

Chapter 6: From the fatigue testing of UD thin-ply hybrid composites, $[SG/TC35_2/SG]$, under two scenarios: without any initial damage (pristine hybrids) and after the introduction of damage in the laminates by loading past the pseudo-yield point (overloaded hybrids), it was discovered that when pristine hybrid specimens were fatigued at 80% of σ_k (knee-point stress) no stiffness reduction or damage up until 100000 cycles was observed because the specimens were loaded well below the first carbon layer fracture strain. It was observed that there are three stages of damage growth when UD pristine hybrid specimens are fatigued at 90% of σ_k. The first stage has negligible stiffness loss, the second stage involves slow growth of delamination from fragmentations, and the third stage when the delamination becomes established across the full width, with a higher delamination rate. For the overloaded hybrid composites, there are three stages of damage growth. The initial stage, which is equivalent to the third stage for the UD pristine hybrid specimens, involves rapid stiffness loss and accelerated delamination growth from the existing initial fractures, the next stage with slower stiffness loss due to delamination approaching saturation, and the last

stage with negligible stiffness loss rate when the specimen is fully delaminated, but the glass layers are still able to carry the load. When the overloaded hybrid laminates were fatigued at 70% and 80% of σ_k, they showed more gradual stiffness reduction and slower damage growth compared to the fatigued overloaded hybrids at 90% load level. The stiffness loss rate of the overloaded UD thin-ply hybrid composites fatigued at 90% of σ_k is higher compared to the pristine UD thin-ply hybrid composites because there are already more carbon layer fractures which act as sites for delamination propagation. The final stiffness of the tested hybrid specimens went below the expected final stiffness without any carbon contribution, due to ply splitting from the edge of the specimens observed during testing. Delamination growth as a function of the strain energy release rate associated with the delamination of the carbon plies for overloaded UD thin-ply hybrid composites complies with the Paris law and this could be used as the basis for life estimation.

The response of UD thin-ply hybrid composites has shown promising behaviour, including higher strain to failure compared to the carbon fibre reinforced epoxy composites, along with gradual failure under static and fatigue loading. The mechanical behaviour is found to be dependent on a combination of material and the design of stacking sequences, but there are trade-offs between each mechanical properties. As an example, the tensile response of UD thin-ply hybrid composites, for the hybrid laminates with high modulus central carbon plies, has the highest initial modulus but relatively low knee-point strain and stress. At the other extreme, the configuration comprising the highest carbon failure strain has a relatively high knee-point strain and stress but moderate initial modulus. Both configurations have a high final strain to failure which demonstrates that it is possible to combine the stiffness of carbon and final failure strain of S-glass composites. This indicates the flexibility in designing the stress-strain response of UD thin-ply hybrid composites to meet the specific requirements.

The stiffness and strength of UD thin-ply hybrid composites are inferior compared to the traditional carbon fibre composites due to the low mechanical properties of S-glass composites. However, taking into account the benefits of high strain to failure and load-carrying capacity of these pseudo-ductile composites, reduced safety margins is possible when designing structural parts made of these novel materials than current traditional composites. Together with the impressive fatigue performance of pristine and overloaded hybrid composites, the actual load design limit of pseudo-ductile composites could be pushed close to the knee-point stress and therefore improve the structural efficiency of the composites. Furthermore, gradual and progressive failure will ensure a non-catastrophic failure in the structure, thus any over-loading before final failure can be visually inspected.

Nonetheless, there are also some drawbacks of these UD thin-ply hybrid composites limiting their use in industrial applications. The first limitation is the high cost of the thin-ply laminates compared to the standard thickness laminates. Thickness requirement of a structure is in the order of more than several plies, meaning that an increase of the total cost of materials and time for lay-up is inevitable if using thin-ply laminates. The quality of the thin-ply prepregs was

such that they are difficult to handle in manufacturing since the prepregs do not stick to each other easily without additional heat and pressure being applied. Although only moderate heat and pressure are needed to attach the plies together, it will add more time for the lay-up process. The cured thin-ply hybrid laminates can be very flexible when only one or two thin-plies are incorporated, making them prone to mishandling during cutting. To alleviate this limitation, a proper rig for machining which could guide the hybrid laminates through the cutting process is needed. This rig should be able to cut the thin-ply and standard thickness hybrid laminates into a relatively precise dimension with minimal damage.

Another limitation is that the unidirectional thin-ply hybrid laminates can only be applied in the case where the structure is loaded primarily in the longitudinal fibre direction, due to the lack of plies in the other loading directions (90^o, 45^o, 30^o, 60^o, etc), which is not realistic in many industrial application. However, unidirectional hybrids have potential to be used in rotor blades, where tensile and compressive stress are acting on the blade when it is flapping and with continuous operation, they may also suffer from fatigue loading. It has been shown in this work, that it is possible to achieve gradual and progressive failure in tension, compression and fatigue loading when using UD thin-ply hybrid composites. Because damage is visible in this hybrid material, it can be used as a damage indicator (sensor) for structural applications such as a gas pressure vessel by having the material located at the outer layer of the vessel so any overloading can be detected easily.

7.2 Recommendation for future work

Characterisation of unidirectional thin-ply hybrid composites under various loading configurations has been presented in this thesis and several key areas in this field deserve further attention which will be explained below:

7.2.1 Quasi-static cyclic loading of UD thin-ply hybrid composites

Some results of the quasi-static cyclic loading-unloading response of UD thin-ply hybrid laminates have shown that the stiffness loss for the hybrids was due to fragmentation of the carbon plies and stable delamination. Small amounts of hysteresis and residual strain due to significant reversed shear stress between the ply interface were observed. The high shear stresses between the carbon and glass plies cause the matrix to deform, leaving a residual strain at zero load point. The results suggested that the observed deformation is permanent at the zero load point of eacy cycle. However, after reaching this point, the specimens were immediately reloaded without any time for relaxation. To examine the permanence of the deformations, the loading at zero load point of each cycle could be halted for a predetermined time. If the deformations were not permanent, then there would be a reduction of strain at zero load on the stress-strain curve. Another possible explanation for the existence of residual strain is due to the accumulation of debris between the open cracks preventing the surface cracks to return to the original state when unloaded.

In order to fully understand the source of hysteresis and residual strain in the UD hybrid laminates, it would be interesting to also conduct in-situ testing of the hybrid to study in detail the damage behaviour (fibre breakage, matrix deformation, etc) of these hybrid laminates during quasi-static cyclic loading.

At the end of each loading cycle, there are residual black-lines (intact carbon ply) where the shear stress is less than the yield shear strength at the interface, thus leaving the residual carbon ply undamaged. Not much information from the general literature review is known about the yield shear strength of the UD thin-ply hybrid composites. Because the yield shear strength is also an important parameter in the design of hybrid composites, experimental work to accurately determine the shear yield strength could be conducted in the future.

Subsequently, it is of interest to study the stress-strain behaviour for a complete tension-compression loading-unloading cycle conducted on this hybrid composite. This will allow a complete stress-strain envelope to be observed and to study the different damage behaviour of both load cases. Careful specimen design needs to be considered to avoid global buckling of the specimen, due to the compression loading.

7.2.2 Compression loading of UD thin-ply hybrid composites

Pseudo-ductile behaviour under direct compression loading has been successfully obtained for $[SG_1/(C_1/SG_1)_{17}]$ and $[SG_1/(C_2/SG_1)_{17}]$ hybrid configurations due to fragmentation of the carbon plies followed by stable delamination. It is of interest to conduct in-situ compression testing (inside a tomography facility) for the UD thin-ply hybrid composites to study the detailed damage mechanisms after fragmentation of the carbon plies. This would explain the stress or strain transfer mechanisms between the fragmented carbon and glass plies and deduce the residual stress or strain in the carbon and glass ply. The goal is then to develop a compressive strain energy release rate equation for UD thin-ply hybrid composites based on the in-situ compression testing results.

From the compression results presented in **Chapter 4**, it is explained that the fibre fragments are in contact and still able to transfer load through the fragmented surface which further fractured the ply below the 'critical length'. This means that 'critical length' which is usually found in tension to describe the effective load transfer length is not applicable to the compression case. A complete observation and measurement of the fragmented ply length at a predetermined compressive strain level is important to conduct. The aim would be to develop a definition of 'critical length' in compression which has not been explored extensively in other works.

Preparing hybrid specimens for longitudinal compression testing is time consuming and requires precise machining. An alternative testing method could be a four-point bending test of a sandwich beam made of a wood core and the hybrid laminates to be examined used as the top skin, loaded in compression, while a standard modulus carbon ply is used as the bottom skin. This method is less time consuming because less machining is involved compared to the hybrid specimens for longitudinal compression testing. The thickness of the wood core should be thick

enough to ensure a low enough strain gradient in the hybrid laminates, so that the compression strain to failure is not affected by the strain gradient. This would make the strain to failure comparable to the strain obtained from longitudinal compression testing.

The present work has focussed solely on the compression response of UD thin-ply hybrid composites made of standard thickness S-glass/epoxy ply and a high modulus thin carbon/epoxy ply. It is of interest to replace the S-glass/epoxy ply with another standard modulus thin carbon/epoxy ply to produce all carbon UD thin ply hybrid composites. This material combination has the advantage of lower density compared to carbon/glass hybrid composites and higher stiffness. Careful design should be carried out to select the appropriate thin carbon/epoxy which has sufficient strain margin to carry the load after the high modulus thin carbon/epoxy has fragmented.

7.2.3 Flexural loading of UD thin-ply hybrid composites

Pseudo-ductile response under four-point bending has been obtained for UD thin-ply hybrid composites made of S-glass/epoxy and thin carbon/epoxy with two different moduli. It is presented in **Chapter 5** that a size effect could be responsible for the high knee-point strain on the tension side for both hybrid configurations. To examine if there is a size effect, hybrid laminates with different lengths and thicknesses could be tested in four-point bending. The length of the laminates should be carefully designed to avoid premature failure due to shear. By changing the ratio between the glass and carbon plies but keeping the length constant, it is possible to study the hybrid effect in four-point bending.

7.2.4 Fatigue loading of UD thin-ply hybrid composites

The strain to failure of the carbon ply incorporated in the UD thin-ply hybrid composites for the fatigue testing described in Chapter 6 was 1.95% resulting in full delamination of the specimens at more than thousand number of cycles. Incorporating lower strain to failure carbon such as M55 carbon/epoxy, with its 0.80 % strain, could potentially prolong the fatigue life of UD thin-ply hybrid composites, because of the lower strain in the carbon fibres, thus resulting in lower stress within the surrounding glass fibres leading to a slower fatigue damage propagation. Delamination fatigue behaviour is also governed by the matrix properties and it can be significantly affected by the hydrothermal conditions. The effect of environmental factors such as temperature and humidity on the fatigue behaviour of UD thin-ply hybrid composites should also be explored to understand its response and to possibly improve the fatigue performance at different environments.

7.2.5 Investigation of UD thin-ply hybrid composites under other loading conditions

The pseudo-ductile behaviour of UD thin-ply hybrid composites could also be exploited under different loading condition such as impact and compression after impact. With the ability of the thin plies to resist delamination, there is the potential to improve the impact performance of a structural component. A possible improvement may be seen in an increase in energy being

absorbed due to impact. It would also be interesting to study the compression after impact of this material, because as has been shown in this thesis, UD thin-ply hybrid composites are able to fail gradually after the carbon ply fragmented, so if it is designed properly, the ability of the UD thin-ply hybrid composites to fail gradually by resisting sudden delamination after carbon fibre failure could possibly improve the structure's performance in compression after impact tests.

The notched response of fibre composites is usually brittle and catastrophic failure usually occurs due to stress concentrations. Multiple fragmentation in thin-ply hybrid composites has the advantage that the stress is being distributed thereby avoiding high stress concentration in a structural component containing a notch.

APPENDIX A Elastic thermal residual strain

The elastic thermal residual strain which is determined by using the following method:

1. Calculate the free thermal strains in the central carbon layer, ε_{th} (the strain each ply would undergo if unconstrained). The free thermal strain in the longitudinal (ε_x^{th}) and transverse direction (ε_y^{th}) as given in **Equation A.12** and **Equation A.2** respectively:

$$\varepsilon_x^{th} = \alpha_{11}(T_o - T) \qquad \textbf{Equation A.12)}$$

$$\varepsilon_y^{th} = \alpha_{22}(T_o - T) \qquad \textbf{(A.2)}$$

where, T is the curing temperature which is 125 °C and T_o is the room temperature assumed at 25 °C. α_{11} is calculated by using the rule of mixtures shown in **Equation A.3**

$$\alpha_{11} = \vartheta_f \,.\, \alpha_f \,.\, \frac{E_f}{E_{comp}} + (1 - \vartheta_f) \,.\, \alpha_m \,.\, \frac{E_m}{E_{comp}} \qquad \textbf{Equation A.)}$$

Equation A.13 is applicable to calculate the coefficient of thermal expansion in the 0° fibre direction (α_{11}) where ϑ_f , α_f and E_f are the volume fraction [%], the CTE [1/K] and the elastic modulus of the fibres [GPa] respectively while α_m and E_m are the CTE and modulus of the matrix material. For the coefficient of thermal expansion in the transverse direction (α_{22}), typical values of $2.6*10^{-5}$ 1/K was chosen from the general literature. The CTE values for the different fibres shown in **Chapter 3, 4, 5 and 6** were taken from the product datasheets. For both epoxy matrices in the hybrid composite, typical values of α_m = 6.10^{-5} [1/K] and E_m = 3 GPa were assumed from the general literature. E_{comp} from **Error! Reference source not found.** is calculated based on the rule of mixtures in **Equation A.4:**

$$E_{comp} = E_f \cdot v_f + E_m \cdot (1 - v_f)$$ **Equation A.13)**

2. Calculate the [Q] matrix for each material by using **Equation A.5:**

$$[Q] = \begin{bmatrix} Q_{11} & Q_{12} & 0 \\ Q_{12} & Q_{22} & 0 \\ 0 & 0 & Q_{66} \end{bmatrix} = \begin{bmatrix} \left(\frac{E_{11}^2}{E_{11} - v_{12}^2 E_{22}}\right) & \left(\frac{v_{12} E_{11} E_{22}}{E_{11} - v_{12}^2 E_{22}}\right) & 0 \\ \left(\frac{v_{12} E_{11} E_{22}}{E_{11} - v_{12}^2 E_{22}}\right) & \left(\frac{E_{11} E_{22}}{E_{11} - v_{12}^2 E_{22}}\right) & 0 \\ 0 & 0 & (G_{12}) \end{bmatrix} \quad \textbf{(A.5)}$$

3. Calculate the $\left[\ \overline{Q}\ \right]$ for each ply by using **Equation A.6:**

$$[\overline{Q}] = \begin{bmatrix} \overline{Q_{11}} & \overline{Q_{12}} & \overline{Q_{16}} \\ \overline{Q_{12}} & \overline{Q_{22}} & \overline{Q_{26}} \\ \overline{Q_{16}} & \overline{Q_{26}} & \overline{Q_{66}} \end{bmatrix} \quad \textbf{(A.6)}$$

$\overline{Q_{11}}$, $\overline{Q_{12}}$, $\overline{Q_{16}}$, $\overline{Q_{22}}$, $\overline{Q_{26}}$, $\overline{Q_{66}}$ Are calculated through **Equation A.7**- **Equation A.12** respectively:

$$\overline{Q_{11}} = Q_{11} cos^4\theta + 2(Q_{12} + 2Q_{66}) cos^2\theta sin^2\theta + Q_{22} sin^4\theta \quad \textbf{(A.7)}$$

$$\overline{Q_{12}} = Q_{12}(cos^4\theta + sin^4\theta) + (Q_{11} + Q_{12} - 4Q_{66}) cos^2\theta sin^2\theta \quad \textbf{(A.8)}$$

$$\overline{Q_{16}} = (Q_{11} - Q_{12} - 2Q_{66}) cos^3\theta sin\theta - (Q_{22} - Q_{12} - 2Q_{66}) sin^3\theta cos\theta \quad \textbf{(A.9)}$$

$$\overline{Q_{22}} = Q_{11} sin^4\theta + 2(Q_{12} + 2Q_{66}) cos^2\theta sin^2\theta + Q_{22} cos^4\theta \quad \textbf{(A.10)}$$

$$\overline{Q_{26}} = (Q_{11} - Q_{12} - 2Q_{66}) sin^3\theta cos\theta - (Q_{22} - Q_{12} - 2Q_{66}) cos^3\theta sin\theta \quad \textbf{(A.11)}$$

$$\overline{Q_{66}} = (Q_{11} + Q_{22} - 2Q_{12} - 2Q_{66}) cos^2\theta sin^2\theta + Q_{66}(cos^4\theta + sin^4\theta) \quad \textbf{(A.12)}$$

Since θ is 0 in the UD thin-ply hybrid composites , [Q] is equal to $\left[\ \overline{Q}\ \right]$.

4. Calculate the [A_{ij}], [B_{ij}] and [D_{ij}] matrices by using **Equation A.13**- **Equation A.15** respectively:

$$A_{ij} = \sum_{k=1}^{n} \{\overline{Q_{ij}}\}_k (z_k - z_{k-1}) \quad \textbf{(A.13)}$$

$$B_{ij} = \frac{1}{2} \sum_{k=1}^{n} \{\overline{Q_{ij}}\}_k \left(z^2{}_k - z_{k-1}^2 \right) \quad \textbf{(A.14)}$$

$$D_{ij} = \frac{1}{3} \sum_{k=1}^{n} \{\overline{Q_{ij}}\}_k \left(z^3{}_k - z_{k-1}^3 \right) \quad \textbf{(A.15)}$$

Where Z_k is the thickness of each ply measured from the neutral axis (Z) of the hybrid laminate.

5. Asemble the [A B D] matrix and calculate the compliance by using **Equation A.16**:

$$[abd] = [ABD]^{-1} = \begin{bmatrix} a_{11} & a_{12} & a_{16} & b_{11} & b_{12} & b_{16} \\ a_{12} & a_{22} & a_{26} & b_{12} & b_{22} & b_{26} \\ a_{16} & a_{26} & a_{66} & b_{16} & b_{26} & b_{66} \\ b_{11} & b_{21} & b_{61} & d_{11} & d_{12} & d_{16} \\ b_{12} & b_{22} & b_{62} & d_{12} & d_{22} & d_{26} \\ b_{16} & b_{26} & b_{66} & d_{16} & d_{26} & d_{66} \end{bmatrix} \quad \textbf{(A.16)}$$

6. Calculate the thermal stress resultants by using **Equation A.17:**

$$\begin{bmatrix} N_x^{th} \\ N_y^{th} \\ N_{xy}^{th} \end{bmatrix} = \sum_{k=1}^{n} \begin{bmatrix} \overline{Q_{11}} & \overline{Q_{12}} & \overline{Q_{16}} \\ \overline{Q_{12}} & \overline{Q_{22}} & \overline{Q_{26}} \\ \overline{Q_{16}} & \overline{Q_{26}} & \overline{Q_{66}} \end{bmatrix}_k \begin{bmatrix} \varepsilon_x^{th} \\ \varepsilon_y^{th} \\ \gamma_{xy}^{th} \end{bmatrix}_k (z_k - z_{k-1}) \quad \textbf{(A.17)}$$

7. Calculate the thermal moment resultants by using **Equation A.18**:

$$\begin{bmatrix} M_x^{th} \\ M_y^{th} \\ M_{xy}^{th} \end{bmatrix} = \sum_{k=1}^{n} \begin{bmatrix} \overline{Q_{11}} & \overline{Q_{12}} & \overline{Q_{16}} \\ \overline{Q_{12}} & \overline{Q_{22}} & \overline{Q_{26}} \\ \overline{Q_{16}} & \overline{Q_{26}} & \overline{Q_{66}} \end{bmatrix}_k \begin{bmatrix} \varepsilon_x^{th} \\ \varepsilon_y^{th} \\ \gamma_{xy}^{th} \end{bmatrix}_k \frac{1}{2}(z_k^2 - z_{k-1}^2) \quad \textbf{(A.18)}$$

8. Calculate the midplane strains ($\boldsymbol{\varepsilon^0}$)and curvatures (**k**) by using **Equation A.19:**

$$\begin{Bmatrix} \varepsilon_x^0 \\ \varepsilon_y^0 \\ \gamma_{xy}^0 \\ k_x \\ k_y \\ k_{xy} \end{Bmatrix} = \begin{bmatrix} a_{11} & a_{12} & a_{16} & b_{11} & b_{12} & b_{16} \\ a_{12} & a_{22} & a_{26} & b_{12} & b_{22} & b_{26} \\ a_{16} & a_{26} & a_{66} & b_{16} & b_{26} & b_{66} \\ b_{11} & b_{21} & b_{61} & d_{11} & d_{12} & d_{16} \\ b_{12} & b_{22} & b_{62} & d_{12} & d_{22} & d_{26} \\ b_{16} & b_{26} & b_{66} & d_{16} & d_{26} & d_{66} \end{bmatrix} \begin{Bmatrix} N_x^{th} \\ N_y^{th} \\ N_{xy}^{th} \\ M_x^{th} \\ M_y^{th} \\ M_{xy}^{th} \end{Bmatrix} \quad \textbf{(A.19)}$$

9. For each ply, calculate the total ply strains ($\boldsymbol{\varepsilon}_{\text{total}}$) by using **Equation A.20**:

$$\begin{Bmatrix} \varepsilon_x^{total} \\ \varepsilon_y^{total} \\ \gamma_{xy}^{total} \end{Bmatrix} = \begin{Bmatrix} \varepsilon_x^0 \\ \varepsilon_y^0 \\ \gamma_{xy}^0 \end{Bmatrix} + z \begin{Bmatrix} k_x \\ k_y \\ k_{xy} \end{Bmatrix} \quad \textbf{(A.20)}$$

10. After the free thermal and total ply strains have been determined, the elastic thermal residual strain in the 0^o fibre direction, ε_{el} , is calculated by using **Equation A.21**:

$$\varepsilon_{\text{el}} = \varepsilon_x^{total} - \varepsilon_x^{th} \quad \textbf{(A.21)}$$

The elastic thermal residual strain in the transverse direction is not taken into account in this work since the fibre in the hyrid laminate is in the 0^o direction and the load is mainly carried by the fibre.

APPENDIX B Neutral axis

The position of the neutral axis (Z) for the asymmetric M55 and asymmetric TC35 hybrid laminates is calculated by using **Equation B.1 and Equation B.2** respectively**:**

$$Z = \frac{\overline{Z_{SG2}}\frac{1}{(a_{11})_{SG2}} + \overline{Z_{EG13}}\frac{1}{(a_{11})_{EG13}} + \overline{Z_{SG2}}\frac{1}{(a_{11})_{SG2}} + \overline{Z_{Cn}}\frac{1}{(a_{11})_{Cn}} + \overline{Z_{SG1}}\frac{1}{(a_{11})_{SG1}}}{\frac{1}{(a_{11})_{SG2}} + \frac{1}{(a_{11})_{EG13}} + \frac{1}{(a_{11})_{SG2}} + \frac{1}{(a_{11})_{Cn}} + \frac{1}{(a_{11})_{SG1}}} \quad \textbf{(B.1)}$$

$$Z = \frac{\overline{Z_{SG1}}\frac{1}{(a_{11})_{SG1}} + \overline{Z_{EG14}}\frac{1}{(a_{11})_{EG14}} + \overline{Z_{SG2}}\frac{1}{(a_{11})_{SG2}} + \overline{Z_{Cn}}\frac{1}{(a_{11})_{Cn}} + \overline{Z_{SG1}}\frac{1}{(a_{11})_{SG1}}}{\frac{1}{(a_{11})_{SG1}} + \frac{1}{(a_{11})_{EG14}} + \frac{1}{(a_{11})_{SG2}} + \frac{1}{(a_{11})_{Cn}} + \frac{1}{(a_{11})_{SG1}}} \quad \textbf{(B.2)}$$

Where a_{11} is the compliance in the fibre direction and is calculated by using **Equation A.5**-**Equation A.16.** With n is the number of carbon layers.

APPENDIX C Additional results from fatigue testing

Results from fatigue testing of pristine UD thin-ply hybrid composites at 90% of σ_k:

Specimen 1:

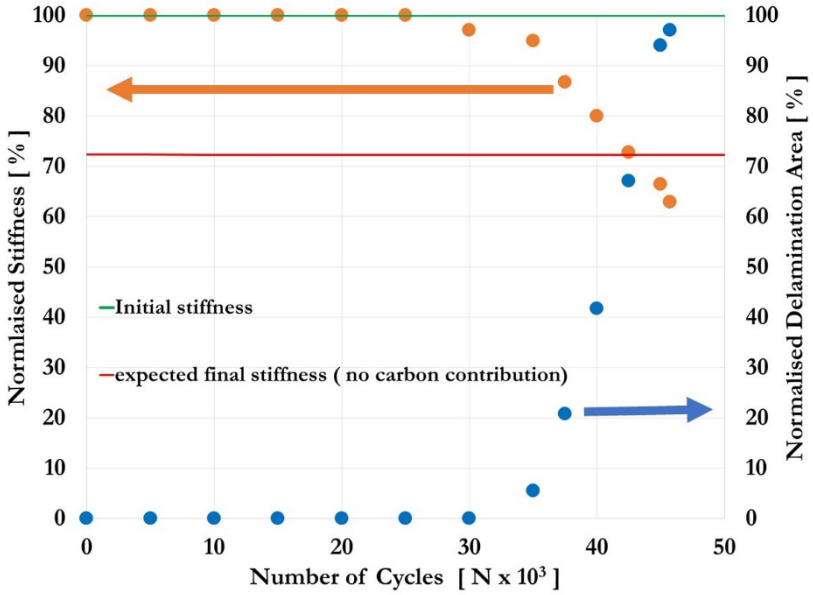

Figure C.70. Stiffness reduction and delamination area development for specimen 1 fatigued at 90% of σ_k.

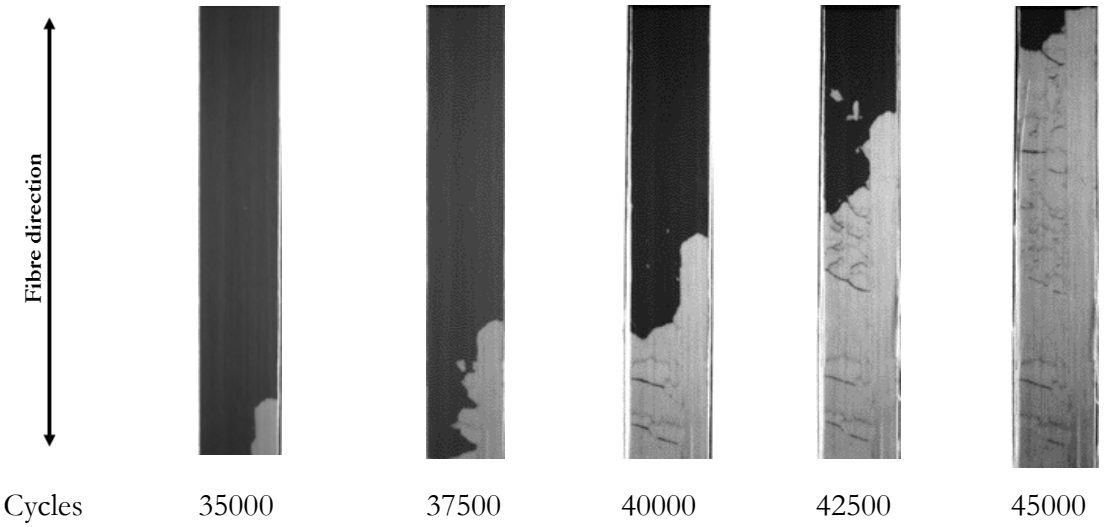

Figure C.71. Fatigue damage development for specimen 1 fatigued at 90% of σ_k.

Specimen 3:

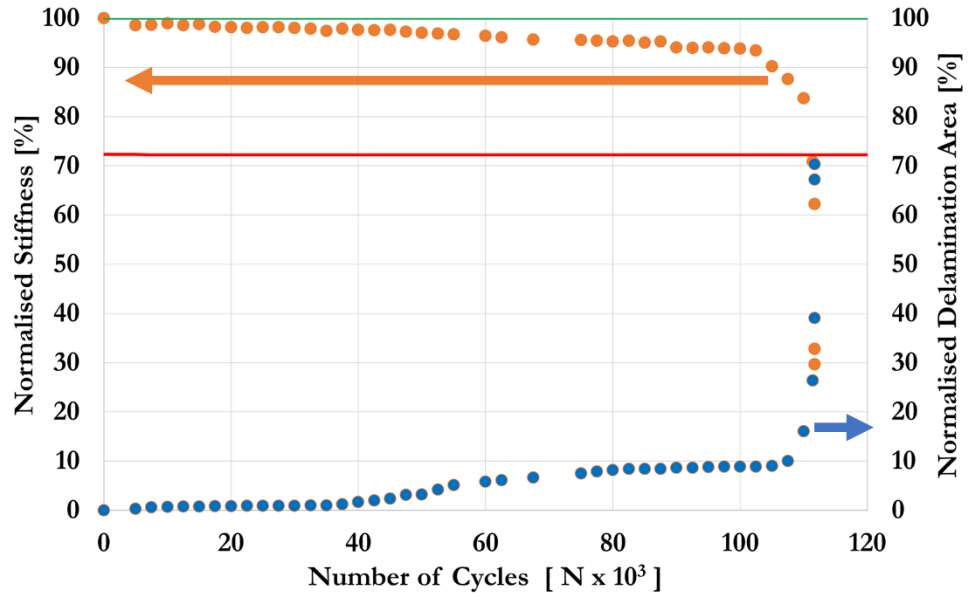

Figure C.72. Stiffness reduction and delamination area development for specimen 3 fatigued at 90% of σ_k.

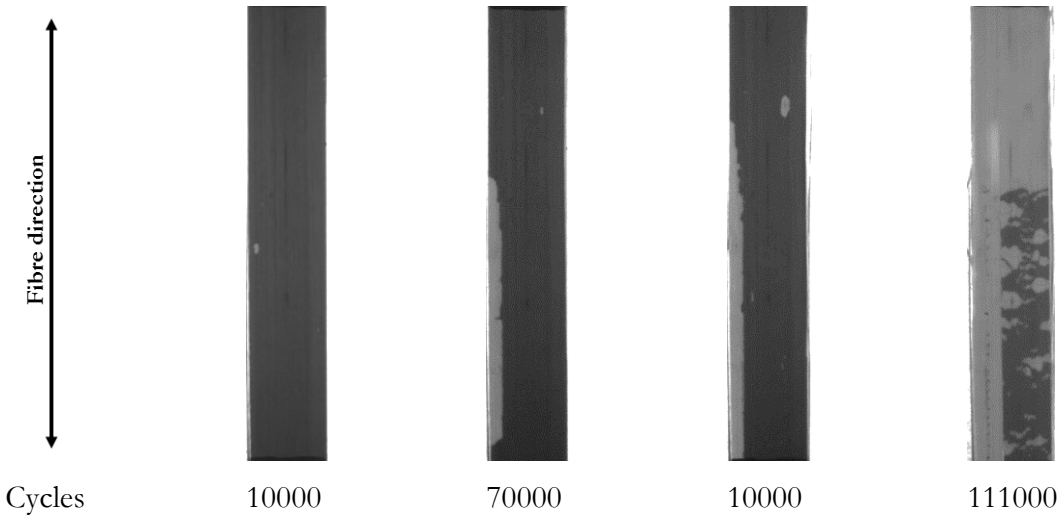

Figure C.73. Fatigue damage development for specimen 3 fatigued at 90% of σ_k.

Specimen 4:

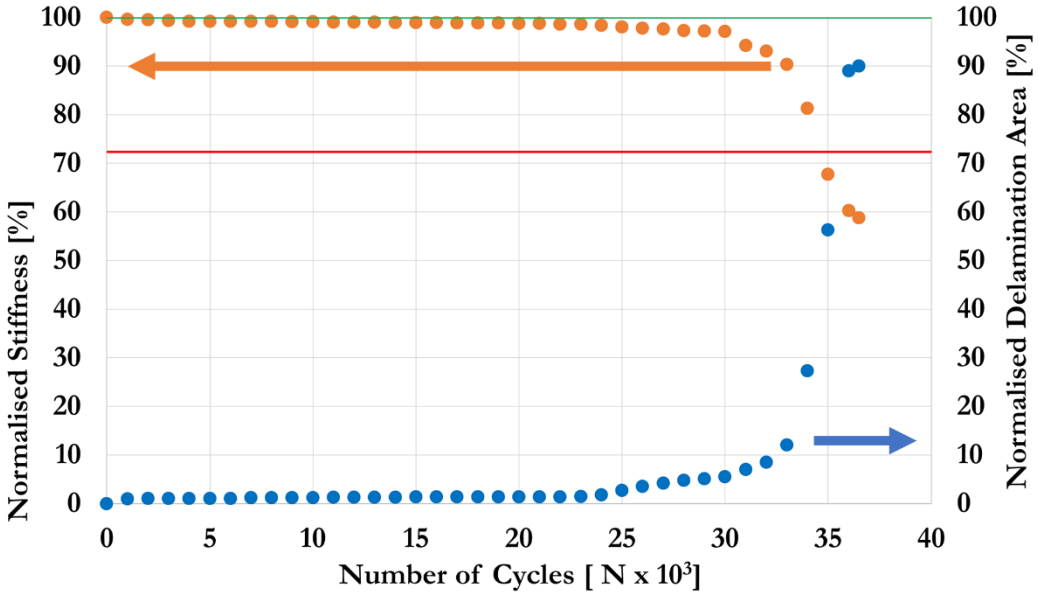

Figure C.74. Stiffness reduction and delamination area development for specimen 4 fatigued at 90% of σ_k.

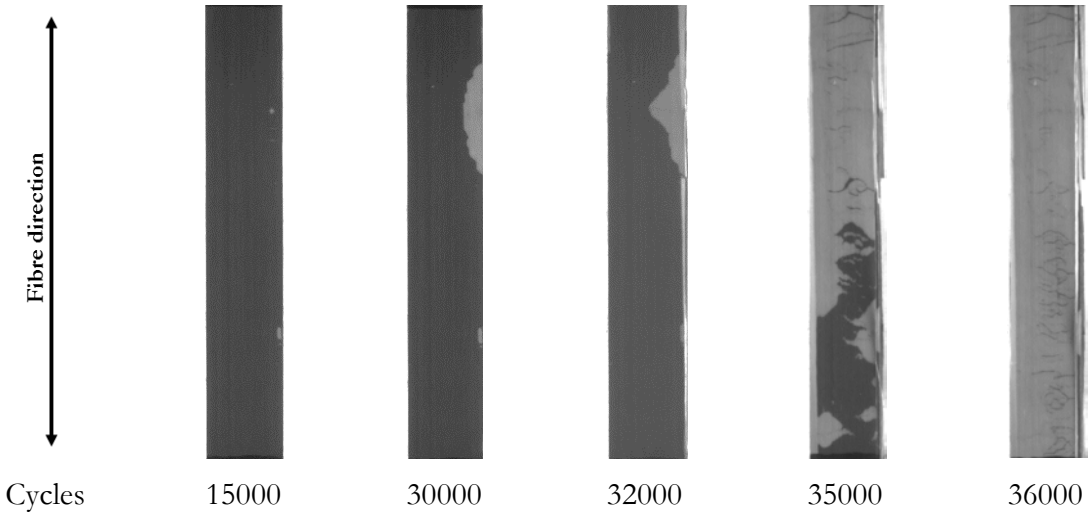

Figure C.75. Fatigue damage development for specimen 4 fatigued at 90% of σ_k.

Results from fatigue testing of overloaded UD thin-ply hybrid composites at 70% of σ_k:

Specimen 13:

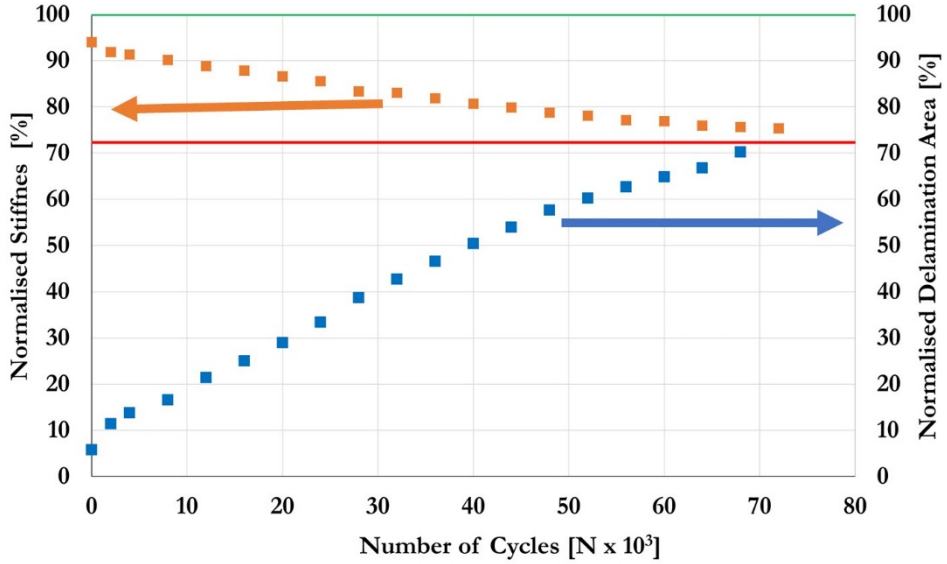

Figure C.76. Stiffness reduction and delamination area development for specimen 13 fatigued at 70% of σ_k

.

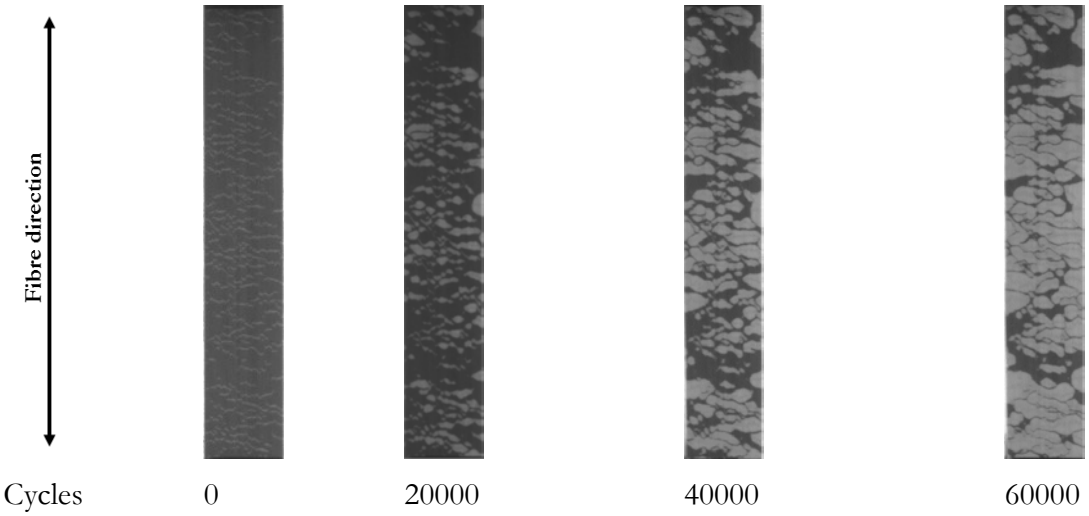

Figure C.77. Fatigue damage development for specimen 13 fatigued at 70% of σ_k.

Specimen 15:

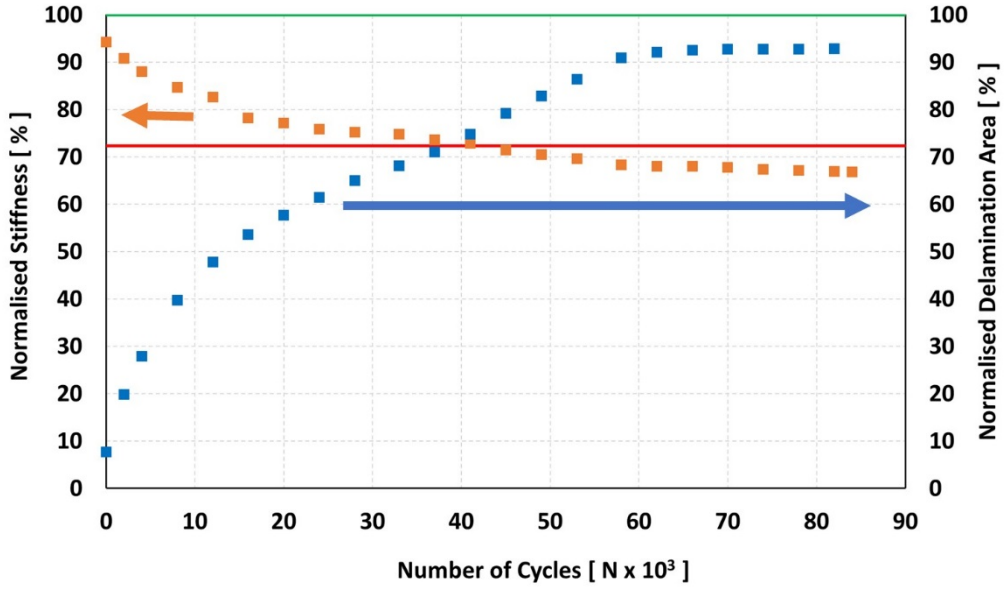

Figure C.78. Stiffness reduction and delamination area development for specimen 15 fatigued at 70% of σ_k.

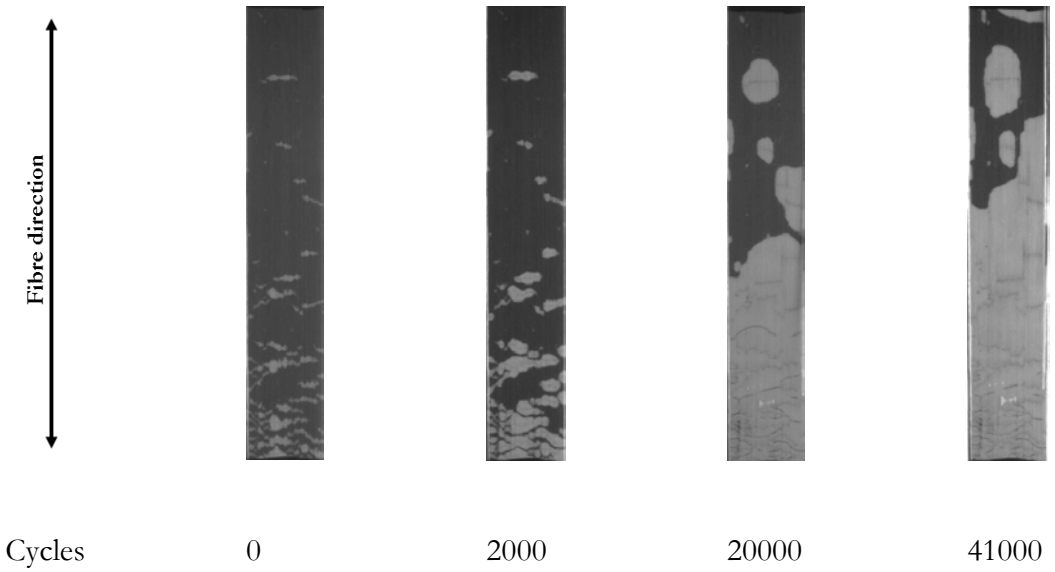

Figure C.79. Fatigue damage development for specimen 15 fatigued at 70% of σ_k.

Results from fatigue testing of overloaded UD thin-ply hybrid composites at 80% of σ_k:

Specimen 5:

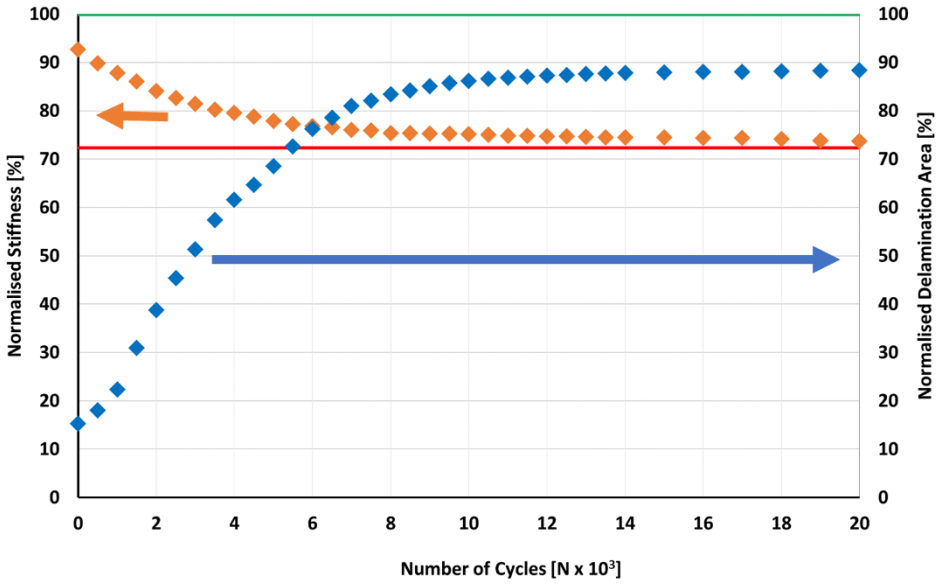

Figure C.80. Stiffness reduction and delamination area development for specimen 5 fatigued at 80% of σ_k.

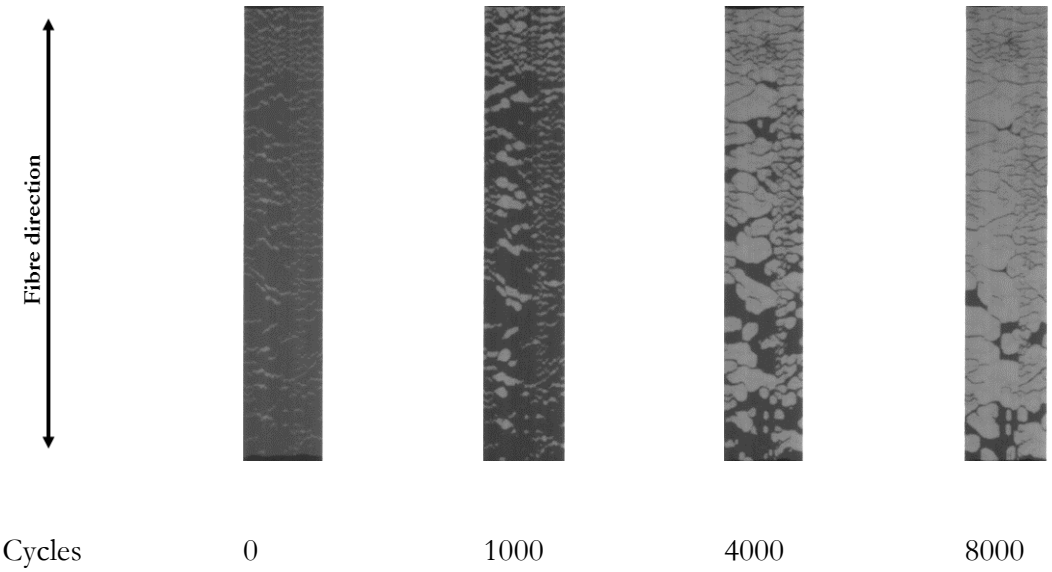

Figure C.81. Fatigue damage development for specimen 5 fatigued at 80% of σ_k.

Specimen 6:

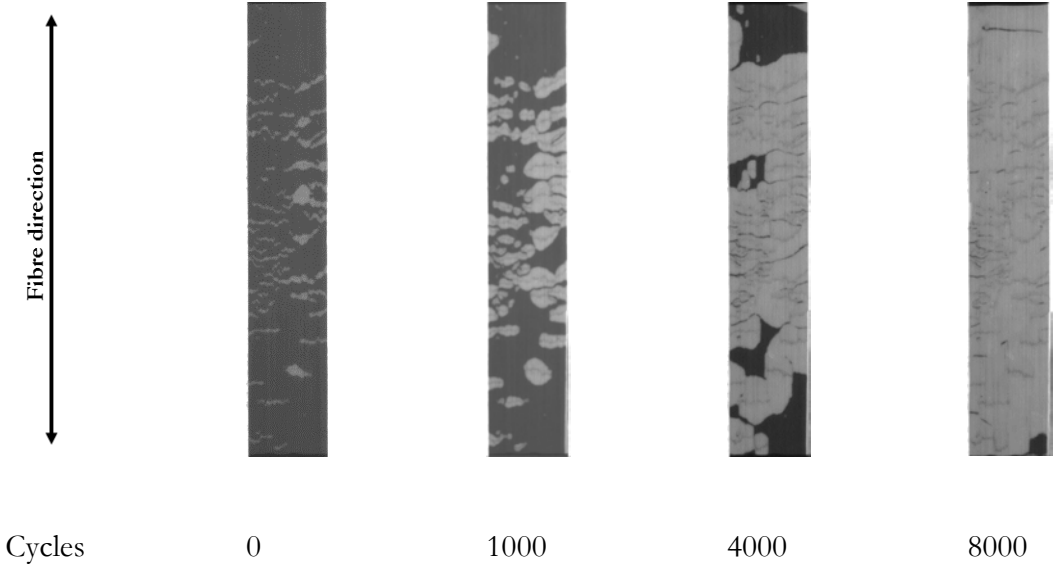

Figure C.82. Fatigue damage development for specimen 6 fatigued at 80% of σ_k..

Specimen 7:

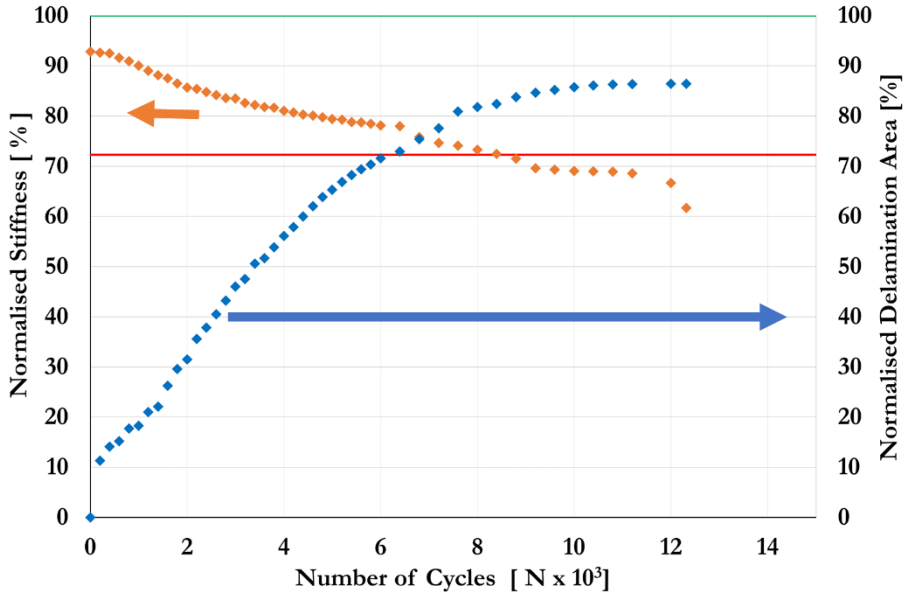

Figure C.83. Stiffness reduction and delamination area development for specimen 7 fatigued at 80% of σ_k.

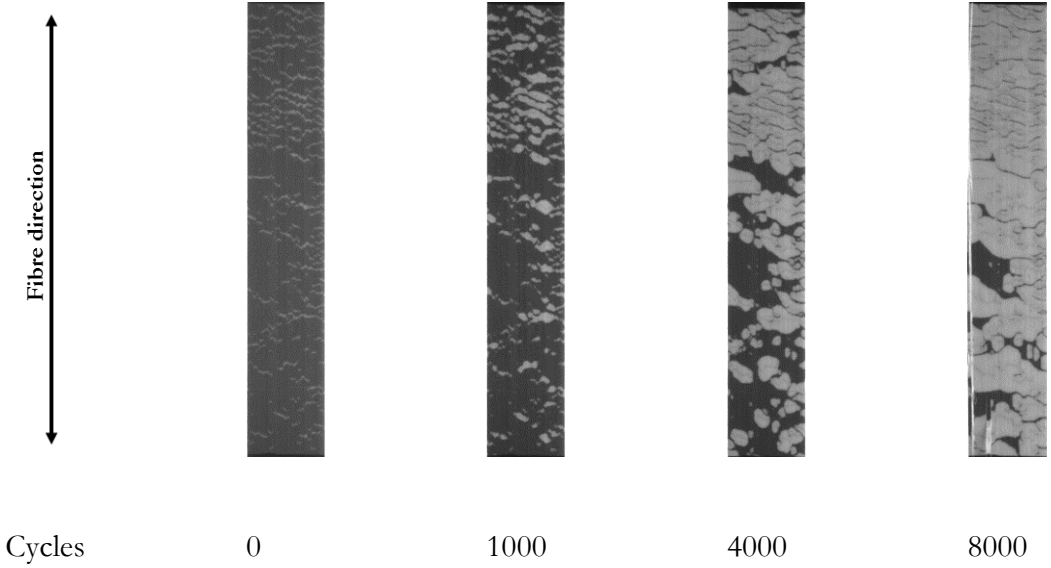

Figure C.84. Fatigue damage development for specimen 7 fatigued at 80% of σ_k..

Specimen 8

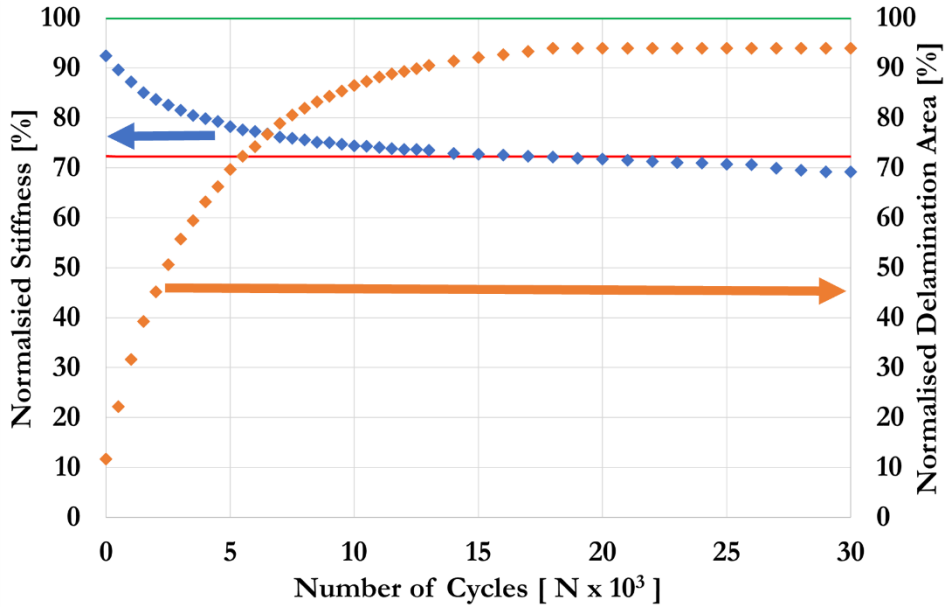

Figure C.85. Stiffness reduction and delamination area development for specimen 8 fatigued at 80% of σ_k.

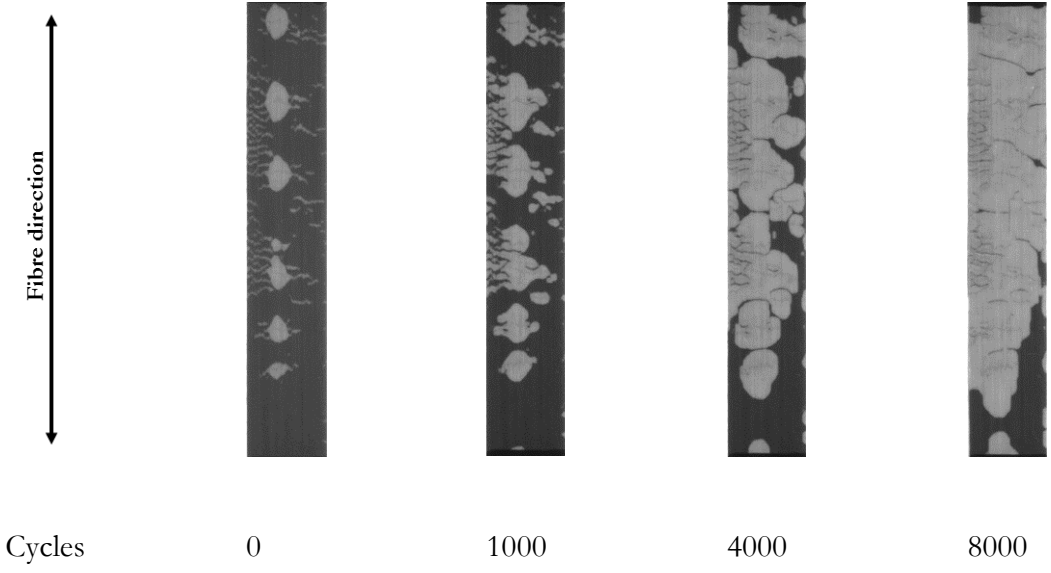

Figure C.86. Fatigue damage development for specimen 8 fatigued at 80% of σ_k.

Results from fatigue testing of overloaded UD thin-ply hybrid composites at 90% of σ_k:

Specimen 1

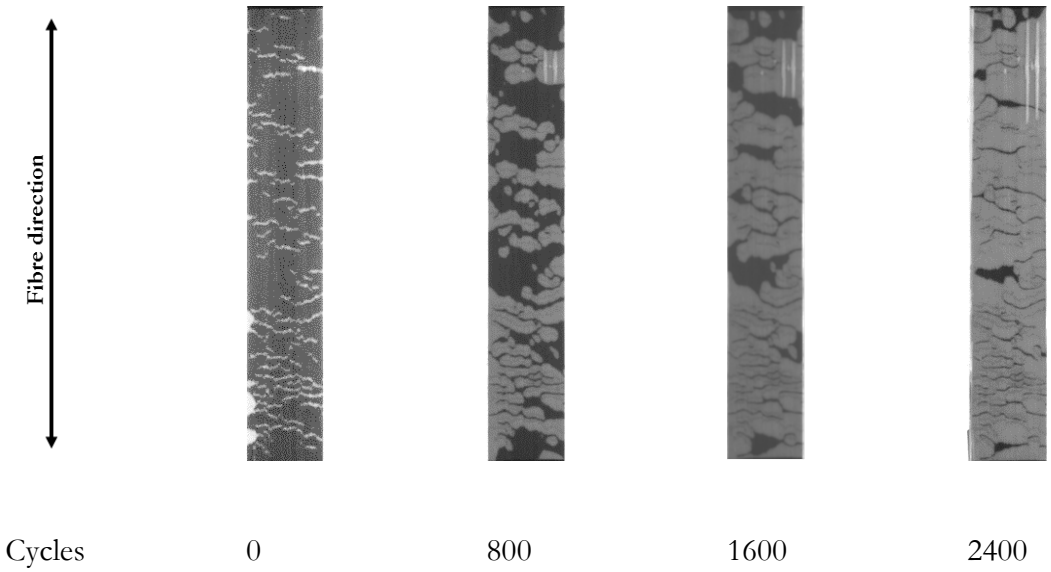

Figure C.87. Fatigue damage development for specimen 1 fatigued at 90% of σ_k.

Specimen 2

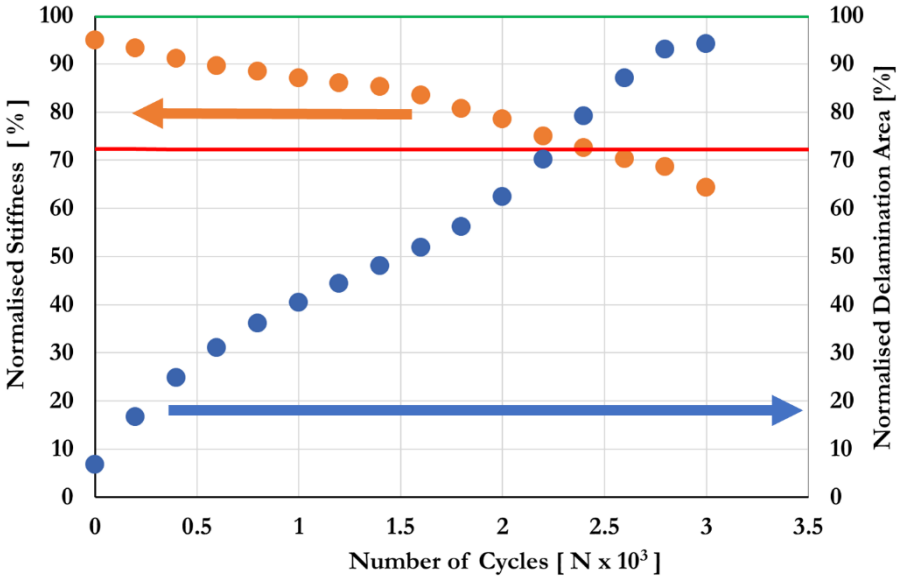

Figure C.88. Stiffness reduction and delamination area development for specimen 2 fatigued at 90% of σ_k.

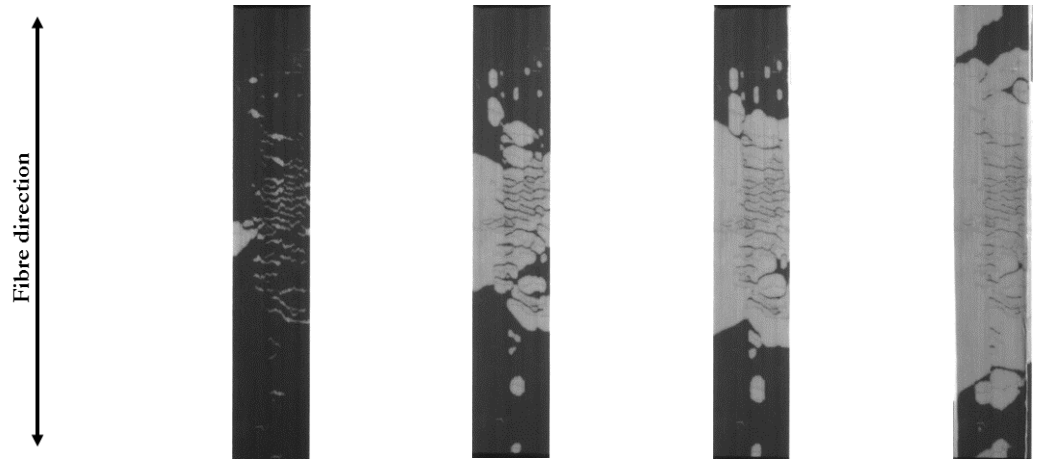

Cycles 0 800 1600 2400

Figure C.89. Fatigue damage development for specimen 2 fatigued at 90% of σ_k.

Specimen 3

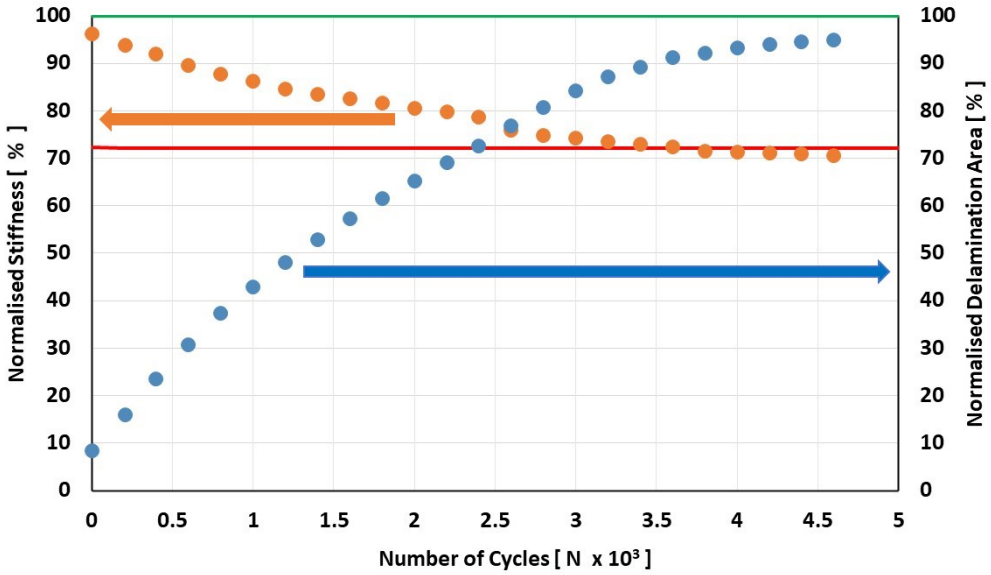

Figure C.21. Stiffness reduction and delamination area development for specimen 3 fatigued at 90% of σ_k.

Specimen 3

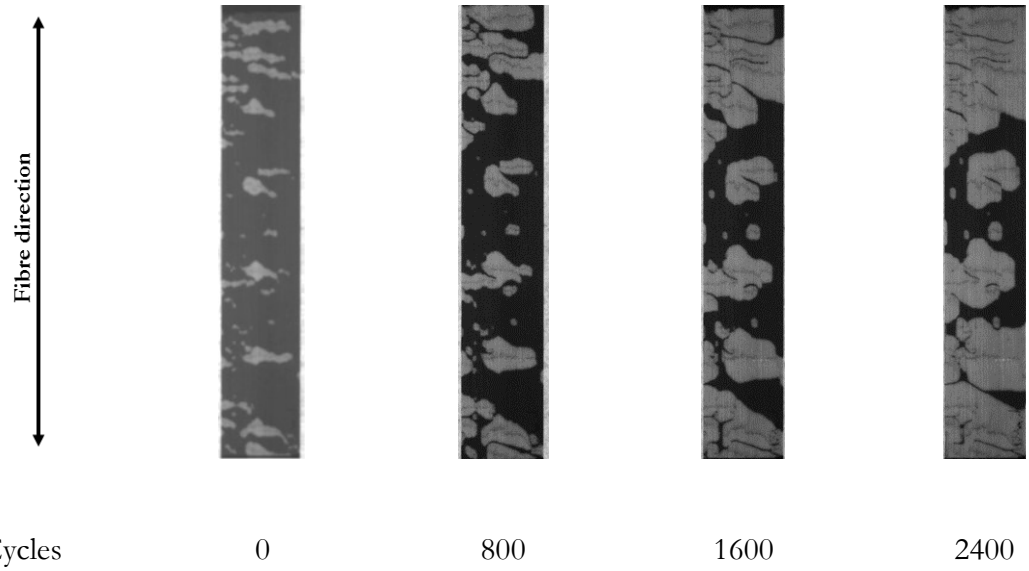

Figure C.22. Fatigue damage development for specimen 3 fatigued at 90% of σ_k.

Specimen 4

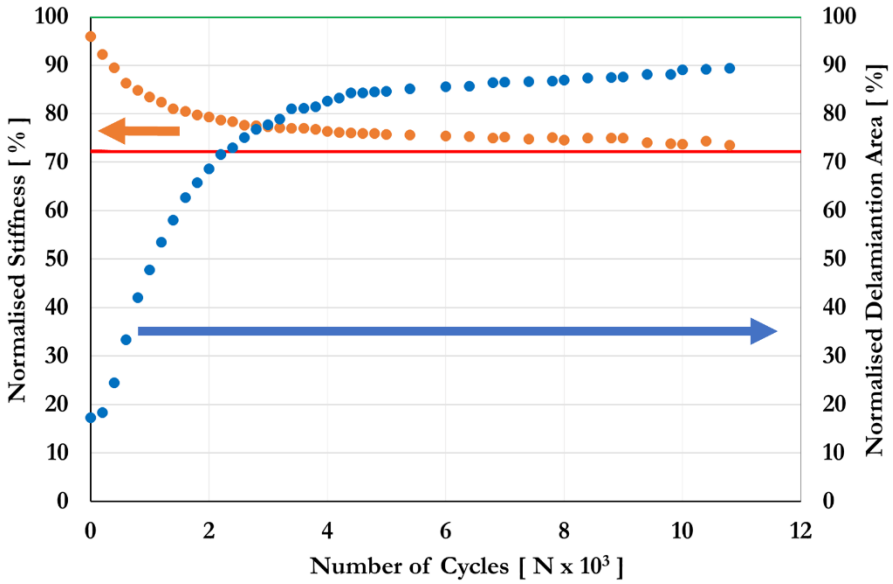

Figure C.23. Stiffness reduction and delamination area development for specimen 4 fatigued at 90% of σ_k.

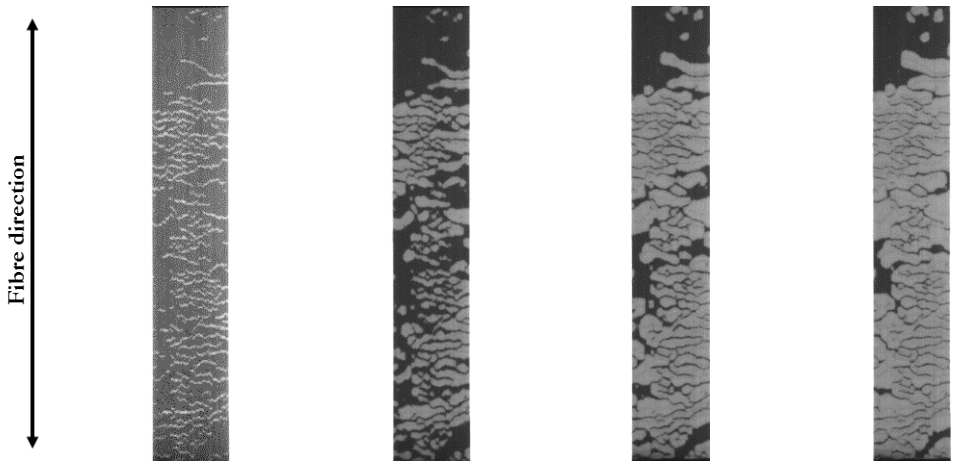

Cycles 0 800 1600 2400

Figure C.24. Fatigue damage development for specimen 4 fatigued at 90% of σ_k..

Bibliography

[1] G. P. Thomas, "Composites in Aerospace," *AZO Materials*, 2013. .

[2] S. S. Brinson LC, Reifsnider KL, Bartolotta PA, Buczek MB, Davis JW, Johnston NJ, Sastry AM, *Going to Extremes: Meeting the Emerging Demand for Durable Polymer Matrix Composites*. The National Academies, 2005.

[3] J. Fraga, "Boeing 787 from the Ground Up," *AERO Mag.*, pp. 17–23, 2006.

[4] "Airbus Group. A350 XWB: Sensational - Shape - Modern.," *2006*. [Online]. Available: http://www.a350xwb.com.

[5] A. Jacob, "Carbon fibre and cars – 2013 in review," *Reinf. Plast.*, vol. 58, no. 1, pp. 18–19, 2014.

[6] A. Jacob, "Lamborghini: 30 years of carbon fibre," *Reinf. Plast.*, vol. 57, no. 4, pp. 30–32, 2013.

[7] W. Paton, "Carbon fibre in sports equipment," *Composites*, vol. 1, no. 4, pp. 221–226, 1970.

[8] O. O. Ochoa and M. M. Salama, "Offshore composites: Transition barriers to an enabling technology," *Compos. Sci. Technol.*, vol. 65, no. 15-16 SPEC. ISS., pp. 2588–2596, 2005.

[9] M. Roseman, R. Martin, and G. Morgan, "Composites in offshore oil and gas applications," in *Marine Applications of Advanced Fibre-Reinforced Composites*, 2015, pp. 233–257.

[10] F. Taheri, *Advanced Fibre-Reinforced Polymer (FRP) Composites for Structural Applications*. Woodhead Publishing Series in Civil and Structural Engineering, 2013.

[11] L. Mishnaevsky, K. Branner, H. N. Petersen, J. Beauson, M. McGugan, and B. F. Sørensen, "Materials for wind turbine blades: An overview," *Materials (Basel).*, vol. 10, no. 11, pp. 1–24, 2017.

[12] CarbonRepairFrame, "damage-you-cant-see." [Online]. Available: http://www.carbonframerepair.com/index.php/damage-you-cant-see/.

[13] F. C. Campbell, "Chapter 1: Introduction to composite materials," *Struct. Compos. Mater.*, p. 3, 2010.

[14] B. W. ROSEN, "Tensile failure of fibrous composites," *AIAA J.*, vol. 2, no. 11, pp. 1985–1991, 1964.

[15] A. R. B. M. Fuwa, B. Harris, "Tensile failure mechanisms in carbon fibre reinforced plastics," *J. Mater. Sci.*, vol. 10, pp. 2062–2070, 1975.

[16] R. Moreton, "The effect of gauge length on the tensile strength of R.A.E. carbon fibres," *Fibre Sci. Technol.*, vol. 1, no. 4, pp. 273–284, 1969.

[17] M. El Asloun, J. B. Donnet, G. Guilpain, M. Nardin, and J. Schultz, "On the estimation of the tensile strength of carbon fibres at short lengths," *J. Mater. Sci.*, vol. 24, no. 10, pp. 3504–3510, 1989.

[18] T. Tagawa and T. Miyata, "Size effect on tensile strength of carbon fibers," *Mater. Sci. Eng. A*, vol. 238, no. 2, pp. 336–342, 1997.

[19] K. L. Pickering and T. L. Murray, "Weak link scaling analysis of high-strength carbon fibre," *Compos. Part A Appl. Sci. Manuf.*, vol. 30, no. 8, pp. 1017–1021, 1999.

[20] K. Naito, J. M. Yang, Y. Tanaka, and Y. Kagawa, "The effect of gauge length on tensile

strength and Weibull modulus of polyacrylonitrile (PAN)- and pitch-based carbon fibers," *J. Mater. Sci.*, vol. 47, no. 2, pp. 632–642, 2012.

[21] K. Honjo, "Fracture toughness of PAN-based carbon fibers estimated from strength-mirror size relation," *Carbon N. Y.*, vol. 41, no. 5, pp. 979–984, 2003.

[22] S. Ogihara, Y. Imafuku, R. Yamamoto, and Y. Kogo, "Direct evaluation of fracture toughness in a carbon fiber," *ICCM Int. Conf. Compos. Mater.*, 2009.

[23] M. Kant and D. Penumadu, "Fracture behavior of individual carbon fibers in tension using nano-fabricated notches," *Compos. Sci. Technol.*, vol. 89, pp. 83–88, 2013.

[24] H. Okuda, R. J. Young, F. Tanaka, J. Watanabe, and T. Okabe, "Tensile failure phenomena in carbon fibres," *Carbon N. Y.*, vol. 107, pp. 474–481, 2016.

[25] M. Ueda, W. Saito, R. Imahori, D. Kanazawa, and T. K. Jeong, "Longitudinal direct compression test of a single carbon fiber in a scanning electron microscope," *Compos. Part A Appl. Sci. Manuf.*, vol. 67, pp. 96–101, 2014.

[26] P. M. Jelf and N. A. Fleck, "Compression Failure Mechanisms in Unidirectional Composites," *J. Compos. Mater.*, vol. 26, no. 18, pp. 2706–2726, 1992.

[27] M. R. Wisnom, "The effect of fibre misalignment on the compressive strength of unidirectional carbon fibre/epoxy," *Composites*, vol. 21, no. 5, pp. 403–407, 1990.

[28] M. R. Wisnom and J. W. Atkinson, "Compressive failure due to shear instability: Experimental investigation of waviness and correlation with analysis," *J. Reinf. Plast. Compos.*, vol. 15, no. 4, pp. 420–439, 1996.

[29] S. H. Lee and A. M. Waas, "Compressive response and failure of fiber reinforced unidirectional composites," *Int. J. Fract.*, vol. 100, no. 3, pp. 275–306, 1999.

[30] M. C. Serna Moreno, A. Romero Gutiérrez, and J. L. Martínez Vicente, "Different response under tension and compression of unidirectional carbon fibre laminates in a three-point bending test," *Compos. Struct.*, vol. 136, pp. 706–711, 2016.

[31] M. C. Serna Moreno, A. Romero Gutiérrez, and J. L. Martínez Vicente, "First flexural and interlaminar shear failure in symmetric cross-ply carbon-fibre laminates with different response under tension and compression," *Compos. Struct.*, vol. 146, pp. 62–68, 2016.

[32] G. C. Shih and L. J. Ebert, "Flexural failure mechanisms and global stress plane for unidirectional composites subjected to four-point bending tests," *Composites*, vol. 17, no. 4, pp. 309–320, 1986.

[33] B. Harris, H. Reiter, R. Dickson, and G. Fernando, "Fatigue behaviour of carbon fibre reinforced plastics," vol. 21, no. 3, pp. 232–242, 1990.

[34] R. Talreja, "Fatigue of Composite Materials: Damage Mechanisms and Fatigue-Life Diagrams," *Proc. R. Soc. A Math. Phys. Eng. Sci.*, vol. 378, no. 1775, pp. 461–475, 1981.

[35] Y. Swolfs, I. Verpoest, and L. Gorbatikh, "Recent advances in fibre-hybrid composites : materials selection , opportunities and applications," *Int. Mater. Rev.*, vol. 64, no. 4, pp. 181–215, 2019.

[36] Hayashi T, Koyama K, Yamazaki A, Kihira M, "Development of new material properties by hybrid composition.2nd report." Composite Materials, pp. 21–25, 1972.

[37] J. Aveston and J. M. Sillwood, "Synergistic fibre strengthening in hybrid composites," *J. Mater. Sci.*, vol. 11, no. 10, pp. 1877–1883, 1976.

[38] J. Aveston and A. Kelly, "Theory of multiple fracture of fibrous composites," *J. Mater. Sci.*, vol. 8, no. 3, pp. 352–362, 1973.

[39] G. Czél and M. R. Wisnom, "Demonstration of pseudo-ductility in high performance glass/epoxy composites by hybridisation with thin-ply carbon prepreg," *Compos. Part A Appl. Sci. Manuf.*, vol. 52, pp. 23–30, 2013.

[40] J. Aveston and A. Kelly, "Tensile First Cracking Strain and Strength of Hybrid Composites and Laminates," *Philos. Trans. R. Soc. A Math. Phys. Eng. Sci.*, vol. 294, no. 1411, pp. 519–534, 1980.

[41] A. R. Bunsell and B. Harris, "Hybrid carbon and glass fibre composites," *Composites*, vol. 5, no. 4, pp. 157–164, 1974.

[42] P. W. Manders and M. G. Bader, "The strength of hybrid glass/carbon fibre composites - Part 1 failure strain enhancement and failure mode," *J. Mater. Sci.*, vol. 16, no. 8, pp. 2233–2245, 1981.

[43] K. A. Aveston J, Cooper GA, "Single and multiple fracture," *Guildf. Natl. Phys. Lab.*, pp. 15–25, 1971.

[44] J. Summerscales and D. Short, "Carbon fibre and glass fibre hybrid reinforced plastics," *Composites*, vol. 9, no. 3, pp. 157–166, 1978.

[45] D. Short and J. Summerscales, "Hybrids-a review: Part 1. Techniques, design and construction," *Composites*, vol. 10, no. 4, pp. 215–222, 1979.

[46] D. Short and J. Summerscales, "Hybrids - a review: Part 2. Physical properties," *Composites*, vol. 11, no. 1, pp. 33–38, 1980.

[47] G. Kretsis, "A review of the tensile, compressive, flexural and shear properties of hybrid fibre-reinforced plastics," *Composites*, vol. 18, no. 1, pp. 13–23, 1987.

[48] G. Marom, S. Fischer, F. R. Tuler, and H. D. Wagner, "Hybrid effects in composites: conditions for positive or negative effects versus rule-of-mixtures behaviour," *J. Mater. Sci.*, vol. 13, no. 7, pp. 1419–1426, 1978.

[49] N. Svensson, R. Shishoo, and M. Gilchrist, "Manufacturing of Thermoplastic Composites from Commingled Yarns-A Review," *J. Thermoplast. Compos. Mater.*, vol. 11, no. 1, pp. 22–56, 1998.

[50] D. Leguillon, G. Marion, R. Harry, and F. L??cuyer, "The onset of delamination at stress-free edges in angle-ply laminates - analysis of two creteria," *Compos. Sci. Technol.*, vol. 61, no. 3, pp. 377–382, 2001.

[51] R. Y. Kim, "Experimental Observations of Free-Edge Delamination," *Compos. Mater. Ser.*, vol. 5, no. C, pp. 111–160, 1989.

[52] S. Sihn, R. Y. Kim, K. Kawabe, and S. W. Tsai, "Experimental studies of thin-ply laminated composites," *Compos. Sci. Technol.*, vol. 67, no. 6, pp. 996–1008, 2007.

[53] K. Kawabe, S. Tomoda, and T. Matsuo, "Technology for spreading tow and its application to composite materials. I. A new pneumatic method for spreading carbon tow," *J. Text. Mach. Soc. Japan*, vol. 50, no. 3, pp. 50–57, Mar. 1997.

[54] R. Y. Kim and S. R. Soni, "Experimental and Analytical Studies On the Onset of Delamination in Laminated Composites," *J. Compos. Mater.*, vol. 18, no. 1, pp. 70–80, 1984.

[55] H. Saito, H. Takeuchi, and I. Kimpara, "A study of crack suppression mechanism of thin-ply carbon-fiber-reinforced polymer laminate with mesoscopic numerical simulation," *J. Compos. Mater.*, pp. 0021998313494430-, 2013.

[56] R. Amacher, J. Cugnoni, and J. Botsis, "Thin ply composites: experimental characterisation and modelling," *19th Int. Conf. Compos. Mater.*, pp. 4364–4376, 2013.

[57] R. Amacher, J. Cugnoni, J. Botsis, L. Sorensen, W. Smith, and C. Dransfeld, "Thin ply composites: Experimental characterization and modeling of size-effects," *Compos. Sci. Technol.*, vol. 101, pp. 121–132, 2014.

[58] T. Yokozeki, Y. Aoki, and T. Ogasawara, "Experimental characterization of strength and damage resistance properties of thin-ply carbon fiber/toughened epoxy laminates," *Compos. Struct.*, vol. 82, no. 3, pp. 382–389, 2008.

[59] T. Yokozeki, A. Kuroda, A. Yoshimura, T. Ogasawara, and T. Aoki, "Damage characterization in thin-ply composite laminates under out-of-plane transverse loadings," *Compos. Struct.*, vol. 93, no. 1, pp. 49–57, 2010.

[60] G. Czél, M. Jalalvand, and M. R. Wisnom, "Design and characterisation of advanced pseudo-ductile unidirectional thin-ply carbon/epoxy-glass/epoxy hybrid composites," *Compos. Struct.*, vol. 143, pp. 362–370, 2016.

[61] G. Czél and M. R. Wisnom, "Demonstration of pseudo-ductility in high performance glass/epoxy composites by hybridisation with thin-ply carbon prepreg," *Compos. Part A Appl. Sci. Manuf.*, vol. 52, pp. 23–30, 2013.

[62] M. Jalalvand, G. Czél, and M. R. Wisnom, "Damage analysis of pseudo-ductile thin-ply UD hybrid composites – A new analytical method," *Compos. Part A Appl. Sci. Manuf.*, vol. 69, pp. 83–93, Feb. 2015.

[63] M. Jalalvand, G. Czél, and M. R. Wisnom, "Parametric study of failure mechanisms and optimal configurations of pseudo-ductile thin-ply UD hybrid composites," *Compos. Part A Appl. Sci. Manuf.*, vol. 74, pp. 123–131, 2015.

[64] M. Jalalvand, G. Czél, and M. R. Wisnom, "Numerical modelling of the damage modes in UD thin carbon/glass hybrid laminates," *Compos. Sci. Technol.*, vol. 94, pp. 39–47, 2014.

[65] M. R. Wisnom, G. Cz??l, Y. Swolfs, M. Jalalvand, L. Gorbatikh, and I. Verpoest, "Hybrid effects in thin ply carbon/glass unidirectional laminates: Accurate experimental determination and prediction," *Compos. Part A Appl. Sci. Manuf.*, vol. 88, pp. 131–139, 2016.

[66] Y. Swolfs, L. Gorbatikh, and I. Verpoest, "Fibre hybridisation in polymer composites: A review," *Compos. Part A Appl. Sci. Manuf.*, vol. 67, pp. 181–200, 2014.

[67] M. Jalalvand, G. Czél, and M. R. Wisnom, "Damage analysis of pseudo-ductile thin-ply UD hybrid composites – A new analytical method," *Compos. Part A Appl. Sci. Manuf.*, vol. 69, pp. 83–93, 2015.

[68] G. Czél, M. Jalalvand, and M. R. Wisnom, "Design and characterisation of advanced pseudo-ductile unidirectional thin-ply carbon/epoxy-glass/epoxy hybrid composites," *Compos. Struct.*, vol. 143, pp. 362–370, 2016.

[69] M. R. Wisnom, "The effect of fibre misalignment on the compressive strength of unidirectional carbon fibre/epoxy," *Composites*, vol. 21, no. 5, pp. 403–407, 1990.

[70] C. Soutis, "Measurement of the Static Compressive Strength of Carbon-Fiber Epoxy Laminates," *Compos. Sci. Technol.*, vol. 42, no. 4, pp. 373–392, 1991.

[71] S. R. Frost, "Compressive Behaviour of Long-Fibre Unidirectional Composites," *J. Compos. Mater.*, vol. 26, no. 8, pp. 1151–1172, 1992.

[72] E. C. J. Wung and S. N. Chatterjee, "On the Failure Mechanisms in Laminate Compression Specimens and the Measurement of Strengths," *J. Compos. Mater.*, vol. 26, no. 13, pp. 1885–1914, 1992.

[73] G. Czél, M. Jalalvand, and M. R. Wisnom, "Demonstration of pseudo-ductility in unidirectional hybrid composites made of discontinuous carbon/epoxy and continuous glass/epoxy plies," *Compos. Part A Appl. Sci. Manuf.*, vol. 72, pp. 75–84, 2015.

[74] M. R. Wisnom, "Analysis of Shear Instability in Compression Due to Fibre Waviness," *J. Reinf. Plast. Compos.*, vol. 12, no. 11, pp. 1171–1189, 1993.

[75] B. Budiansky and N. a. Fleck, "Compressive failure of fibre composites," *J. Mech. Phys. Solids*, vol. 41, no. I, pp. 183–211, 1993.

[76] B. Budiansky and N. A. Fleck, "Compressive Kinking of Fiber Composites: A Topical Review," *Appl. Mech. Rev.*, vol. 47, no. 6S, p. S246, 1994.

[77] M. R. Wisnom, "Nonlinear analysis of misaligned unidirectional carbon fibre-epoxy compression specimens," *Compos. Eng.*, vol. 3, no. 6, pp. 547–556, 1993.

[78] P. Berbinau, C. Soutis, and I. A. Guz, "Compressive failure of 0° unidirectional carbon-fibre-reinforced plastic (CFRP) laminates by fibre microbuckling," *Compos. Sci. Technol.*, vol. 59, no. 9, pp. 1451–1455, 1999.

[79] A. Jumahat, C. Soutis, F. R. Jones, and A. Hodzic, "Fracture mechanisms and failure analysis of carbon fibre/toughened epoxy composites subjected to compressive loading," *Compos. Struct.*, vol. 92, no. 2, pp. 295–305, 2010.

[80] T. Yokozeki, T. Ogasawara, and T. Ishikawa, "Effects of fiber nonlinear properties on the compressive strength prediction of unidirectional carbon-fiber composites," *Compos. Sci. Technol.*, vol. 65, no. 14, pp. 2140–2147, 2005.

[81] T. Yokozeki, T. Ogasawara, and T. Ishikawa, "Nonlinear behavior and compressive

strength of unidirectional and multidirectional carbon fiber composite laminates," *Compos. Part A Appl. Sci. Manuf.*, vol. 37, no. 11, pp. 2069–2079, 2006.

[82] R. A. Chaudhuri, "Prediction of the Compressive Strength of Thick-Section Advanced Composite Laminates," *J. Compos. Mater.*, vol. 25, no. 10, pp. 1244–1276, 1991.

[83] R. A. Chaudhuri and H. J. Garala, "Analytical/Experimental Evaluation of Hybrid Commingled Carbon/Glass/Epoxy Thick-Section Composites under Compression," *J. Compos. Mater.*, vol. 29, no. 13, pp. 1695–1718, 1995.

[84] D. POST, F. L. DAI, Y. GUO, and P. IFJU, "Interlaminar Shear Moduli of Cross-Ply Laminates - an Experimental-Analysis," *J. Compos. Mater.*, vol. 23, no. 3, pp. 264–279, 1989.

[85] Sudarisman, I. J. Davies, and H. Hamada, "Compressive failure of unidirectional hybrid fibre-reinforced epoxy composites containing carbon and silicon carbide fibres," *Compos. Part A Appl. Sci. Manuf.*, vol. 38, no. 3, pp. 1070–1074, 2007.

[86] S. A. Tsampas, E. S. Greenhalgh, J. Ankersen, and P. T. Curtis, "Compressive failure of hybrid multidirectional fibre-reinforced composites," *Compos. Part A Appl. Sci. Manuf.*, vol. 71, pp. 40–58, 2015.

[87] H. Ikbal, Q. Wang, A. Azzam, and W. Li, "Effect of hybrid ratio and laminate geometry on compressive properties of carbon/glass hybrid composites," *Fibers Polym.*, vol. 17, no. 1, pp. 117–129, 2016.

[88] G. Czél, M. Jalalvand, and M. R. Wisnom, "Hybrid specimens eliminating stress concentrations in tensile and compressive testing of unidirectional composites," *Compos. Part A Appl. Sci. Manuf.*, vol. 91, pp. 436–447, 2016.

[89] C. Dong, J. Duong, and I. J. Davies, "Flexural properties of S-2 glass and TR30S carbon fiber-reinforced epoxy hybrid composites," *Polym. Compos.*, vol. 33, no. 5, pp. 773–781, 2012.

[90] J. W. Giancaspro and G. Christos, "Flexural Response of Inorganic Hybrid Composites With E-Glass and Carbon Fibers," *J. Eng. Mater. Technol.*, vol. 132, no. April 2010, pp. 1–8, 2014.

[91] C. Dong and I. J. Davies, "Optimal design for the flexural behaviour of glass and carbon fibre reinforced polymer hybrid composites," *Mater. Des.*, vol. 37, pp. 450–457, 2012.

[92] R. K. Prusty, D. K. Rathore, B. P. Singh, S. C. Mohanty, K. K. Mahato, and B. C. Ray, "Experimental optimization of flexural behaviour through inter-ply fibre hybridization in FRP composite," *Constr. Build. Mater.*, vol. 118, pp. 327–336, 2016.

[93] B. Burks, J. Middleton, and M. Kumosa, "Micromechanics modeling of fatigue failure mechanisms in a hybrid polymer matrix composite," *Compos. Sci. Technol.*, vol. 72, no. 15, pp. 1863–1869, 2012.

[94] Z. Wu, X. Wang, K. Iwashita, T. Sasaki, and Y. Hamaguchi, "Tensile fatigue behaviour of FRP and hybrid FRP sheets," *Compos. Part B Eng.*, vol. 41, no. 5, pp. 396–402, 2010.

[95] J. Militký, V. Kovačič, and J. Rubnerová, "Influence of thermal treatment on tensile failure of basalt fibers," *Eng. Fract. Mech.*, vol. 69, no. 9, pp. 1025–1033, 2002.

[96] A. A. J. M. Peijs and J. M. M. de Kok, "Hybrid composites based on polyethylene and carbon fibres. Part 6: Tensile and fatigue behaviour," *Composites*, vol. 24, no. 1, pp. 19–32, 1993.

[97] R. F. Dickson, G. Fernando, T. Adam, H. Reiter, and B. Harris, "Fatigue behaviour of hybrid composites," *J. Mater. Sci.*, vol. 24, pp. 227–233, 1989.

[98] G. Fernando, R. F. Dickson, T. Adam, H. Reiter, and B. Harris, "Fatigue behaviour of hybrid composites - Part 1 Carbon/Kevlar hybrids," *J. Mater. Sci.*, vol. 23, no. 10, pp. 3732–3743, 1988.

[99] G. Dai and L. Mishnaevsky, "Fatigue of hybrid glass/carbon composites: 3D computational studies," *Compos. Sci. Technol.*, vol. 94, pp. 71–79, 2014.

[100] J. D. Fuller and M. R. Wisnom, "Pseudo-ductility and damage suppression in thin ply CFRP angle-ply laminates," *Compos. Part A Appl. Sci. Manuf.*, vol. 69, pp. 64–71, 2015.

[101] J. D. Fuller and M. R. Wisnom, "Exploration of the potential for pseudo-ductility in thin ply CFRP angle-ply laminates via an analytical method," *Compos. Sci. Technol.*, vol. 112, pp. 8–15, 2015.

[102] S. Pimenta and P. Robinson, "Wavy-ply sandwich with composite skins and crushable core for ductility and energy absorption," *Compos. Struct.*, vol. 116, no. 1, pp. 364–376, 2014.

[103] H. Qian, A. Bismarck, E. S. Greenhalgh, and M. S. P. Shaffer, "Carbon nanotube grafted carbon fibres: A study of wetting and fibre fragmentation," in *Composites Part A: Applied Science and Manufacturing*, 2010, vol. 41, no. 9, pp. 1107–1114.

[104] A. Asadi, M. Miller, R. J. Moon, and K. Kalaitzidou, "Improving the interfacial and mechanical properties of short glass fiber/epoxy composites by coating the glass fibers with cellulose nanocrystals," *Express Polym. Lett.*, vol. 10, no. 7, pp. 587–597, 2016.

[105] G. Grail, S. Pimenta, S. T. Pinho, and P. Robinson, "Exploring the potential of interleaving to delay catastrophic failure in unidirectional composites under tensile loading," *Composites Science and Technology*, vol. 106. pp. 100–109, 2015.

[106] G. Czél, S. Pimenta, M. R. Wisnom, and P. Robinson, "Demonstration of pseudo-ductility in unidirectional discontinuous carbon fibre/epoxy prepreg composites," *Compos. Sci. Technol.*, vol. 106, pp. 110–119, 2015.

[107] S. Pimenta and P. Robinson, "An analytical shear-lag model for composites with 'brick-and-mortar' architecture considering non-linear matrix response and failure," *Compos. Sci. Technol.*, vol. 104, pp. 111–124, 2014.

[108] H. Yu, M. L. Longana, M. Jalalvand, M. R. Wisnom, and K. D. Potter, "Pseudo-ductility in intermingled carbon/glass hybrid composites with highly aligned discontinuous fibres," *Compos. Part A Appl. Sci. Manuf.*, vol. 73, pp. 35–44, 2015.

[109] S. Boncel, R. M. Sundaram, A. H. Windle, and K. K. K. Koziol, "Enhancement of the mechanical properties of directly spun CNT fibers by chemical treatment," *ACS Nano*, vol. 5, no. 12, pp. 9339–9344, 2011.

[110] W. J. Lee, A. J. Clancy, E. Kontturi, A. Bismarck, and M. S. P. Shaffer, "Strong and stiff: High-performance cellulose nanocrystal/poly(vinyl alcohol) composite fibers," *ACS Appl. Mater. Interfaces*, vol. 8, no. 46, pp. 31500–31504, 2016.

[111] H. Yu, K. D. Potter, and M. R. Wisnom, "A novel manufacturing method for aligned discontinuous fibre composites (High Performance-Discontinuous Fibre method)," *Compos. Part A Appl. Sci. Manuf.*, vol. 65, pp. 175–185, 2014.

[112] J. D. Fuller, "Pseudo-ductility of thin ply angle-ply laminates," 2015.

[113] Mitsubishi-Rayon, "Mitsubishi-Rayon. Mitsubishi Rayon Pyro l Carbon Fibres." [Online]. Available: https://www.mrc.co.jp/pyrofil/english/product/index.html.

[114] SKChemicals, "SKChemicals. Standard Resin : K 50." [Online]. Available: http://www.skchemicals.com/en/business2/bs_skyflex.asp.

[115] Owens Corning, "OCV Reinforcements Flite Strand S -glass." [Online]. Available: http://www.ocvreinforcements.com/hp/docs/FliteStrand_DS.pdf.

[116] Hexcel, "HexPly Prepreg," *HexPly*, 2013. .

[117] F. Laurin, N. Carrère, and J. F. Maire, "A multiscale progressive failure approach for composite laminates based on thermodynamical viscoelastic and damage models," *Compos. Part A Appl. Sci. Manuf.*, vol. 38, no. 1, pp. 198–209, 2007.

[118] M. Jalalvand *et al.*, "Energy dissipation during delamination in composite materials – An experimental assessment of the cohesive law and the stress-strain field ahead of a crack tip," *Compos. Sci. Technol.*, vol. 134, pp. 115–124, 2016.

[119] E. K. Gamstedt and R. Talreja, "Fatigue damage mechanisms in unidirectional carbon-fibre-reinforced plastics," *J. Mater. Sci.*, vol. 34, no. 11, pp. 2535–2546, 1999.

[120] M. R. Wisnom, J. Fuller, P. Suwarta, and G. Czel, "Repeated tensile loading of thin-ply pseudo-ductile laminates," *ASC proceeding 2015*, pp. 2–9, 2015.

[121] S. Kumar, D. P. Anderson, and A. S. Crasto, "Carbon fibre compressive strength and its dependence on structure and morphology," *J. Mater. Sci.*, vol. 28, no. 2, pp. 423–439, 1993.

[122] M. Nakatani, M. Shioya, and J. Yamashita, "Axial compressive fracture of carbon fibers," *Carbon N. Y.*, vol. 37, no. 4, pp. 601–608, 1999.

[123] I. Vinçon, O. Allix, P. Sigety, and M. H. Auvray, "Compressive performance of carbon fibres: experiment and analysis," *Compos. Sci. Technol.*, vol. 58, no. 10, pp. 1649–1658, 1998.

[124] Y. Sugimoto, T. Kato, M. Shioya, T. Kobayashi, K. Sumiya, and M. Fujie, "Structure change of carbon fibers during axial compression," *Carbon N. Y.*, vol. 57, pp. 416–424, 2013.

[125] P. M. Jelf and N. A. Fleck, "Compression Failure Mechanisms in Unidirectional Composites," *J. Compos. Mater.*, vol. 26, no. 18, pp. 2706–2726, 1992.

[126] B. Budiansky and N. a. Fleck, "Compressive failure of fibre composites," *Journal of the Mechanics and Physics of Solids*, vol. 41, no. I. pp. 183–211, 1993.

[127] M. R. Wisnom, "The Effect of Fibre Waviness on the Relationship between Compressive and Flexural Strengths of Unidirectional Composites," *J. Compos. Mater.*, vol. 28, no. 1, pp.

66–76, 1994.

[128] M. R. Wisnom and J. W. Atkinson, "Fibre waviness generation and measurement and its effect on compressive strength," *J. Reinf. Plast. Compos.*, vol. 19, no. 2, pp. 96–110, 2000.

[129] I. M. Daniel and H. M. Hsiao, "Is there a thickness effect on compressive strength of unnotched composite laminates?," *Int. J. Fract.*, vol. 95, no. 1–4, pp. 143–158, 1999.

[130] J. G. Häberle and F. L. Matthews, "An improved technique for compression testing of unidirectional fibre-reinforced plastics; development and results," *Composites*, vol. 25, no. 5, pp. 358–371, 1994.

[131] M. Xie and D. F. Adams, "Effect of Specimen Tab Configuration on Compression Testing of Composite Materials," *J. Compos. Mater.*, vol. 29, no. 12, pp. 1581–1600, 1995.

[132] Torayca, "M55J Data Sheet," pp. 1–2.

[133] F. Chen, S. Bazhenov, A. Hiltner, and E. Baer, "Flexural failure mechanisms in unidirectional glass fibre-reinforced thermoplastics," *Composites*, vol. 25, no. 1, pp. 11–20, 1994.

[134] C. R. P. M.G.Dobb, D.J. Johnson, "Compression behaviour of carbon fibre," *Mater. Sci.*, pp. 829–834, 1990.

[135] M. R. Wisnom and M. I. Jones, "Delamination of Unidirectional Glass Fibre-Epoxy with Cut Plies Loaded in Four Point Bending," *J. Reinf. Plast. Compos.*, vol. 14, no. 1, pp. 45–59, 1995.

[136] J. R. Wood, D. H. Wagner, and G. Marom, "The Compressive Fragmentation Phenomenon : Using Microcomposites to Evaluate Thermal Stresses , Single Fibre Compressive Strengths , Weibull Parameters and Interfacial Shear Strengths," *Proc. R. Soc. A*, no. February, 1996.

[137] G. Czél, P. Suwarta, M. Jalalvand, M. R. Wisnom, Q. Building, and U. Kingdom, "Investigation of the Compression Performance and Failure Mechanism of Pseudo-Ductile Thin Ply Hybrid," in *ICCM International Conferences on Composite Materials*, 2017, no. August, pp. 20–25.

[138] F. Tanaka, T. Okabe, H. Okuda, I. A. Kinloch, and R. J. Young, "The effect of nanostructure upon the compressive strength of carbon fibres," *J. Mater. Sci.*, vol. 48, no. 5, pp. 3–9, 2013.

[139] Formosa Plastics Corporation, "Tairfil data sheet," 2012.

[140] P. Suwarta, M. Fotouhi, G. Czel, and M. R. Wisnom, "Fatigue behaviour of pseudo-ductile thin ply hybrid composites," *ICCM21*, no. August, pp. 20–25, 2017.

[141] M. R. Wisnom, G. Czél, Y. Swolfs, M. Jalalvand, L. Gorbatikh, and I. Verpoest, "Hybrid effects in thin ply carbon/glass unidirectional laminates: Accurate experimental determination and prediction," *Compos. Part A Appl. Sci. Manuf.*, vol. 88, pp. 131–139, 2016.

[142] M. R. Wisnom, "Limitations of Linear Elastic Bending Theory Applied to Four Point Bending of Unidirectional Carbon Fibre-Epoxy," in *Proceeding of 31st Structure, Structure*

Dynamics and Materials Conference 1990, 1990, pp. 740–747.

[143] M. M. S. Isidor M. Djordjevic, Danioela R. Sekulic, Midrog N. Mitric, "Non-Hookean Elastic Behavior and Crystallite Orientation in Carbon Fibers," *J. Compos. Mater.*, vol. 44, no. 14, 2010.

[144] M. Kant and D. Penumadu, "Dynamic mechanical characterization for nonlinear behavior of single carbon fibers," *Compos. Part A Appl. Sci. Manuf.*, 2014.

[145] J. L. M. Kamp, "Non Hookean Behaviour in the Fibre Direction of Carbon-Fibre Composites and the Influence of Fibre Waviness on the Tensile Properties," *J. Compos. Mater.*, vol. 11, pp. 461–469, 1977.

[146] R.E. Bullock, "Strength Ratios of Composite Materials in Flexure and Tension," *Compos. Mater.*, 1974.

[147] M. R. Wisnom, "The Relationship between Tensile and Flexural Strength of Unidirectional Composites," *J. Compos. Mater.*, vol. 26, no. 8, pp. 1173–1180, 1992.

[148] M. R. Wisnom, "The effect of specimen size on the bending strength of unidirectional carbon fibre-epoxy," *Compos. Struct.*, vol. 18, no. 1, pp. 47–63, 1991.

[149] M. R. Wisnom, "Size effects in the testing of fibre-composite materials," *Compos. Sci. Technol.*, vol. 59, no. 13, pp. 1937–1957, 1999.

[150] M. R. W. Gergely Czél, M. Asun Cantera, Meisam Jalalvand, "Experimental determination of the volume effect on the tensile failure strain of carbon/epoxy composites," in *Comptest2017*, 2017, p. 10.

[151] M. Fotouhi, P. Suwarta, M. Jalalvand, G. Czel, and M. R. Wisnom, "Detection of fibre fracture and ply fragmentation in thin-ply UD carbon/glass hybrid laminates using acoustic emission," *Compos. Part A Appl. Sci. Manuf.*, vol. 86, 2016.

[152] A. A. J. M. Peijs and J. M. M. de Kok, "Hybrid composites based on polyethylene and carbon fibres. Part 6: Tensile and fatigue behaviour," *Composites*, vol. 24, no. 1, pp. 19–32, 1993.

[153] S. Sihn, R. Y. Kim, K. Kawabe, and S. W. Tsai, "Experimental studies of thin-ply laminated composites," *Compos. Sci. Technol.*, vol. 67, pp. 996–1008, 2007.

[154] T. K. O'Brien, "Characterization of delamination onset and growth in a composite laminate," *Damage Compos. Mater. Basic Mech. Accumulation, Toler. Charact.*, pp. 140–167, 1982.

[155] T. K. O. Brien and K. L. Reifsnider, "Fatigue damage evaluation through stiffness measurements in Boron-Epoxy Laminates," vol. 15, no. January, 1981.

[156] R. Jamison, K. Schulte, K. Reifsnider, and W. Stinchcomb, "Characterization and Analysis of Damage Mechanisms in Tension-Tension Fatigue of Graphite/Epoxy Laminates," *Eff. Defects Compos. Mater.*, pp. 21-21–35, 1984.

[157] H. T. Hahn and R. Y. Kim, "Fatigue Behavior of Composite Laminate," *J. Compos. Mater.*, vol. 10, no. 2, pp. 156–180, 1976.

[158] M. R. Wisnom, M. I. Jones, and W. Cui, "Delamination in composites with terminating

internal plies under tension fatigue loading," *ASTM Spec. Tech. Publ.*, no. 1230, pp. 486–508, 1995.

[159] G. Czél, M. Jalalvand, M. R. Wisnom, and T. Czigány, "Design and characterisation of high performance, pseudo-ductile all-carbon/epoxy unidirectional hybrid composites," *Compos. Part B Eng.*, vol. 111, pp. 348–356, 2017.

[160] G. Frossard, "Fracture of thin-ply composites : effects of ply thickness PAR," *PhD thesis*, vol. 8032, 2017.

[161] G. Allegri, M. I. Jones, M. R. Wisnom, and S. R. Hallett, "A new semi-empirical model for stress ratio effect on mode II fatigue delamination growth," *Compos. Part A Appl. Sci. Manuf.*, vol. 42, no. 7, pp. 733–740, 2011.

[162] G. Allegri, M. R. Wisnom, and S. R. Hallett, "A new semi-empirical law for variable stress-ratio and mixed-mode fatigue delamination growth," *Compos. Part A Appl. Sci. Manuf.*, vol. 48, no. 1, pp. 192–200, 2013.